Surface Science Reports 79 (2024) 100637

Contents lists available at ScienceDirect

Surface Science Reports

journal homepage: www.elsevier.com/locate/surfrep

Review Article

Hexagonal boron nitride on metal surfaces as a support and template

László Óvári [a,b], Arnold Péter Farkas [a,b], Krisztián Palotás [a,c], Gábor Vári [d], Imre Szenti [a], András Berkó [a], János Kiss [a,*], Zoltán Kónya [a,d,**]

[a] HUN-REN-SZTE Reaction Kinetics and Surface Chemistry Research Group, University of Szeged, H-6720 Szeged, Hungary
[b] Extreme Light Infrastructure-ALPS, ELI-HU Non-Profit Ltd., Szeged, 6720, Hungary
[c] Institute for Solid State Physics and Optics, HUN-REN Wigner Research Center for Physics, Budapest, Hungary
[d] University of Szeged, Interdisciplinary Excellence Centre, Department of Applied and Environmental Chemistry, H-6720, Rerrich Béla Tér 1, Szeged, Hungary

ARTICLE INFO

Keywords:
hexagonal boron nitride
template
Heterostructures
reduced dimensional materials
Catalysis
Interfaces

ABSTRACT

The synthesis and characterization of two dimensional materials are in the focus of nanomaterial and surface science, heterogeneous catalytic and nanoelectronic research laying the basis for various technological applications. Hexagonal boron nitride (h-BN) is an important member of 3D and reduced dimensional materials. Atomically clean sp^2-hybridized 2D nano-layers can be grown on various metal supports by different chemical and physical vapor deposition techniques. In case of a significant lattice mismatch and a strong interaction at the h-BN/metal interface, a periodically undulating monolayer - a so-called "moirè structure" - is formed. In the present review, we address some important characteristics of h-BN prepared on several metal surfaces, and we focus on its application as a template for individual atoms, metal clusters and molecules. Moreover, several experimental findings are collected about the features and applications of monolayer h-BN nanosheets as supporting materials. We highlight the results of recent surface science studies, which emphasize the unique role of h-BN including nanomeshes in characteristic adsorption properties, stability and catalytic activity. The characterization of few layer and defective h-BN involving their catalytic applications are also the subject of the present review. We present a comprehensive overview on the electronic and vibrational states of nanoparticles (covered by adsorbates, as well) monitored by surface spectroscopy tools, e.g. XPS, ARPES, UPS, LEIS, AES, STS and HREELS. We also elaborate on the structural and morphological information of h-BN nanoobjects obtained by scanning probe microscopy (SPM). It is also highlighted that density functional theory (DFT) is considered as a very important complementary technique contributing to the better understanding of experimental results. Beside updated recollection of key findings, we outline the present and future research directions of 2D materials and their heterostructures including h-BN-based systems.

1. Introduction

Boron nitride (BN) is a compound family with alternating linked boron and nitrogen atoms of 1:1 stoichiometry. BN (so-called "white graphene") has recently gained considerable interest, since its different allotropes are structural analogues to carbon phases [1]. From a structural point of view, beside the hexagonal, graphite-like layered BN form, there exist other crystalline forms such as cubic BN (*c*-BN) similar to diamond and wurtzite BN (w-BN) analogous to lonsdaleite. Concerning dimensionality, different morphological BN configurations can be synthetized [2–5] fullerene-like BN nanospheres, 1D nanotubes, wires (fibers) and nanoribbons, 2D nanosheets as well as 3D nanoporous BN [6]. Two sp^2-bonded layered configurations can be distinguished, i.e. hexagonal BN (h-BN) and rhombohedral BN (*r*-BN) corresponding to h-graphite and r-graphite. Among these structures, h-BN sheets have been mostly studied [7–12]. These sheets are isostructural and isoelectronic to graphene [13,14]. The h-BN is composed of B and N atoms forming a honeycomb-like structure, where the atoms are linked with strong covalent bonds [15–17]. However, the electron distribution between the B–N atoms is significantly different than for *C*–C as N has a higher electronegativity than B, therefore attracting the electrons more strongly [15,18–20]. 3D and 2D h-BN have been applied in many technological applications in recent years, owing to their interesting electronic and chemical properties [21–23]. Most importantly, the electrically insulating 2D h-BN is an excellent decoupling support for

* Corresponding author.
** Corresponding author.
E-mail address: jkiss@chem.u-szeged.hu (J. Kiss).

https://doi.org/10.1016/j.surfrep.2024.100637
Received 17 November 2023; Received in revised form 3 June 2024; Accepted 3 June 2024
Available online 8 June 2024

List of acronyms (in alphabetical order)

0-3D	0, 1, 2, 3 dimensional materials
AES	Auger electron spectroscopy
AFM	Atomic force microscopy
ALE	Atomic layer epitaxy
APCVD	Atmospheric pressure chemical vapor deposition
ARPES	Angle-resolved photoemission spectroscopy
BCN	Boron carbon nitride
BE	Binding energy in photoelectron spectroscopy
BN	Boron nitride
BNNF	Boron nitride nanofiber
BNNS	Boron nitride nanosheet
BNNT	Boron nitride nanotube
CNT	Carbon nanotube
COFs	Covalent organic frameworks
CVD	Chemical vapor deposition
DCA	Aromatic organic molecules
DFT	Density functional theory
DRIFTS	Diffuse reflection infrared Fourier transform spectroscopy
DRM	Dry reforming of methane
EELS	Electron energy loss spectroscopy
E_g	Band gap
ESCA	Electron spectroscopy for chemical analysis
Gr	Graphene
h-BN	Hexagonal boron nitride
HER	Hydrogen evolution reaction
HOMO	Highest occupied molecular orbital
HREELS	High resolution electron energy loss spectroscopy
HRTEM	High resolution transmission microscopy
HRXPS	High resolution photoelectron spectroscopy
IPS	Ionization potentials
IR	Infrared spectroscopy
K	Kelvin (temperature unit)
L	Langmuir ($1L = 10^{-6}$ Torr*s)
LEED	Low energy electron diffraction
LEIS	Low energy ion scattering
LH	Langmuir-Hinshelwood
LO	Longitudinal optical phonon
LUMO	Lowest unoccupied molecular orbital
MALDI	Matrix-assisted laser desorption/ionization mass spectroscopy
MBE	Molecular beam epitaxy
MD	Molecular dynamics
ML	Monolayer
MLP	Machine-learning potential
MO	Molecular orbital
MUC	Moirè unit cell
MS	Mass spectrometry
NEXAFS	Near edge x-ray absorption fine structure
NP	Nanoparticle
OER	Oxygen evolution reaction
ORR	Oxygen reduction reaction
PAX	Photoemission of adsorbed xenon
PES	Photoelectron spectroscopy
QD_s	Quantum dots
RHEED	Reflection high-energy electron diffraction
RT	Room temperature
RWGS	Reversed water gas shift reaction
SAA	Single atom adsorbent
SAC	Single atom catalysis
SEM	Scanning electron microscopy
SFG	Sum-frequency generation
SMSI	Strong metal support interaction
SPE	Single-photon emitter
SPM	Scanning probe microscopy
SS	Surface states
STEM	Scanning transmission electron microscopy
STM	Scanning tunneling microscopy
STS	Scanning tunneling spectroscopy
TDS	Thermal desorption spectroscopy
TEM	Transmission electron microscopy
TO	Transverse optical phonon
TPD	Temperature programmed desorption
TPXPS	Temperature programmed x-ray photoelectron spectroscopy
UHV	Ultra-high vacuum
UPS	Ultraviolet photoelectron spectroscopy
vdW	Van der Waals
VTSTM	Variable-temperature scanning tunneling microscopy
WHSV	Weight hourly space velocities
XAS	X-ray absorption spectroscopy
XC	Exchange correlation function
XMCD	X-ray magnetic circular dichroism
XMLD	X-ray magnetic linear dichroism
XPD	X-ray photoelectron diffraction
XPS	X-ray photoelectron spectroscopy
XRD	X-ray diffraction
Φ	Work function
Θ	Coverage expressed in monolayer

graphene nanoelectronics [24–27]. The extraordinary properties of h-BN are also beneficial for advancements in emerging photonic and electronic applications [28]. Nanopores containing 2D h-BN offer exciting opportunities for applications in energy storage, optical modulation, DNA sequencing, and quantum information technologies [29,30]. Recently, it was demonstrated that h-BN is a proper candidate as oxideless catalyst support [31,32]. Extremely small Au nanoclusters (Au_{55}) supported on chemically and electronically inert BN surface can adsorb and activate O_2 for selective oxidation [33]. Decomposition of C_2H_5OH on Au/h-BN/Rh (111), at an optimal Au coverage, showed high selectivity towards "CO-free" hydrogen production where C_2H_5OH dehydrogenates to hydrogen and acetaldehyde without further transformation [23]. Besides, recent studies demonstrated that h-BN alone or decorated by small metal nanoparticles is a highly selective catalyst in hydrogen formation, oxygen evolution, oxidative dehydrogenation, hydrogenation or partial oxidation reactions [34–38]. Furthermore, it also turned out that h-BN is an active support or additive in photo- and electrocatalysis and in electrochemical energy storage including batteries [39–42]. Recent technological advances opened up a new direction of h-BN research associated with promising gas sensors. A nice review published recently summarizes several target gases as ethanol, H_2, CH_4, C_3H_6, NO_x where the performance of h-BN based sensors were outstanding [43].

The application spectrum of h-BN has been markedly broadened since it was recognized that the h-BN monolayer formed on Rh (111) has a highly regular corrugation, which is often termed in the literature as a "nanomesh", which is a geometric "moirè" pattern. The periodic undulation of continuous h-BN monolayers on Rh (111) and on some other low index metal surfaces is mostly governed by the lattice mismatch and the strength of interaction between h-BN and the metal substrate [7,15]. This type of h-BN structure was confirmed using specific spectroscopic, diffraction and microscopic techniques [44–50]. The fundamental details of the nanomesh formation was reviewed recently by W. Auwärter [15]. The unique properties of the moirè structure offer a possibility for

a tailored/templated adsorption of atoms, molecules or metal clusters. Template effects of 2D nanomaterials, including h-BN, play an essential role in the integration of supramolecular arrays as well. The resulting self-assemblies after adsorption of organic molecules, e.g., long chain alkanes or aromatic molecules have gained more and more interest primarily due to potential applications in functionalization of two dimensional nanostructures for tuning their electronic properties and in nanostructure fabrication [51–53].

In the present review we collect the most recent results about the h-BN nanomesh, and we emphasize the importance of the template effect of moiré structures prepared on metal surfaces for adsorption and catalysis. We also summarize the synthesis of 2D h-BN in different structures and morphology and the modification of h-BN with different metal adatoms and metal nanoparticles and clusters, which play a decisive role in certain catalytic processes. The 2D h-BN nanosheets, especially the nanomesh structure may direct and control the adsorption of metal nanoparticles in appropriate electronic and geometric configuration, which can lead the catalytic reaction with the desirable selectivity and activity. In this review, we summarize the literature data obtained on main features of nanoparticles and interfaces collected by several surface spectroscopic tools, such as XPS, ARPES, UPS, LEIS, AES, HREELS, etc. We also summarize the morphological information of the nanoobjects obtained by scanning probe microscopy (SPM) and transmission electron microscopy (TEM). Density functional theory (DFT) as a complementary tool contributes supporting the experimental findings and reveal aspects inaccessible to experimental investigations.

2. Preparation of hexagonal boron nitride

2.1. Synthesis of boron nitride in different structure and morphology

First, we briefly introduce the different structural forms of BN nanomaterials. Reduced dimensional BN nanomaterials were developed along with their carbon counterparts such as 0D $B_{24}N_{24}$ fullerene (sphere), 1D nanowires (nanofibers), nanotubes, nanoribbons and 2D monolayer h-BN nanosheets [6]. Spherical BN nanoparticles can be prepared by temperature controlled pyrolysis in a N_2 atmosphere, using boric acid and urea as precursors [54]. The BN nanotubes have the same nanostructure as carbon nanotubes but are characterized by a significantly higher resistance to oxidation at high temperatures. The pronounced resistance of BN nanotubes to oxidation is similar to hexagonal BN [55]. The structural models of BN nanomaterials are represented in Fig. 1.

A suggested preparation method of h-BN nanomaterials is continuously operated chemical vapor deposition (CVD) using different precursor molecules [11,16,56,57]. Table 1 Shows precursor molecules for preparation of different BN nanomaterials in the dimensionality (0-3D) of the BN products. $B(OMe)_3$ can be applied as a B source, while NH_3 can be used as a N source in the synthesis of 0D BN [58]. Boron nitride quantum dots, BNQDs, are a 0D version of h-BN nanosheets. In zero dimension, the ratio of dangling bonds at the surface of BNQDs to the saturated sp^2 BN bonds on the bulk of the 0D structure is significant. Several preparation methods for BNQDs are described in recent publications [59,60]. The BNQDs are relevant also for biology, they can be used in bio- and chemical sensing. BNQDs have already shown potential in photocatalysis, and biomedicine [59].

In the literature, a limited number of synthesis routes are suggested for nanowires and nanotubes. Preparation of h-BN nanowires through the reaction of N_2 and NH_3 over nanoscale α-FeB particles at 1100 °C is described [61]. Other methods include heating boric acid with activated carbon, multi-walled carbon nanotubes, catalytic Fe particles or a mixture of activated C and Fe nanoparticles, in the presence of ammonia [62,63]. A thick layer of pristine BN nanowires with a uniform diameter of 20 nm was produced using a CVD process with a new precursor of boron triiodide (BI_3) where N_2 and NH_3 were used as a nitrogen source [64,65]. A metal-free synthesis for BN wires (fibers) was reported recently [66] with some modifications [67]. Boric acid and melamine are used as starting materials in this preparation method. The precursor can be defined by composition as melamine-diborate ($C_3N_6H_6$ + $2H_3BO_3$) [68]. Afterwards, a second step of heat treatment of the precursor in inert atmosphere is necessary to obtain the wire- or fiber-like structure of the BN lattice.

$$H_3BO_3 + C_3N_6H_6 \rightarrow C_3N_6H_6 \bullet 2H_3BO_3 \rightarrow h-BN \quad (1)$$

A suggested method for BN tube formation is the transformation of BCN by a subsequent oxidation treatment at 650 °C [11,58]. One of the important tasks here is to find the optimal preparation procedure for the synthesis of reduced dimensional BCN. Nanotubes were produced by a substitution reaction using multiwall carbon nanotubes as a template using B_2O_3 and N_2 [69]. In this way, BCN tubes with 6–8 nm diameter can be obtained. Apart from that report, there has been much effort toward the synthesis of BCN nanotubes applying different methods, e.g., arc discharge, hot-filament assisted or CVD methods [70]. BN nanotubes were prepared in reaction of NiB_x powders with N_2 atmosphere at high temperatures [71]. The as-prepared BNNTs were sonicated in 8 M HCl acid to dissolve the residual Ni particles. BN nanotubes were also produced by a ball milling and annealing process [72,73]. Amorphous boron was ball milled in a vertical rolling mill filled by NH_3 gas at 300

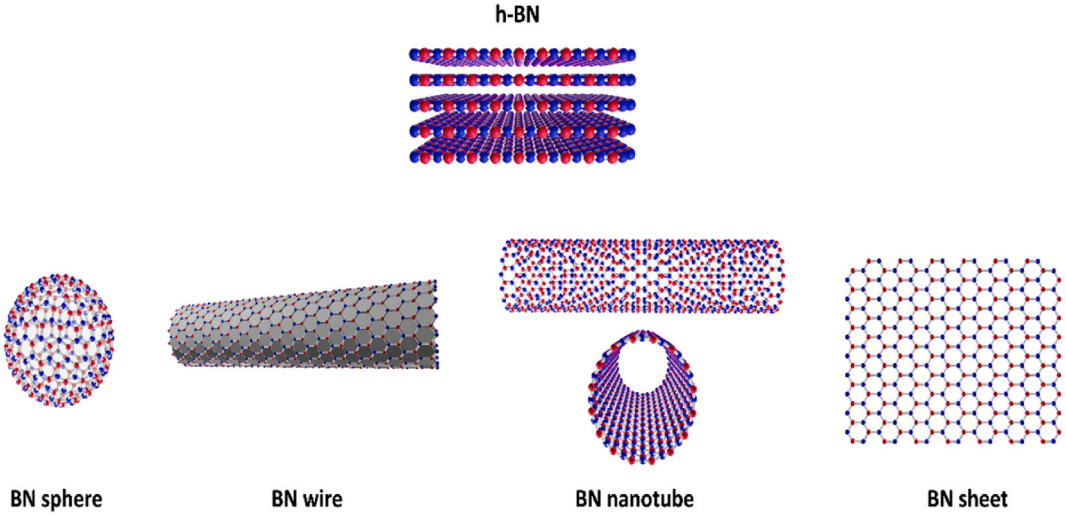

Fig. 1. Structural models of different dimensionality BN nanomaterials.

Table 1
B and N containing starting species (precursor molecules) for formation of different BN nanostructures *(concerning the content of this table - which presents only examples for special precursors -, we call the attention for several recent overview works for a more completeness* [11,15,16,59,60,75,76]*).*

B containing species	N containing species	substrate for formation	preparation technique	BN nanostructure produced	References
name/formula	name/formula				
boric acid H_3BO_3	carbamid $CO(NH_2)_2$	carbon spheres	pyrolysis	$B_{24}N_{24}$ sphere	[54]
trimethyl borate $B(OMe)_3$	ammonia NH_3	carbon spheres	pyrolysis	B_xN_y sphere	[58]
ammonia-borane BH_3NH_3		metals & non-metals	CVD	BN quantum dot & nanoribbon	[59,60]
α-FeB nanoparticles α-FeB	nitrogen & ammonia N_2 & NH_3	α-FeB nanoparticles	CVD	BN nanowire	[61]
boric acid	melamine $(NH_2)_3N_3C_3$	self-assembly	pyrolysis	BNnanofibre,	[67–69]
boron triiodide BI_3	nitrogen & ammonia N_2 & NH_3	Fe nanoparticles	pyrolysis	BN nanowire	[64]
boric acid H_3BO_3	nitrogen & ammonia N_2 & NH_3	Fe nanoparticles	pyrolysis	BN nanotube	[62]
nikkel-borid powder NiB_x	nitrogen N_2	–	pyrolysis	BN nanotube	[71]
amorf boron B	ammonia NH_3	stainless steel balls	high pressure milling	BN nanotube	[72,73]
hexamethyl borazine $C_6H_{18}B_3N_3$		Rh (111), Ir (111)	CVD	h-BN nanodonuts	[77]
trimetihyl borate (CH_3) BO_3	ammonia NH_3	Rh (111)	three-step boration-oxidation-nitration	h-BN nanomesh	[78]
ammoniaborane BH_3NH_3		metals & non-metals	CVD	partial and full h-BN monolayer	[80]
borazine $H_6B_3N_3$		Cu(111), Ag (111)	ion beam assisted CVD	h-BN nanosheet	[13,78]
borazine $H_6B_3N_3$		numerous TRMetal surfaces	CVD	h-BN monolayer	[15]
borazine $H_6B_3N_3$		Rh (111)	CVD	h-BN nanomesh	[79–81]
borazine $H_6B_3N_3$		Ag (111)	single moleculedecomposition induced by STM	functionalized BN-units	[82]
trichloro-borazine $B_3Cl_3H_3N_3$		Ni(111) Pt (111)	CVD	h-BN nanosheet	[83,84]
diborane B_2H_6	ammonia NH_3	Ni(100)	CVD	h-BN thin films	[85]
boron (target) B	nitrogen N_2	Au (111)	magnetron sputtering	BN nanoflakes	[88]
boron (segregated) B	nitrogen-monoxide NO	polycrystalline Rh surface	surface reaction	BN layers	[86]

kPa. The milled boron was heated in a horizontal tube furnace in an NH_3 atmosphere at 1300 °C. Recently, a successful fabrication process of BNNTs was also reported by using combination of APCVD, thermal oxidation, and vacuum filtration [74]. Note a recently published review which collected the synthesis routes and methods for the efficient production of h-BN and h-BCN materials for different application purposes [75].

A plausible route for the preparation of h-BN is the decomposition of ammonia borane (BH3NH3) or borazine ($B_3N_3H_6$). These starting materials are applied mainly to obtain 2D modifications of h-BN in UHV conditions. Fabrication techniques, emphasizing new potential applications for different dimensional BN nanostructures from 0D quantum dots, 1D BN tubes, 2D nanosheets and 3D framework were summarized very recently [76].

2.2. Growth of h-BN sheets on metals, hexagonal boron nitride/metal interfaces

In this section, we focus on the formation of h-BN nanosheets on metal surfaces. The first successful attempts for producing h-BN monolayer on metals were reported in the 1990s; it was distinguished that h-BN monolayers can be produced on transition metal supports via chemical vapor deposition (CVD) in ultra-high vacuum (UHV) conditions [87–89]. Note that in the interaction of NO with boron segregated from the bulk of polycrystalline Rh above 900 K, a single h-BN layer in monolayer or close to monolayer regime was formed as established by AES, XPS and UPS [86]. Formation kinetics of an h-BN monolayer on Rh (111) was first analyzed applying in-situ STM by Frenkens' group [79]. The preparation of h-BN sheets and the properties of h-BN/metal interfaces have been comprehensively reviewed by Auwärter [15]. The atomic adsorption energies of boron, nitrogen, hydrogen, atomic oxygen, C_2, BN dimers, C_6, and $(BN)_3$ hexamers, graphene and h-BN without atomic vacancies were also calculated very recently [90]. Borazine ($B_3N_3H_6$) was used most often as precursor, despite its moisture sensitivity and slow limited shelf life at room temperature. Alternatively, B-trichloroborazine ($B_3Cl_3H_3N_3$), a solid at room temperature, was also applied in a few cases on selected supports [83,84]. Ammonia borane (NH_3BH_3) is also a popular precursor material [85,91,92]. On Rh (111) a three-step boration-oxidation-nitration process employing trimethyl borate was applied for h-BN synthesis [93]. The dehydrogenation of decaborane with N containing adsorbents was studied on Pt (111) in order to produce h-BN layer [94]. On catalytically inactive supports like Ag (111) [13] and Cu(111) [78], in order to enhance h-BN synthesis and to catalyze growth at lower substrate temperature, electron or ion beam assisted deposition (CVD) of borazine was applied. At this point we note that B–N (for example: borazine, ammonia borane) compounds and boron nitride are not only precursor for h-BN but also have high hydrogen storage capacity [95–98].

The adsorption-desorption properties of borazine were investigated on Re (0001) by means of LEED, TDS, AES and EELS [87]. The

adsorption studies of borazine on Pt (111) and Ru (001) suggested that the molecule is a planar analog of benzene and exhibits aromaticity in the ground state [88]. Recently, He ion scattering was used to monitor and control the growth of a rich variety of h-BN nanoporous phases due to partial dehydrogenation, breaking of the borazine ring and polymerization of the precursor during the CVD process [99]. The epitaxial growth of h-BN on Ru metal substrate is schematically illustrated on Fig. 2.

HREELS, UPS, and TDS investigations of adsorbed borazine on Pt (111) and Au (111) surfaces gave basic information about the adsorption geometry [89]. The HREELS data show that the borazine is adsorbed with the ring oriented perpendicular to the Pt (111) surface at low temperatures. In contrast, under similar conditions the borazine adsorbs with the ring parallel to the Au (111) surface. The dehydrogenation process was followed by HREELS and TDS. The important B–H, B–N and N–H vibrational modes were determined [89]. Adsorbed borazine dehydrogenates on Pt (111) above 170 K, forming h-BN on the surface. Characteristic vibrations of the produced h-BN species by HREELS on Ni (111), Pd (111), Pt (111) and bulk h-BN were also determined [100].

The adsorption of borazine multilayers, dehydrogenation and h-BN formation were studied in detail by HREELS complemented by AES and TPD on Rh (111) [81]. Desorption products were only H_2 and $B_3N_3H_6$ (borazine) in the temperature range of 100–1000 K (Fig. 3). Borazine desorbed from the surface with one sharp peak at $T_p = 176$ K, which is connected to the desorption of the condensed layer with zero order desorption kinetics. After multilayer desorption at ~176 K hydrogen abstraction was noticed. TPD spectra indicated that H_2 desorption already started below 200 K and continued – in a very broad temperature range – up to ~800 K. Proposed dehydrogenation steps are the following:

$$B_3N_3H_{6\ (a)} \rightarrow B_3N_3H_{6-n\ (a)} + nH_{\ (a)} \quad (2)$$

$$B_3N_3H_{6-n\ (a)} \rightarrow BN + (6-n)\,H_{\ (a)} \quad (3)$$

$$H_{\ (a)} + H_{\ (a)} \rightarrow H_{2\ (g)} \quad (4)$$

The adsorbed borazine on Rh (111) was characterized by HREELS at 140 K [81]. The vibration modes of borazine obtained on Rh (111) together with gas phase and adsorbed modes on some surfaces (Pt and Au) are collected in Table 2. The vibrations of borazine detected on Rh (111) surface at 140 K agree well with the gas phase spectrum of borazine.

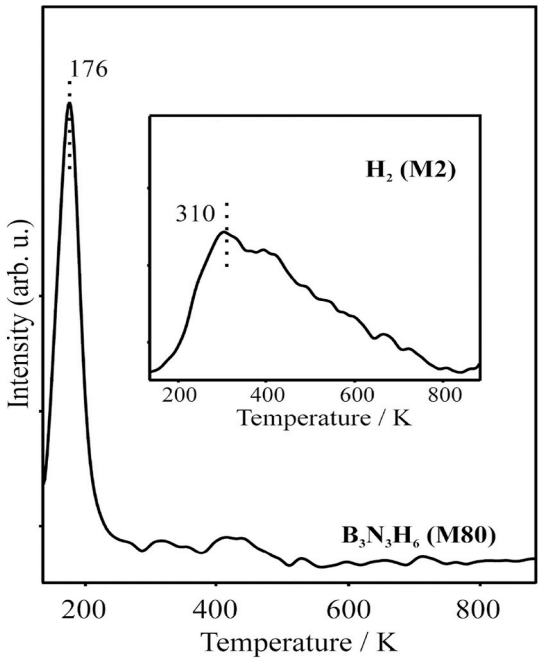

Fig. 3. Borazine, M(80) and hydrogen, (M2) TPD spectra following 0.15 L borazine adsorption on Rh (111) surface at 140 K. Reproduced from Ref. [81].

The observed vibrations for borazine and their changes with temperature are suitable to describe the subsequent dehydrogenation of borazine on the surface. The peak at 1460 cm^{-1} is attributed to the B–N asymmetric modes, and the peaks detected with smaller intensity at 2510 and 3480 cm^{-1} are associated with the B–H and N–H asymmetric vibrations, respectively. All peaks shrink in intensity due to the multilayer desorption at 200 K. Further heating of the adsorbed layer to 300 K led to the significant attenuation of the HREELS peaks belonging to B–H, N–H and γ-BN at 410, 720 and 920 cm^{-1}, respectively. The spectra at and above 500 K exhibited completely different results. The peaks from the B–H and N–H regions disappeared probably due to the almost complete dehydrogenation process of borazine. At the same time, the broadened peak at ~720-750 cm^{-1} intensified, and above 500 K it was the strongest one on the HREEL spectra (Fig. 4). The remaining two main loss peaks are signed to the phonons of h-BN with in-plane polarization;

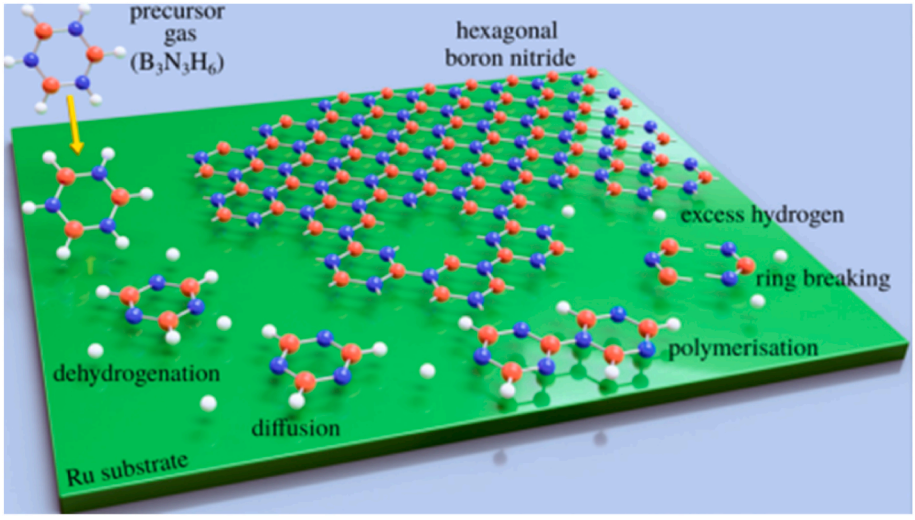

Fig. 2. Schematic illustration of the epitaxial growth of h-BN by chemical vapor deposition: a gaseous precursor (e.g. borazine, $B_3N_3H_6$) is brought into contact with a (hot) metal surface (Ru), triggering chemical reactions such as dehydrogenation and breaking of the borazine rings followed by the assembly of the epitaxial overlayer. Reproduced from Ref. [99].

Table 2
Characteristic vibrations of borazine in gas phase and on different single crystal surfaces. Recreated from Ref. [81].

	Vibration mode	$B_3N_3H_6$ gasphase D_{3h} [89]	$B_3N_3H_6$ on Pt (111) at 110 K [89]	$B_3N_3H_6$ on Pt (111) at 170 K [89]	$B_3N_3H_6$ on Au (111) at 110 K [89]	$B_3N_3H_6$ on Au (111) at 180 K [89]	$B_3N_3H_6$ on Rh (111) at 140 K [81]	$B_3N_3H_6$ on Rh (111) at 300 K [81]
A_2"	ν_8, γ-BH	918	915		910	910	920	920
	ν_9, γ-NH	719	710		710	710	720	730
	ν_{10}, γ-BN	394	400		400	400	410	405
E'	ν_{11}, ν_{as}-NH	3486	3485	3485	3460		3480	3480
	ν_{12}, ν_{as}-BH	2520	2535	2535	2490		2510	2530
	ν_{13}, ν_{as}-BN	1465	1465	1465	1460		1460	1450
	ν_{14}, ν_{as}-BN	1460						
	ν_{15}, δ-BH	1096						
	ν_{16}, δ-NH	990		955				
	ν_{17}, δ-BN	518		560 (?)				

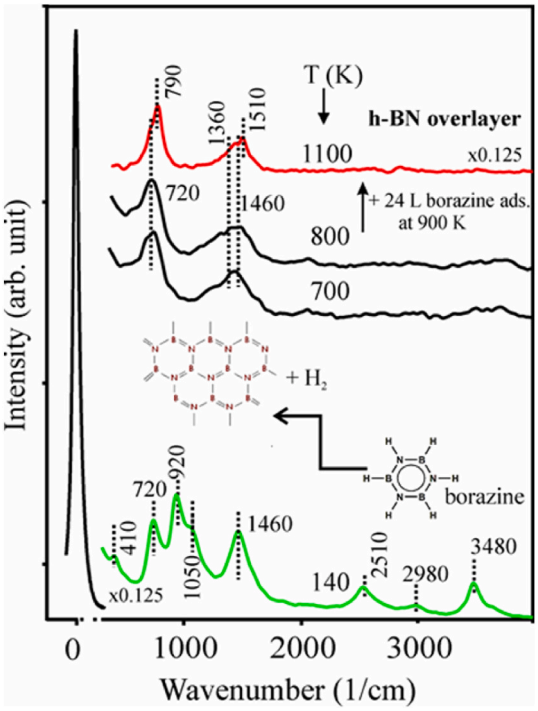

Fig. 4. HREEL spectra detected during transformation of borazine to h-BN sheet.

the higher energy peak originates from the longitudinal optical (LO) phonon, and the lower energy one from the TO (transverse optical) phonon. The detected HREELS curves at 1100 K agreed with the literature data on h-BN layer [100]. The characteristic vibrations of h-BN species obtained on various single crystal surfaces (Ni, Pd, Pt and Rh) together with bulk h-BN are collected in Table 3. The formation of h-BN using borazine dehydrogenation was also proved by other spectroscopic methods (XPS, UPS, LEIS) and STM [8,15,46–50].

Table 3 Is reproduced from Ref. [81].

The low temperature adsorption, desorption and decomposition processes of borazine were also investigated on Pt (110) using TPD and UPS [101]. The dehydrogenation (production of H_2) started from 200 K. Molecular borazine desorption occurred at ~130 K (multilayer) and 140 K due to the desorption of a weakly chemisorbed state including the recombination of partially dehydrogenated fragments and atomic hydrogen. Complementary DFT calculations identified the borazine molecular adsorption occurring at the (111) facet of the (1 × 2) missing row reconstructed Pt (110) surface with an adsorption energy of −1.88 eV and a work function decrease of 878 meV [101]. The DFT results showed weaker bonding to the Pt (110) and a smaller work function change due to the vertical BN ring plane, whose best azimuthal orientation was also identified [101]. The bonding characteristic and electronic structure of h–BN/Pt (110) were reported [102,103]. Interestingly, it was shown that the Pt (110) (1 × 2) missing row reconstruction is converted to (1 × n) with a regular alteration of $n = 5$ and 6, thus, the reconstructed surface layer of Pt (110) adapts to the h-BN overlayer and exhibits a quasi-liquid behavior below single-domain h-BN. In another study, the nucleation process of h-BN on Pt (110) was reported. It was concluded from STM and UV photoemission experiments that large single-crystalline domains can be produced on this substrate [104]. Concerning non-metal substrates, the lack of stabilization of an electronically decoupled h-BN layer on the SiC(0001) surface was reported [105]. On Pt (110) surface the nucleation of h-BN is a nonclassical two-step mechanism. The first step is the nucleation of a h-BN/Pt double layer on the Pt (110) surface. In the second step h-BN islands are formed in the size of a moirè unit cell.

The growth of h-BN was studied by LEIS for the first time on Rh (111) (Fig. 5) [48]. The adsorption and surface decomposition of borazine at 1000 K led to the attenuation and disappearance of the Rh LEIS signal (Fig. 5A). The contributions from B and N were not detectable, attributed to the lower sensitivity of LEIS for light elements. The continuous

Table 3
Characteristic vibrations of BN species on different single crystal surfaces.

System	[a]TO⊥ (cm^{-1})	[a]TO∥ (cm^{-1})	LO (cm^{-1})
h-BN/Ni(111) [100]	728	1360	1360
h-BN/Pd (111) [100]	784	1384	1432
h-BN/Pt (111) [100]	792	1384	1464
h-BN/Rh (111) [81]	790	1360	1460, 1510
Bulk h-BN [100]	776, 824	1352, 1360	1600

[a] TO⊥ transverse optical phonons with out-of-plane, LO (longitudinal optical) and TO∥ phonons with the in plane polarization.

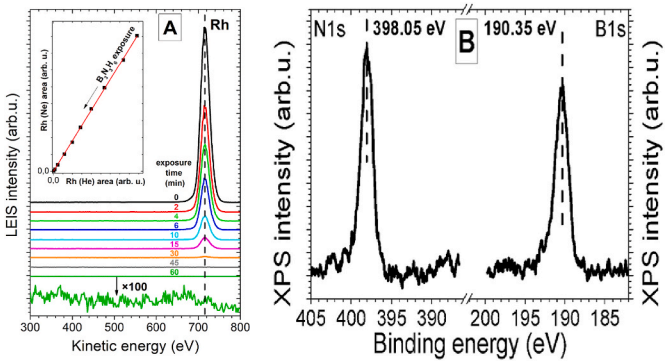

Fig. 5. (A) LEIS spectra obtained at 300 K with He, after exposing the Rh (111) surface to ~2×10^{-8} mbar borazine at 1000 K for successively increasing time. The last spectrum is also shown after magnification. (B) Standard XPS spectra of h-BN/Rh (111) after borazine decomposition at 1000 K. Partially reproduced from Ref. [48].

decrease in Rh signal implies that Rh is covered by B–N containing compounds. Quantitative analysis of LEIS data indicated that the prepared h-BN monolayer was almost fully continuous, exposing <0.001 ML of uncovered metal sites. Parallel XPS measurements show the development of N 1s and B 1s peak due to h-BN overlayer (Fig. 5B). The STM image corresponds to h-BN nanosheets with nanomesh (Fig. 11a). 1 ML h-BN coverage means that the h-BN continuously cover the substrate metal.

Very recently distinct self-assembled borazine structures on Ag (111) and controlled dehydrogenation of single borazine molecules were investigated by STM and DFT [82]. The adsorption geometry can be modified by manipulation of individual $B_3N_3H_6$ molecules via tip-induced voltage pulses, causing higher dehydrogenation yield. This reaction results in an upright standing configuration of the molecule.

The hydrogen-rich ammonia borane (AB) is also a possible precursor to produce h-BN. The solid AB is isoelectric to ethane and therefore it is extremely interesting as a possible hydrogen storage compound [106]. During the h-BN synthesis from AB similar dehydrogenation steps and intermediates were detected as those identified in borazine decomposition [107]. Ammonia borane shows multiple dehydrogenation steps at the B and N atoms up to 300 K. The TPD experiments of AB for H_2 show the hydrogen loss over a broad temperature range with a desorption maximum at 350 K and a tail up to 580 K. This results in various BH_xNH_y species, before the formation of disordered BN and finally h-BN, analogous to the borazine dehydrogenation. The ammonium borane (AB) decomposition was systematically followed by temperature programmed X-ray photoelectron spectroscopy (TPXPS) on Ni(111) as presented in Fig. 6.

The decomposition pathways of borazine and AB exhibit great similarities. Based on TPD and TPXPS results both successive dehydrogenation of borazine as well as ring breaking and formation could be the reaction paths. It can be concluded that the decomposition of ammonium borane (AB) proceeds via ring formation thus borazine is a possible reaction intermediate. Above 300 K, where equal intermediates are present with disordered BN and defective BN, eventually are leading to h-BN.

The substrate temperature and partial pressure of borazine basically influences the growth process of two-dimensional h-BN. The formation of single domain and polydomain structures was presented on Pd (111) [108]. In situ variable-temperature STM (VT-STM) (300–673 K) was applied to monitor CVD growth of h-BN on Pd (111) from borazine precursor at pressures up to 10^{-6} mbar. VT-STM identified the processes leading to carpet-like uphill or downhill growth across the Pd steps. Fig. 7 displays images from two different Pd (111) surfaces during h-BN deposition from borazine at T = 573 K and p = 10^{-6} mbar (A) and T = 673 K and p = 10^{-7} mbar (B).

The presented results demonstrated that the higher pressure and low temperature promote the uphill growth via preferential attachment at the step-edges. A lower deposition pressure (lower rate) and higher temperature lead to downhill growth via nucleation and development of islands on Pd terraces. The results are illustrated in Fig. 8.

Theoretical work simulating the formation of h-BN thin films are rare up to now. First-principles calculation has only been carried out for the diffusion of boron and nitrogen atoms on the Pt (111) surface [109,110]. Very recently, the results of theoretical research on the mechanism of h-BN development on different metal substrates (Cu, Ni, Ru, Ir) are summarized [111]. This work elaborated that the substrates play a decisive role in the h-BN formation mechanism. Another new research trend, the machine learning potential (MLP) calculations based on DFT are also applied in the growth process of h-BN [112]. The formation of monolayer h-BN on Pt (111) was studied very recently applying molecular dynamics combined with machine-learning potentials trained based on first-principles data. In the growth mechanism, a Y-shaped node is produced around B, which then creates a quadrangular ring that transforms into the hexagonal ring [110,113]. Fig. 9 shows the process for the formation 1D chains (a), thereafter hexagonal structures are developed (b) during the simulation.

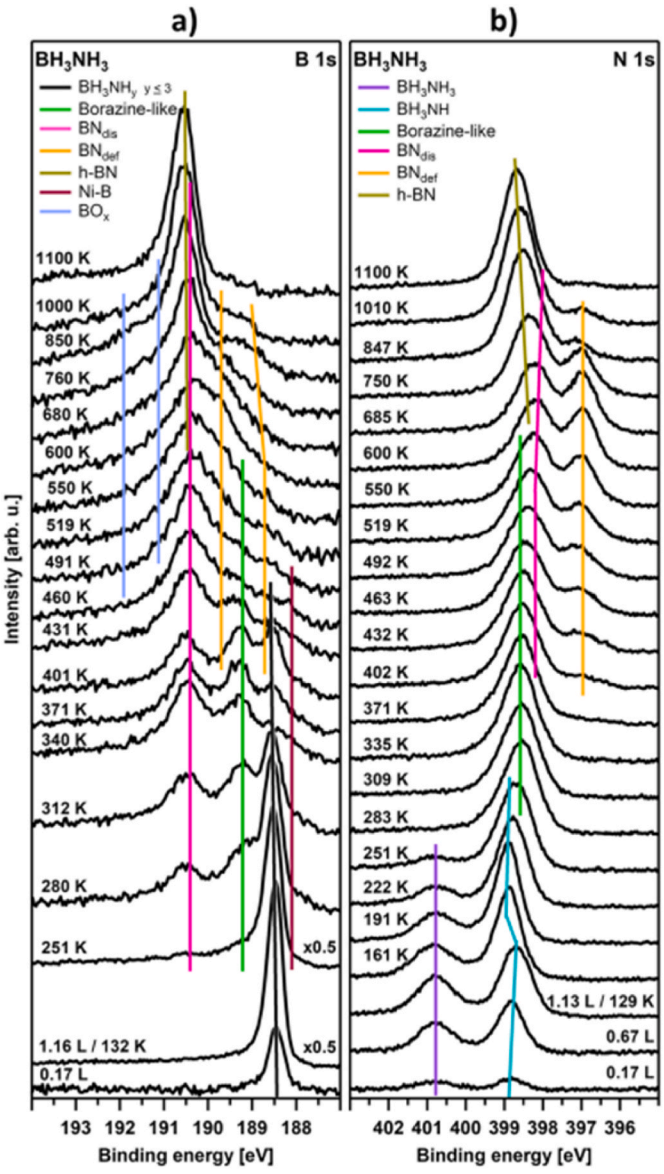

Fig. 6. TPXPS spectra of adsorption of ammonia borane on Ni(111). Reproduced from Ref. [107].

Fine tuning of the deposition ratio of boron and nitrogen can improve the quality of the produced h-BN crystal on Pt (111). The growth mechanism of h-BN on the Pt (111) surface is different from that found on Ni(111), although the solubility of B is high, and the N solubility is low in both cases. On Ni(111) surface, the hexagon is developed by the production of B–N bonds at two places between nearby parallel 1D chains [114–116].

From a technological point of view, the investigation of the exfoliation of h-BN 2D layers is crucial. In this work the h-BN has been transferred back onto Rh substrate successfully where the bottom-up CVD grown h-BN was delaminated from Rh (111) and transferred onto the clean metal surface [117]. This procedure suggests a way to obtain a 2D material from CVD. As we know, the exfoliation is a standard top-down technique in the application of 2D materials. In the case of h-BN, few of these methods can meet the crucial demand of preparing large surface area sheets with high yield and purity [118,119]. Three most effective methods were frequently applied; (A) based on refluxing and vigorous sonication in isopropyl alcohol (C_3H_8O); (B) ball-milling in urea; (C) with the aid of NH_3 in a hydrothermal method [118]. Recently,

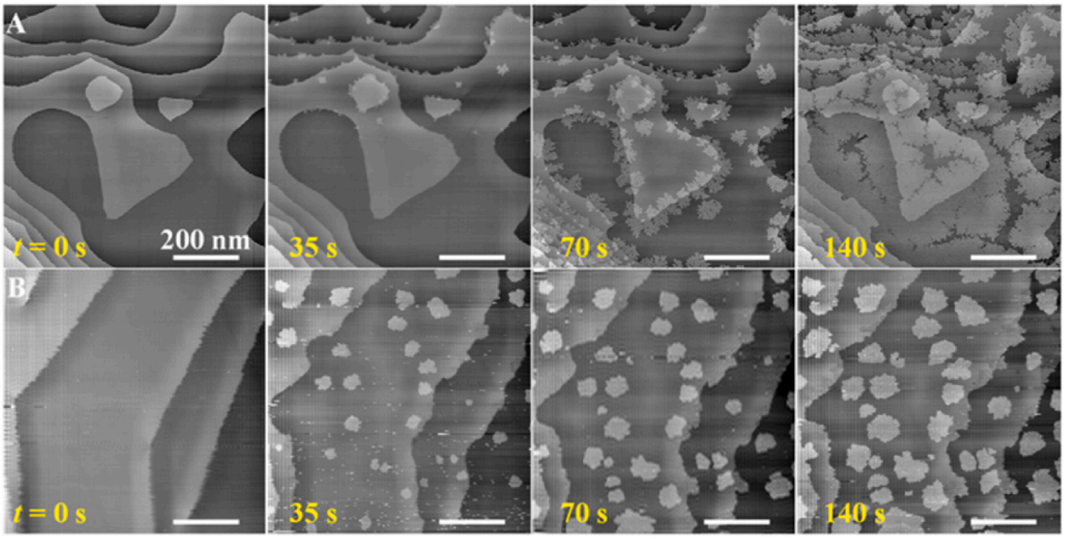

Fig. 7. Representative STM images (800 × 800 nm^2) acquired in situ during CVD of h-BN on Pd (111) at (A) temperature T = 573 K, borazine pressure p = 10^{-6} mbar and (B) T = 673 K, p = 10^{-7} mbar. Deposition times *t* indicated in the image panels are with respect to an arbitrary time during annealing the sample at the set T in UHV, at which borazine is introduced into the STM system. The images in the first column show bare Pd surfaces. In panels A and B, complete monolayer coverages are achieved in *t* = 245 and 735 s, respectively. STM image acquisition parameters, tunneling bias V_T and current I_T, are (A) V_T = 1.0 V, I_T = 0.5 nA and (B) V_T = 0.8 V, I_T = 0.6 nA. Step-edge contrast in these images is enhanced for clarity. Reproduced from Ref. [108].

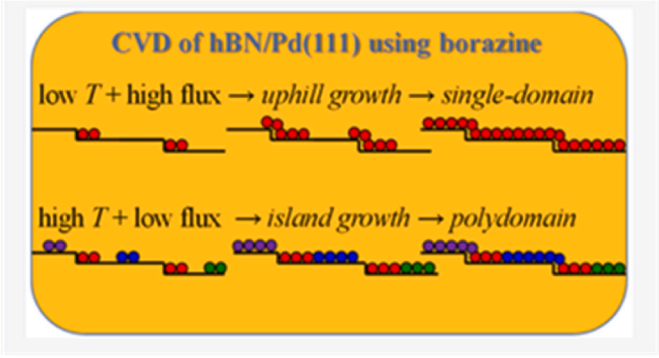

Fig. 8. CVD of h-BN/Pd (111) using borazine at low and high temperature and at high flux and low flux. Reproduced from Ref. [108].

a two-step gas expansion and alkali intercalation seems to be also an excellent approach to prepare large portions of layered h-BN nanosheets with vacancies [38].

Here, we mainly focused on the synthesis of monolayer h-BN controlled by atomic level characterization on different substrates for model studies. h-BN exhibits unique properties including physical, chemical, electronic, quantum optics, and many others. It is important to develop growth strategies producing high-quality h-BN. Recently the preparation of mono- and multi-layer h-BN on metallic, insulating, alloyed, single-crystalline, polycrystalline, and liquid catalysts or supports are reviewed [120,121].

3. Morphology and electronic structure of h-BN monolayers – the effect of substrate and orientation

3.1. Spectroscopy and microscopy study of h-BN monolayers on closed, open surfaces and alloys

The epitaxial growth of h-BN layers on metal surfaces has attracted a lot of attention [15–17]. The h-BN layer has many structural similarities with graphene, but its electronic properties are significantly different from the semi-metal graphene, namely, h-BN is an insulator with a band gap of ~6 eV [122,123]. This value exhibits only a slight difference with dimensionality. The h-BN/metal interface systems can be categorized on the basis of lattice mismatch and the strength of interaction. Auwärter in recent review distinguished weakly and strongly interacting systems [15]. Weak interaction exists in h-BN/Cu, h-BN/Ag, h-BN/Au and h-BN/Pt cases where the large average h-BN-metal separation is comparable to the h-BN bulk interlayer spacing of 3.33 Å. On these metal substrates h-BN forms a rather flat single monolayer. The group of h-BN/Co, h-BN/Ni, h-BN/Ru, h-BN/Rh, h-BN/Pd, h-BN/Re and h-BN/Ir group belongs to the strongly interacting systems [15]. These interfaces can be described with smaller h-BN-metal separation of around 2.2 Å. This group may have a single domain structure, and a nanomesh structure appears in case of significant lattice mismatch, i.e., emergence of a moirè-like superstructure with large corrugation in the order of 1–2 Å. The moirè systems formed by 2D atomic layer have widely tunable electronic and optical properties, accompanied by strongly correlated electronic and topological phenomena [124,125]. Strongly buckled 2D materials are formed on several hexagonal metal surfaces. Fig. 10 displays a schematic illustration of top and side view of a proposed h-BN nanomesh. In this structure the interfacial chemical bond is strong resulting in an efficient orbital overlap.

Formation of nanomesh of h-BN was evidenced first on Rh (111) surfaces [7]. In the regular nanomesh formation cases, the appearance of periodic z-depression zones (“pore”) in the continuous h-BN monolayer, is driven by the lattice mismatch of the film and the substrate. In the case of h-BN/Rh (111) this value is relatively high, 6.7 %, the mesh formation is very pronounced. In the pore regions, N atoms are approximately in on top positions with respect to the underlying Rh (111). The STM images confirmed by low-energy electron diffraction (LEED) patterns provide an atomic structure of the nanomesh. The superlattice spots around the principal spots show a periodicity of 32 ± 1 Å, which corresponds to a supercell of 12-by-12 R h unit cells, or 13-by-13 h-BN unit cells. The elevated regions (mesh “wires”) of 0.9 ± 0.2 nm width are also produced by the atomic h-BN lattice [7]. In these regions the energetically preferred on-top coordination is not possible for N atoms due to the lattice mismatch. The nanomesh structure is thermally stable and can serve as a template to organize atoms, metal clusters and molecules. A great part of previous works has been focused on the lattice matched system of h-BN on Ni(111), where large flat terraces of ML h-BN are formed with N atoms on top of Ni atoms [126].

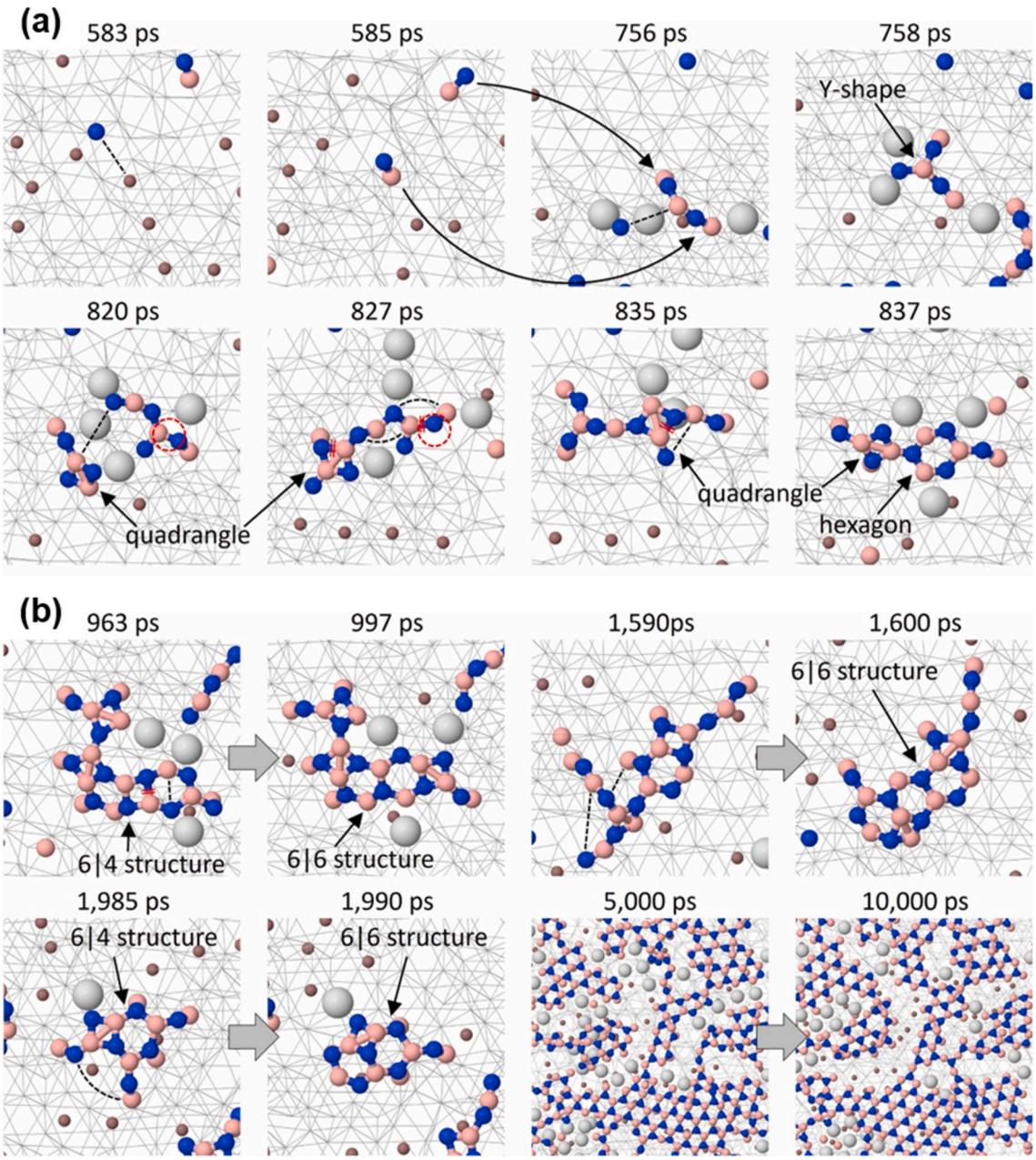

Fig. 9. Atomistic processes are calculated on Pt (111) for the formation of (a) 1D chains and (b) hexagonal structures during the MD simulation at 1300 K. The blue, light pink, dark pink, and gray balls represent N atoms, surface B atoms, interlayer B atoms, and Pt adatoms, respectively. The gray lines in the background indicate the substrate Pt atoms. The black dashed lines and red double lines mark the bond formation and breaks between atoms, respectively. The red dashed circles indicate the location of Pt vacancies. The number above each snapshot is the elapsed time from the beginning of the MD simulation. Reproduced from Ref. [110].

It has been found by LEED, STM, XPS and X-ray absorption spectroscopy that on Pt (111) surface, h-BN exhibits a nearly flat monolayer [127]. On Rh (111), h-BN grows in form of a nanomesh, as originally observed. The difference between the h-BN/Pt (111) and h-BN/Rh (111) interface structures is in connection with the strength of chemical interaction between h-BN layer and the substrate surface. The difference between the two systems can be recognized in the STM images in Fig. 11. Note that the vertical corrugations are different in the two cases.

High resolution XPS confirms that there a strongly and weakly bonding parts of the moirè on Rh (111) surface [127].

After preparation of h-BN on Pt (111), the spectrum represents one signal at binding energy of 397.18 eV. The second peak can result from a rather weak corrugation of the h-BN monolayer. The spectrum obtained on Rh (111) is significantly different being composed of two components N1 and N2 with $E_B = 397.90 \pm 0.05$ and 398.58 ± 0.05 eV, respectively. The two-peak structure of the spectrum confirms the coexistence of two types of h-BN species on Rh (111) in agreement with the STM conclusion. The B 1s XPS peaks from h-BN on Pt and Rh are also consist of one and two signals, respectively. At the same time, the energy separation in the case of nanomesh between the two B 1s signals is smaller (~0.42 eV) than between N 1s peaks, where the separation is ~0.7 eV).

The corrugation of a h-BN nanomesh layer was determined recently on the (111) surface of rhodium. The corrugation of h-BN nanomesh from angle- and energy-resolved photoelectron diffraction experiments was given [49]. These experiments with chemical state resolution give accurate values for the peak-to-peak corrugation amplitude (0.80 Å), the bonding distance to the substrate (2.20 Å) and the buckling of the B and N atoms in the strongly bound pore regions (0.07 Å) [44]. From the STM

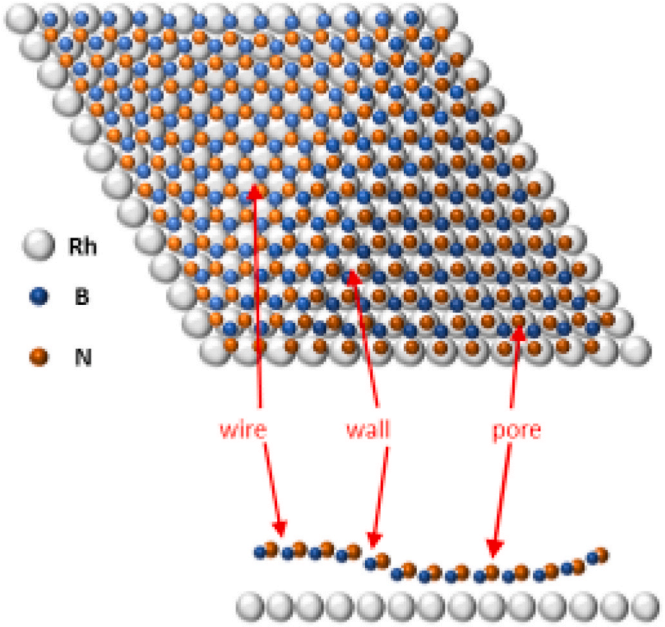

Fig. 10. Schematic illustration of h-BN nanomesh produced on Rh (111) surface.

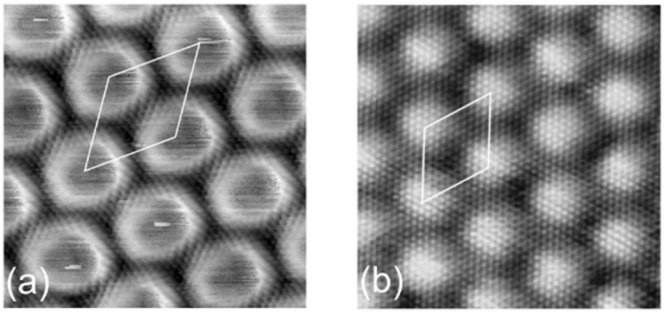

Fig. 11. Atomically resolved (10 × 10 nm^2) STM images of h-BN (a) on Rh (111) and (b) on Pt (111). The supercells are indicated. The tunneling parameters are V = 70 mV, I = 3 nA for (a) and V = −10 mV, I = 2 nA for (b). Note the formation of a nanomesh on Rh (111) and a relatively flat monolayer on Pt (111). Reproduced from Ref. [127].

image of h-BN nanomesh the superstructure unit cell was measured, the lattice parameter is 3.2 nm (Fig. 12).

The most investigations on interactions between 2D nanomaterials and their substrates have been carried out for h-BN monolayers grown on surfaces with hexagonal symmetry, i.e., the (111) surfaces of face-centered cubic (fcc) systems or the (0001) ones of hexagonal close-packed (hcp) materials. Nevertheless, (110)-oriented fcc metals could be also important, because their atomic arrangements show rectangular symmetry. This surface plane could be an ideal substrate for developing h-BN-based- or graphene templates for growing one dimensional (1D) adsorbate superlattices. The characteristics of h-BN monolayers grown on Rh (110) were investigated by STM and LEED [128]. The h-BN monolayer grown on Rh (110) surface was dominated by a unique quasi one dimensional moirè pattern, suggesting considerable interface interaction. However, an important difference was that the moirè vertical corrugation was significantly smaller than those of the hexagonal-terminated Rh (111) substrate, due to differences in the binding scenarios at interfaces with differently oriented substrates. The wavelength of the 1D periodicity of the moirè structure on h-BN/Rh (110) is approximately only half of the 2D moirè wavelength for h-BN/Rh (111). The Pt (110) surface behaves differently from Pt (111)

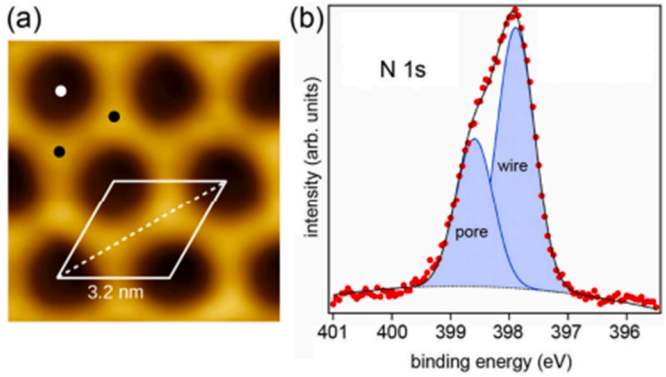

Fig. 12. (a) STM topography image of h-BN nanomesh on Rh (111), I_t = 10 pA, V_t = 1.0 V. The dark regions are depressions ('pores') in the continuous h-BN layer, the bright regions are the elevated 'wires'. The superstructure unit cell is highlighted; the lattice parameter is 3.2 nm. The white and black dots mark the high-symmetry points in the pore and on the wires. (b) N 1s core-level XPS spectrum measured at hν = 565 eV and normal emission. The plot shows experimental data (red dots) and a curve-fit with a two-component Gaussian profile (lines and shaded areas). Reproduced from Ref. [49].

surface due to its missing row structure, so it is a promising template for nanowire arrays. Some Pt surface atoms are mobile underneath the h-BN monolayer, even at room temperature [101,102]. The h-BN/Pt (110) system is a borderline case between nonlocal van der Waals and strong local interaction. The Pt (110) surface adapts to the h-BN overlayer by formation of alternating (1 × 5) and (1 × 6) reconstructions [102]. The work-function change as well as the π and σ band binding energies correlate with other weakly interacting h-BN/metal systems. Alternatively, the structural corrugation, the estimated band structure, and the LDOS of nitrogen atoms adsorbed close to on-top positions gives strong indication for a local covalent bonding. The contribution of this local bonding interaction is rather strong thereby leading to a missing-row reconstruction [103]. Very recently STM and UPS studies confirmed the two-step process. The 1st step is the nucleation process on Pt (110), in the second step h-BN islands are formed in moirè unit cell dimension [104].

Recently, the formation of a moirè was also studied on the Pt (110) [101], Pd (110) [129] and Ir (111) [130–134] surfaces. The STM topography shows atomic resolution of the h-BN layer and, through a hole, of the Ir (111) surface (Fig. 13). A corrugated hill-and-valley pattern was observed.

The atomic rows of Ir (111) surface and h-BN are practically parallel. The magnifying effect of the moirè makes also a small angular misalignment visible. It was estimated that an angular scatter in the moirè directions is less than ±12° and thus an alignment of h-BN and Ir atomic rows is approximately ±1°. The edges of the hole in the h-BN layer are aligned along the dense-packed directions, which indicates that they are of zigzag type [134]. The characterized h-BN/Ir (111) with other related systems represent promising applications in diverse areas such as magnetic data storage [135], catalysis [136,137] and logical operation [138]. The Ir (110) substrate offers a very interesting moirè pattern formation during the development of h-BN at low pressure CVD at 1050–1450 K [139]. At 1500 K, h-BN exhibits single domain aligned with its zigzag directions parallel to the [110] direction, similar to Pt (110). At 1050–1450 K, an additional h-BN twisted structure by ±(4.7° ± 1.0°) is detected by LEED. Together with twisted h-BN formation an (1 × n) reconstruction of Ir (110) was observed. It was suggested that the same process of domain twist and twin selection could be valid also for Pd (110), and Rh (110) revealing {112} steps. Electrostatic potential of the moirè from twisted h-BN layers could play an important role in controlling the properties of an adjacent semiconductor monolayer [140].

Regarding template applications of nanomesh, the superstructure

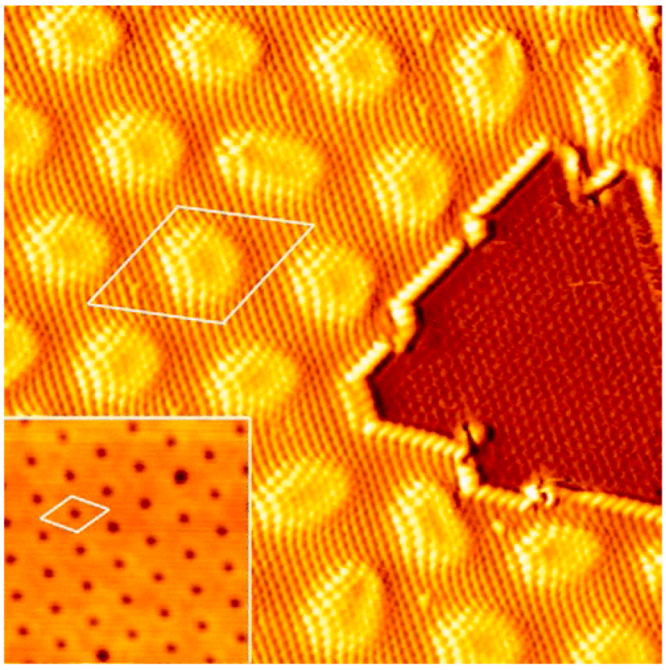

Fig. 13. Atomically resolved h-BN layer with a triangular hole exposing Ir (111). Unit cell is indicated by a white rhombus (also in inset). Image size is 144 × 144 Å^2, U_b = 0.48 V, I_t = 8.5 nA. Inset: STM topography with imaging conditions representing h-BN with qualitative geometric contrast (see text). Image size is 180 × 180 Å^2, U_b = −1.0 V, I_t = 0.3 nA. The h-BN for the image and inset was grown by exposure to 2 L of borazine with an exposure time of 30 s at 1100 K. Reproduced from Ref. [134].

periodicities are of considerable interest. The periodicity is changing from large superstructure periodicities in Ru and Rh cases to small periodicities in Pt case in the following order; Ru (3.5 nm), Rh (3.22 nm), Re (3 nm), Ir (2.91 nm), Pt (2.5 nm) and Ag (1 nm). Apart from superstructure periodicity and corrugation, the structural homogeneity is also an important factor. A single domain orientation with low defect concentration is advantageous for the application of h-BN/metal interfaces as templates. It was reported that h-BN on Rh (111) and Ru (0001) exhibited a reduced structural uniformity with distortions [141,142]. Structural defects can diminish the quality of the template in the case of h-BN/metal systems, especially in the Ru (0001) case, where intercalation is facilitated [143]. Oxygen intercalation of BN presents smaller activation energy than that of graphene. In real systems the imperfection might hinder the performance of h-BN sheets as templates as it is already discussed in the previous review [15]. Published experimental data of defects at the h-BN/metal interfaces mainly deal with defect lines at domain boundaries analyzed especially bonding and non-bonding patching defects in h-BN/Ni(111) [8], h-BN/Ru (0001) [142], and h-BN/Re (0001) [144]. One dimensional corrugation was observed on Fe (110) [145]. For mainly catalytic applications, it is worth mentioning that the defective h-BN on Ni(111) with N vacancy provides possibility for engineering h-BN-based catalysts [146].

The h-BN-induced faceting across curved surfaces opens a new direction in 2D research. The growth of h-BN on stepped Ni surfaces has been considered [147]. STM, LEED, ARPES, XPS and NEXAFS techniques showed homogeneous h-BN coating on stepped surfaces with alternating (111)/(115) and (111)/(110) faceting of Ni. Fig. 14 represents STM and LEED results for a monolayer of h-BN covering the curved Ni surface. Both methods suggest the homogeneous wetting by a single h-BN monolayer, which in turn initiates a structural rearrangement of the curved Ni substrate underneath.

NEXAFS and XPS investigations support the corrugated interface

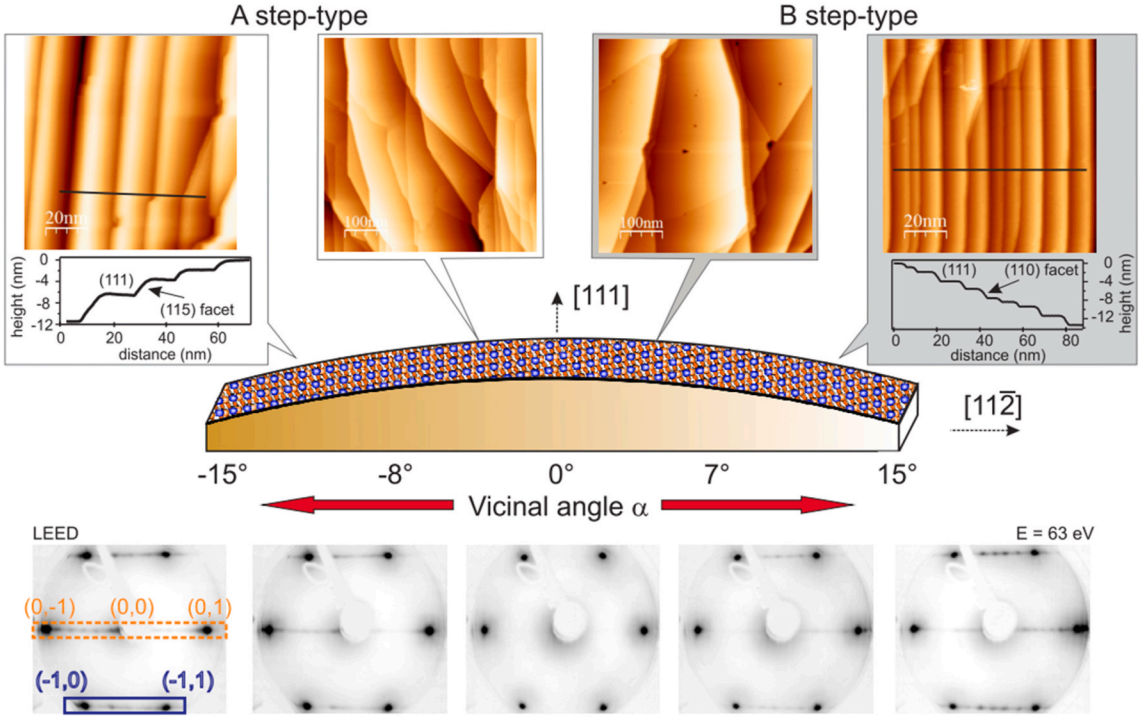

Fig. 14. h-BN monolayer on curved Ni(111). Top, STM and, bottom, LEED for a monolayer of h-BN homogeneously covering the curved Ni crystal sketched in the center. The STM images have been taken at the positions roughly indicated over the sample. LEED patterns correspond to the center ((111) plane), midway (vicinal angle α = ±7°), and densely stepped edges (α = ±15°) of the sample and have been acquired using 63 eV electron impinging parallel to the [111] direction in all cases. Insets in STM images belong to the indicated line profiles, which prove the presence of h-BN-covered microfacets. Reproduced from Ref. [147].

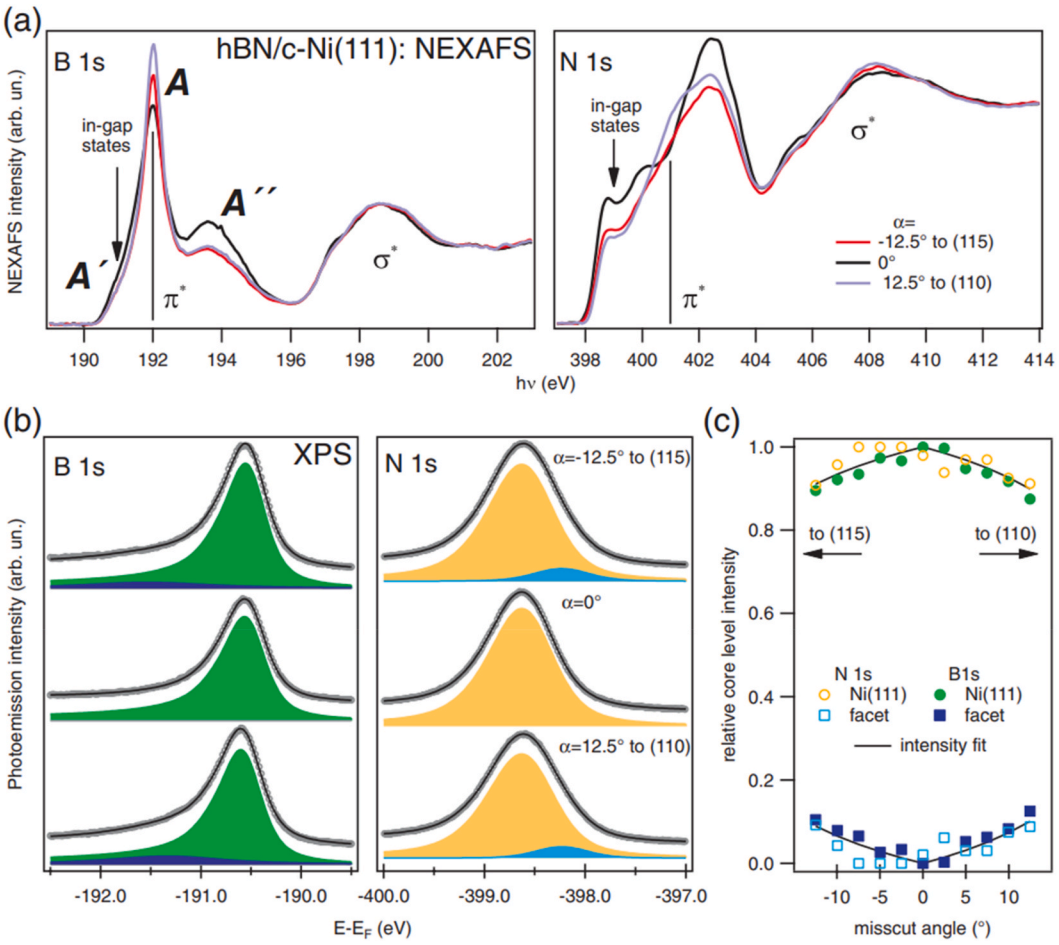

Fig. 15. Near-edge X-ray absorption (NEXAFS) and X-ray photoemission spectroscopy (XPS) of h-BN/c-Ni(111): (a) NEXAFS at the B and N K adsorption edge and (b) XPS spectra for the B and N 1s core levels, measured at $\alpha = \pm 12.5^\circ$ and 0° vicinal angles on the sample sketched in Fig. 14. NEXAF spectra have been normalized using the σ* band, and π* features have been named following Ref. [148] from this study. In XP spectra, each N and B 1s peak has been fitted using the same pair of Doniach Sunjic (DS) lines at high and low binding energy. (c) Intensity of N and B 1s XPS peaks (top, main lines, bottom, satellites) as a function of the vicinal angle. Experimental data are indicated by markers, whereas solid lines correspond to the expected variation assuming a satellite intensity that varies proportionally to the area nominally covered by tilted facets. Reproduced from Ref. [147].

scheme in both Ni(115) and Ni(110) tilted facets. In Fig. 15 the B and N NEXAFS K adsorption edges and photoelectron spectra taken at the (111) center and near the densely-stepped edges of the h-BN/c-Ni(111) structure are compared.

Growth of h-BN on vicinal Rh (111) causes periodic (111)/(337) faceting [149]. Hexagonal BN film develops a continuous layer over the faceted system with alternated (111) and (337) facets. The h-BN (111)/(337) heterostructure is an ideal platform to study phonon-polariton excitations and their dynamics [150]. Rh (111)/Rh (337) interface covered by h-BN was prepared and characterized by STM and angle resolved PES (ARPES). The schematic representation of the h-BN-covered Rh (111)/Rh (337) interface is shown in Fig. 16. CVD growth of h-BN initiates periodic (111)/(337) faceting of the Rh surface. The monolayer of h-BN uniformly covers the faceted substrate, illustrating an effective lateral h-BN/h-BN heterointerface with periodic surface potential character. The electronic structure discloses a nanoscale periodic modulation of the h-BN atomic potential.

The nanomesh formation on alloy system is very interesting. The structure of h-BN/PtRh (111) intermetallic compound by a multimethod access was investigated [151]. The h-BN monolayer forms a similar nanomesh structure as on Rh (111), but the lattice constant is smaller. Interestingly, during h-BN production, the interfacial layer is enriched with Rh, while the second layer gets depleted from Rh. The pore regions of the h-BN nanomesh are bound to Rh sites, while the wire

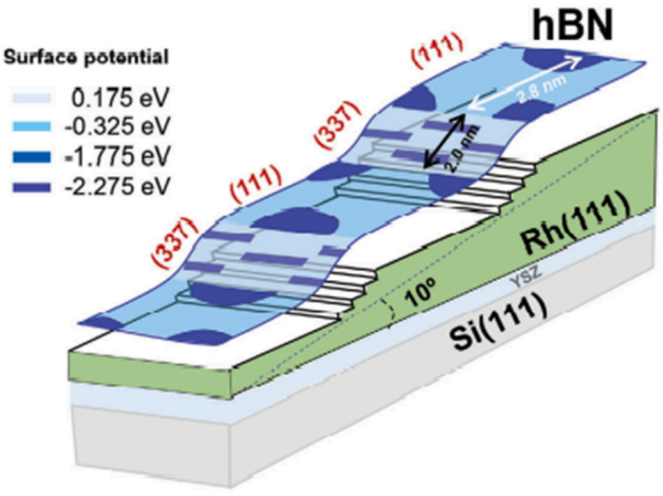

Fig. 16. Lateral nanopatterning of h-BN through epitaxial growth. Partially reproduced from Ref. [149].

regions occur on Pt patches. It is a remarkable finding that while h-BN forms the nanomesh on Rh (111), and this superstructure is absent on gold, the nanomesh is present on RhAu alloys up to a gold coverage of ~0.9 ML albeit with a smaller pore diameter. The nanomesh gradually disappeared at higher gold amounts [48]. This unexpected feature obtained on RhAu alloys offers a new possibility for using the nanomesh as a template for controlling the underneath composition of surface alloys. It was shown that the introduction of Au atoms at selected positions within the nanomesh, i.e. in the weakly interacting wire regions, increases the spatial variation of the electrostatic potential and the local work function of the h-BN/Au/Rh (111) system by more than 30 %. This enhanced spatial variation of the electrostatic potential is reflected by a characteristic signature in the h-BN valence band structure, namely the increase of the so-called minigap, which we observed in a momentum-resolved photoemission experiment [152].

3.2. DFT complementary studies for nanomesh characterization supporting the experimental findings

There is a large number of theoretical works in the literature, which deal with the formation and characterization of h-BN nanomeshes on various metal supports, including a review article [153]. Most of the works employ density functional theory (DFT) at different levels of exchange-correlation (XC) functionals and dispersion correction (van der Waals, vdW) schemes to try to accurately describe the systems [154, 155]. The difficulty from the theoretical side is that there is neither a universal XC functional nor a unique vdW scheme that describes all h-BN nanomesh structures with experimental accuracy on the same footing. The various modeling parameters complicate the comparisons among theoretical studies, and benchmarking among different theoretical treatments as well as comparisons with experiments are essential, as was shown, e.g., for h-BN/Ir (111) (and graphene/Ir (111)) [156]. For this reason the type of experimental research reported in Ref. [49] is highly useful that provides the "true corrugation" of h-BN nanomesh layer on Rh (111) in their studied example. Such highly accurate experimental results are clearly important to help developing theoretical methods by providing well-defined benchmark systems. The present review gives a brief discussion of a few selected theoretical results on the characterization of pure h-BN nanomeshes on metals in the last few years, driven by the above-described difficulties of theoretical modeling. A complementary overview of the significance of DFT results on h-BN nanomeshes on metal supports including Ir (111) was given by the excellent review paper of Auwärter [15]. Recently a h-BN/Ir (111) was investigated. The recent experimental data and DFT calculations are in agreement with the structure presented in Figs. 13, and Fig. 17 h-BN/Ir (111) was studied by AFM [132] and the corrugation of the h-BN layer was reported to be 1.65 Å. The moirè of h-BN/Ir (111) is significantly different than what is found on e.g. Rh (111).

The origin of the difference between the true geometric corrugation and the apparent corrugation obtained in STM experiments for h-BN/Rh (111) (and graphene/Ru (0001)) was theoretically studied [157]. It was proposed that the origin of this effect is of electronic nature, and is due to the unequal contributions of the low-lying and high-lying atoms in the 2D material layer to the local density of states around the Fermi energy. The ultimate reason is that the B and N atoms in the pore/wire of the nanomesh are bound stronger/weaker to the underlying metal substrate. Interestingly, the obtained true corrugation of h-BN/Rh (111) obtained by XPD agrees very well with the apparent corrugation observed in STM [48] and most of the theoretical models overestimate the geometric corrugation, see Table 1 of Ref. [48]. Recent theoretical results [158] on the geometric parameters of h-BN/Rh (111) and simulated STM apparent heights agree very well with the available literature. The moirè pattern wavelength-dependent work function and band gap modulations in h-BN/Cu(111) heterostructures were studied by STM, STS and DFT. The Cu(111) surface covered by h-BN, Φ value of the system is reduced compared to the bare Cu(111) surface due to the interlayer interaction

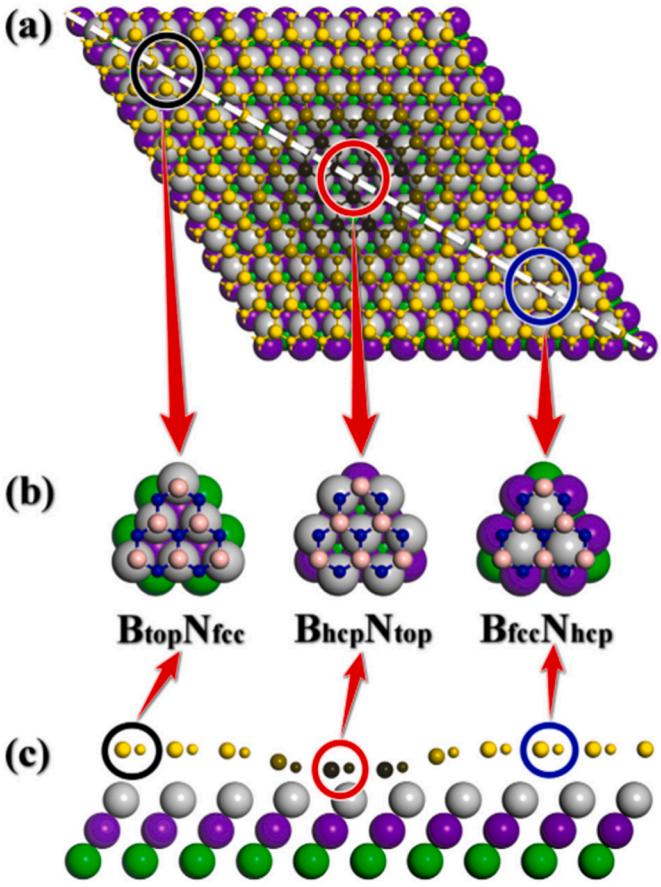

Fig. 17. (a) Top and (c) side views of GGA + vdW resultant h-BN/Ir (111) moirè structure for (12 × 12) h-BN monolayer on (11 × 11) Ir (111) substrate. The gray, purple and green spheres represent the first, second, and third layer of Ir atoms, respectively; vertical heights of B (large spheres) and N atoms (small spheres) relative to surface Ir layer are indicated by the color scale from black to yellow. (b) Three representative regions with high local structural symmetry are abbreviated as $B_{top}N_{fcc}$ (fcc), $B_{hcp}N_{top}$ (top), and $B_{fcc}N_{hcp}$ (hcp), respectively; pink and blue spheres denote B and N atoms, respectively. Reproduced from Ref. [132].

[159]. It is expected that the results are helpful in the understanding of the electronic character of moirè patterns in other 2D materials.

For electronic structure characterization of h-BN, we highlight the recent review on band structure measurements and complementary theoretical calculations mostly focusing on h-BN/Ni(111) [160]. Such combined experimental-theoretical approach will be useful to study the electronic structures of strong corrugated h-BN layers on further metals in the future.

As discussed above [156], the current status of vdW-DFT methods is insufficient to predict material structures and properties for strongly corrugated h-BN, 2D materials, or for solids in general. It is anticipated that recently emerging machine learning and artificial intelligence methods employed on sufficiently big data will reach that purpose and speed up materials research and development considerably [161,162].

4. Interactions of h-BN with adsorbates

4.1. Spectroscopy, microscopy and DFT studies of the adsorption and reaction of molecules on h-BN nanomesh formed on metal surfaces

In this section, we primarily highlight some of the works of recent years, in which, new information was obtained about the adsorption properties, stability and modification possibilities of h-BN through molecular adsorption processes in UHV (Table 4).

Table 4
Adsorption of selected molecules on different type of h-BN/metal surfaces.

adsorbent	T ads	exposure/dosing pressure	Substrate and Ref.	observed effect/main results	Exp. method(s)
hydrogen	at and above 180 K	1×10^{-6} mbar	h-BN/Ni(111) [163,164]	no adsorption	STM
	RT	1×10^{-5} Torr	h-BN/Pt (111) [165]	no dissociation	XPS and UPS
	RT	1×10^{-1} Torr	h-BN/Pt (111) [165]	intercalation, partial dissociation	STM, XPS, UPS
	170 K	1 L	h-BN/Ni(111) [166]	hydrogenation, covalently bond to B–H, T_{des} at 600 K	HR XPS, NEXAFS, UPS, TPXPS and TPD
	170 K	600 L	h-BN/Ni(111) [166]	intercalation, lifting the h-BN, desorption at 390 K	HR XPS, NEXAFS, UPS, TPXPS and TPD
H atom	170 K	1 L H	h-BN/Rh (111) [167]	hydrogenation, covalently bond to B–H, T_{des} at 640 K	HR XPS UPS, TPXPS
	1000 K	from 1260 L	h-BN/Rh (111) [27]	h-BN started to breakdown above 1100 K	HREELS, TPD
	170 K	100–600 L	h-BN/Ni(111) [166]	B–H formation	TPD, XPS
oxygen	170 K	_	h-BN/Ni(111) [168,169]	no reaction	HR XPS, NEXAFS, UPS, TPXPS and TPD
	240 K	72 L*	h-BN/Ni(111) [168,169]	(*oxygen with kinetic E ~0.7 eV) covalently bonded molecular oxygen species	HR XPS, NEXAFS
	300 K	57 L*	h-BN/Rh (111) [167]	(*oxygen with kinetic E ~0.7 eV) covalently bonded molecular oxygen species	HR XPS UPS, TPXPS
	1000 K	from 130 L	h-BN/Rh (111) [27]	h-BN started to breakdown	HREELS, TPD
water	52 K	2 L	h-BN/Rh (111) [170,171]	ice clusters featuring a water bilayer structure in the nanomesh pores	STM DFT
halogens (bromine)	170–640 K	1 ML	h-BN/Rh (111) [172]	adsorption in the nanomesh pores	XPS DFT
CO	170 and 300 K	50 L	h-BN/Rh (111) [27,173]	no adsorption	HREELS, TPD
CO_2	300 K	low and high exposures	h-BN nanoflakes [67]	no adsorption	TPD, DRIFTS
CH_3OH	140 K	6 L	h-BN/Rh (111) [81]	weak chemisorption, no decomposition	TPD, HREELS
C_2H_5OH	170 K	4 L	h-BN/Rh (111) [23]	weak interaction, molecular adsorption and complete desorption below 250 K	HREELS, TPD
C_2H_4O	170 K	5 L	h-BN/Rh (111) [174]	no adsorption	HREELS, TPD
C_6H_{10}	160 K	3 L	h-BN/Rh (111) [27]	weak interaction	TPD, HREELS
	1000 K	≥13 L	h-BN/Rh (111) [27]	carburization, broken up the BN nanomesh	AES, HREELS
C_6H_6	160 K	3 L	h-BN/Rh (111) [27]	weak interaction	TPD, HREELS
	1000 K	~2600 L	h-BN/Rh (111) [27]	graphene-like layer, without damaging the h-BN nanomesh	AES, HREELS
C_{60}	300 K 40 K and RT	monolayer	h-BN/Rh (111) h-BN/Rh (110) [7, 175]	supramolecular str. On h-BN/Rh (111) similar to bulk solid C_{60} on h-BN/Rh (110)	STM, STS
azobenzene	130, 170 and 300 K	0–100 L	h-BN/Rh (111) [176]	stability decreases on the order of pore–wall–wire regions two peaks in the sub monolayer regime	TPD, HREELS, STM, DFT
phthalocyanine	5 K 77 K	sub monolayer coverages	h-BN/Rh (111) h-BN/Ir (111) [177,178]	selective adsorption in the pore region, weak interaction with wire region	STM, DFT
$C_{12}F_4N_4$	RT	1 molecule per unit	h-BN/Rh (111) [179]	electron transfer from the substrate to the F4 TCNQ molecules	UPS, XPS, STM, DFT

Several small molecules such as CO, CO_2, H_2O, N_2O, NO, NO_2, and O_2 on h-BN monolayers supported on metal surfaces bind very weakly on the bare h-BN as determined by density functional theory [180]. Interestingly, same particular compounds and gas molecules are chemisorbed strongly on h-BN, with binding energies of >1 eV, whereas other molecules still physisorbed, with binding energies about 0.1 eV at most.

Selective covalent functionalization of the h-BN/Rh (111) nanomesh pores with oxygen molecules and hydrogen atoms was achieved [167]. In this study the adsorption and thermal stability were studied applying synchrotron radiation-based in situ HRXPS, temperature-programmed XPS and UPS. When 10 L O_2 molecules were dosed via backfilling of the vacuum chamber at room temperature, oxygen functionalization of the h-BN nanostructure did not occur. However, when supersonic molecular beam (SSMB) (kinetic energies of 0.3–0.7 eV) was used significant adsorption was observed at 300 K. The N 1s was followed during adsorption, the results are represented in Fig. 18.

The N 1s XPS shape changes dramatically. While the spectrum at 398.11 eV attributed to the wire region of h-BN nanomesh stays almost constant regarding peak intensity and position, the pore signal decreases in intensity and a new peak develops at 398.47 eV. This new feature is dedicated to the oxygen-functionalized pore arising from the modified chemical environment of the N atoms in the pores. The oxygen functionalization is stable up to about 700 K. After annealing the bare h-BN nanomesh is restored.

Since molecular H_2 doesn't adsorb on h-BN, atomic hydrogen was used for functionalization of h-BN on Rh (111) [167]. Fig. 19 displays the B 1s and N 1s spectra recorded prior to hydrogen functionalization, after functionalization at 170 K and after annealing to 1000 K.

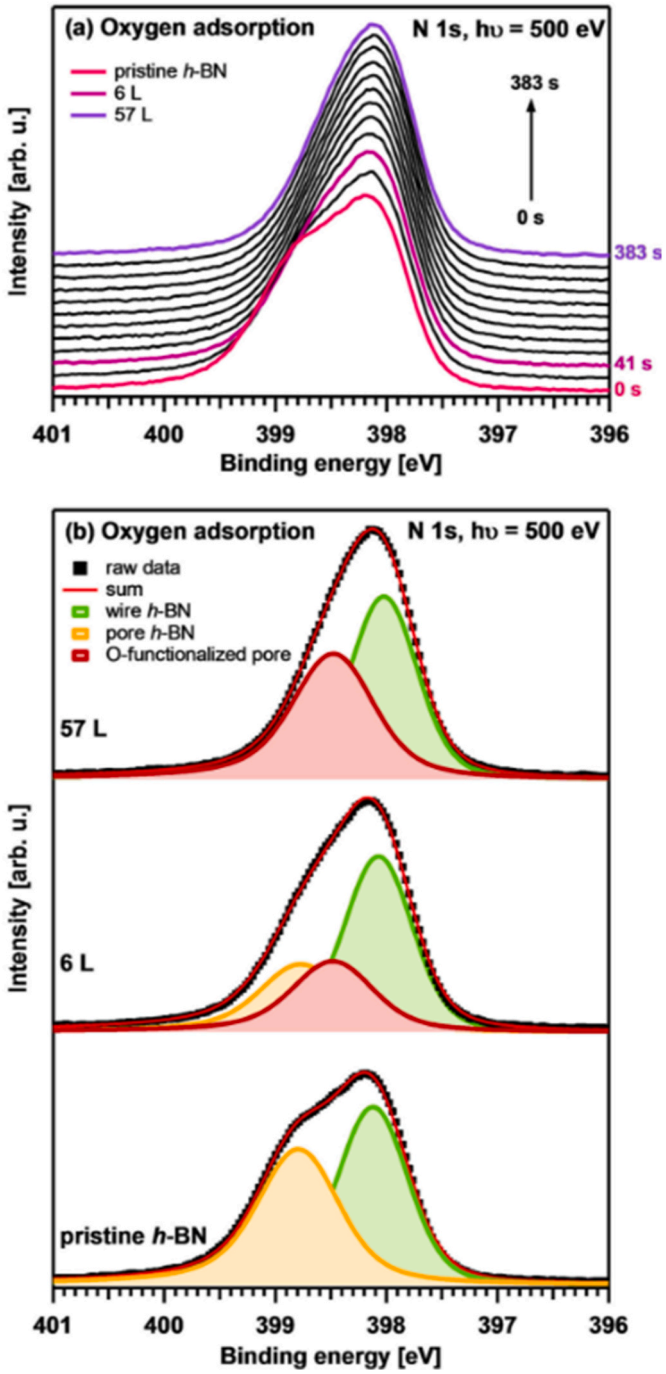

Fig. 18. a) N 1s XP spectra recorded normal to the SSMB at 300 K during exposure of h-BN/Rh (111) to 57 L oxygen with a kinetic energy of 0.7 eV; b) Fits of selected N 1s XP spectra recorded of pristine h-BN/Rh (111) and of h-BN/Rh (111) after exposure to oxygen (0.7 eV; 2×10^{-7} mbar) for 41 and 383 s. Reproduced from Ref. [167].

The B 1s XPS of h-BN/Rh (111) before adsorption exhibits a broad signal containing two peaks at 190.72 and 190.29 eV, which corresponds to the pores and wires of the nanomesh. After atomic H adsorption, a shift to lower BE were observed for both components, and a new peak developed at 190.45 eV, which was assigned to hydrogen functionalization in the pore of h-BN. The N 1s behaves similarly, upon atomic hydrogen adsorption a new species appeared at 398.46 eV attributed to the hydrogen-functionalized pores. In contrast to the h-BN/Ni(111) system [166], intercalation of hydrogen atoms was not found. TPXPS experiments showed that hydrogen atomic hydrogen functionalization is reversible up to 640 K. In a separate experiment it was observed that above 1100 K applying high doses (~1260 L) the h-BN nanomesh started to decompose [27].

From the experiment it became clear, the oxygen molecules and the atomic hydrogen prefer to bind in the pores of the nanomesh shown in Fig. 20.

Strong oxygen-BN interaction was detected in the case of Ni(111) [168], Rh (111) [27] and on Ru (0001) [181] especially when high temperature or activated oxygen was used. The electron transfers from the metal substrate to p_z states of h-BN is responsible for the strong binding at boron atoms [180]. Efficient molecular adsorption and high selectivity would make the h-BN/metal interface suitable for the applications such as active component in catalysis, catalyst support, templates, and gas sensors. Alcohols and aldehydes interact weakly with boron nitride [27,101,174].

The interaction of hydrogen with h-BN structure is an important factor. The molecular hydrogen cannot interact strongly with perfect h-BN layer without activation [27,163–166]. When h-BN/Pt (111) was the substrate for h-BN, hydrogen dissociation was not observed at low pressure (10^{-5} Torr) at room temperature. At higher pressure (0.1 Torr) due to hydrogen intercalation, the dissociation can happen. XPS, NEXAFS, and UPS were used in studying the interaction of h-BN nanosheets on Ni(111) surface with atomic hydrogen and subsequently the thermal stability of the system [166]. The study shows hydrogen bond at low hydrogen exposures and only at medium exposures intercalation is observed, intercalation and hydrogenation were observed at high dose of hydrogen. The intercalation leads to quasi-free-standing h-BN. In hydrogenation reaction, B–H bond formation is detected, which is accompanied by charge redistribution of the h-BN structure. When Rh (111) surface was the substrate for h-BN nanomesh formation, the high doses of hydrogen at 1000 K, the BN started to break up as manifested by the appearance of CO–Rh HREELS losses at around 1900–2000 cm^{-1}. At high temperature exposures, the BN phonon features diminished, and the CO band dominated the HREEL spectrum [27]. In the light of presented data about the interaction of hydrogen with h-BN produced on different substrates and the hydrogen intercalation obtained in different laboratories, it can be concluded that not only the nature of substrate metal but the applied pressure and preactivation of the hydrogen play a crucial role.

Recently the adsorption behaviors of different gas molecules (H_2, CO, NO) on h-BN monolayers were investigated on defective h-BN with theoretical and experimental methods [182]. The presented data show that the defective h-BN monolayers strongly adsorbed hydrogen molecules. These new findings help a better understanding for the growth process of h-BN layer with different gas mixtures.

When significant amount of water is introduced to a pristine h-BN/Rh (111) nanomesh, the formation of ordered and stable nano-ice crystals in the pores has been detected [171]. The applied model proposed for the nano-ice cluster trapped in the pore of the nanomesh, which contains 38 molecules. Nano-ice gives individual insight into the self-assembly of H_2O and suggests it to be a good candidate to study proton disorder in 2D ice layer [170]. Sum-frequency generation spectroscopy (SFG) was used characterizing the hydrophobic behavior of h-BN [183]. The disappearance of the O–H stretch in adsorbed H_2O is used as an indicator of a hydrophobic surface. This bond originates from the dangling, nonhydrogen-bonded, O–H group.

The interaction of h-BN nanosheets with different halogens was investigated mostly by DFT calculations. On F-doped h-BN a significantly decreased band gap was calculated compared to pristine h-BN [184]. A comparative investigation of halogen-doped (Cl, Br, I) h-BN structures has been performed [185]. DFT data suggested that stronger halogen bond was found at boron edge during the interaction. The important message for the experimental studies is that all halogen-doped h-BN systems have high adsorptive desulfurization ability. Bromine adsorbs exclusively in pores on nanomesh of h-BN prepared on Rh (111) surface. No such selective adsorption on graphene

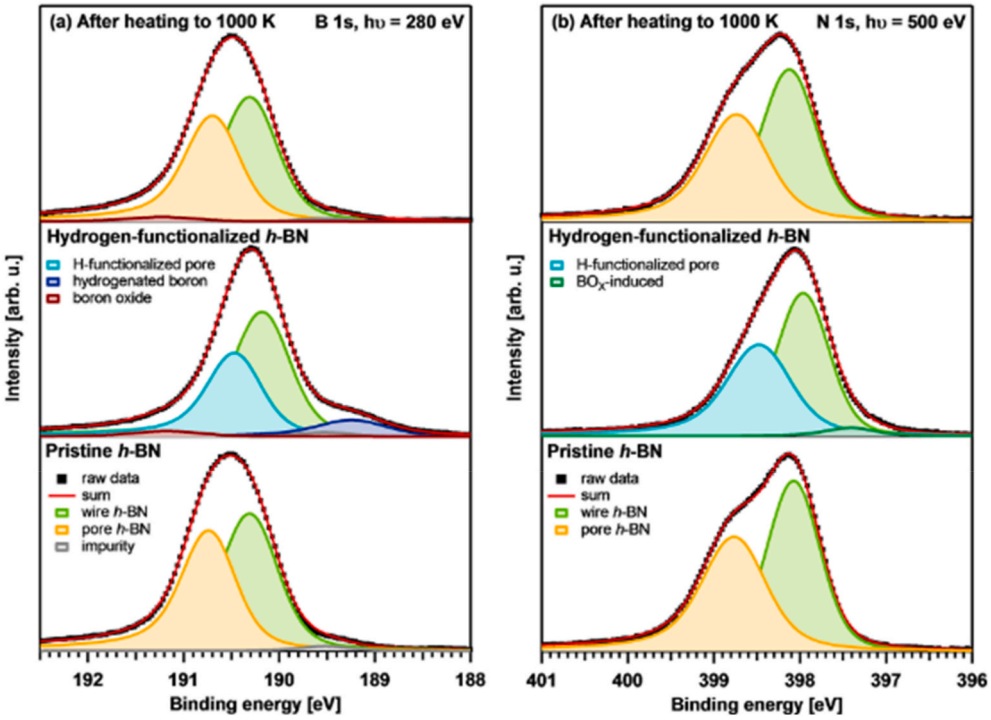

Fig. 19. a) B 1s and b) N 1s XP spectra of pristine h-BN/Rh (111), 1 L H/h-BN/Rh (111) at 170 K and 1 L H/h-BN/Rh (111) after heating to 1000 K. Reproduced from Ref. [167].

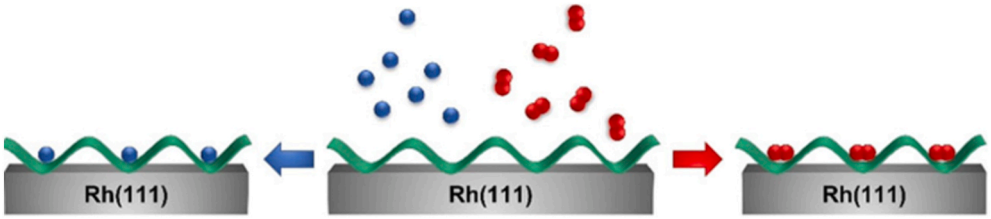

Fig. 20. Schematic representation of the arrangement of oxygen molecules and atomic hydrogens in h-BN pores prepared on Rh (111). Reproduced from Ref. [167].

was detected [172].

Several spectroscopic results and theoretical calculations indicate that the hydrocarbons interact weakly with h-BN nanomesh due to the interaction strength, although it is believed that hydrocarbon moieties could be a source for the production of graphene on h-BN [15]. Nowadays, the preparation of the graphene layer on non-metal substrates is one of the exciting fields in surface and nano science [27,186,187]. Continuous efforts are made in this direction in nanoscience and in material science due to its technological importance. It was observed by TPD and HREELS that there is only a weak interaction between cyclic hydrocarbons (cyclohexane and benzene) and h-BN [27]. Therefore, the surface activity was investigated at high temperature (~1000 K) in order to decompose C6 cyclic hydrocarbons to cover the h-BN nanosheets containing nanomesh by a carbon layer. It turned out that with the high temperature decomposition of cyclohexene the h-BN is not only covered, but the nanomesh is also destroyed, and the C layer started to develop in parallel with the decomposition of h-BN layer. The formation of graphene layer from high temperature decomposition of C6 cyclic hydrocarbons is displayed in Fig. 21. The layer is complete from C_6H_6, while partial carbonization occurs from C_6H_{10} decomposition.

In another work, the formation of graphene nanoflakes below the nanomesh wires of the h-BN/Rh (111) structure was reported using segregation growth, and its effect on pentacene molecular adsorption has been investigated [20].

Concerning the application of h-BN nanomesh for templated

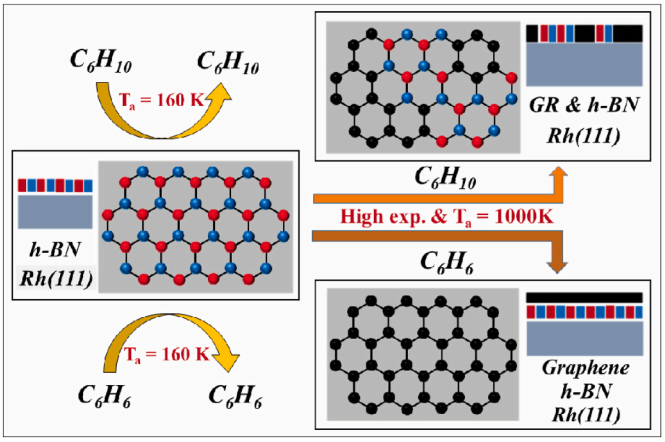

Fig. 21. Schematic representation of the formation of graphene layer from high temperature decomposition of C6 hydrocarbons. Reproduced from Ref. [27].

supramolecular structures, C_{60} adsorption gives an excellent example. The formation of ordered/tailored supramolecular arrangement was clearly observed by STM with preferential adsorption in the pores of the nanomesh after deposition of C_{60} molecules at roughly a ML coverage on

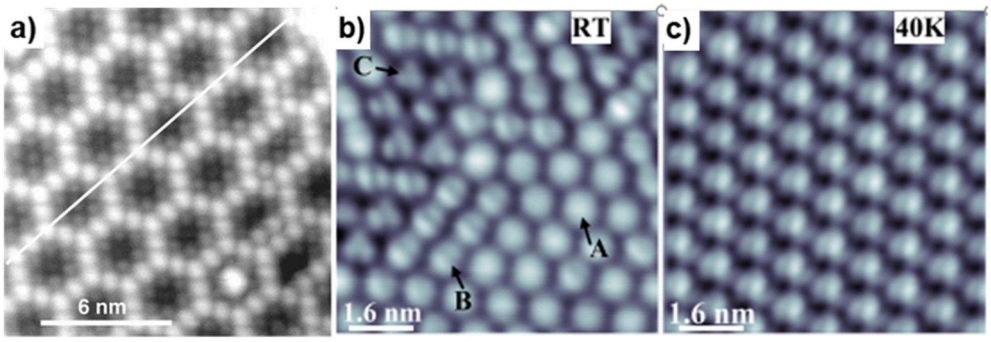

Fig. 22. (a) High-resolution image of a region of h-BN nanomesh decorated by C_{60} molecules on (Rh (111). Individual molecules are imaged throughout this region, following closely the topography of the mesh. The positions in the hole centers are occupied by either zero or one C_{60} molecule; at two places, large protrusions may represent additional corralled molecules. (b,c) Orientational order-disorder transition of C_{60} on h-BN/Rh (110). Intramolecular features of C_{60} acquired at RT and 40 K, indicating an orientational disorder/ordering at RT/40 K. Partially reproduced from Ref. [175].

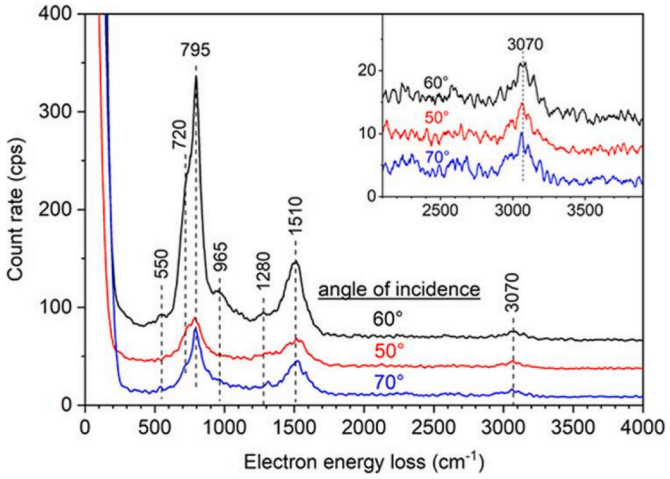

Fig. 23. HREEL spectra obtained at different angles of incidence after the exposure of h-BN/Rh (111) to 100 L of azobenzene at 300 K. The specular geometry is at 60°. Spectra are not normalized to the elastic peak intensity. The C–H stretch region is shown magnified in the inset. Reproduced from Ref. [176].

h-BN/Rh (111) at 300 K [7]. STM imige of C_{60} covered h-BN/Rh (111) is shown in Fig. 23a. When Rh (110) was used as a substrate, which is an anisotropic and more open surface, and a 1D h-BN superstructure with smaller corrugation is formed with a much smaller periodicity, a different C_{60} arrangement was detected (Fig. 22b and c) [175]. The images demonstrate the phase transition of C_{60} on h-BN/Rh (110) interface similar to that observed on bulk solid C_{60}. The decrease in thermal energy allows recognition between C_{60} molecules. Fullerene molecules show random orientations at 300 K, while at 40 K such rotational disorder vanishes and they adopt a general orientation on h-BN/Rh (110). The orientation, the order-disorder transition and the orbital appearance of C_{60} on h-BN/Rh (110) interface are represented in Fig. 22.

The azobenzene adsorbs preferentially in pores of the h-BN/Rh (111) [176]. Adsorption properties of azobenzene – the prototypical molecular switch – were investigated by means of angle resolved HREELS, TPD and STM on h-BN nanomesh prepared on Rh (111) surface. TPD results propose an inhomogeneity of adsorption sites on h-BN nanomesh. At low coverages azobenzene preferably adsorbs in the pore, followed by wall- and wire-adsorption, exhibiting a template effect. At larger exposures, the development of the multilayer structure is controlled by the complex cooperation between template-driven and molecule–molecule interactions. The production of the second molecular layer simultaneously covers the wall and wire regions of the nanomesh [176]. HREEL spectra were recorded at different angles of incidence after dosing h-BN/Rh (111) interface to 100 L at 300 K to explore the adsorption geometry of the molecules (Fig. 23.). The intensities of out-of-plane modes at 720, 796, 965 cm^{-1} decreased drastically at the off-specular geometries, while the intensity loss of the in-plane peaks (1280, 1510 cm^{-1}) was lower. Especially the band belonging to the C–H stretch (3070 cm^{-1}) is important in this case because h-BN has no contribution to the spectral feature. The intensity of C–H stretch can give information about the geometry of adsorbed molecules. The HREELS measurements, in angle-resolved mode, strongly suggest that the adsorption geometry of azobenzene is parallel to h-BN. If both phenyl rings are parallel to the surface, then it also implies that the *trans*-azobenzene is preferred compared to the cis isomer. STM experiments also revealed a template effect of the periodically corrugated nanomesh: a strong tendency for adsorption in the pores is pictured as individual nanodots by STM (Fig. 24).

DFT approaches gave further details regarding the adsorption energetics and bonding, and confirmed the experimental results that the azobenzene adsorbs with the phenyl rings parallel to the surface, favorably in the pores, and also proved an attractive interaction between the molecules. *Trans*-azobenzene was found to be most stable. The energetically favored *trans*- and *cis*-azobenzene adsorption configurations are shown on Fig. 25. The cis configuration was not observed experimentally.

Very recently, an Ullmann-like coupling reaction by a planar biphenylene compounds, i.e., 1,8-dibromobiphenylene ($BPBr_2$), on h-BN/Rh (111) surface with an excellent selectivity of the dimer biphenylene compound, containing 4-, 6-, and 8-membered rings was realized [188]. The rhodium atom is incorporated into a carbon–halogen bond, developing organometallic surface intermediate complexes and form C–C covalent bond [189–191]. The $BPBr_2$ precursor was chosen, because it is a planar molecule and it is suitable for direct STM visualizations, on the other hand it is a candidate to prepare functional low-dimensional carbon nanostructures in 2D electronic devices [192]. 2D h-BN exhibits a wide band gap with no states near the Fermi level, therefore it is suitable to decouple the catalyst from the reactions while preserving the catalytic activity [193]. Fig. 26 represents the scheme of the proposed model for Ullmann reaction catalyzed by h-BN/Rh (111) without forming any organometallic intermediate. The investigations were carried out by means of a combination of STM and DFT. The single layer of h-BN can protect the Rh (111) surface underneath, while preserving the reactivity of the Rh (111) [188].

The detailed STM results showed that the $BPBr_2$ molecules favor selective adsorption on the pores. After heating the $BPBr_2$/h-BN/Rh (111) system to 200 °C, the Ullmann-like coupling of $BPBr_2$ molecules to a dimer, biphenylene occurred. It was concluded that the electron wave of Rh (111) can penetrate through the single-layer h-BN and generates

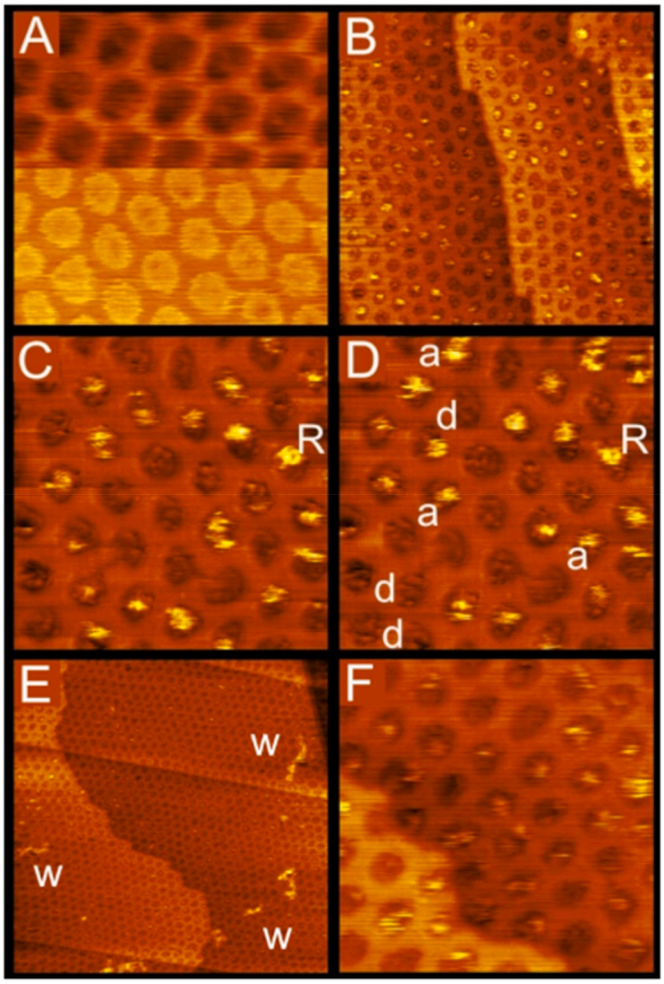

Fig. 24. STM images recorded at room temperature (A) before and after different exposures of azobenzene on h-BN/Rh (111) surface at 320 K: (B, C, D) 30 L, (E, F) 90 L. C and D images show two records (refernce point R) taken up subsequently, suggesting a tip-induced surface diffusion (newly appeared/a and disappeared/d) of the molecules. The chain structures indicated by „w" in E image refer to 1D-coupling of molecules at high exposure. The size of the images: (A, C, D, F) 20 × 20 nm^2, (B) 50 × 50 nm^2, (E) 100 × 100 nm^2. The parameters found for the best imaging of the surface covered by azobenzene molecules: $U_t = -1$ V voltage on the sample and $I_t = 20$ pA current. Reproduced from Ref. [176].

the Ullmann-like process of $BPBr_2$. Together with the participation of the h-BN template effect, an outstanding selectivity of the covalently bonded compound could be realized.

4.2. Adsorption of large organic molecules and organic semiconductors on h-BN nanosheets supported by metal surfaces

Hexagonal boron nitride has attracted significant attention because its van der Waals properties together with its insulating character makes it an ideal substrate for preparation of high quality organic crystalline thin films without disturbing effect of the substrate. The possibility of surface fabrication of organic materials for electronic, optoelectronic, straintronic and spintronic devices are demonstrated nowadays using h-BN nanosheet [194,195]. Adsorbed rubrene, C_8-BTBT, pentacene, *para*-hexaphenyl, dihydrotetraazaheptacene, hexacontane, diacetylene, melamine, 2D porphyrine were studied on exfoliated h-BN by means of STM, AFM and DFT calculation [196]. The structural, energetic, and electronic behavior of five molecular donors and acceptors such as tetrathiofulvalene (TTF), bithiophene (2 T), pyrene, tetracyanoquinodimethane (TCNQ), and fluorinated TCNQ (F4−TCNQ) adsorbed on freestanding h-BN (and MoS_2) single layers were investigated by DFT [197]. These five considered interfaces are stable due to dispersion interactions with overall flat arrangement on both substrates. The new observations offer useful directions to design low-dimensional hybrid interfaces for opto-electronic applications. The hybrid model interfaces are shown on Fig. 27.

A comparative study of $C_{64}H_{36}$ (Dibenzo{[f,f']-4,4′,7,7′-tetraphenyl} diindeno [1,2,3-cd:1′,2′,3′-lm]perylene) adsorption on h-BN and graphene on Ru (0001) and Pt (111) substrates was reported, and unlike graphene, only h-BN showed sharp orbital resonances in the vibration spectrum irrespective of the chosen metal substrate [198]. The h-BN/Cu (111) interface is a frequently used template for investigating other molecular systems, either individual molecules or self-assembled supramolecular structures, by a combination of experimental and DFT methods: bis(tetraphenylporphyrinato)thorium (Th $(TPP)_2$) for actinide-based metal organic complexes [199] and photoactive pyridin-4-ylethynyl functionalized pyrene derivatives [200] were studied. The molecular level alignment and charge states of fluorinated cobalt phthalocyanines on thin h-BN sheets on Cu(111) surface are published using STM and STS, as well as AFM and complementary theoretical calculations [201]. The adsorption geometry of F_{16}CoPc on h-BN/Cu(111) is presented in Fig. 28.

Recently, the formation of azaullazine units and its polymerization by cycloaddition was studied on Au (111), Ag (111) and h-BN/Cu(111) using STM, AFM and matrix-assisted laser desorption and/or ionization (MALDI) mass spectrometry in solid state in the absence of catalysts. Such kind of intermolecular reactions give a promising route for direct synthesis of polyaromatic polymers.

The behavior of the adsorbed supramolecular layer depends strongly on the nature of the substrate material and on the properties of the interface layers. On surfaces, where the interaction between the substrate surface and the molecules are weak (homogenous metallic surfaces or inert 2D materials, like h-BN) typically weak secondary binding forces (e.g., van der Waals) are formed and the final structure of the molecular layer is driven by the intermolecular forces. It was found that the hexacontane monolayer behaves as a representative case of two-dimensional supramolecular organization on BN structures [52]. Using h-BN as an insulating substrate enables to study the optical properties of such structures which were difficult on conducting surfaces. It is believed that combination of h-BN and van der Waals mediated molecular organization could be the model system in the research and technology of surface-stabilized supramolecular arrays [52]. van der Waals forces result in close-packed constructions in organic field-effect transistors (OFETs) where the symmetry is controlled by the geometry of adsorbed molecules. In the operation of OFETs interfaces play a key role because charge carrier transport is influenced by the interfaces between semiconductors and electrodes and interfaces between semiconductors and insulators [53]. The red shift of the fluorescence of a two-dimensional supramolecular network on h-BN is due to the adsorbate-substrate van der Waals interactions. Hydrogen bonding is utilized to steer porphyrin dye molecules into a stable planar arrangement. As a consequence of this forcing effect the fluorescence spectrum is influenced significantly by the substrate, and their intermolecular spacing is determined [202]. Moreover, the template behavior of graphene and h-BN is not confined to the monolayer of molecules (Θ, coverage) [203]. The molecules of the second layer of CoPc on h-BN/Ir (111) align themselves with the pores of the underlying h-BN moirè pattern [178]. Nevertheless, the molecules in the second layer are electronically more decoupled from the substrate than the first layer and the third layer will be further decoupled.

Organic molecules on 2D h-BN could be the sources of visible-range single photon emission (SPEs) which are promising candidates for quantum information processing [204,205]. The energy of this main emission peak often changes between emitters within the same sample from 1.6 to 2.2 eV. SPEs can be prepared from different materials,

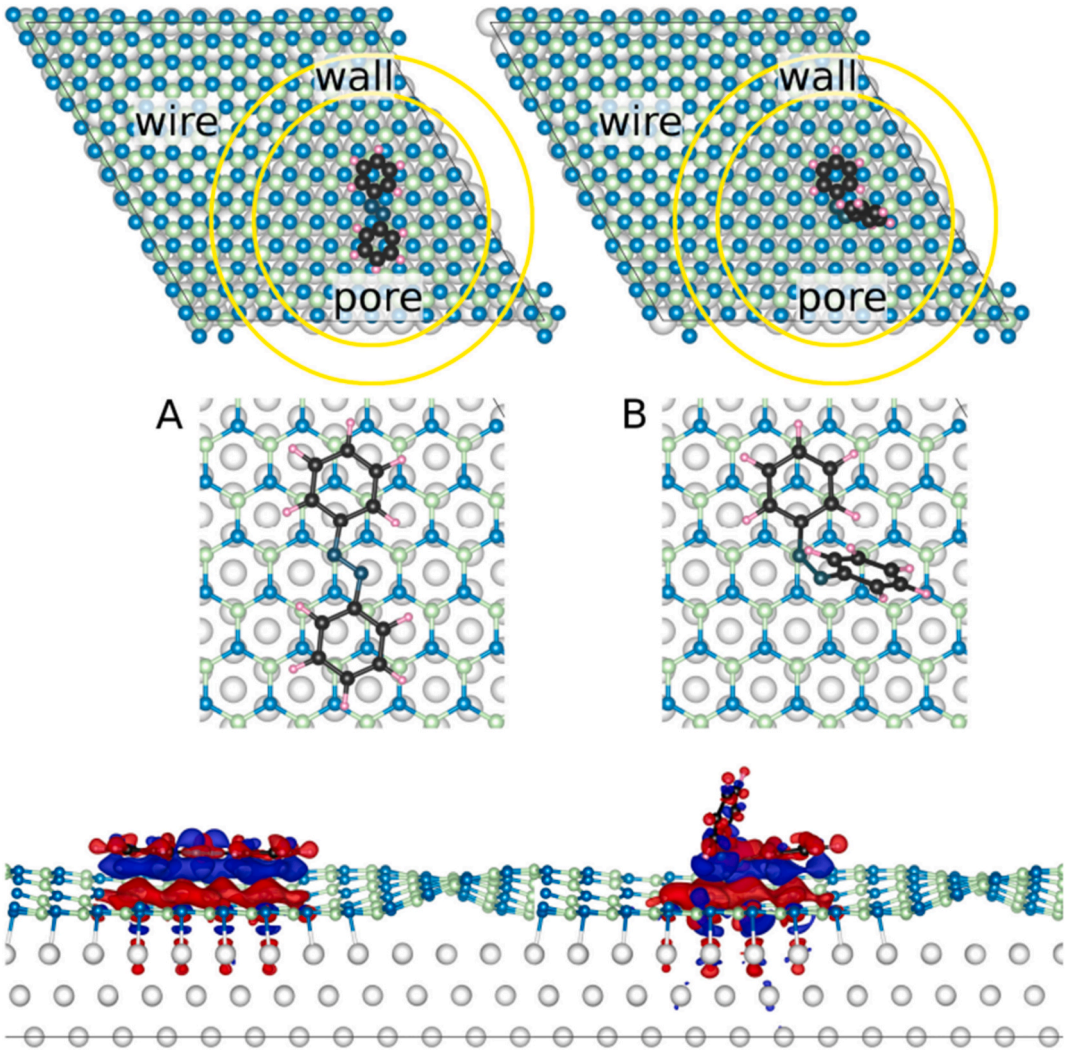

Fig. 25. The energetically favored *trans*- (A, left) and *cis*- (B, right, 0.82 eV higher in total energy) azobenzene adsorption configurations after geometry optimizations with dipole correction (top: top view showing the surface unit cell and the different surface regions: pore, wall, wire; middle: top view zoomed on the molecules; bottom: side view showing the charge transfer upon adsorption). For both isomers the pore region of h-BN/Rh (111) is preferred. The 3D charge transfers ($\rho_{sub\ +\ mol}$-ρ_{sub}-ρ_{mol}) upon molecular adsorption on the substrate are explicitly shown at the bottom of the figure (isosurface value: 2×10^{-4} |e|/Å^3; blue: electron accumulation, red: electron depletion). Colors for the atoms: gray (Rh), light green (B), light blue (substrate-N), dark blue (molecule-N), black (C), pink (H). Reproduced from Ref. [176].

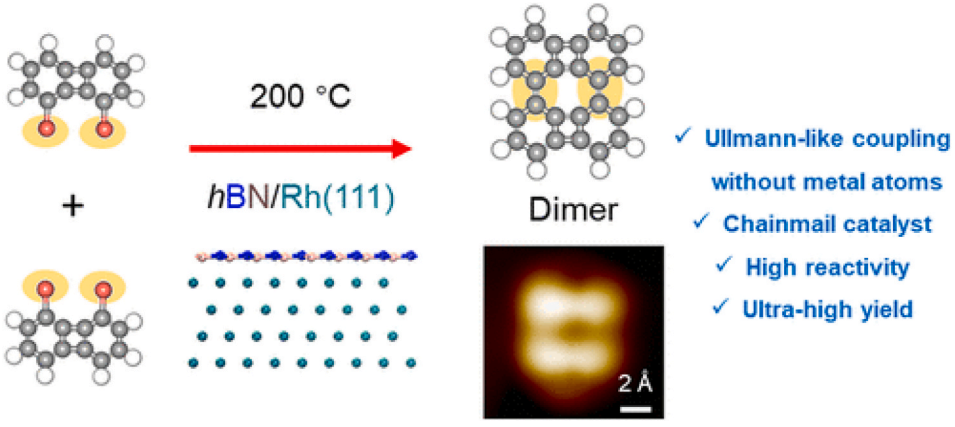

Fig. 26. Illustration of Ullmann-like coupling without metal atoms on h-BN/Rh (111). Reproduced from Ref. [188] Graph. Abstract.

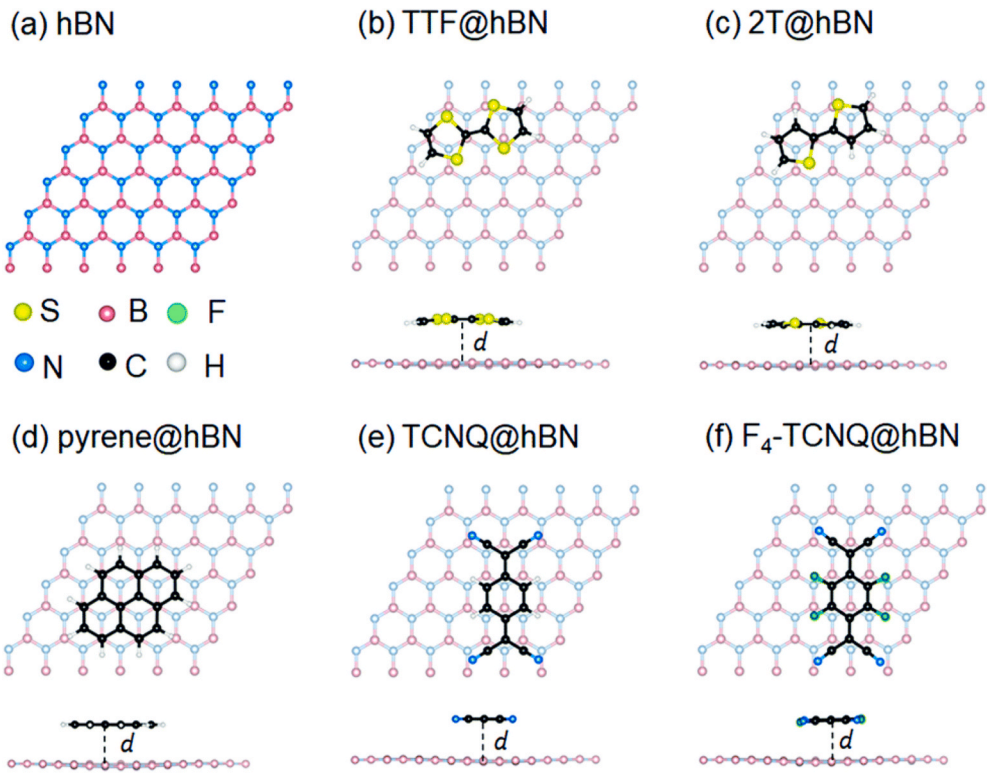

Fig. 27. (a) A 6 × 6 supercell of h-BN monolayer; top and side views of the hybrid interfaces formed by (b) tetrathiafulvalene (TTF), (c) bithiophene (2 T), (d) pyrene, (e) tetracyanoquinodimethane (TCNQ), and (f) fluorinated TCNQ (F_4–TCNQ) adsorbates. Reproduced from Ref. [197].

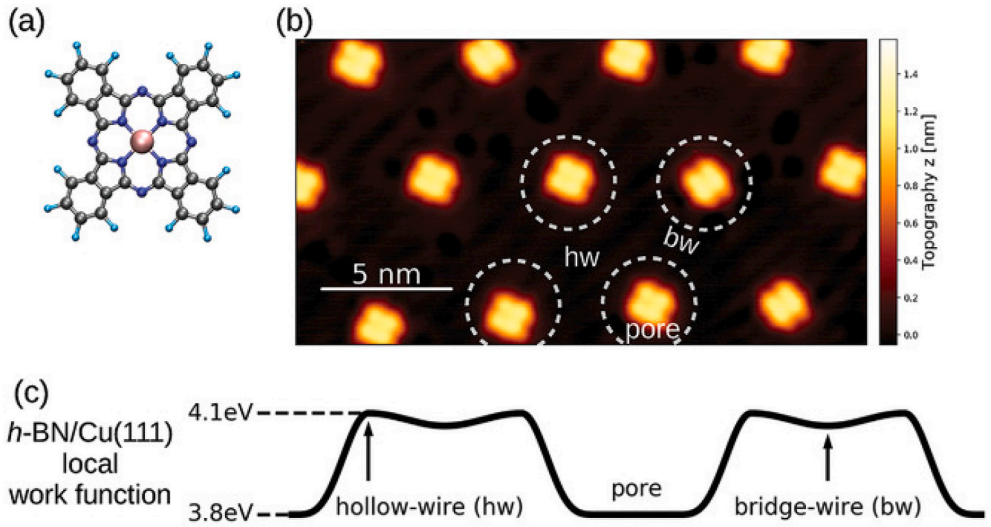

Fig. 28. Preferential adsorption of F_{16}CoPc on h-BN/Cu(111). a) Chemical structure model of F_{16}CoPc (light blue:fluorine, gray:carbon, dark blue:nitrogen, pink: cobalt). b) STM image of 0.06 ML F_{16}CoPc on h-BN/Cu(111) (V_S = 1 V, I = 38 pA). Dashed white circles mark the pore areas of the h-BN/Cu(111) moirè superstructure. The two types of wire regions are labeled with "hw" (hollow-wire) and "bw" (bridge-wire). c) Schematic illustration of the local work function modulation of h-BN/Cu(111), varying by 0.3 eV between the hollow-wire and the pore areas. Reproduced from Ref. [200].

included liquid exfoliated and mechanically cleaved h-BN as well as h-BN grown by CVD [206]. It turns out that the large family of polycyclic aromatic hydrocarbons (PAHs) on h-BN are the best candidates to produce suitable emitters [204,207,208].

Molecule-based 2D materials belonging to covalent organic frameworks (COFs) have a broad range of physico-chemical and mechanical properties. They have potential applications in energy storage, organic electronics and even in catalysis. One of the representatives of this group is the oligomeric biphenyl-COF (BP–COF) (a boroxine-linked COF with biphenyl linking groups) which was prepared on h-BN/Cu(111) and characterized by STM and DFT methods [209]. Its energy gap, bandwidth, and inter-bridge-site hopping amplitudes were determined, the data are well correlated with the results of first-principles theoretical predictions. The noncovalent 2D self-assembly of flat aromatic organic molecules (DCA) becomes increasingly important which have similar importance as that of covalent organic frameworks.

The molecular film which consists of flat, aromatic 9,10-di-cyano-anthracene molecules, DCA was investigated on h-BN/Cu(111)

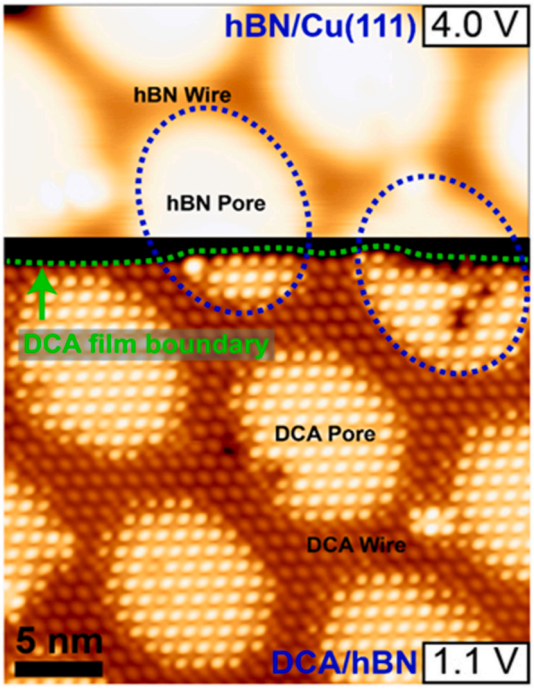

Fig. 29. Constant-current STM imaging at boundary (indicated by dashed green curve) of self-assembled DCA domain on h-BN/Cu(111) (bottom half: V_b = 1.1 V, I_t = 50 pA over DCA film; top half: V_b = 4.0 V, I_t = 50 pA over h-BN surface). The DCA LUMO-related superstructure (defined by bright 'DCA pores' at bottom half, where DCA LUMO contributes to STM imaging) follows the moirè pattern of the underlying h-BN/Cu(111) substrate (dashed blue ellipses). Bright 'h-BN pores' at top half have lower work function than 'h-BN wires'. Reproduced from Ref. [210].

interface [210]. STM imaging at boundary of self-assembled DCA domain on h-BN/Cu(111) is presented in Fig. 29. The low-temperature STM and STS experiments disclosed mesoscopic (>100 × 100 nm^2), morphologically homogeneous crystalline domains produced from flat molecular adsorption and noncovalent in-plane cyano-ring bonding, with electronically decoupled MO lying within the hexagonal boron nitride electronic gap. The observed results give directions and useful information for large-area, atomically-precise, highly-crystalline 2D organics on electronically-functional broad bandgap insulators.

5. Modification of h-BN nanomesh with metal nanoparticles

5.1. Spectroscopy, microscopy and DFT studies on metal nanoparticles on h-BN nanomesh; adsorption and intercalation

The highly regular moirè of h-BN produced by self-assembly on several metal surfaces is exhibiting an outstanding role. The moirè pattern, due to its unique properties, can serve as a template for metal atoms and metal clusters. The template effect often results in a narrower size-distribution of the metal nanoparticles compared to classic supports like metal- or oxide surfaces, potentially providing a structurally well-defined catalyst model. We recall that while templating ability of the moirè h-BN has been demonstrated for several metals for deposition near room temperature (Table 5.), it is not a general rule. Beside gold, it has been experimentally verified also for Pt, but not for Ag on h-BN/Rh (111) in a combined DFT STM study [211]. DFT calculations on Au, Pt, Ag, Pd, Cu, and Ni on h BN/Rh (111) revealed that although all these metal adatoms get negatively charged upon adsorption, only Au and Pt has a sufficiently large pore-to-pore diffusion barrier for the templating. Moreover, neither Pd nor Ni atoms have a special affinity to any specific regions of h BN [211]. Accordingly, the formation of large 3D nanoparticles has been observed after Ni deposition on h-BN/Rh (111) at 300 K [212]. As another example for the lack of Volmer-Weber growth mode and the absence of template effect, the deposition of Sn on h-BN/Ir (111) resulted in the formation of large metallic 2D islands with $\sqrt{7} \times \sqrt{7}$ buckled honeycomb and square structures according to STM. DFT results indicated only slightly smaller formation energy of the honeycomb structure in the pores compared to the wires [213]. Intercalation of metal on the h-BN nanomesh is a common feature in several cases as indicated in Table 5. Intercalated Au atoms are mostly located in or on the topmost atomic plane of the Rh (111) surface, since bulk alloying of gold in rhodium is thermodynamically not allowed, but surface alloying of Au in Rh (111) is feasible [48,214]. For the better survey of the obtained results published recently, a table is presented, containing the substrate metal, the precursor molecule(s) used for boron nitride synthesis, the structure of h-BN, the post-deposited metal and their main characteristics at the interface (Table 5).

In the following, we review relevant results from the literature obtained after the last review paper published by Auwärter [15]. We focus mainly on the post-deposited catalytically active metals, nanoclusters, nanoparticles (Au, Pt, Pd, Co, Fe, Ni, Cu). We briefly summarize the main conclusions about other elements, which are potential candidates for the modification of the surface with their electron donor-acceptor properties (Li, K, Cs, Mn). From optical, magnetic and electronic application point of view, Si and Sm are of interest.

A relatively large number of data has been collected about the growth, (electronic) structure, morphology, and surface chemistry of Au nanoparticles on h-BN using different metal substrates for boron nitride growth. A template effect was identified on h-BN moirè prepared on Rh (111) [47,48,211,212], Ru (0001) [141,279] and Ir (111) [131]. DFT calculations, XPS and vibrational spectroscopy on CO adsorption revealed that gold clusters prepared on h-BN are negatively charged using Rh (111) [23,44,173,211,277] and Ni(111) [258] as substrates. However, recent DFT calculations indicate that the charge state of small Au particles located on h-BN covered Au (111) is characterized by an odd-even oscillatory behavior: Au clusters consisting of 3, 5 or 7 atoms are positively charged by up to ~0.3 eV, because the clusters tend to donate unpaired valence electron to the h-BN/Au (111) substrate [284]. On the other hand, clusters consisting of an even number of gold atoms are partially negatively charged [284]. This comparison underlines the role of substrate metal in the charge state of Au clusters, which in turn can significantly influence their chemical reactivity. The presence of h-BN defects can also play an important role in charge transfers. For example, recent DFT studies about h-BN/Ni(111) indicate that gold adatoms are positively/negatively charged, when adsorbed on boron/nitrogen vacancies, respectively, in accordance with the electronegativity of nearest neighbors [258]. The growth of gold on h-BN/Rh (111) nanomesh has recently been investigated by low energy ion scattering (LEIS) [48,158]. This technique gives information on the outermost atomic layer [285], therefore it is very well suited to analyze the growth mode (e.g. 3D vs. 2D) and intercalation phenomena. LEIS, XPS and STM experiments pointed out that the growth of Au at h-BN/Rh (111) interface at room temperature leads to the formation of mainly 3D gold nanoparticles, although at low coverages (≤0.2 ML) 2D particles were found, which is even more pronounced if gold is deposited at cryogenic substrate temperatures [47,48]. The intensity of Au LEIS signal increased steeply at small Au coverages, while it changed moderately at higher Au doses. The Volmer-Weber growth mode of Au on h-BN/Rh (111) is illustrated by the STM measurements presented in Fig. 30. XPS measurements of room temperature deposition of Au on the nanomesh revealed a lower Au 4f7/2 binding energy [47,48]. Since previous theoretical studies [44,47] pointed out that Au atoms and small Au clusters are partially negatively charged on h-BN/Rh (111), the observed low binding energy can be assigned to an electron transfer from h-BN (and Rh (111)) to Au nanoparticles.

When gold was added on h-BN/Rh (111) at elevated substrate temperatures (400 K), mainly one atomic layer thick 2D islands formed

Table 5
Adsorption and intercalation of metals on h-BN monolayers prepared on metal substrates.

Substrate metal (orientation)	Precursor	Corrugation (2D/1D/flat), superstructure periodicity	Metal deposits on h-BN	Intercalation	Template effect
Ag(001)	borazine [215]	**N/A**	**N/A**	**N/A**	**N/A**
Ag(111)	borazine [216]	Nearly flat with 2D moirè, 1 nm periodicity [216] non-epitaxial [13]	**N/A**	**N/A**	**N/A**
Au(111)	magnetron sputtering of B in 5 % N_2/Ar at 1000 K [217]	flat epitaxial [197]	**Au** **Li** [218] **K** [218]	**Li** – no [218] **K** – yes [218]	**N/A**
Co(0001)	ammonia-borane [219,220] BCl_3+NH_3 [221,222] borazine [223,224]	flat 1 × 1 epitaxial [219,223]	**Co** [222] **Ta** [222] **Au** [224]	**Au** – yes [224]	**N/A**
Cr(110)	borazine [225] BCl_3+NH_3 [226]	1D 1 × 5 [225]	**N/A**	**N/A**	**N/A**
Cu(100)	ammonia-borane [227]	flat epitaxial domains [227,228]	**N/A**	**N/A**	**N/A**
Cu(110)	borazine [229] ammonia-borane [227,230]	flat epitaxial domains [227,228]	**N/A**	**N/A**	**N/A**
Cu(111)	Borazine [216,229,231] ammonia-borane [227,230]	moderate corrugation with 2D moirè [231,232]	**N/A**	**Ag** [216]	**N/A**
Fe(110)	borazine [145]	1D, waves [145]	**N/A**	**N/A**	**N/A**
Ir(111)	ammonia-borane [133] borazine [46,130,132,134,178,233–241]	2D epitaxial 13 B N on 12 Ir [133,134,178,236,240]	**Pt** [233,241] **Sm** [132] **Si** [242] **Co** [234] **Sn** [213] **Au** [131] **C** [131] **Ir** [131] **Li** [235] **Cs** [243]	**Pt** – yes [233,241] **Si** – no [242] **C** – yes [131] **Ir** – yes [131] **Au** – no [131] **Li** – yes [235] **Cs** – yes [243]	**Pt** – yes **Si** – yes, but depend on deposition temperature [242] **C** – yes [131] **Ir** – yes [131] **Au** – yes [131] **Sn** – large 2D islands [213]
Mo(110)	borazine [244]	1D epitaxial waves 4 × 1 [244]	**N/A**	**N/A**	**N/A**
Ni(100)	B_2H_6+NH_3 [85] B_2O_3+NH_3 [245–247] NH_3–BH_3 [248]	1 × 7 structure [85]	**Ni** [247]	**N/A**	**N/A**
Ni(110)	borazine [249,250] B_2O_3+NH_3 [246,251]	flat [250,251]	**N/A**	**N/A**	**N/A**
Ni(111)	borazine [10,107,126,252–255] B-trichloroborazine [83] ammonia-borane [107,256] B_2O_3+NH_3 [246]	flat [126,254–256]	**Au** [254,256–258] **Co** [255]	**Au** – yes [254,256] **Co** – yes [255]	**N/A**
Pd(110)	borazine [129]	„stripe-like" and „dot-like" moirè structures [129]	**N/A**	**N/A**	**N/A**
Pd(111)	borazine [10,108,259]	2 types of moirè (aligned to the substrate, rotated by 30°) [259]	**N/A**	**N/A**	**N/A**
Pt(110)	borazine [101,102,260] B_2O_3+NH_3 [261,262]	nanomesh [102,260–262]	**Cu** [260]	**Cu** – no [260]	**Cu** – only a weak templating effect [260]
Pt(111)	borazine [10,46,88,89,127,193,252,263–265] B-trichloroborazine [84]	nanomesh [46,84,127,193,264–266]	**Co** [265]	**N/A**	**Co** – no [265]
Re(0001)	ammonia-borane [267]	12 B N on 11 Re nanomesh [267]	**N/A**	**N/A**	**N/A**
Rh(110)	borazine [128,175,268]	stripe-like moirè structure [128,175,268]	**N/A**	**N/A**	**N/A**
Rh(111)	borazine [7,46–48,127,211,212,269–275] ammonia-borane [45]	13 B N on 12 R h nanomesh [7,45–48,127,211,212,271,273,276]	**Au** [44,47,48,211,212,277] **Rh** [158] **Co** [272,273,278] **Fe** [273,274] **Mn** [45,273] **Ag** [211] **Pd** [211] **Pt** [211,270,275] **Cu** [211] **Ni** [211,212] **Sn** [269]	**Au** – yes [48,158] **Rh** – yes [158] **Co** – yes, only in oxygen presence [272] **Mn** – yes [45] **Pt** – no [275] **Sn** – yes [269]	**Au** – yes [47,48,211,212] **Pt** – yes [211,275] **Co** – yes BLAG [278] **Fe** – yes [274] **Rh** – yes [158] **Ni** – no [212] **Ag** – no [211]
Ru(0001)	borazine [46,88,99,141,142,279,280] ammonia-borane [281]	14 B N on 13 Ru nanomesh [46,99,141,142,279,280,282]	**Au** [141,279] **Cs, K** [283]	**Au** – yes [279]	**Au** – yes [279] **Cs, K** – yes [283]
W(110)	BCl_3+NH_3 [226]	**N/A**	**N/A**	**N/A**	**N/A**

*yes: experienced.
**no: not experienced.

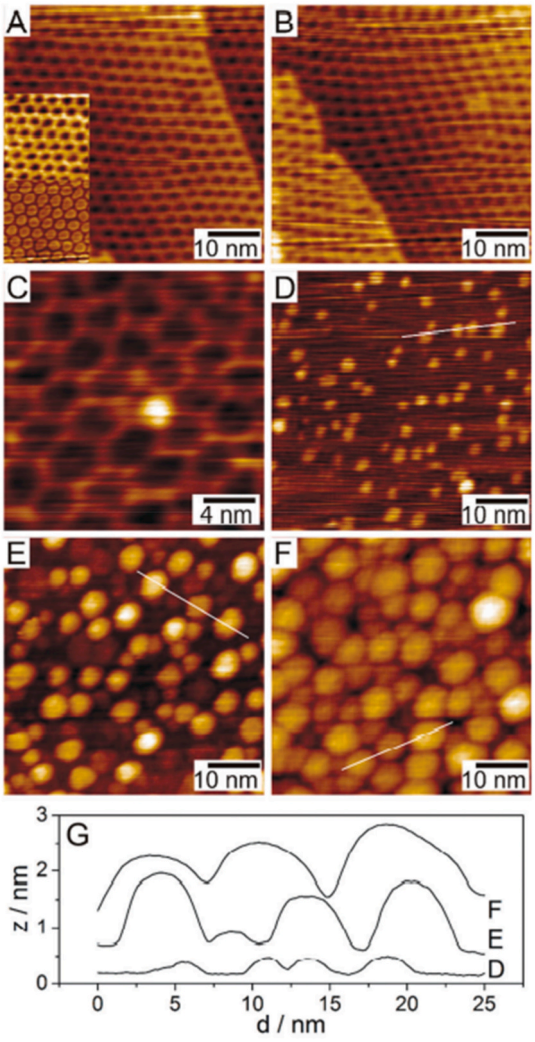

Fig. 30. STM images recorded before and after the deposition of Au at room temperature. (A and B) h-BN/Rh (111) surface before Au deposition. The two images of 20 × 20 nm^2 inserted in (A) (left bottom) show the ''pore-wire'' and ''separated coin''. The size of the images (A and B) is 50 × 50 nm^2. (C) After the deposition of a very small amount of Au (<0.002 ML) exhibiting a separate Au nanoparticle grown above the h-BN mesh. Image size is 20 × 20 nm^2. (D–F) STM images taken after the deposition of different amounts of Au at 300 K: (D) 0.13 ML, (E) 1.0 ML and (F) 3.2 ML. The size of the latter images is 50 × 50 nm^2. (G) Height profiles along the lines drawn on the corresponding images (D–F). Reproduced from Ref. [48].

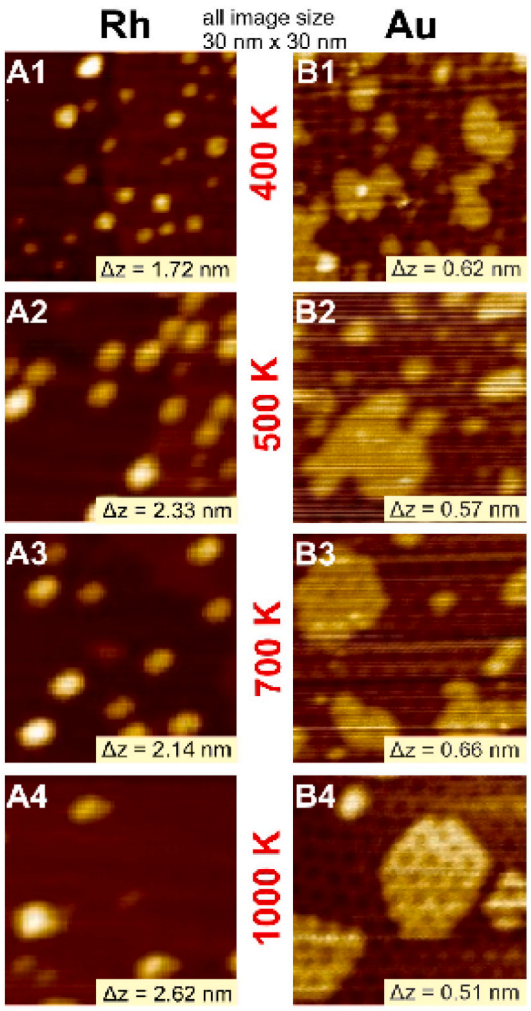

Fig. 31. STM images of 30 × 30 nm^2 recorded after the deposition of approximately 0.25 ML of (A1) Rh and (B1) Au on the h-BN covered Rh (111) surface at 400 K, followed by 5 min annealing at (B) 500 K, (C) 700 K, (D) 1000 K. Reproduced from Ref. [158].

(Fig. 31B). Since gold LEIS intensities proved to be much smaller at 400 K deposition compared to gold deposition at room temperature (Fig. 32), these islands are very probably located below h-BN. At this higher temperature, the diffusion of gold atoms is more facile, allowing intercalation during growth [158].

Post annealing of gold deposits formed at 300 K has been studied on h-BN/Rh (111) [48,158,286]. Sintering (cluster ripening), intercalation, surface alloying and desorption of gold have been postulated as thermally activated processes. Even large amounts of gold can be intercalated below h-BN [158,256], which was proven by the disappearance of Au LEIS peak upon annealing completed at ~1050 K (Fig. 33D). At an initial gold amount of 10 ML, the amount of intercalated gold was ~4 ML, estimated by XPS, while the rest of gold desorbed [158]. LEIS has also been used to monitor the decomposition of the h-BN monolayer, which results in the appearance of substrate metal signal at ~1150 K–1200 K (Fig. 33E, F). It has been shown that an interfacing gold layer significantly improves the thermal stability of h-BN on Rh (111),

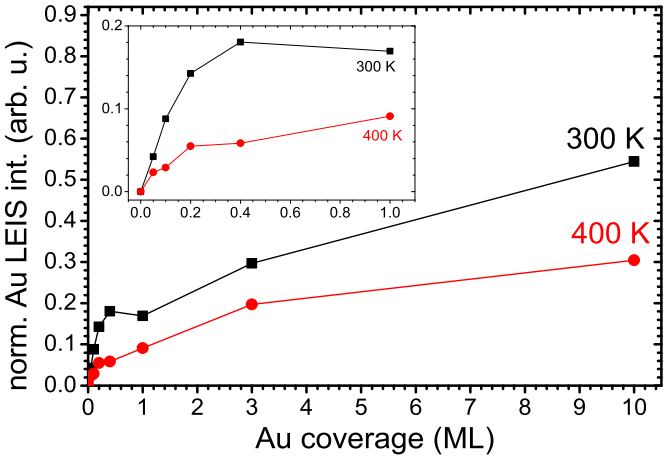

Fig. 32. Au LEIS intensity normalized to the Rh intensity of the clean Rh (111 surface obtained during deposition of Au on h-BN/Rh (111) at 300 K and 400 K.

attributed to the lower reactivity of gold in the dissociation of B–N bonds (Fig. 33E, F). The intact h-BN overlayer, in turn, inhibits the desorption of gold from the interface [158].

Intercalation initiated the investigation of the formation of h-BN

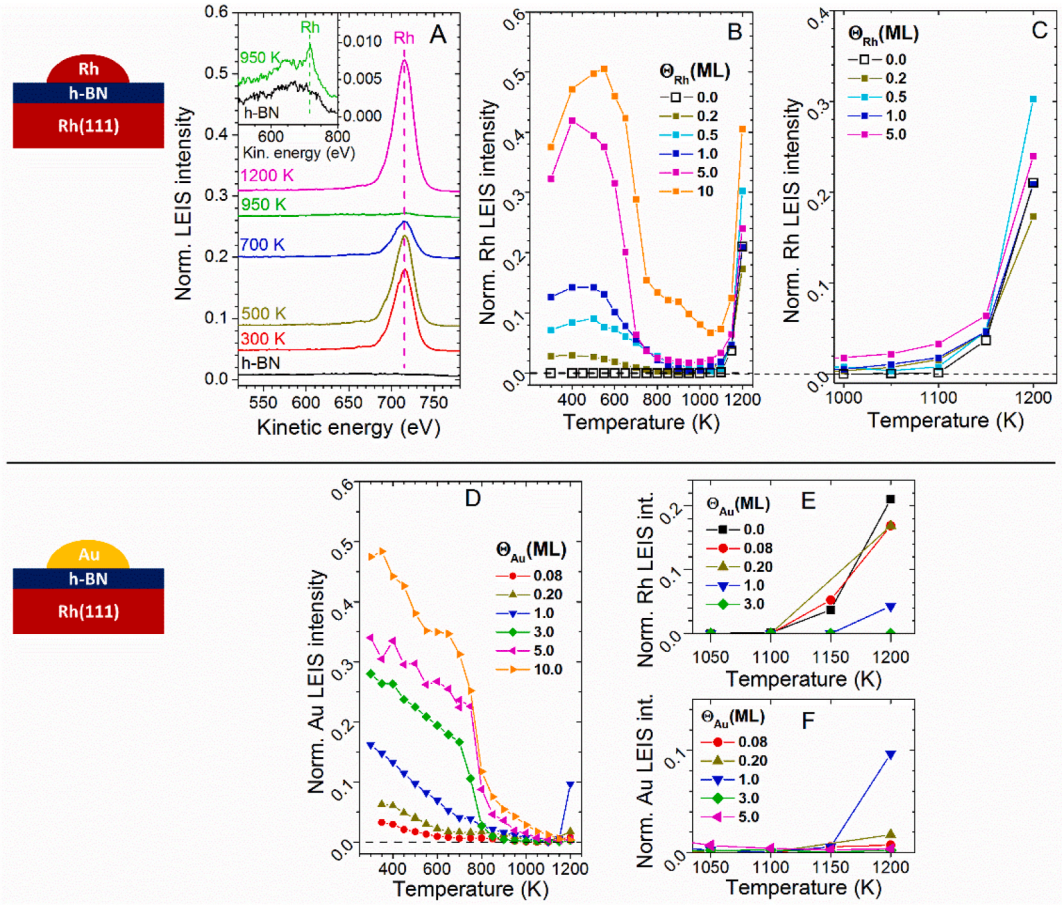

Fig. 33. LEIS results about metal deposition on h-BN/Rh (111) at 300 K, followed by annealing treatments for 5 min. (A) LEIS spectra after 1 ML Rh deposition and annealing. For comparison, the LEIS spectrum of the h-BN covered Rh (111) surface is also shown. Inset: magnified spectra of h-BN/Rh (111) and after 1 ML Rh deposition and annealing at 950 K. (B) Rh peak intensities with different amounts of rhodium dosed on h-BN/Rh (111). (C) A selection of experiments presented in (B) zooming in the high temperature region. (D) Au intensities obtained after gold deposition and annealing. (E, F) Rh and Au intensities obtained in a selection of measurements presented in (D) zooming in the high temperature region. (B–F) LEIS intensities are normalized to the Rh intensity of the clean Rh (111) surface. The sketches on the left serve only to display the sequence of layers after the metal deposition step. Reproduced from Ref. [158].

from borazine on a bimetallic surface, namely on an Au/Rh (111) surface alloy [48]. Au/Rh (111) surface alloys were prepared by dosing gold at 500 K, followed by annealing at 1000 K. According to XPS analysis, gold atoms are located in the outermost surface even after annealing due to the bulk immiscibility of Rh and Au. For subsequent h-BN growth, LEIS results presented that Rh atoms get covered at much smaller borazine exposures than Au. It was an important observation that the nanomesh structure is essentially observable by STM up to relatively large amounts of gold (0.9 ML). At Au coverages in the range of 0–0.9 ML the nanomesh periodicity is the same, but it is less regular, and the pore diameter is decreasing [48]. At large gold amounts (~1.5 ML), the h-BN layer flattens out, as expected because of the weak interaction between gold and boron nitride.

The adsorption and thermal processes of Rh and gold have been compared on the same nanomesh prepared on Rh (111) [158]. Both metals show an essentially 3D growth on h-BN. As shown in Fig. 33, at larger metal doses (3–10 ML) a sharp drop in metal LEIS intensity was observed at ~650 K for Rh, and at ~750 K for Au. Since STM measurements indicated only mild changes in Rh cluster parameters (cluster diameter, height, particle density, cluster-covered area) in this temperature range, it was concluded that the steep LEIS intensity loss is not due to Rh diffusion and intercalation, but it can be attributed to an encapsulation phenomenon. In this scenario, Rh nanoparticles initiate the dissociation of B–N bonds and the clusters get covered by BN fragments. It has also been postulated that the rupture of B–N bonds may open new intercalation channels as well [158]. For the less reactive Au, this mechanism is probably not applicable.

DFT calculations [158] of atomic Au and Rh adsorption on h-BN/Rh (111) revealed that Rh has a larger adsorption energy than Au, which is in line with the experimentally found larger Rh activation energy for desorption. While both Au and Rh atoms exhibit preferred adsorption sites on the nanomesh pore rather than on the nanomesh wire or wall, there are fundamental differences: (1) Rh-on-top-N and Au-on-top-B adsorption sites are found energetically favored with negatively charged Rh and Au atoms of 0.17 and 0.49 excess electrons on them, respectively. (2) Optimizing the atomic geometries of small atomic clusters consisting of 19 atoms (~0.13 ML coverage) of Au and Rh revealed that the Au prefers the formation of a slightly bent 1-atom thick 2D island, and the Rh forms a 2-atoms thick 3D island.

Considering Au and Rh atomic intercalation in h-BN/Rh (111), it was shown by DFT calculations in several model systems that there is an energetic driving force for intercalation [158]. Both Au and Rh single atoms have energetic preference to be located below the h-BN layer in the wire region rather than adsorbed on the h-BN layer in the pore of the nanomesh, or located below the h-BN layer in the pore region. The latter configuration is energetically unfavored since it locally modifies the h-BN layer and results in a weaker overall interaction of h-BN with the underlying Rh (111) substrate. In the presence of the Rh substrate it was also found that Rh atomic intercalation is energetically preferred compared to that of Au. Further extensive DFT calculations of Au and Rh atoms on/in defected free-standing h-BN layers revealed some trends of the atomic intercalation mechanisms [158]. While N vacancies exhibit

generally higher energy barrier than B vacancies for Au and Rh atomic intercalation, there is no such identifiable general relation between Au and Rh as this highly depends on the defect type. A BN divacancy provided the smallest atomic intercalation energy barrier among the studied simple h-BN defects. It was also found that the considered simple defects are too small to promote Au or Rh atomic intercalation through them, and it was proposed that spatially more extended h-BN defects or h-BN edges might play a more important role in the atomic intercalation of Au and Rh, and presumably other metal atoms as well. These calculations did not address the ability of Rh nanoparticles to break B–N bonds. However, they are in agreement with the above assumption that sufficiently large defects created during an encapsulation process may serve as intercalation channels [158]. Conceptually, during intercalation the diffusion of metal atoms is the key process, while during encapsulation the dissociation of B–N bonds, and the migration of BN fragments are the dominant changes. Actually, these two processes can be deeply intertwined.

At this point, it is worth to mention that the general mechanism of metal intercalation through h-BN is still elusive. Typically, the formation of one atomic layer high 2D islands in STM measurements has been taken as evidence for intercalation. More recently, LEIS with its topmost layer sensitivity has also been applied to monitor the diffusion of admetals below h-BN [48,158]. In a combined STM-LEIS study on Au/h-BN/Rh (111) it was pointed out that intercalation is not always accompanied by the formation of 2D islands, probably because of the quick diffusion of gold atoms below h-BN to Rh (111) step edges, and their alloying into the outermost layer of Rh (111) [48]. On non-corrugated h-BN/Ni(111), evaporated Co atoms were collected by defect lines of h-BN. Deposition at 300 K substrate temperature led mostly to the formation of 3D clusters along these lines, while dosing at 450 K resulted in intercalated 2D islands below the defect lines. In this case, intercalation therefore mostly proceeds through defects [255]. However, on Ir/h-BN/Ir (111) it was pointed out based on STM measurements that the intercalation of admetal during post annealing is very local, and proceeds through preexisting defects, or defects created during annealing [131].

The h-BN nanomesh behaves as an outstanding template for Pt nanoparticles [275]. HR-XPS is suitable tool for differentiating empty and filled pores of Pt nanoclusters entrapped in the moirè-pattern of h-BN/Rh (111). For a Pt coverage of 0.1 ML, all pores of the h-BN nanomesh are filled with nanoclusters with an exceptionally uniform cluster size of ~12 Pt atoms per pore, and high stability up to 400 K. The stability of Pt clusters, above 0.2 ML coverages, is less. It is a very interesting observation that Pt cluster superlattice on h-BN/Ir (111) were observed to be stable up to 650 K [241]. This temperature is at least 200 K higher than that detected for Pt cluster superlattice on other templates such as h-BN/Rh (111). The thermally stable Pt cluster superlattice on h-BN/Ir (111) provides with their tunable size and electronic structure are extremely suitable for systematic catalytic works with Pt clusters. The aim is to develop a new type of Pt-nanoparticle carbon-support electrocatalyst [233]. XPS study established conformal C embedding of the Pt clusters on the moirè of h-BN/Ir (111) surface without degradation of superlattice order, and upon annealing the production of a homogeneous amorphous carbon (a-C) matrix (Fig. 34).

XPS studies, following C co-adsorption, were executed for a Pt cluster superlattice produced by deposition of 0.1 ML Pt on h-BN on Ir (111) surface [50,233]. The Ir $4f_{7/2}$ core level of the substrate was monitored and fitted with three components (Fig. 35). Ir_B is attributed to the Ir bulk atoms at the binding energy 60.86 eV (blue in Fig. 35a). Ir_S is corresponded to Ir surface atoms without bonds to h-BN at 60.34 eV (brown in Fig. 35a), and Ir_{int} is attributed to Ir surface atoms binding to the h-BN at 60.63 eV (ochre in Fig. 35a). After deposition of increased amount of carbon, the Ir_{int} component has grown significantly at the expense of the Ir_S component. The increase of Ir_{int} includes an increase of sp^3 hybridization of h-BN, which has to be triggered by chemical bond generation between carbon and nanosheet.

The moirè of a monolayer of h-BN on Ir (111) surface is observed to be a template also for Ir, C, and Au cluster superlattices [131]. The Ir and

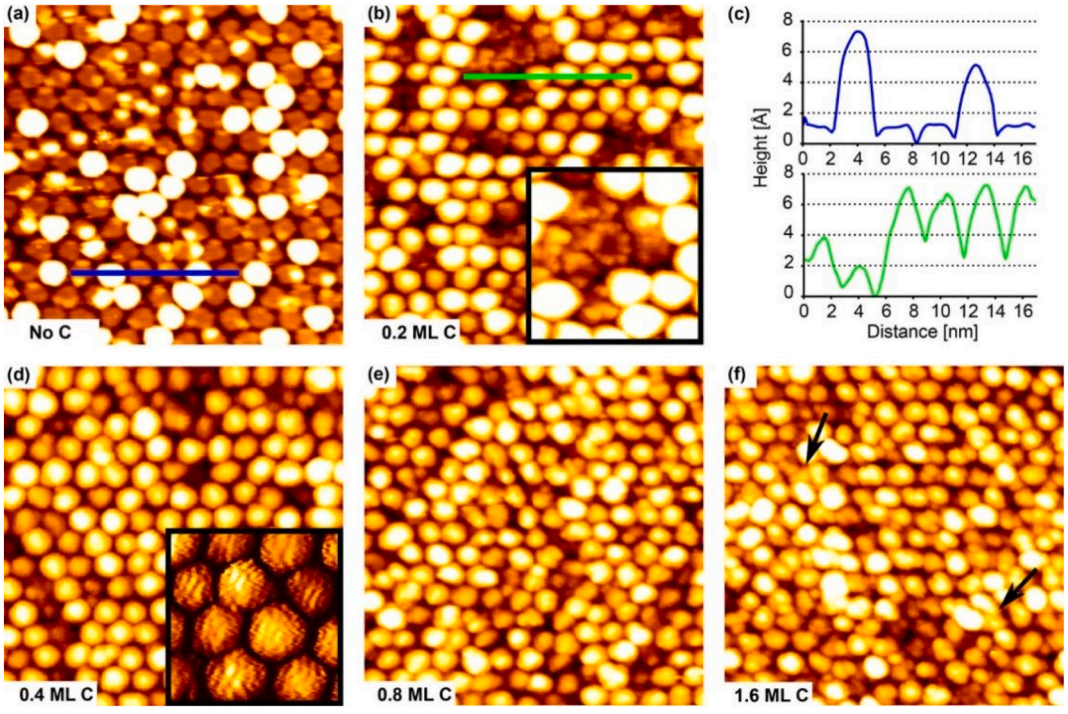

Fig. 34. STM topographs of Pt cluster superlattices on h-BN/Ir (111) formed by deposition of 0.55 ML Pt at 300 K (a) without and (b, *d*-f) with additional C deposited. Carbon amounts are (b) 0.2, (d) 0.4, (e) 0.8, and (f) 1.6 ML. (c) Shows the height along the blue line in (a) and the green line in (b). The inset in (d) is a composite of the topograph and its derivative to increase the contrast of the molecular orbital resolution. The image size is 34 nm × 34 nm in all cases. Reproduced from Ref. [233].

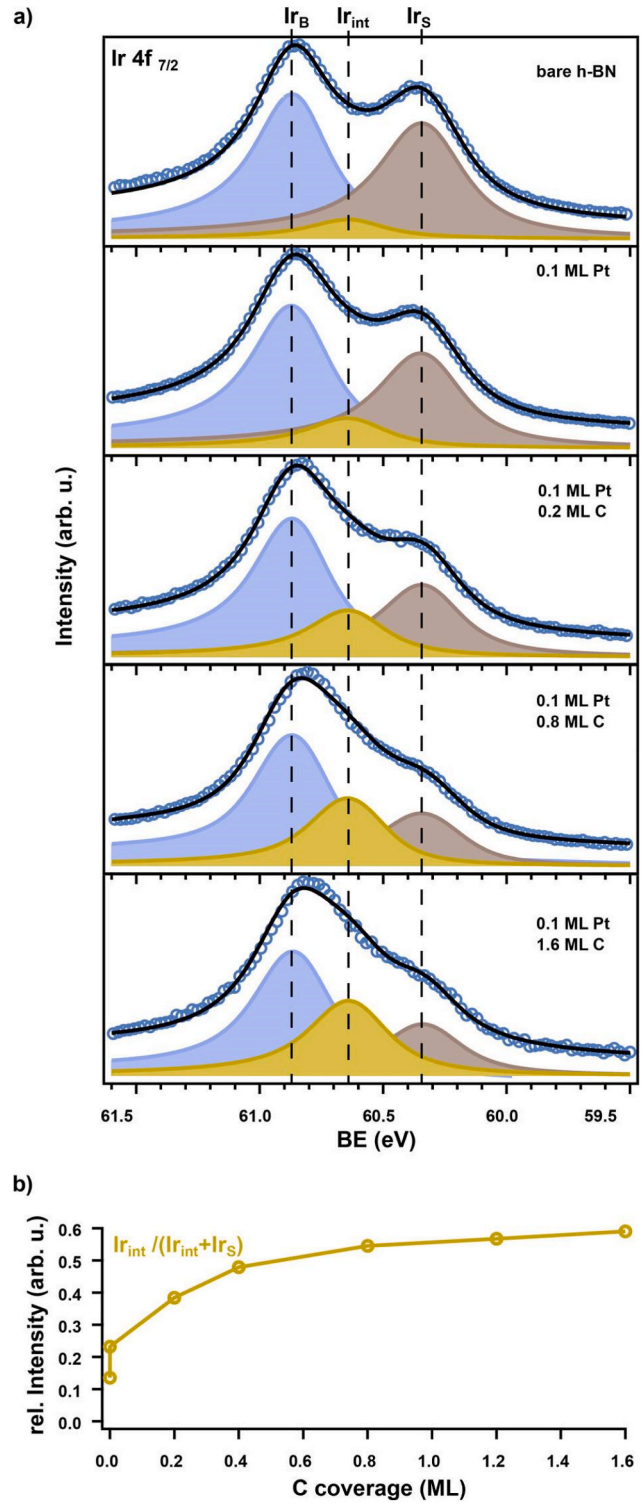

Fig. 35. (a) XP spectra of the Ir $4f_{7/2}$ core level of the Ir (111) substrate with a monolayer of h-BN and after subsequent deposition of 0.1 ML Pt and increasing amounts of carbon measured at a photon energy of $h\nu = 140$ eV at room temperature. The measured data are indicated by blue circles, and the fit is a black line. From top to bottom: pristine h-BN prior to deposition, after deposition of 0.1 ML Pt resulting in bare clusters and after embedding in 0.2, 0.8, and 1.6 ML carbon. (b) Intensity of the interface component (Ir_{int}) normalized to the sum of the interface and surface component ($Ir_{int} + Ir_s$) as a function of carbon coverage. The lower and upper data points at zero coverage represent the system before and after deposition of 0.1 ML Pt, respectively. Reproduced from Ref. [233].

C cluster super lattices show a high thermal stability, before they deterioration by intercalation and Smoluchowski ripening. The template behavior of an h-BN nanomesh on Ir (111) is visualized in Fig. 36. Deposition of 0.57 ML Ir at 250 K results in the development of a hexagonal lattice of clusters as was observed previously [134]. The topograph taken after larger deposition (1.5 ML) at 350 K exhibits larger clusters with 175 atoms (Fig. 36b) [131]. The image in Fig. 36c displays the structure after the deposition of 0.05 ML Ir resulting in small clusters with 6 atoms at 250 K and after that heating to 350 K. One of the final conclusions of the experiments is that the moirè of a monolayer of h-BN on Ir (111) substrate successfully templates highly ordered clusters of different materials with average cluster sizes of up to 175 atoms. Ir superlattice degradation is negligible up to 700 K. Ir clusters bind to the h-BN moirè valley, forming strong Ir cluster atom–B atom bonds, and strengthening the Ir substrate atom–N atom bonds, which are supported by *ab inito* calculations [131].

The morphology and properties of nanoparticles are extremely important in catalysis. Therefore, the above mentioned conclusions help to understand certain catalytic processes and the highly regular h-BN nanosheets and mainly the h-BN nanomesh could fit for catalytically active metals as suitable template. Supported heterogeneous catalysts consist of highly dispersed metal clusters on a high surface area support. The particle size and dispersion of metal are very important factors for the catalytic efficiency. The frequently used oxide supports can influence the activity of the oxide supported catalysts, while the oxides themselves are also active in many cases. One particularly interesting issue is to follow the catalytic process on metal nanoparticle arrays grown on a moirè patterned two-dimensional support, which is usually chemically inert, such as h-BN, thereby excluding the effect of the support.

The highly ordered h-BN moirè has other important application fields such as quantum computing or magnetic storage. The structures of Sn on h-BN/Ir (111) [213] and h-BN/Rh (111) [269] are of interest in quantum-based applications due to unique optical and electronic properties. Co adatom behaves differently on h-BN depending on the substrate. Co composes small nanoparticles in the pores of the h-BN/Rh (111) nanomesh, which start to coalescence at elevated temperatures without any significant intercalation. However, even the small amount of coadsorbed oxygen decreases Co agglomeration and significantly enhances its intercalation [272,273]. It is remarkable that a significant effect of metal substrate on the magnetic anisotropy of cobalt on h-BN nanomesh was observed [234] XAS, XMLD and XMCD experiments show a large out-of-plane magnetic anisotropy for cobalt individual atoms adsorbed on h-BN/Ru (0001), while cobalt atoms on h-BN/Ir (111) surface have basically no anisotropy. The experimental data with DFT calculation infer that the different magnetic anisotropy derives from various Co adsorption sites, namely atop nitrogen on h-BN/Ru (0001) and 6-fold hollow on h-BN/Ir (111) surfaces. The experimental and theoretical studies clearly represent the dissimilar corrugations of h-BN on Ru (0001) and Ir (111) substrates [235].

Interestingly, it was reported that the Mn, Fe and Co adsorption on h-BN/Rh (111) drastically influences the bonding of the nanomesh to the metal, a single transition metal atom weakens the interaction of more than 60 neighboring h-BN unit cells to the underlying metal substrate [273]. Sm growth on h-BN supported by Ir (111) offers a new route to the formation of magnetic cluster superlattice [132]. The data showed that Sm_{13} clusters are negatively charged upon deposition on the top center of pore region of h-BN/Ir (111) support. The evolution of a significant magnetic moment and huge magnetic anisotropy energy of Sm_{13} cluster as well as its high stability enables the Sm_{13}@h-BN/Ir (111) system for application in magnetic storage.

5.2. *Functionalization of h-BN by alkali metals and ions*

Functionalization and intercalation of h-BN produced on Au (111), Ir (111) Ru (0001) [217,235,243,283] and on h-BN film [287] with K, Cs

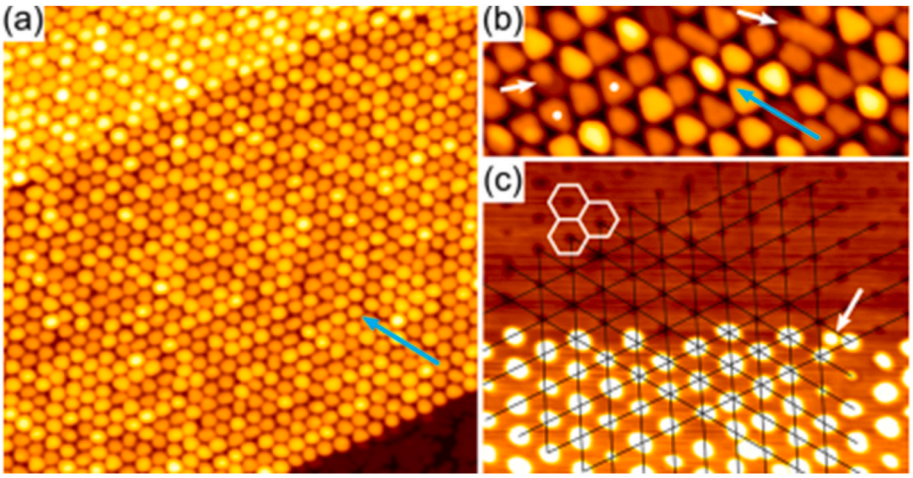

Fig. 36. (a) STM topograph of h-BN/Ir (111) after deposition of 0.57 ML Ir at 250 K. Average cluster size, $s_{av} = 65$ atoms. Cluster number density $n = 1.00$ islands per moirè unit cell. In the upper left, a substrate step is located underneath the h-BN template. In the lower right, bare Ir is present. (b) Topograph after deposition of 1.5 ML Ir at 350 K, $s_{av} = 175$ atoms and $n = 0.98$. Two clusters with opposing triangular envelop are marked by white dots. Two clusters each displaying two different height levels are highlighted by white arrows. (c) STM topograph after deposition of 0.05 ML Ir at 250 K and subsequent annealing to 350 K resulting in $s_{av} = 6$ atoms. Reproduced from Ref. [131].

and Li were investigated earlier. By combining ARPES, XPS and DFT calculations, it was shown that the metallic substrate easily ionizes the alkali dopants and exposes h-BN to strong electric fields leading to large band-energy changes [218]. Adsorbed Cs does not alter the morphology of h-BN/Ir (111) markedly, whereas an intercalated layer of Cs decouples the 2D sheet and smoothens its corrugation [243]. Recently, detailed STM investigations were carried out on the adsorption of Cs and K ions in the valleys of h-BN/Ru (0001) [283]. Fig. 37a and b presents STM topographs of h-BN/Ru (0001) at two Cs surface concentrations. The moirè pattern with periodicity $d_m \approx 3.2$ nm originates from the lattice mismatch between h-BN layer and Ru (0001) surface. The circular darker areas correspond to the valley regions, where the distance between h-BN and the metal substrate is small. The bright dots are alkali adatoms in the valleys. At low coverages of Cs (Fig. 37a), the majority of cells are occupied by an alkali atom.

As illustrated above, it turned out that the moirè pattern of h-BN/Ru (0001) is a good template for alkali (Cs and K) atoms. At increasing alkali coverages, more and more alkali atoms are adsorbed in the pores. Due to charge transfer from the alkali metal to the Ru (0001) substrate, a static electric field is formed. The positive charge on Cs and K atoms makes them repulsive to each other. Furthermore, the different sizes of Cs and K, the shapes of the template are different for Cs and K, which leads to the various effective diameter.

Deposition of Li atoms on h-BN monolayer on Ir (111) substrate was investigated with ARPES and LEED [235]. Stepwise Li deposition continuously shifts the band structure of h-BN to larger binding energies due to charge transfer by alkali atoms. At low coverages, Li atoms intercalate under the h-BN layer, where they are highly charged and induce a large shift of the band structure. Besides, intercalated Li atoms effectively decouple h-BN from the Ir (111) surface and as a consequence decrease its moirè corrugation. Fig. 38 shows a typical ARPES map of h-BN/Ir (111) interface in the ΓK direction, which provides proof of good quality of the h-BN layer, with σ_1, σ_2 and π bands noticeable. The shift of σ bands upon Li deposition is visualized in Fig. 39.

Li atom has small size, therefore it is a fascinating candidate for intercalation of h-BN mono- or multi-layers at a wide range of concentrations. It has been pointed out that Li-functionalized h-BN has a potential to serve as an electrode in batteries [288]. Li reduces the band gap of h-BN from 5.7 eV to 3.7 eV [289]. The transport behavior of Li ions has an important factor in batteries. A recent study confirmed that Li ions can migrate with less damping and smaller transport energy barrier with the help of h-BN in form of nanoflakes (BNNFs). It is demonstrated that an attractive coupling exists between Li ions and BNNFs, the tested BN containing electrolyte exhibits excellent ion transportability [290]. The observed migration property is very similar to the proton transport in layered h-BN membrane [291].

Mg doping procedure is a promising way to high-quality p-type doped h-BN films [292]. The important characteristic feature of

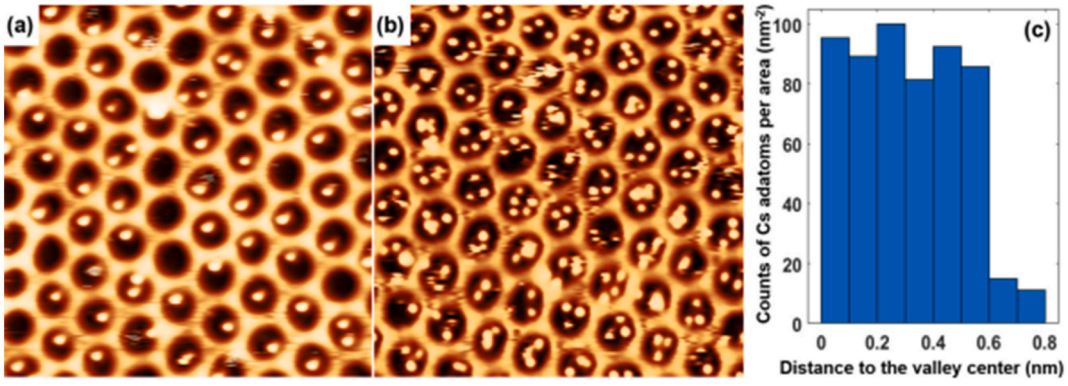

Fig. 37. (a) and (b) STM images of h-BN/Ru (0001) with Cs adsorption. Cs concentration is $\lambda = 1.11$ MUC^{-1} (moirè unit cell) (a) and $\lambda = 3.19$ MUC^{-1} (b). Image size is 25.6×25.6 nm^2. Bias voltage is $U_b = -2.0$ V (a) and $U_b = -2.4$ V (b) Tunneling current is $I_t = 20$ pA. (c) Cs density dependence on the distance to the cell center obtained from over a hundred singly occupied cells for $\lambda = 1.11$ MUC^{-1}. Reproduced from Ref. [283].

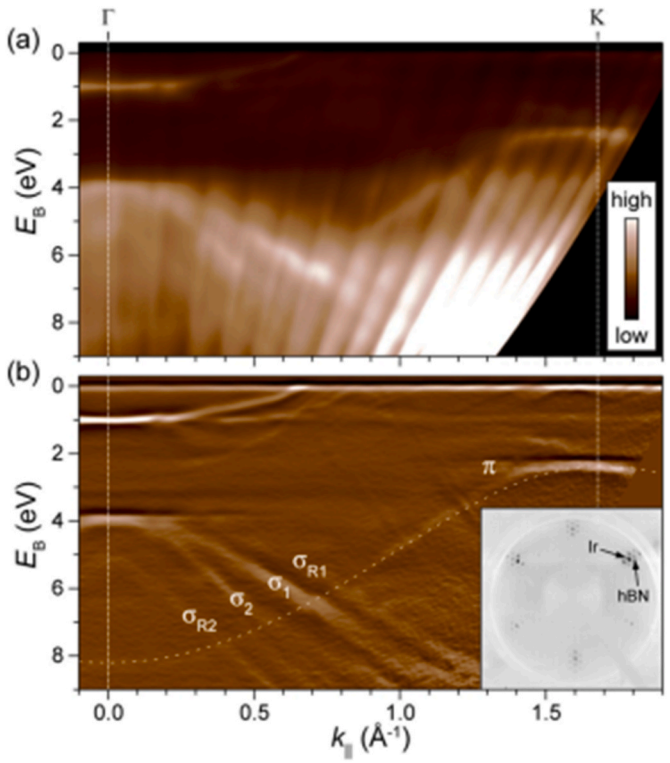

Fig. 38. ARPES map of h-BN/Ir (111) system along the ΓK direction presented as (a) raw data and (b) second derivative in the *y* coordinate. Electronic bands of h-BN, π and the two σ bands (σ_1 and σ_2) are visible. Additionally, replicated σ bands (σ_{R1} and σ_{R2}) can be discerned as well. Thin dashed line in panel (b) is the TBA fit to the π band. The inset in panel (b) shows LEED image of system (E = 56 eV), with the moirè diffraction spots surrounding the first order diffraction spots of Ir and h-BN. Reproduced from Ref. [235].

Mg-doped h-BN is a collective up shift of the valence bands, which gives an application possibility for wide bandgap optoelectronic devices.

5.3. The role of vacancies in the interaction with adatoms

Defects in h-BN monolayers can strongly influence adsorption properties of several gases, for example activated H_2 molecules or hydrogen atoms and certain metals atoms like Cr. Such kind of modifiers may play a decisive role in the growth process of h-BN on different substrates (metal single crystals, Si(100) or Au/Cr bilayer). The efficiency of the defective h-BN monolayers highly depends on the density of boron and nitrogen vacancies [181]. The advantages of defects in the sp^2 sheet and other imperfections in h-BN system have been discussed in a nice review published in the last decade [15]. The result obtained in the near feature will deliver significant development in interface engineering, in the field of magnetic and (opto)electronic including computer science.

Nowadays, a large effort is being made to improve the single atom catalysis (SAC) in order to achieve high activity and selectivity. At the same time, the application of such type of catalyst in technology is limited by their stability. Atom-like active components easily aggregate on the support under catalytic conditions. The results obtained in this prosperous and rapidly growing research area are collected recently in a minireview [293] and in other comprehensive works [294,295] Recently published works demonstrate that vacancies influence the binding strength of adatom on h-BN structure [296]. In certain cases, the metal atoms are more stable on the B vacancy than N vacancy site in h-BN, in other case, in Au modified system, opposite trend was observed. The geometry, stability and electronic character of several metal atoms such as Co, Ni, Cu, Ag, and Au on the vacancy defected h-BNNS/Cu(111)

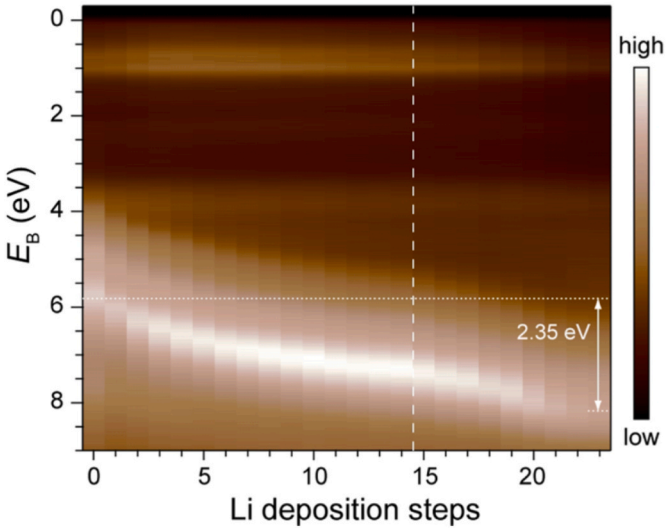

Fig. 39. A stack of EDCs at $k_{\parallel} = 0.4$ Å^{-1} for a sequence of Li deposition steps. 1-Minute-long (left of dashed line) and 2-, 4- and 6-min long deposition steps (right of dashed line) have been employed. The shifting bands are the σ bands of h-BN. Non-shifting Ir bands are also visible. Reproduced from Ref. [235].

systems were investigated by DFT calculation [297]. Both boron and nitrogen vacancy defects were used for this purpose. The schematic summary picture of single-atom-catalysts (SAC) on h-BN/Cu(111) is shown in Fig. 40.

The structures of metal atoms (Co, Ni, Cu, Ag, Au) on B and N vacancy defected h-BN supported on the Cu(111) were optimized [297]. According to the results, the metal atoms are stabilized at vacancy sites (B and/or N) by strong chemical bonds. The stronger chemical bond prevents surface diffusion and coalescence to form large particles. The sequence in the BE of metals is the following: Co > Ni > Cu > Au > Ag. The metals at the vacancy site bond to three B atoms. The length between metal and boron increases in the opposite from Co < Ni < Cu < Au < Ag direction. It should be emphasized that the binding strength of metal atoms, except Au atom on the N^V/Cu is less than that for B^V/Cu. The reason is that the larger electronegativity of Au atoms attracts the electronic charge from the B atoms of the h-BN sheet. The majority of metal adatoms is stable on h-BN nanosheet support. The stability of

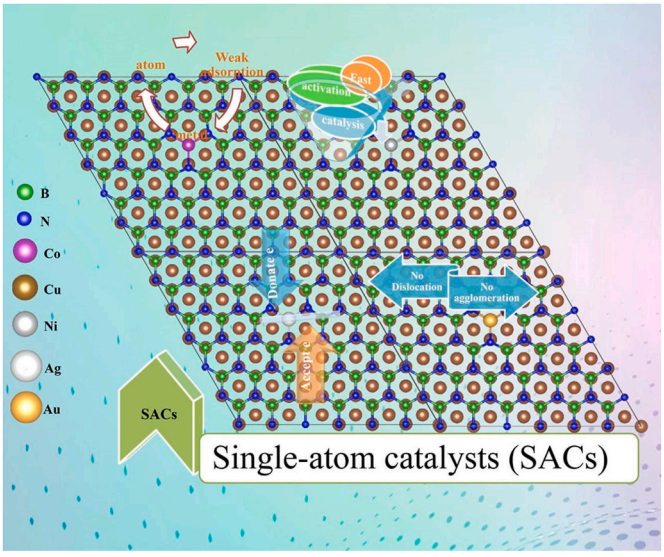

Fig. 40. Representation of single-atom catalysts on h-BN/Cu(111). Reproduced from Ref. [297] Graphical abstract.

metal atoms is higher on B-vacancy site than *N*-vacancy site.

The preparation of atomically dispersed metal catalysts is rather difficult due to coexistence of sites with different nature such as nanoclusters and nanoparticles. Recently a macro-kinetic theory captured the competing processes of nucleation and production of single atoms (SA) stabilized by point defects on h-BN [298]. The theoretical results are supported experimentally. Pt on exfoliated h-BN was investigated by aberration-corrected scanning transmission electron microscopy. Fig. 41a display the elementary reactions with the kinetic model. It contains different steps: re-evaporation, surface diffusion, capture of adsorbed Pt atom by point defect, lateral attachment of metal atom and on-top attachment of metal atom from gas phase to growing nanocluster (NC). Fig. 41b represents the SA:NC ration with key kinetic parameters.

The 2D h-BN atomic sheets are important electrically insulating materials, their deep UV bandgap is ~5.5 eV. It is an important finding that the transition metal doping of h-BN without metal support successfully engineers the BN bandgap [299].

In quantum technology it is crucial to protect the engineered electronic state. h-BN is an outstanding candidate for this purpose due to its physical, chemical and mechanical properties [15,300–303]. Oxidation and sulfurization processes were used for this purpose. The formed nanostructure is passivated by chemically inert (h-BN) layer. The h-BN/CuS heterostructure are confined within the nanopores, effectively forming an extended array of quantum dots (QD). Very recently, a scalable segregation-based growth approach, managed by the h-BN overlayer to develop quantum dot arrays at the h-BN/Cu(111) interface was presented [304]. The segregated sulfur generated quasi-hexagonal CuS nanostructures initiating creases in h-BN layer, and increasing scattering potential and local work function (Φ) change that allow to restrict both the Shockley surface state and image potential states (IPS) of the h-BN/Cu structure. Fig. 42a illustrates the h-BN covered QD array growth mechanism and the resulting a new electronic structure. A h-BN layer was produced on Cu(111) through borazine decomposition, and a high-temperature treatment initiated the segregation of sulfur from the Cu(111) bulk (Fig. 42b).

Fig. 42c represents the production of quasi-hexagonal nanoporous CuS network below the h-BN layer. The local Φ is significantly enhanced atop wrinkles (h-BN/CuS/Cu(111)) as compared to the pore (h-BN/Cu (111)) regions (Fig. 42c and d). STM and STS confirmed that both the surface state and the IPSs are trapped at the pore regions of the system (Fig. 42e and f).

6. Catalytic reactions on functionalized h-BN nanosheets

6.1. Surface reactions of small molecules on metal-supported 2D h-BN

The knowledge of the adsorption properties and reactivity of several gas molecules on transition metal-supported h-BN monolayer is important to understand the mechanism of technologically important surface reactions. For the first time, BN as an inert support for 55-atom gold clusters (~1.4 nm) was used in selective oxidation of styrene with dioxygen [33]. Somewhat smaller conversion was measured on inert h-BN than on the other small activity SiO_2 at the same surface concentration and Au particles size. A sharp cluster size threshold in catalytic activity was found, in that particle with diameter of ~2 nm, and above no activity was found. It was suggested that the small activity increases from the altered electronic structure intrinsic to small gold nanoclusters. The surface adsorption behavior for several gas molecules (H_2, N_2, CO, NO and CO_2) on bare and transition metal-modified h-BN layer has been studied by means of DFT calculations [305]. Furthermore, a first-principles study was extended very recently on the adsorption of NO_2, NO, NH_3 and CO on noble metal (Rh, Pd, Ag, Pt, Au) modified h-BN monolayers [306]. NO is easily adsorbed on h-BN monolayer with metal dopants, principally Pt doped system results in the lowest adsorption energy of NO. It could not be directly decomposed. In the case of CO oxidation, the adsorbed product O_{ads} can bind with CO and produce CO_2

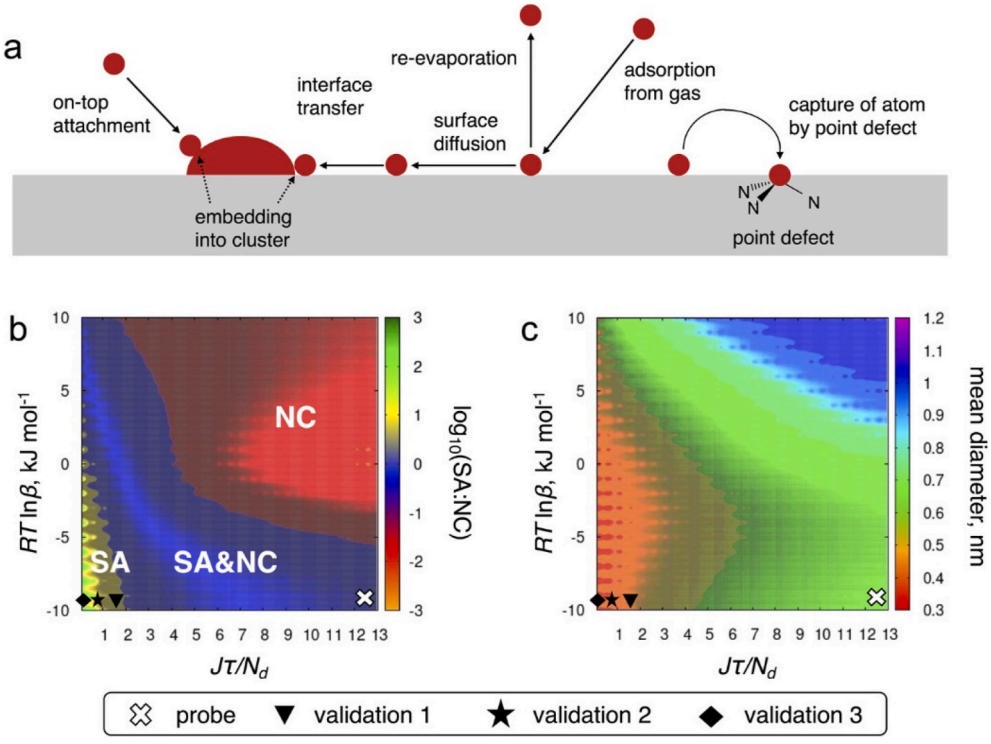

Fig. 41. (a) Competing processes included in the kinetic nucleation theory. (b, c) Phase diagrams showing the dependence of the SA:NC ratio (logarithmic scale) and the mean diameter of NCs on the kinetic parameters involving the total loading of metal atoms, Jτ, the density of point defects, N_d, and the effective change in the nucleation barrier caused by the point defects, RT lnβ. The white cross and black symbols on the phase diagrams correspond to the probe and validation experiments; their approximate positions on the $J\tau/N_d$ axis are 12.55, 1.55, 0.35, and 0.07. Reproduced from Ref. [298].

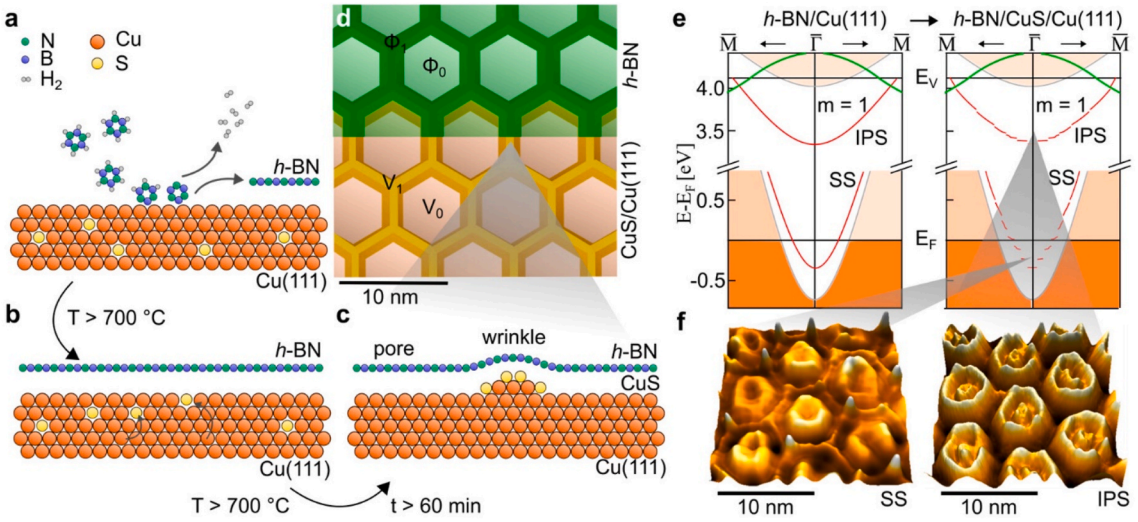

Fig. 42. Illustration of the h-BN covered QD array growth process and the resulting electronic structure. (a) Growth of h-BN/Cu(111) through borazine decomposition. (b) High-temperature annealing inducing segregation of sulfur from the Cu(111) bulk. (c) Formation of quasi hexagonal nanoporous CuS network below the h-BN layer after extended annealing. (d) Illustration of the topographic and potential landscape of the architecture. CuS quasi hexagonal structures scatter the Cu (111) surface state (SS) while the h-BN wrinkle region (h-BN/CuS) with Φ1>Φ0 scatter the IPS. (e) Schematic of the h-BN/Cu(111) and h-BN/CuS/Cu(111) band structures. Dark (light) orange indicates occupied (unoccupied) bulk states of Cu(111), while green indicates the h-BN conduction band. The red parabola around E_F corresponds to the Shockley surface state of Cu(111), while the one below the vacuum level EV corresponds to the m = 1 IPS. (f) 3D rendered dI/dV maps of the confined surface state (V = −0.2 V) (left) and confined IPS (V = 3.8 V) (right). Reproduced from Ref. [304].

in gas phase. The knowledge of adsorption behavior of CO is a key issue in the establishment of the related catalytic reactions and the vibrational spectroscopy is frequently used to probe the surface properties of metals on supports by assessing adsorbed CO [307–310]. The adsorption of CO was investigated by HREELS, TPD, DFT methods on Au/h-BN/Rh (111) [173,174]. In the case of gold nanoparticles produced on different oxides a significant size effects were concluded based on IR spectra of adsorbed CO. CO does not adsorbs on defect free h-BN nanomesh produced on Rh (111). On Au/TiO_2 the CO band shifts from 2126 to 2122 cm^{-1} with gold deposition (from 1.8 to 3.1 nm) [311]. On Au/FeO(111) this main character continuously grows and shifts to lower wavenumbers from 2131 to 2108 cm^{-1} as a function of Au coverage [312].

The HREELS measurements were performed on a clean and Au deposited h-BN/Rh (111) surfaces [173]. The CO was dosed at 90 K, Au coverages were varied between 0.1 and 1.0 ML, the deposition temperature was at room temperature. On the h-BN/Rh (111) interface, only the transverse optical phonon feature with out-of-plane polarization (TO⊥) and the overlapping longitudinal optical (LO), in addition, the in plane polarization (TO||) phonon peaks appeared (Fig. 43a). The absence of any vibrational mode attributable to CO bands on bare

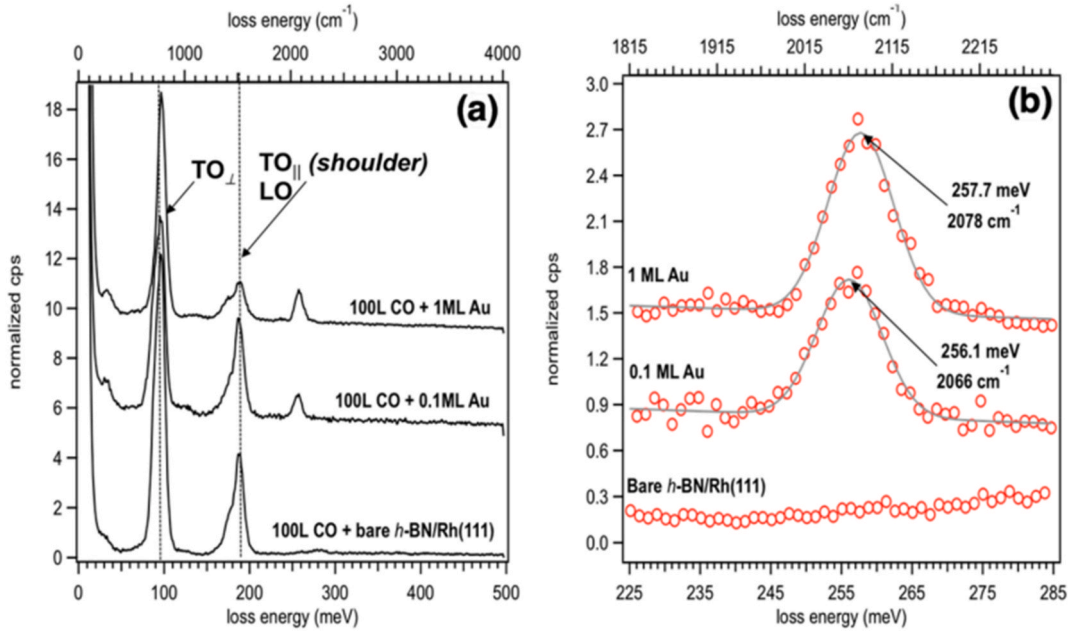

Fig. 43. HREELS vibrational spectra of 100 L of CO dosed on bare h-BN/Rh (111), and on 0.1 and 1 ML of Au deposited on h-BN/Rh (111) at room temperature. CO dosing and measurement were done at 90 K. (a) Survey spectra showing all recorded vibrational peaks from 0 to 500 meV (0~4000 cm^{-1}). (b) Close-up of the C–O stretching region. Data points are open circles, and fits to the data are solid lines. Each spectrum is fit with a single Gaussian peak using a linear background subtraction. Reproduced from Ref. [173].

h-BN/Rh (111) certified that h-BN nanomesh is inert to CO (Fig. 43b). Following deposition of Au on h-BN/Rh (111), peaks appeared at the C–O stretching region. CO frequencies depended on the gold coverages. At very low coverages band was observed at 2066 cm^{-1}. A blue-shifts in CO band with increasing Au coverage was measured, at 1 ML Au coverage the band appeared at 2078 cm^{-1}. The observed tendency in CO frequency shift could be associated with decreased back-donation [173].

The interaction of CO with Au/h-BN/Rh (111) structure was investigated parallel with XPS and HREELS [174]. In Fig. 44a the Au $4f_{7/2}$ XPS peak was followed as a function of Au coverage on h-BN/Rh (111) at 300 K. At very low coverages the Au $4f_{7/2}$ XPS was detected at ~83.7 eV, which is less than bulk value (84.0 eV). This lower binding energy value at low coverages can be attributed to negative charge on Au particles due to electron transfer from h-BN/Rh (111) system supported by DFT calculations [47,173]. The size of Au nanoclusters and the negative charge at low coverage influenced the position of the CO vibrations on HREELS on Au/h-BN/Rh (111). In contrast to large particle size, at these submonolayer gold coverages (small particle sizes) the CO vibration appeared at 2090 cm^{-1}. At higher gold coverages the peak position continuously shifts towards the bulk value (Fig. 44b). Small Au clusters with negative charge and the shift from lower CO frequency to the higher up to gas phase value (2143 cm^{-1}) were published [313,314].

It turned out that Pt doping can increase the absorption capacity of h-BN monolayer for the gas molecules and enhance the catalytic activity for electrochemical elimination of NO. Up to now, there are no systematic, comprehensive studies available on catalytic behavior for metal atoms modified h BN. In recent past, it was proven that metal adatom on h-BN shows excellent catalytic performance for NO reduction [315]. The interaction of CO with Pt (111) surface has been investigated under 2D h BN overlayer [316–318]. TEM and in situ surface spectroscopic results obtained under near ambient pressure conditions suggest that CO molecules intercalate in monolayer h-BN nanosheets on Pt (111) substrate in CO atmosphere but desorb from the h-BN/Pt (111) surface even at 300 K. CO oxidation on the single Cu atom supported on two kinds of h-BN monolayer (boron vacancy, Bv and nitrogen vacancy Nv) was studied by DFT calculations [296]. Interestingly, spontaneous CO oxidation has been observed on nitrogen vacancy system. Recently a series of Pt nanoparticles coated with h-BN nanoreactors (Pt@h-BN) were planned for photoreduction of CO_2 to methane [319]. The important results show that as the number of h-BN layers increases the selectivity of the CO_2 photoreaction dramatically changed from CO formation to CH_4 production.

Reactivity and passivation of Fe nanocluster (Fe–NCs) on h-BN/Rh (111) was studied in CO dissociation [274]. Especially in the Fischer-Tropsch synthesis, the reactivity of CO and its interaction with H_2 on low Miller-index Fe single crystal surfaces are technologically important issues. The dissociation of CO on the Fe nanoparticles was followed by in situ high-resolution XPS. TPXPS was applied to study the thermal stability and structural changes of the Fe–NCs.

The as-prepared Fe–NCs were exposed to the CO at 150 K Fig. 45a. With increasing exposures, the main signal was detected shifting from 285.34 to 285.77 eV, and a shoulder at lower binding energies, shifting from 284.41 to 284.92 eV. The XPS peak at 285.77 eV is attributed to CO adsorbed at on-top sites, while the small shoulder at 284.92–284.57 eV originates from the hollow and the edge sites as. The shift in binding energy with increasing coverage, indicates lateral interaction of the adsorbed molecules. The small feature around 284.5–283.8 eV corresponds to graphitic and carbide species, respectively.

After CO adsorption TPXPS was carried out shown in Fig. 45b. The C 1s intensity of CO decreases due to partial desorption. Two new signals emerge at 283.17 (blue) and 282.82 eV (green), which are attributed to CO dissociation at ~298 K to Fe_3C. On carbon and oxygen precovered Fe–NCs no adsorption of CO at hollow/edge sites was detected. Fe sites were blocked by C and O atoms.

6.2. *Surface reactions of hydrocarbons, aldehydes and alcohols on metal-decorated h-BN stabilized on metal supports*

Ethylene adsorption, its reaction and coking on Pt/h-BN/Rh (111) system was followed by synchrotron-based high resolution in-situ XPS [270]. In this study Pt nanocluster arrays supported on the h-BN/Rh (111) moirè served as a model catalyst for C_2H_4 dehydrogenation. The obtained TPXPS results on nanomesh were compared with the C_2H_4 adsorption on Pt (355) see Fig. 46.

Fig. 46 shows the C 1s XP spectra obtained in situ during adsorption at 120 K obtained on stepped Pt (355) and on h-BN supported Pt nanocluster, respectively. The C_2H_4-saturated systems were heated to 600 K while continuously recording the C 1s TPXP-spectra. Up to ~250 K, the amount of C_2H_4 decreases. Above 250 K, there is no ethylene on both surfaces, the dominant species are the $CCH_{3(edge)}$, $CCH_{3(facet)}$ overlapping with CCH_2 intermediate up to ~400–420 K. CCH species appeared from ~400 K up to 531–560 K. Undefined carbonaceous species are produced as the final product of the C_2H_4 decomposition above 451 K. These experiments, with stepped Pt (355) and Pt supported on h-BN nanomesh, well-presented that well defined h-BN monolayer can serve as a template for the Pt nanoclusters exhibiting edge/step sites suitable for model catalysis.

CH_3CHO is a key intermediate in the transformation of primary alcohols, especially CH_3CH_2OH, on supported metal and oxide surfaces [320–322]. It was concluded that CH_3CHO bound in an η^2(C,O)

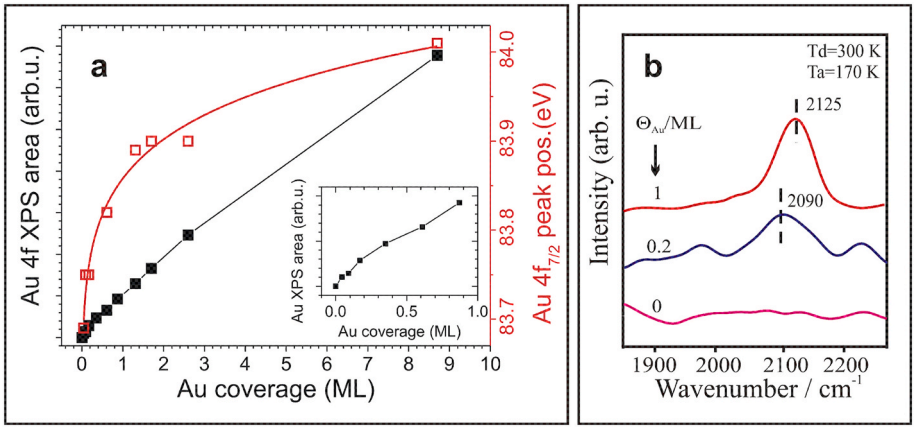

Fig. 44. (a) Changes in the Au $4f_{7/2}$ XPS peak position and integrated area as a function of gold coverage on h-BN/Rh (111). The Rh 4s contribution was subtracted. The solid lines are to guide the eye. (b) Effect of gold coverage on the ν(CO) HREELS peak after adsorption of 5 L CO on clean and gold decorated Rh (111) at 170 K. Reproduced from Ref. [174].

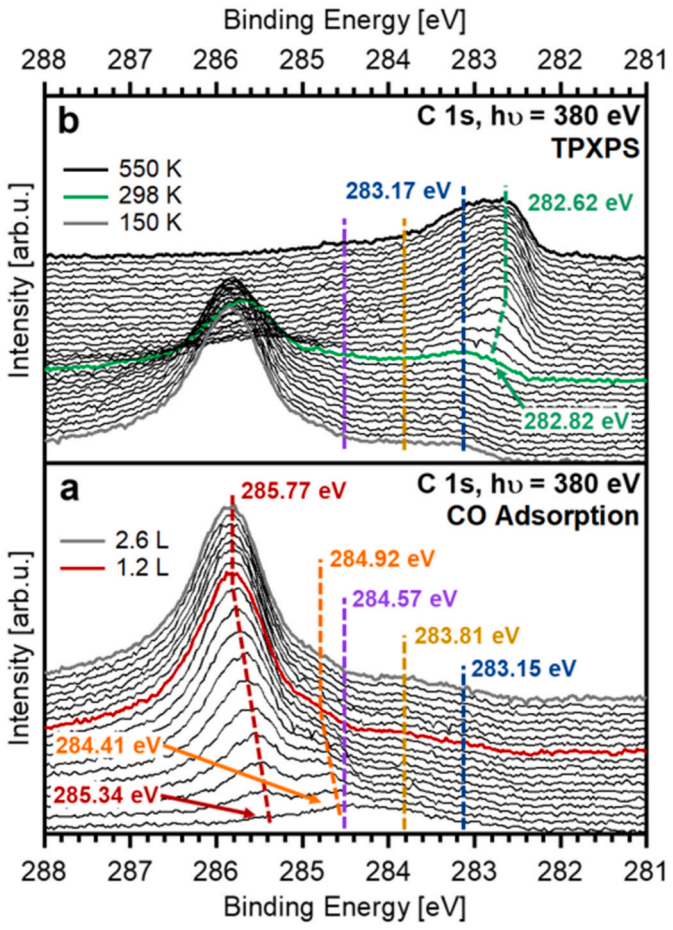

Fig. 45. (a) C 1s spectra collected during CO adsorption on the as-prepared Fe nanoclusters. The dashed lines indicate the shift of the CO_{top} (red) and $CO_{hollow/edge}$ (orange) species during adsorption. Minor amounts of C_{Gr} and C_{Rh} are shown by the purple and ocher dashed lines, respectively. CO saturation was reached at 1.2 L and CO exposure was stopped at 2.6 L. (b) C 1s spectra collected during TPXPS of the as-prepared Fe nanoclusters. The dashed lines show the Fe_3C (blue) and Fe_3C surface (green) species. Reproduced from Ref. [274].

configuration on well-defined Pt surfaces [323–326] η^2-CH_3CHO_a decomposes to different products, such as CH_2CO_a, CH_3, CH_2, CH, H_a, CO_a and adsorbed carbon. The reaction between neighboring η^1-(O)–CH_3CHO species is observed on Rh (111), this interaction leads to the formation of oligomers or polymers [325,326].

The first step of CH_3CH_2OH reactions, is the dehydrogenation forming ethoxide species. Its further reactions are determined by the nature of support oxide [308,309]. It is commonly believed that large gold particles are not reactive in many catalytic reactions. However, it is demonstrated that small particles of Au clusters supported on different metal oxides show enhanced catalytic activity for different reactions because the shape, sizes and electronic structures of Au (<2–3 nm) are different from the bulk properties [137,327–330]. The other dramatic factor known to influence the catalytic activity is the strong-metal-support interaction (SMSI), which could influence the activity and selectivity of catalysts [331,332]. Besides graphene, the other catalytically inactive support is the h-BN. The h-BN formed on metal surfaces can help to avoid the "disturbing effects" of oxides in the explanation of the nature of active sites on gold nanocatalysts.

The interaction of acetaldehyde (CH_3CHO) with Au supported h-BN prepared on Rh (111) was studied by AES, HREELS and TPD [48,174]. STM, XPS and LEIS experiments were performed to characterize the Au nanoparticles on h-BN. First it was demonstrated that the h-BN without Au adatoms is completely inert toward acetaldehyde at 170 K [173]. Au deposition allows only molecular adsorption of CH_3CHO. Below 0.2 ML Au exposures no aldehyde adsorption was detected. At rising Au from 0.3 to 2 ML the adsorbed of CH_3CHO continuously increased. TPD spectra showed only aldehyde desorption. An effort was made to identify CO, H_2, C_2H_5OH or other possible thermal reaction products without any success. Depositing 1 and 2 ML Au at 300 K causes the formation of 3D nanoparticles. As it was observed by STM Au nanoparticles nucleated tendentiously at the pore-wire interface [48,173].

In Fig. 47 a and b the specific vibrations of CH_3CHO on Au nanoparticles for 2 ML (a) and 5 ML (b) gold coverages are demonstrated. Losses showed up at ~850, 1120, 1180, 1350, 1425 and at 2980 cm^{-1}after adsorption of CH_3CHO at 170 K on 2 ML Au covered h-BN/Rh (111) surface in addition to the TO (transverse optical) phonon peak with out-of-plane polarization (~790 cm^{-1}) and to phonon peak in-plane polarization (~1350 cm^{-1}) [264]. In the case of 5 ML gold, the h-BN HREELS loss features were screened by admetal [252]. The characteristic losses for adsorbed CH_3CHO disappeared below 300 K. These HREELS are in agreement with the loss spectra of acetaldehyde detected on annealed Au layer on clean Rh (111) [174]. It was concluded from the loss feature that the adsorption structure of aldehyde on Au nanoparticle sites located at pore-wire interface of h-BN nanomesh is different from η^2-CH_3CHO_a form, it represents a rather mixed (different species) layer. The results obtained on Au covered h-BN/Rh (111) indicated that edge and corner atoms having negative charges (Fig. 45) are responsible for the enhanced adsorption capacity.

Before discussing the ethanol interaction with h-BN/Rh (111) and Au/h-BN/Rh (111), it is useful to make short comparison with the results obtained on clean Rh (111). According to literature, Rh (111) C–C bond dissociation, CO and H_2 desorption after adsorption of ethanol were observed [324]. Desorption of CH_4 was also observed in a smaller amount, which is formed through η^2-CH_3CHO_a intermediate. Characteristic vibrations attributable to η^2-(O,C)–CH_3CHO species at 670, 1105, 1195, 1340, 1410, 2890 and 2980 cm^{-1} were found in agreement with former work [325]. The other observation is that the clean Rh surface acts as an excellent C–C bond rupturing catalyst; the clear indication is that the adsorbed CO is detected at 2040 cm^{-1} [333]. The adsorption of CH_3CH_2OH on monolayer h-BN at 170 K and following heating showed that the ethanol interacts weakly with the surface. The losses due to ethanol appeared but completely disappeared around 250 K [23].

The effect of Au nanoclusters on the reaction path of ethanol on h-BN/Rh (111) was studied by means of TPD and HREELS [23]. TPD data were collected at different Au coverages and all the possible reaction products (CO, H_2, CH_3CHO, CH_4 and H_2O) were searched (Fig. 48). Undecomposed ethanol desorption finished up to 300 K. H_2 and CH_3CHO desorption at amu 2 and 29 were detected simultaneously at 350–450 K from the 1.5 ML Au covered h-BN/Rh (111) (Fig. 48A). These TPD results indicate dehydrogenation reaction path on Au nanoparticles supported on h-BN/Rh (111) surface; the reaction stopped at acetaldehyde formation. The following reaction steps are suggested:

$$C_2H_5OH_{(g)} \rightarrow C_2H_5OH_{(a)} \quad (5)$$

$$C_2H_5OH_{(a)} \rightarrow C_2H_5O_{(a)} + H_{(a)} \quad (6)$$

$$C_2H_5O_{(a)} \rightarrow CH_3CHO_{(a)} + H_{(a)} \quad (7)$$

$$CH_3CHO_{(a)} \rightarrow CH_3CHO_{(g)} \quad (8)$$

$$H_{(a)} + H_{(a)} \rightarrow H_{2(g)} \quad (9)$$

Another interesting feature is the gold coverage dependence: a significant amount of CH_3CHO product was measured only at a certain coverage range (Fig. 48B). Above 1.5 ML gold coverages aldehyde formation was not measurable. The templated Au clusters in the pores of the h-BN and a charge transfer between the substrate and Au occurs at

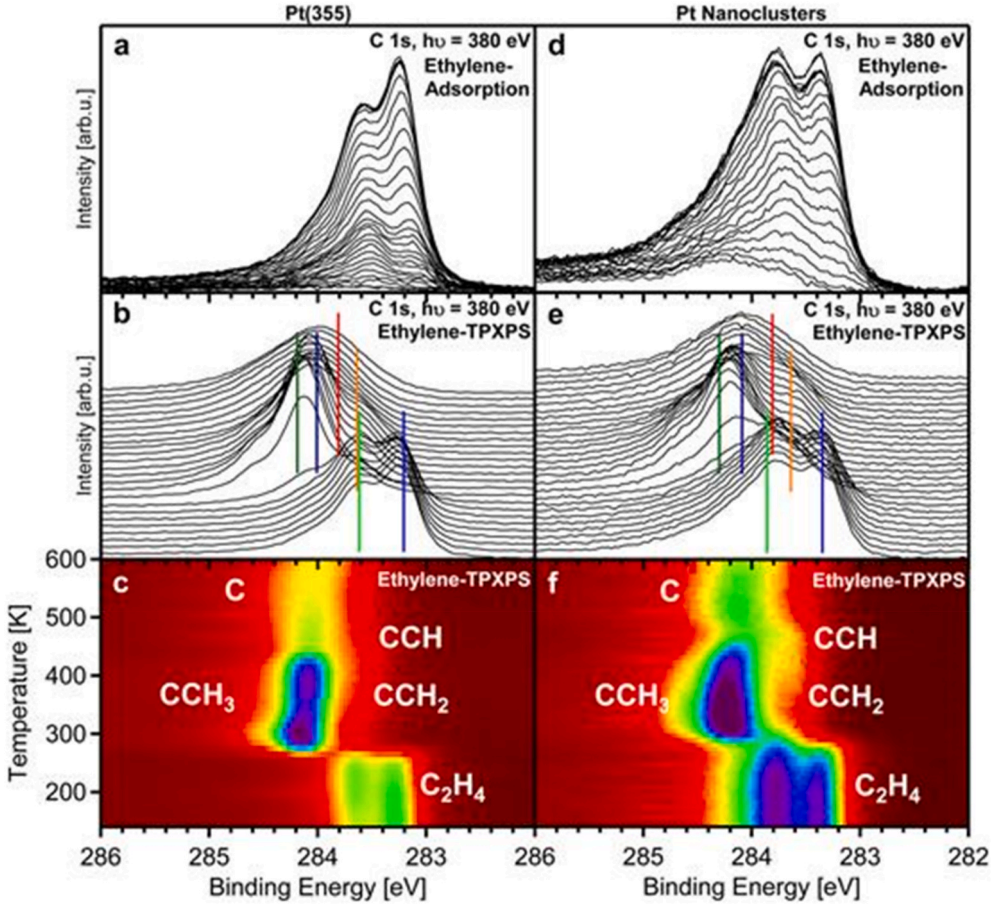

Fig. 46. C 1s XP spectra measured during adsorption and consecutive TPXPS of [(a)–(c)] ethylene on Pt (355) and [(d)–(f)] 0.7 ML Pt/h-BN/Rh (111) nanocluster arrays. (a) Waterfall plot of XP spectra from the ethylene adsorption on Pt (355) at 120 K, $p_{ethylene} = 7 \times 10^{-9}$ mbar; (b) waterfall plot of XP spectra from the follow-up TPXPS, 120–600 K, $\beta = 0.5$ K/s; (c) color-coded density plot of the TPXPS; (d) waterfall plot of XP spectra from the ethylene adsorption on Pt nanoclusters at 140 K, $p_{ethylene} = 7 \times 10^{-9}$ mbar; (e) waterfall plot of XP spectra from the follow-up TPXPS, 140–600 K, $\beta = 0.3$ K/s; (f) color-coded density plot of the TPXPS. Reproduced from Ref. [270].

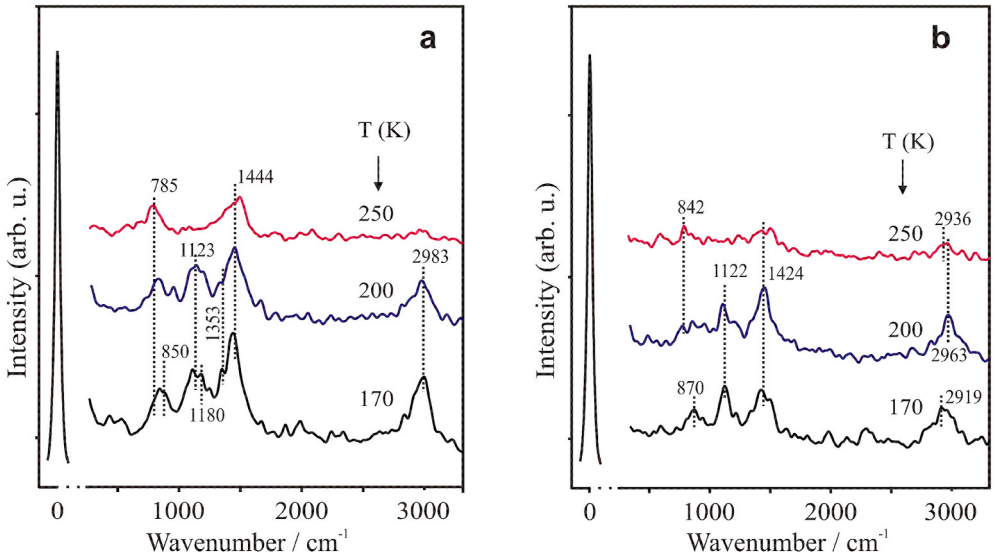

Fig. 47. HREEL spectra showing the effect of annealing after adsorption of acetaldehyde (5 L) at 170 K on h-BN/Rh (111) surface decorated by (a) 2 ML, and (b) 5 ML of gold. Reproduced from Ref. [174].

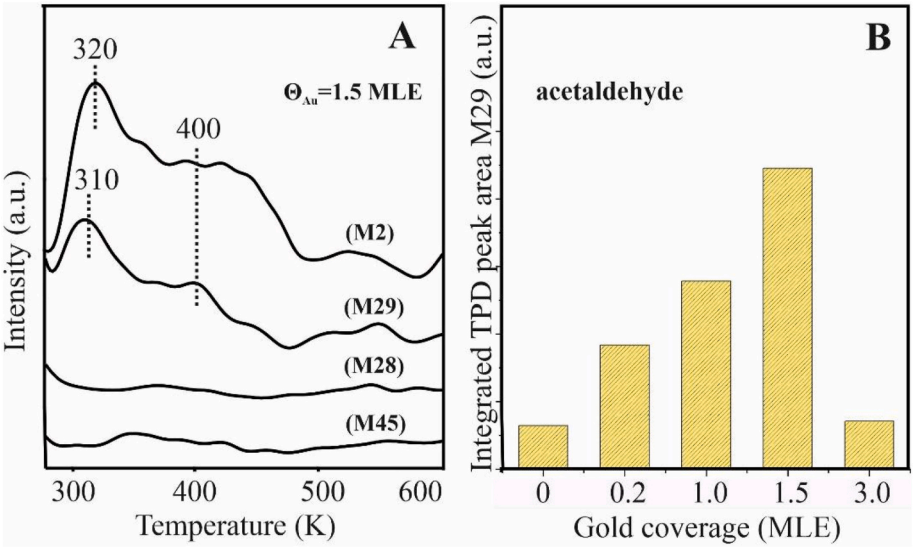

Fig. 48. Desorption spectra after adsorption of 4 L ethanol at 170 K on the 1.5 ML gold covered h-BN/Rh (111) (A) and the changes in the TPD area of amu 29 peak at different gold coverages (B). Reproduced from Ref. [23].

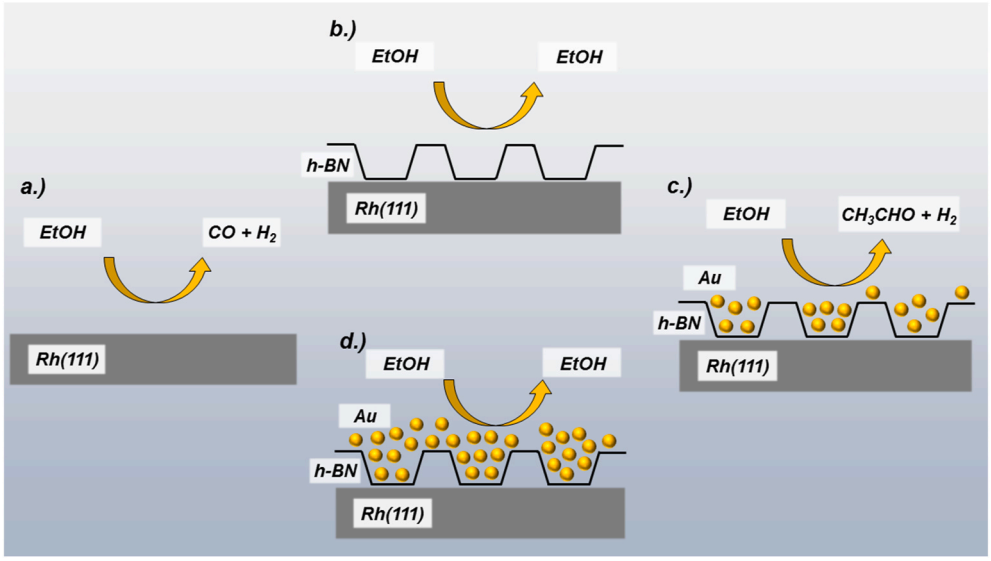

Fig. 49. Schematical representation of different paths of ethanol transformation on h-BN, Au and Au/h-BN modified Rh (111). Reproduced from Ref. [23]. Graphical Abstract.

low Au coverage, which could contribute to the selective behavior of Au/h-BN/Rh (111) catalysts.

It should be mentioned that Au nanoparticles on several supports showed different selectivity in ethanol decomposition, the products (CO, CH_3CHO, ketone, CH_4) were dependent on the nature of oxide supports [334].

Fig. 49 summarizes the interactions of ethanol with clean metal Rh (111), h-BN/(Rh (111), Au/h-BN/Rh (111) with low Au coverages and the fully gold covered Au/h-BN/Rh (111) surfaces. The size of the nanomesh unit cell compared to gold clusters in schematic cartoon are over represented for the best impression.

As described in Ref. [23], the adsorption of the gold adatom and the formation of a 19-atoms Au atomic cluster were modeled by DFT. On-top-B adsorption of the Au adatom in the pore of the h-BN nanomesh on Rh (111) was found energetically preferred with 0.49 electrons negative charge on the Au. To model differently coordinated Au atomic sites, a 19-atoms Au atomic cluster was considered, and a slightly bent 2D island was formed according to DFT optimization. The negative charge on the Au atoms is clearly related to the coordination number of the particular Au site: the less the coordination the larger amount of excess electrons (negative charge) was found. Thus, the larger negative charge at the rim of the Au island can be related to the larger catalytic activity of such Au sites, in agreement with the experimental findings described in the previous subsection.

Without presence of Au, the preferred adsorption site of atomic hydrogen is found at the on-top-B site in the pore of the h-BN nanomesh, just as for the gold adatom. In this case the H has 0.52 electron (negative). Once the model 19-atoms Au atomic island is present on the h-BN nanomesh, it covers the otherwise favorable H adsorption site, and the energetically favored H adsorption occurs at the outer rim of the Au island: the hydrogen is bound to a 3-coordinated vertex Au and a 4-coordinated edge Au atom, and the H is negatively charged with 0.08 excess electron.

In comparison the adsorption of single ethanol on either the pure h-BN or the 19-atoms Au island (mimicking the low-coverage Au regime) in the pore of the h-BN on Rh (111) it was found that there is no clearly

preferred molecular adsorption site and geometry. These results are in agreement with the experimental finding of a very weak interaction between h-BN and ethanol [23]. A 19-atom Au cluster was considered in DFT calculations to model the essential physics and to understand the relationship between atomic coordination number and atomic charges in a small model system.

6.3. Catalytic activity of single-metal atoms, clusters, and nanoparticles on h-BN structures

Presently the studies of single atom catalysis (SAC) and single atom adsorbents (SAA) are in the focus of research. A single atom catalyst based on Co, Ni, Cu atom adsorbed on h-BNNS was investigated using plane wave based pseudo-potential approach [296]. The geometry and electronic structure of these metals on B and N vacancy h-BN sheet were studied first. Fig. 50 represents optimized structures of different atoms on vacancy defected h-BN.

O_2 was used as a probe for the characterization of activity of single atom catalysts. The results showed that the stability of the above mentioned elements is higher at the vacancy site than on vacancy-free h-BN. It was concluded that metal atoms at B vacancy donate electronic charge, while metal atoms at the N vacancy defects accept electronic charge from the h-BN sheet. The interaction of oxygen with h-BN metals adsorbed in vacancies showed that the interaction energy is higher at the N defected site. As a consequence, CO oxidation on Cu@N^V leads to spontaneous CO_2 formation showing that the metals at N vacancy defects are more active for O–O bond activation. The interaction of O_2 with Ni and Au modified h-BNNS was also studied [297]. The obtained results suggested that Ni/h-BN elongates the O–O bond similar to that in the unsupported case. The elongation of the O–O bond is significantly higher in the case of gold atom on h-BNNS than in the unsupported case. These differences are reflected in the catalytic efficiencies of the two metals supported on h-BN nanosheets.

Group IIIA single-metal atoms (Ga, In, Ti) embedded in h-BN for selective adsorption desulfurization via S–M bonds were investigated by DFT calculation [335]. DFT showed that metal atoms prefer to replace boron atoms on h-BNNSs rather than nitrogen atoms. A schematic representation of this substitution is shown in Fig. 51.

It was concluded that Ga atoms have the strongest bond in vacancy due to their smaller atomic radius. Quantum chemical calculations pointed out that the increased adsorption capacity could be contributed to the newly formed S–M bonds, while the π–π interaction is preserved. All metal substituted samples (*M*-BN-SAAs) have better adsorption desulfurization ability than the pristine h-BN nanosheets. In-BN-SAAs

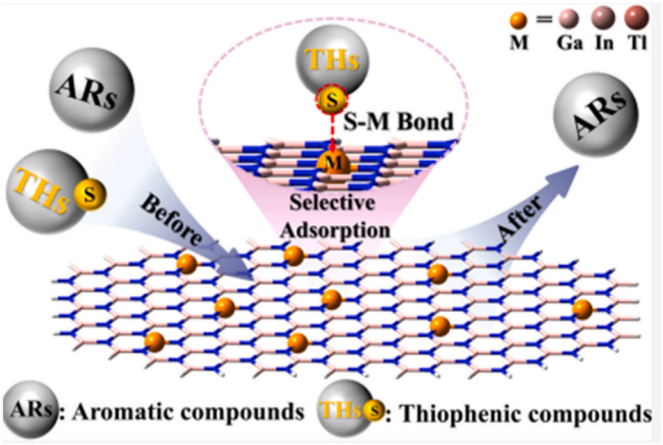

Fig. 51. Representation of substitution of B atom with metal. Reproduced from Ref. [335] Graphical Abstract.

are the best adsorbents. *M*-BN-SAAs exhibit good selectivity to remove thiophenic compound (THs) rather than aromatic compounds.

Au, Au_2 and Au_8 clusters on h-BN nanosheet and its Ni(111) supported analog was investigated in oxygen bond activation by DFT calculations [257]. The optimized geometries of Au, Au_2 and Au_8 on free-standing h-BN sheets are presented on Fig. 52. Au atom likes to sit on-top site of the B atom. As agglomeration is strongly expected, Au_2 and Au_8 clusters are bonded to the N site of h-BN. Au dimer bonds perpendicular with one gold atom attached to the nitrogen atom on-top site on the h-BN with Au–N distance of 2.25 Å. The Au_8 cluster favors planar configuration, the Au–Au distance lie between 2.63 and 2.71 Å.

On free-standing h-BNNS, Au elongates the O–O bond more than Au_2 and Au_8. On the Ni(111) support, the adsorption sites are influenced, both Au and Au_2 favor on-top B atom. On h-BN/Ni(111) the O–O bond elongation is largest for the on the Au_8 cluster. The Ni support can modulate the spin structure of the h-BN sheet and mainly the boron atoms become more activated which control the O–O bond activation along with the gold atoms of Au_8 cluster.

The perfect h-BN could be an ideal support to investigate pure metals due to its chemical inertness. The pristine boron nitride fiber (BNF) showed no catalytic activity in the CO_2 hydrogenation processes [67]. In order to study the catalytic behavior of Pt particles without disturbing effect of oxide support, size-controlled (~4.7 ± 0.6 nm) Pt nanoparticles were impregnated on the BNF, characterized and tested in CO_2 + H_2

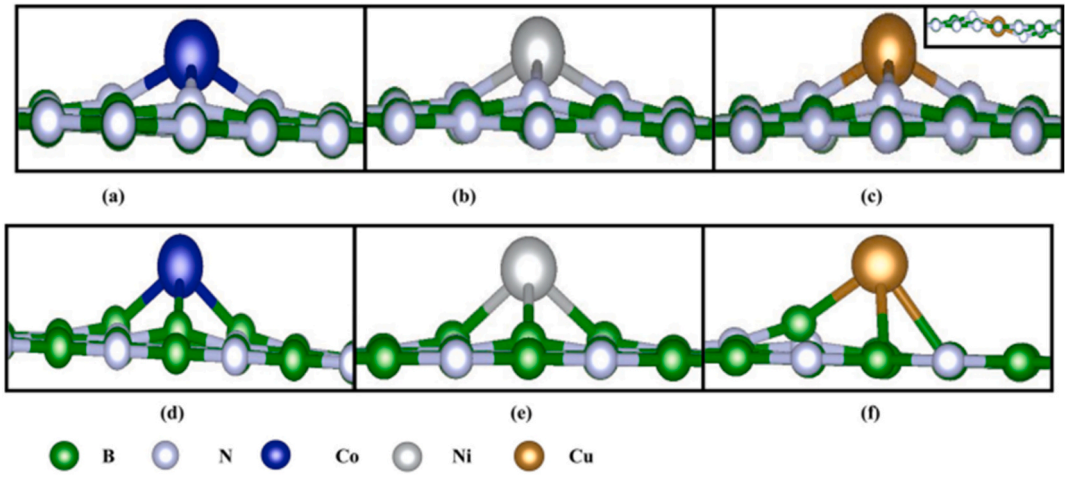

Fig. 50. Optimized structures of the M atom (M = Co, Ni, Cu) on boron and nitrogen vacancy (M@B^V and M@N^V) defected h-BN sheet. While figure a, b and c show the M atoms on boron vacancy, figure d, e and f show M atoms on nitrogen vacancy sites. The inset of Fig. 50(c) shows the stable structure of Cu embedded B^V, where Cu atom can occupy the in-plane location. Reproduced from Ref. [296].

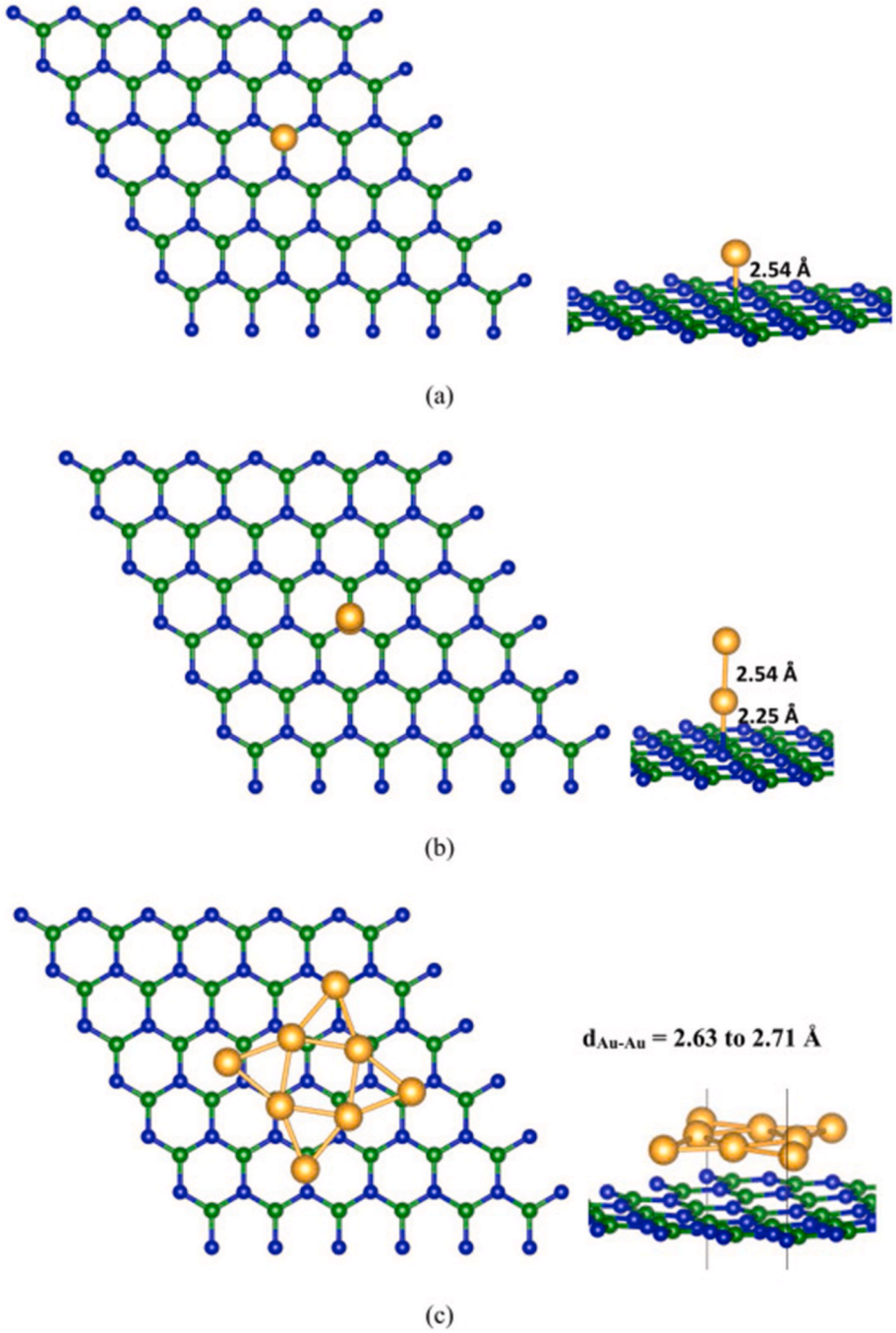

Fig. 52. Optimized geometries of Au atom (a) Au dimer (b) and Au_8 cluster (c) on h-BN sheet. The green, blue and yellow balls indicate B, N and Au atoms, respectively. Reproduced from Ref. [257].

reaction. As it is presented in Fig. 53, the activity of the Pt/BNF catalyst is lower than that of the Pt/SiO_2 (Pt/SBA-15), which is widely used for reference [336].

It was revealed by XPS measurements that there is no electronic interaction between Pt nanoparticles and the h-BN support. In situ DRIFTS experiments suggested that the reaction proceeds via RWGS mechanism as was predicted by DFT calculation on Pt (111) and Pt nanoparticles [337]. CO production occurs via a HOCO intermediate. The nature of active sites was characterized by CO adsorption as a probe molecule. It was supposed that the bands observed on Pt/BNF are related to CO adsorbed on {111} facets of Pt nanoparticles as well as edges, corners, {100} and {110} facets [338]. The band at 2046 cm^{-1} may be associated with higher content of steps, edges [339]. The facets containing Pt structure formed on h-BNF are responsible for the small catalytic activity in CO_2 hydrogenation. The Pt structure on h-BN fibers are presented in Fig. 54.

Although the BN structure is chemically inert in most cases, it may influence the catalytic activity of metals. The h-BN nanosheets have an important behavior, namely they could provide high dispersity for metal nanoclusters. When the catalytic reaction is structure sensitive, the dispersity of the active metal has a crucial role. This was the case in selective hydrogenation of aromatic diamine, which is a technologically important catalytic reaction [340]. Traditionally, the 4,4′-diaminodihexyl-methane (PACM) can be produced by hydrogenation of 4,4′-diaminodicyclohexyl-methane (MDA) at high temperature and pressure with Rh, Ru, or Rh/Ru bimetallic catalysts in the presence of alkali

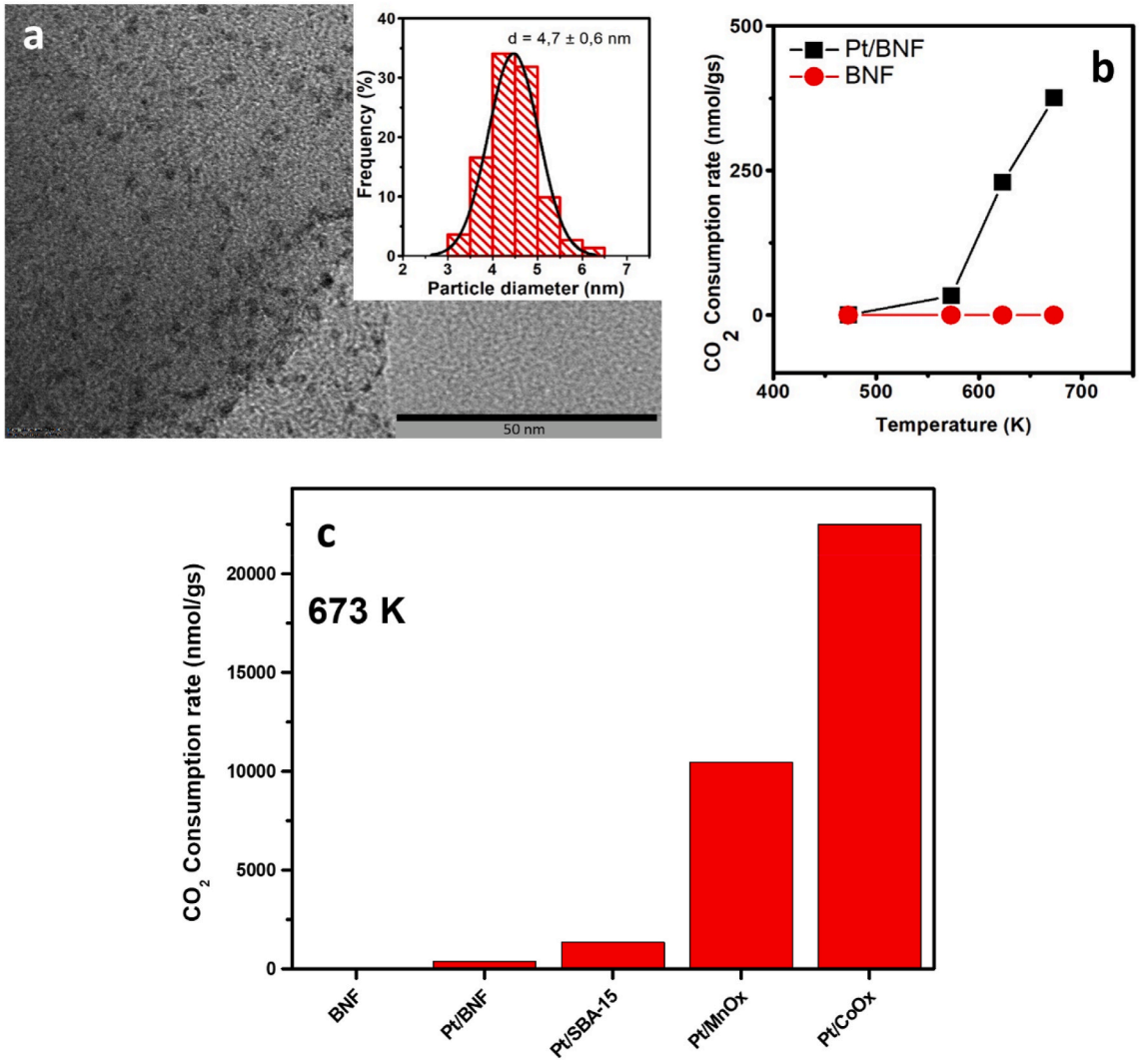

Fig. 53. (a) TEM image of the Pt-impregnated BNFs, the inset is the size distribution of the Pt nanoparticles, (b) the CO_2 consumption rate of the support (BNF) and the Pt/BNF sample, and (c) comparison of the catalytic performance of different chosen catalyst support with the Pt nanoparticles [67].

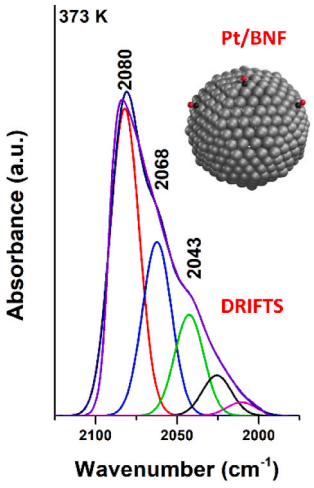

Fig. 54. Schematical representation of Pt structure on h-BN fibers Ref. [67].

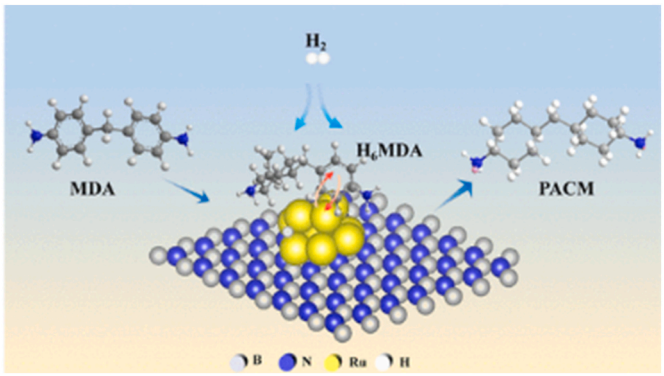

Fig. 55. Illustration of hydrogenation of MDA to PACM on Ru/h-BN. Reproduced from Ref. [35].

ion modifiers [341]. In this type of catalytic process, the reaction is controlled by hydrogen activation. Recently, it was found that h-BN nanosheets provide excellent support for highly dispersed Ru, therefore, the Ru/h-BN nanosheets catalyst exhibited outstanding activity in the hydrogenation of aromatic amines, resulting in corresponding alicyclic amines [35].

XPS experiments suggested that the Ru interacts with B and N sites forming Ru–N and Ru–B coordination and promote the production of ultrasmall particle size Ru clusters. H_2-TPD measurements on Ru/h-BN catalysts showed that the high dispersity promoted more hydrogen

adsorption, 5 % Ru content performed an excellent ability for dissociation of H_2. The catalytic activity of Ru/h-BN catalysts were tested in hydrogenation of MDA to PACM. It is an important observation that although the h-BN nanosheets without Ru loading were not active in the above hydrogenation, with addition of ruthenium the hydrogenation reaction is significantly enhanced. In a temperature range of 90–110 °C almost 100 % conversion was reached, the H_6MDA intermediate practically converted to PACM. The reaction is illustrated in Fig. 55.

In the last couple of years, some studies have reported that not only on oxides but on non-oxide cases support, including h-BN, the SMSI (encapsulation) phenomena may operate [34,37,158]. Generally, the SMSI leads to coating the active sites and decreases the catalytic activity [332,342]. Surprisingly, the SMSI phenomena has been detected recently between metal nanoclusters, e.g., Ni, Fe, Co, and Ru and inert h-BN nanosheets [343]. On few oxide-less supports, like BN, reveal a positive effect of SMSI on stabilizing metal nanoparticles and preventing their aggregation [344–346]. The catalytic study at Rh/BN interface in the dry reforming of CH_4, (DRM) demonstrated that SMSI effect permits the Rh nanoparticles to be encapsulated by BO_x overlayers [347]. Interestingly, when the partial pressure of reactants was increased ($CO_2/CH_4 = 3/1$), no encapsulation layer was observed. At this reaction condition the Rh/BN interface exhibits increased activity and long-term stability during the dry reforming. The reactants destroyed the encapsulated structure. This observation helps to understand the SMSI effect at the interface between metal nanoparticles and non-oxide support like BN. Fig. 56 represents the SMSI effect and catalytic performance of Rh/BN interface during DRM.

6.4. Structure and catalytic activity of metal-oxides on h-BN support

A corundum-Rh_2O_3 was deposited on h-BN after decomposition of the $Rh(NO_3)_3$ during calcination [348]. Based on TEM results and first principle calculations it was found that corundum-Rh_2O_3 with (110) seed plane can be formed on h-BN and successfully applied selectively in methane partial oxidation to syngas. It is well-known that the unmodified and modified Rh_2O_3 exhibit high catalytic activity in partial oxidation of CH_4, but due to their structural heterogeneity complex reaction mechanisms, such as the desired direct path [349] forming CO and H_2, and the undesired indirect route [350], where total CH_4 oxidation occurs, followed by steam- or dry-reforming with the remaining CH_4. From a technological point it is important that the corundum-Rh_2O_3 on h-BN surface works selectively in methane oxidation. Rh_2O_3 structure prepared on h-BN was investigated by H_2-TPR, XPS and TEM. The results are displayed in Fig. 57.

The H_2-TPR picture of Rh/h-BN has only a single symmetric peak with $T_{max} = 146$ °C, which can be assigned to the reduction of Rh_2O_3 (Fig. 57a). The other supports have at least two peaks originating from disordered Rh-oxides species. The Rh 3 d spectra obtained on h-BN were compared to other Rh_2O_3/support systems (Fig. 57b). On Rh_2O_3/h-BN 314.5 eV (Rh^{3+} $3d_{3/2}$) and 309.7 eV (Rh^{3+} $3d_{5/2}$) photoemission peaks were detected, these values indicate that there are fully oxidized Rh^{3+} states from Rh_2O_3 species on Rh/h-BN. The lower binding energies at ~313 and ~308 eV in Rh/γ-Al_2O_3, Rh/SiO_2, and Rh/TiO_2 indicate the presence of $Rh^{\delta+}$ ($0 < \delta < 3$) species, which belong to the oxygen-deficient oxides [351]. STEM profiles represent uniform morphology of Rh_2O_3 on h-BN (Fig. 57c). Rh_2O_3 nanoparticles having an average size of 2.20 ± 0.46 nm (Fig. 57d) with (−116)/(−222)/(006) and (112)/(113)/(005) planes of the corundum-Rh_2O_3 (I) phase are also shown.

The reaction on h-BN without Rh_2O_3 catalyst performed negligible activity up to 750 °C, indicating that the Rh species play a significant role in CO yield of methane oxidation. The catalytic behavior of the supported Rh_2O_3 nanocatalysts (Rh/h-BN, Rh/γ-Al_2O_3, Rh/SiO_2 and Rh/Si_3N_4) heat treated at 600 °C was investigated for methane partial oxidation. The catalytic performances of the tested catalysts are shown in Fig. 58.

Rh/h-BN catalyst demonstrated a 72.5 % yield of CO, as good as that of one of the most active catalysts, Rh/γ-Al_2O_3 at 650 °C at the same reaction conditions. Rh/SiO_2 and Rh/Si_3N_4 showed a somewhat lower yield (Fig. 58a). The lowest yield was measured on Rh/ZrO_2 and Rh/TiO_2 mainly with total oxidation, (CO_2 formation). The H_2/CO ratio at different weight hourly space velocities was constant (WHSV) on Rh_2O_3/h-BN and the stability of the high activity was observed on this catalyst (Fig. 58b). In comparison, Fig. 58c represents the CO selectivity obtained in all catalysts, which clearly shows that the single-phase Rh_2O_3 (I) in Rh/h-BN catalysts have a significant effect on catalytic activity in the partial oxidation of methane. The catalytic behavior of Rh_2O_3 prepared on h-BN support contributes to the understanding of the distinctive metal-oxide support interactions at the nanoscale.

Ag/Fe_3O_4@h-BN exhibited outstanding enzyme-mimicking activity. Both peroxidase- and oxidase-mimicking activities were designed and successfully fabricated for wastewater treatment [339]. The catalyst involved an alternative and supplement for wastewater treatment containing complex and nonbiodegradable pollutants. In principle, under optimal circumstances, over 99.5 % of methyl orange, methylene blue and rhodamine B were degraded by Ag/Fe_3O_4@h-BN, while 63.35 % of As(V) was removed. The Ag can bind stronger to h-BN and it is stabilized on its surface active sites [27,352]. In addition, doping of metal oxides, including Fe_3O_4, is an effective strategy to increase the activity of this type of nanozyme catalysts [353,354]. These are the primary reasons the complex catalyst could mimic the enzymes activity using h-BN support.

6.5. The role of vacancy sites of h-BN in heterogeneous catalytic processes

It was discussed above and it is commonly considered that h-BN behaves as a catalytically inactive material; however, it could serve as ideal support in studying the catalytic effect of active metal without the effect of metal-support interaction [355,356]. However, if vacancy

Fig. 56. Rh/BN catalyst deactivated after dry reforming of methane could be removed by CO_2 or H_2O treatment. Reproduced from Ref. [347] Graphical abstract.

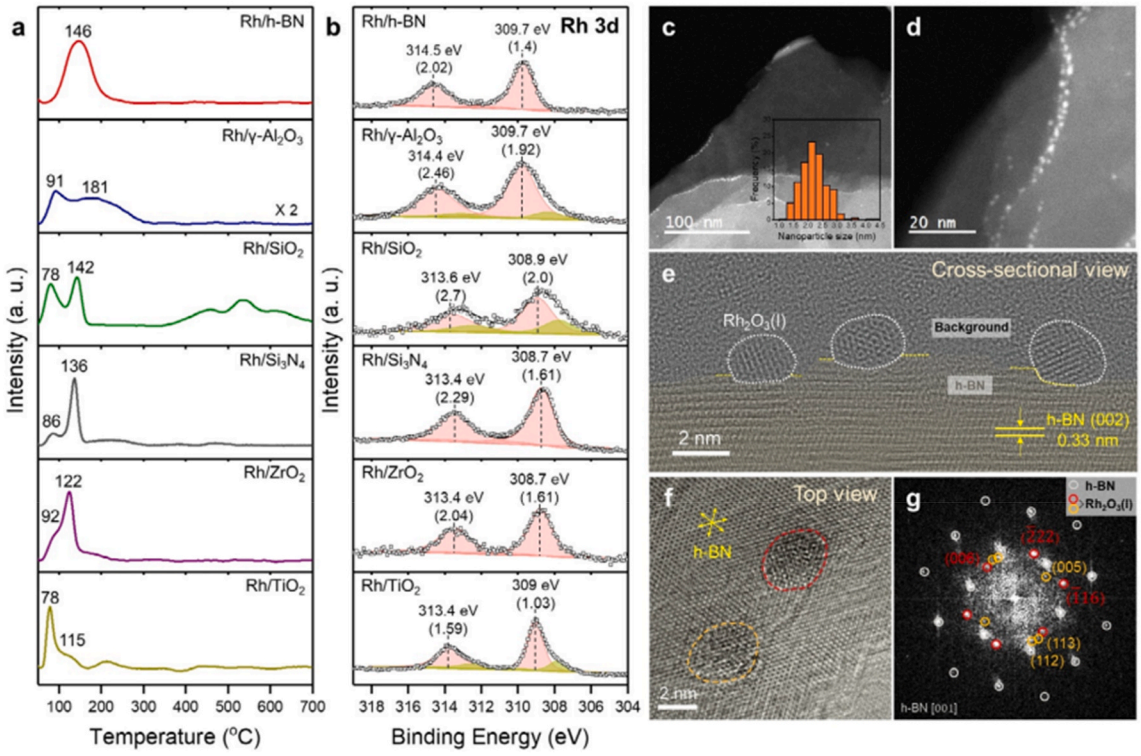

Fig. 57. Ex situ characterization of supported rhodium oxide catalysts. a) H_2 -TPR profiles and b) XP Rh 3 d spectra of Rh/h-BN, Rh/γ-Al_2O_3, Rh/SiO_2, Rh/Si_3N_4, Rh/ZrO_2, and Rh/TiO_2 calcined at 600 °C. c),d) TEM images of Rh/h-BN calcined at 600 °C; the size distribution (inset) is based on over 300 observed rhodium oxide nanoparticles. e) Cs-TEM cross-section image of a focused-ion-beam-processed specimen containing Rh/h-BN with a h-BN [002] zone axis. The region assigned to h-BN is indicated by overlaid pale-yellow-color. f) Top-view Cs-TEM image of Rh/h-BN; the red and yellow dashed circles indicate the Rh_2O_3 nanoparticles and g) the selected-area FFT pattern. Reproduced from Ref. [348].

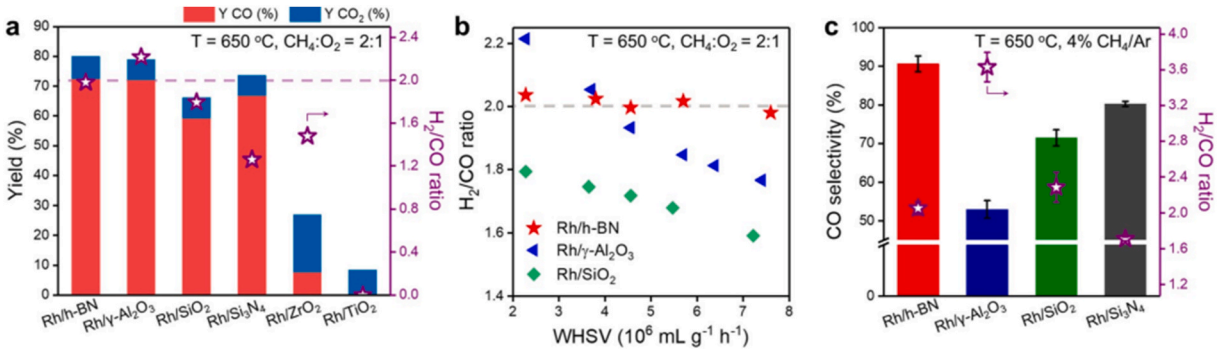

Fig. 58. Catalytic performance of rhodium oxide nanocatalysts. a) MPO test at 650 °C over supported rhodium oxide catalysts (Feed: 4 % CH_4, 2 % O_2 with Ar balance, WHSV: 2280 $Kg^{-1}h^{-1}$). b) H_2/CO ratio versus WHSV conditions for MPO at 650 °C over Rh/h-BN, Rh/γ-Al_2O_3, and Rh/SiO_2 catalysts. c) CO selectivity and H_2/CO ratio for CH_4 isothermal reaction at 650 °C over Rh/h-BN, Rh/γ-Al_2O_3, Rh/SiO_2, and Rh/Si_3N_4 catalysts. Reproduced from Ref. [348].

defects are prepared, then h-BN could be activated. It was presented that h-BN upon steam activation generates B–OH groups at the edges of h-BN, and the activated h-BN efficiently catalyzes the oxidative dehydrogenation of propane with a high selectivity toward propylene. It is supposed that hydrogen abstraction of B–OH groups produces the active sites for propane dehydrogenation [345]. The activation of BNO site in dehydrogenation of C_3H_8 to $CH_2{=}CH{-}CH_3$ is demonstrated in Fig. 59.

Pt nanoparticles on vacancy-rich h-BN nanosheets were investigated and catalytically tested [357]. In a typical fabrication process of B and N vacancies the commercial h-BN was ramped to 800 °C under air several times, kept at this temperature for 5 min. After calcination, the sample was placed into a liquid nitrogen-filled bottle. This catalyst shows an electronic effect on Pt induced by the BN nanosheets with *N*-vacancies and B-vacancies for excellent CO oxidation catalysis [357]. The charge analysis pointed out that with Pt on B-vacancies, the h-BN nanosheets behave as a Lewis acid to accept electrons from Pt, and on the other hand when Pt sits on *N*-vacancies, the h-BN nanosheets act as a Lewis base for donating electrons to Pt. This electronic effect results in an electron-rich character of Pt on h-BN sheets. Fig. 60 gives an illustration about the h-BN sheet with B and N vacancies. Fig. 61 displays TEM and STEM profiles of exfoliated few-layer h-BN nanosheets with high exposure edge and 5 ± 0.5 nm cubic Pt nanoparticles.

On the bare h-BN nanosheets, the charge transfers between Pt and h-BNNS is very small as can be seen in Fig. 62a. The cluster binding energy (BE) is −2.00 eV. In the case of N and B vacancies (N^V and B^V) the Pt cluster binds at these defective sites with E_B of −7.22 eV and −7.77 eV, respectively, by developing Pt–N and Pt–B bonds (Fig. 62b and c).

Electron energy loss spectroscopy (EELS) and in situ CO-DRIFT

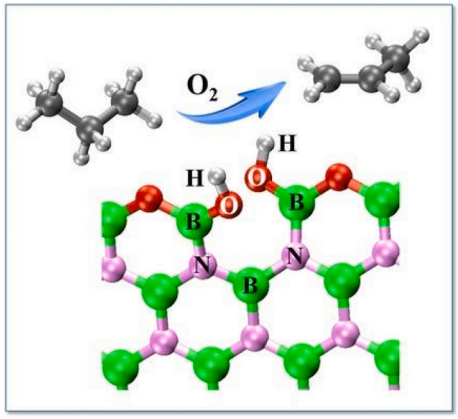

Fig. 59. Edge-hydroxylated h-BN as a catalyst for oxidative dehydrogenation of propane. Reproduced from Ref. [345].

experiments suggest that the interaction between Pt NPs and *N*-vacancies is dominating. The electron-rich Pt favors the adsorption of O_2, weakening CO poisoning, hence promoting the catalysis. This type of new catalytic system may suggest a method to plan and evolve highly stable supported Pt catalysts with controllable activity and desirable selectivity for other heterogeneous reactions.

In some cases the metal nanoparticles tend to accumulate at the edge or grain boundaries of h-BN sheet forming dislocations, B or N defects and OH terminal groups which could induce certain catalytic reactions [31,358]. Recently, confined metal catalysis on h-BN/metal interface was experimentally observed and theoretically studied [15,31,359–361]. The h-BN layers interact weakly with the metal surfaces through van der Waals forces, which are available for intercalation of many small gas molecules (H_2, O_2, H_2O, CO, and CH_4) [15]. The confined catalysis may also offer a unique opportunity to tune the metal-molecule interaction and the catalytic efficiency [359].

An ultrasmall Ni nanoclusters (~1.5 nm) deposited on defective h-BN nanosheet catalysts were prepared for methanol dehydrogenation. The produced catalyst has higher CH_3OH dehydrogenation ability than that of some other nickel-based catalysts [38]. The important part of the preparation of defect-rich h-BN nanosheets consists of combined exfoliation method of gas and lithium intercalation-based exfoliation. In the first step the bulk h-BN was thermally pre-treated at high temperatures (800 °C). The important remark is that this temperature is lower than the oxidation temperature of h-BN (1100 °C). The next step is the Ni nanocluster deposition on the vacancy-abundant BN nanosheets. The process and the proposed "pit" structure of Ni/h-BN are presented in Fig. 63.

The nucleation and growth of Ni nanoclusters preferably occurred at the BN_2O defects. A "pit" model structure was supposed for the Ni/h-BN system, where the nanoclusters sit on bare h-BN nanoflakes and interact with close edges of h-BN so that the small size of nanoclusters is preserved. This arrangement facilitates the CH_3OH adsorption, products transferring resulting in excellent catalytic activity and selectivity. In Fig. 64, the catalytic activity of Ni nanoclusters on different substrates for CH_3OH dehydrogenation is collected.

Fig. 64A displays the size effect of Ni nanoclusters in hydrogen production in methanol decomposition on Ni/h-BN catalysts. It can be seen that the smaller size of Ni nanoclusters favors the dehydrogenation of CH_3OH. In addition, smaller nanoclusters show higher selectivity. On Ni-based catalysts the decomposition products are the H_2 and CO, CH_4 is only by-product. Fig. 64B and C shows the H_2, and CO selectivity obtained on different Ni catalysts. Fig. 64D displays the long-term stability of the catalysts. In all respects, the Ni on defective h-BN nanosheets give the best record in the catalytic decomposition of CH_3OH. In summary it

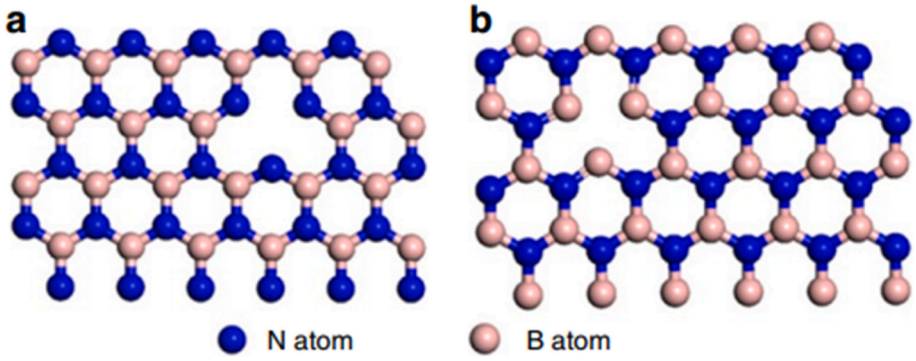

Fig. 60. Schematic illustration of h-BNNS with B and N vacancies. (a) h-BNNS with B vacancy and *N*-terminated edge. (b) h-BNNS with N vacancy and B-terminated edge. Reproduced from Ref. [357].

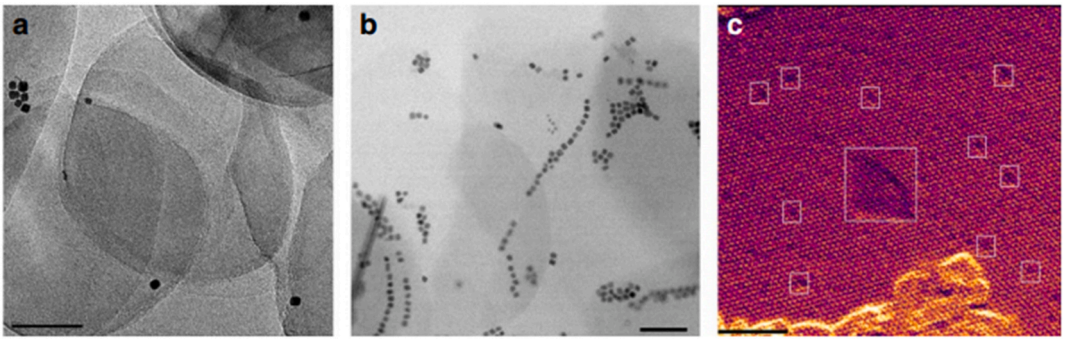

Fig. 61. Representative TEM and STEM images. (a) TEM of Pt/h-BNNS. Scale bar, 50 nm. (b) STEM of Pt/h-BNNS. Scale bar, 50 nm. (c) High-resolution STEM of h-BNNS with vacancies, as indicated by the boxes. Scale bar, 2 nm. Reproduced from Ref. [355].

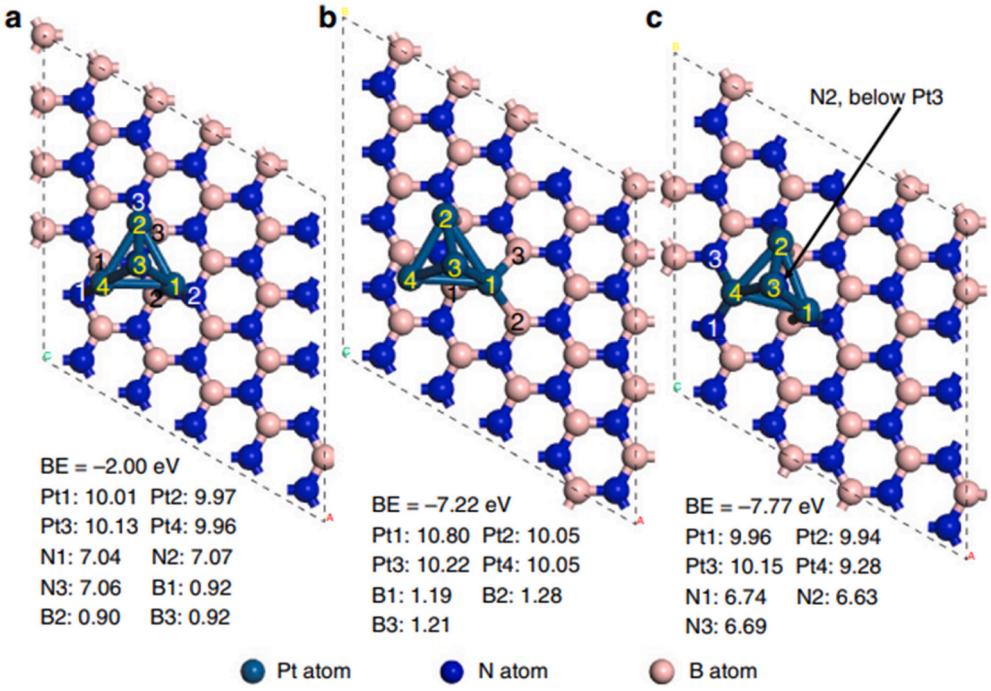

Fig. 62. Optimized structures and valence electrons of pyramidal Pt_4 cluster on h-BNNS. (a) Pt_4 cluster on clean, vacancy-free h-BNNS. (b) Pt_4 cluster h-BNNS with N_V. (c) Pt_4 cluster on h-BNNS with B_V. Reproduced from Ref. [357].

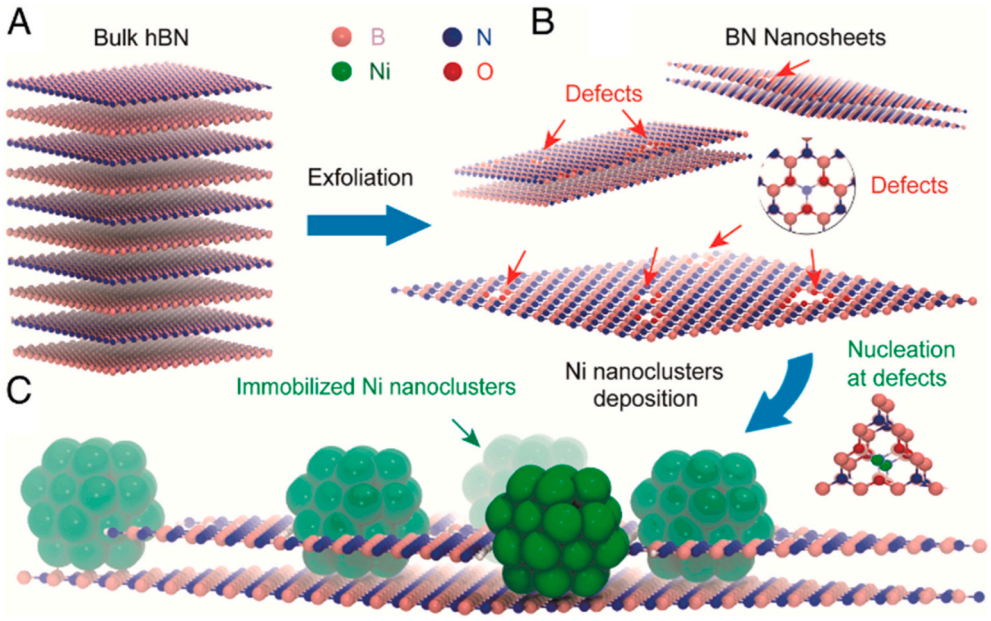

Fig. 63. Schematic illustration of the formation of defective h-BN nanosheets and further deposition of Ni nanoclusters. Defective h-BN nanosheets (B) were prepared from bulk h-BN (A) by a combined exfoliation method of gas exfoliation and lithium intercalation-based exfoliation. Ni nanoclusters were deposited by in situ reaction of lithium naphthalenide with $[Ni(Cp)_2]$ (Cp = C_5H_5) in the h-BN nanosheets solution. Proposed "pit" structure of the Ni/h-BN nanocomposite (C). Reproduced from Ref. [38].

can be concluded that the ultrasmall Ni nanoclusters (~1.5 nm) deposited on vacancy-abundant h-BN nanosheets exhibit outstanding activity and selectivity in CH_3OH dehydrogenation. Calculated turnover frequency (TOF) is the best in comparison with some other Ni supported catalysts published earlier.

Very recently it was observed that the extent of oxidation state of h-BN (h-BN(O)) support influences the catalytic efficiency [362]. Au/h-BN (O) and Pt/h-BN(O) nanohybrid catalysts were studied both in CO oxidation and CO_2 hydrogenation reactions. The h-BN particles were prepared by plasma-chemical method using boron trichloride. The obtained product was annealed under vacuum at 1500 °C denoted as h-BNNPs. The catalytic behavior of this unoxidized, pristine h-BN nanoparticle was compared with its oxidized counterpart (h-BN(O)). The h-BN(O) nanohybrid catalyst (denoted as h-BNNPsOx) was produced by oxidation, the h-BNNPs was exposed to air at 1100 °C for 2 min.

Pt/h-BN(O), and Au/h-BN(O) nanohybrids were prepared by impregnation method from their appropriate salts ($H_2PtCl_6{\cdot}6H_2O$) and

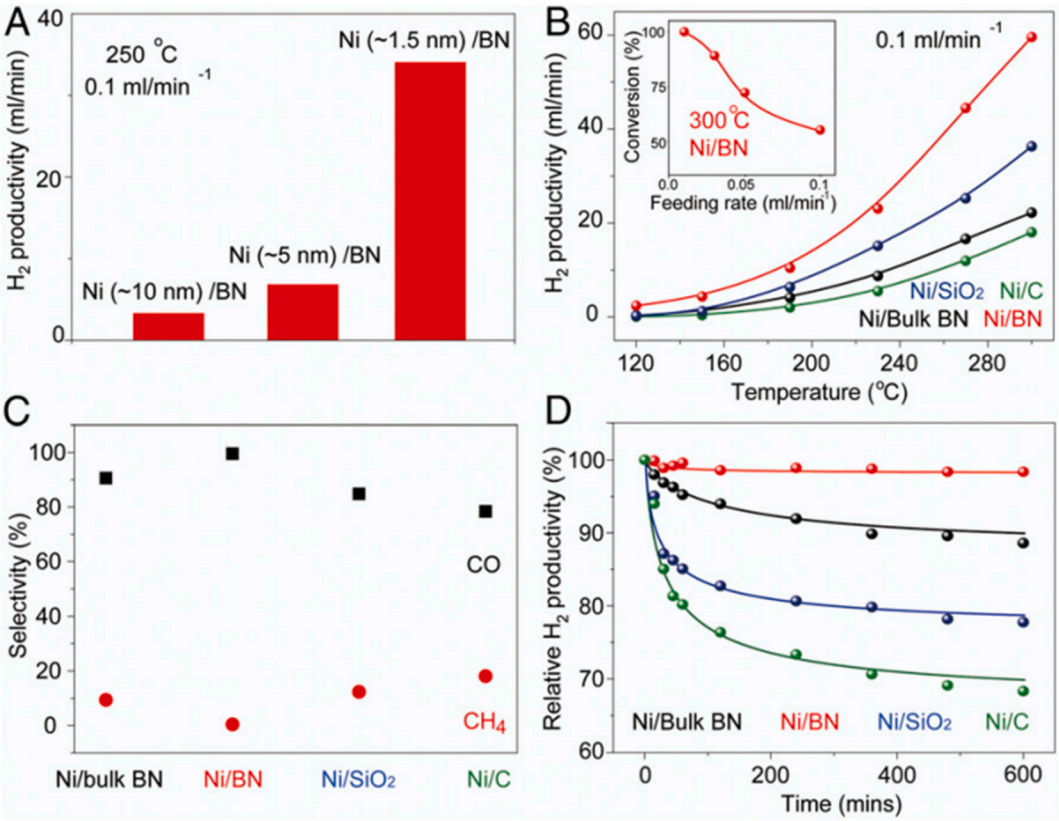

Fig. 64. Catalytic performance of Ni nanoclusters on various substrates for methanol dehydrogenation. (A) Hydrogen productivity of Ni/h-BN nanocomposite with various Ni nanocluster sizes. (B) Temperature-dependent hydrogen productivity of Ni nanoclusters on various substrates at the methanol feeding rate of 0.1 mL/min. (C) Selectivity and (D) the long-term durability of various catalysts for methanol dehydrogenation (methanol feeding rate, 0.1 mL/min; N_2 feeding rate, 30 mL/min; temperature, 300 °C). Reproduced from Ref. [38].

($HAuCl_4{\cdot}nH_2O$) [362]. The supported Au and Pt catalysts were characterized by different spectroscopic and microscopic methods. The summary results are displayed in Fig. 65. Besides the phonon feature of h-BN, the FTIR spectra indicates B–O and OH bands in the case of oxidized samples. According to the HRTEM results, the materials are highly defective and contain several interfaces and edge dislocations. The XPS spectra contain peaks due to B–N bonds and a contribution at 192.0 eV corresponding to B–N–O bond. BNO-based catalysts exhibit higher activity compared to their oxygen-free counterparts. Pt/h-BN(O) shows high catalytic activity in CO conversion and CO_2 hydrogenation. The significantly higher CO_2 conversion rate observed on the BNNPsOx-supported Au and Pt catalysts is connected with better CO_2 adsorption on oxidized h-BN. The activity of Pt/h-BN(O) was higher than that of Au/h-BN(O). The enhanced Pt–h-BN interactions can influence O_2 and H_2 adsorptions, thereby accelerating catalytic reactions.

The encapsulation tendency could be more pronounced when the h-BN contains significant amount of defects created by etching processes. It was found by TEM that weak oxidizing reagents like CO_2 and H_2O promote the encapsulation of Ni nanoparticles by BO_x originated from the h-BN support during the $CH_4 + CO_2$ (DRM) reaction. The encapsulation process on Ni@BO_x/h-BN is presented in Fig. 66. It is suggested that in reaction at 750 °C, BO_x is formed during the strong etching of h-BN. Boron-oxide could encapsulate the Ni nanoparticles.

The results of in-situ surface investigations and theoretical calculations suggested that surface B–O and B–OH sites in the formed BO_x encapsulation overlayers exhibit synergistic effects with the Ni active sites to catalyze the $CH_4 + CO_2$ reaction rather than inhibiting the reactions. The role of the B–OH groups in the DRM reaction is supported by DFT calculations. It is revealed that the stable configuration is a B–O–B structure at the B-zigzag edge of the h-BN nanosheets. The estimated thermodynamic energy in each step for DRM is presented in Fig. 67. Firstly, the CH_4 dissociates hydrogen on Ni sites, the H atom reacts with B–O–B to form B–OH–B sites. CO_2 assists in breaking one B–O bond and adsorbs on B atom and finally dissociates.

6.6. *The role of h-BN nanosheets in electrochemistry and photochemistry; oxygen and hydrogen evolution reactions*

Conductive BN is auspicious catalyst support for the oxygen evolution reaction [40]. The O_2 evolution reaction (OER) is an important electrochemical reaction for batteries, energy storage and conversion. Recently, carbon based catalysts, CNT, Gr, are the best catalyst support for these processes due to their electrical conductivity and low cost [363, 364]. The boron nitride unfortunately has low electrical conductivity which prevents its utilization in electrocatalysis [40]. Very recently, one-atom-thick boron nitride co-catalyst was found for enhanced oxygen evolution reactions. Nowadays, theoretical and experimental results showed that mid-gap state could be prepared with the help of interlayer B–B dipolar interaction [40]. The recently published results showed that laser-modified h-BN with C, O dopants (L-BN) is an excellent support for OER reaction. Pulsed laser is a facile way of breaking chemical bond and create ones. Therefore, the PLA technique may help to create interlayer B–B dipolar interactions in BN, making BN an excellent support for catalysts [365]. Applying laser-induced interlayer B–B dipolar interaction with IrO_x catalyst, N–C═N bonds are formed, which are playing an important role in the high activity and stability. Recently, single-atom doped catalysts on BN sheets were found as cathode for oxygen reduction in proton-exchange membrane fuel cells [366]. Very recently highly efficient OER/ORR bifunctional electrocatalysts were developed on h-BN co-doped with transition metals such as Fe, Co, Ni and carbon

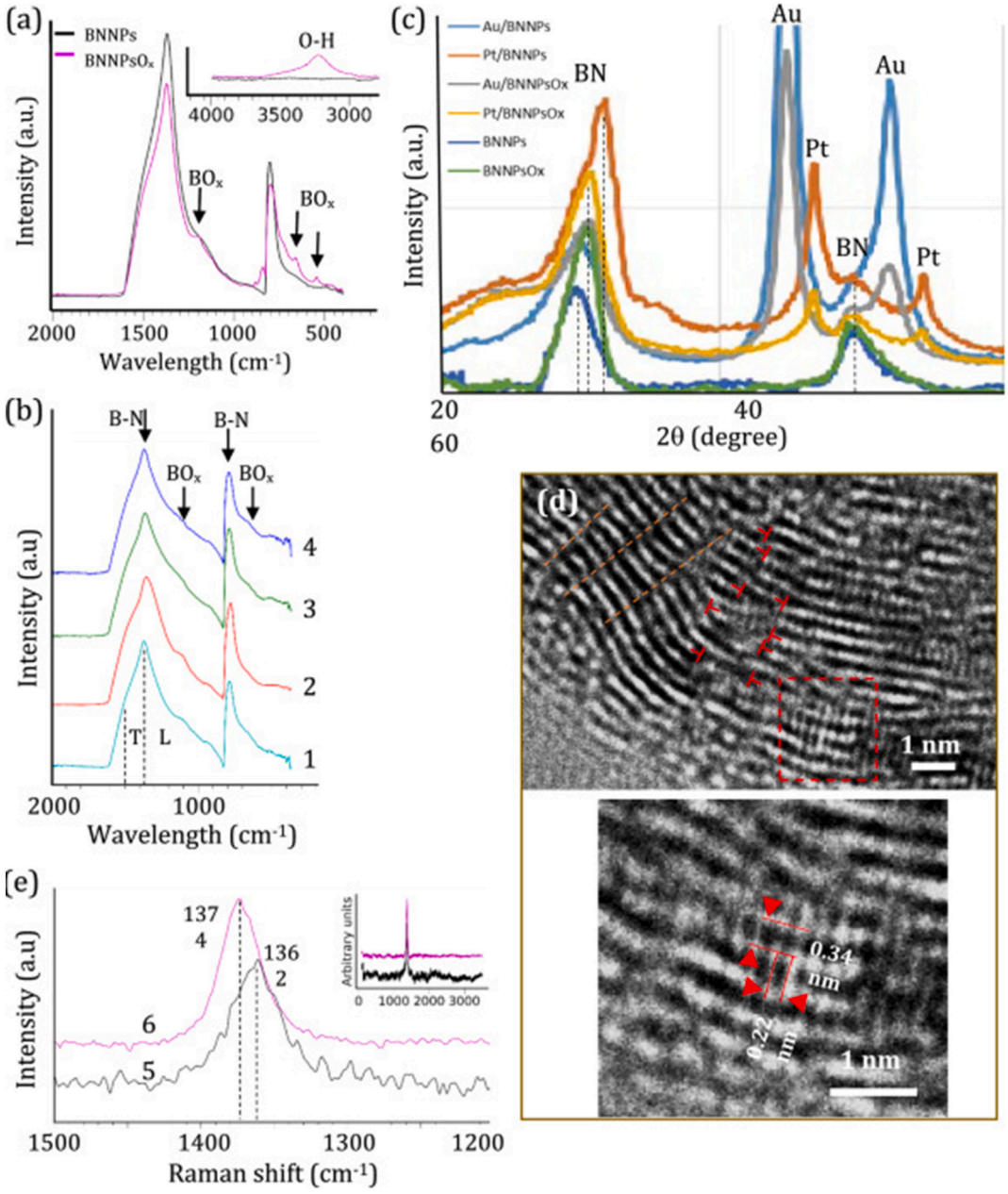

Fig. 65. FTIR spectra (a,b), XRD patterns (c) and Raman spectra (e). 1 – Au/BNNPs, 2 – Au/h-BNNPsOx, 3 – Pt/h-BNNPs, 4 – Pt/h-BNNPsOx. High-resolution TEM images (d) of turbostratic h-BN. Edge dislocations and interfaces are shown by symbol ⊥ and dashed lines, respectively. Reproduced from Ref. [362].

[367]. Their excellent ORR activities are comparable to that of Pt (111). The catalytic systems exhibit high thermodynamic stability. Mn-doped vacancy h-BN turned out as a noble-metal-free active electrocatalyst for ORR reaction by DFT calculation. The ORR reaction was found to be thermodynamically advantageous in the Mn-doped vacancy-BN [366].

In certain cases, metal-supported h-BN monolayers (h-BN/M) were a new candidates for electrocatalytic application in the reduction process [284,368]. Several fabrication methods have been recommended to introduce defective and metal-doped h-BN/Cu(111) systems as electrocatalysts for the HER. DFT calculation results suggested that defective/metal-doped h-BN can be modified successfully and the Cu (111) support plays an important role in tuning the reactivity [368]. It was also demonstrated that Au clusters on the h-BN/Au (111)exhibit significant activity in HER reaction. It is usually observed that h-BN is inert, but a single-layer h-BN with an underlying Au (111) substrate has chemical activity. The observed charge transfer between the supported Au clusters and the h-BN/Au (111) surface enhanced the catalytic activity of the Au_n@h-BN/Au (111) system for HER [284].

An ordered surface oxide on Cu(111) surface protected by an h-BN layer through oxygen intercalation was prepared and characterized. XPS and ARPES features show that the h-BN layer remained intact. Interestingly, during oxidation a new state between the Fermi level (E_F) and the onset of the Cu d bands appeared. It was observed that the conduction band is at a sufficient energy to drive the HER for water splitting, however, the photoexcited electrons showed short lifetimes [369]. For the future, the h-BN deposition and oxygen intercalation to Cu foil may direct this system into a useable photocathode. A few years ago it was observed and studied that fluorinated h-BN nanosheets have effective performance as cathode material in magnesium batteries [370].

It turned out recently that Pt@h-BN/Al_2O_3 nanoreactor is very efficient in CO_2 to CH_4 photoreduction [319]. Nearly 100 % CH_4 selectivity was achieved. The best way to reduce the level of CO_2 is to use it as a

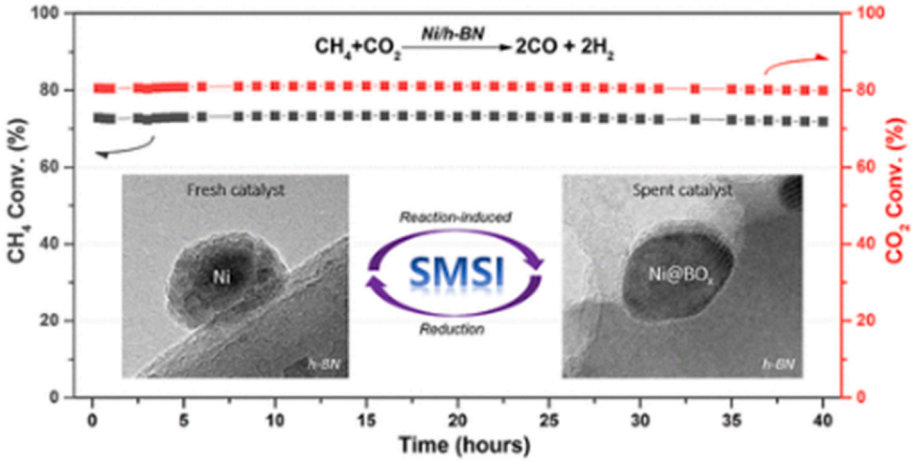

Fig. 66. SMSI process on Ni@BO_x/h-BN during dry reforming of methane at 750 °C. Reprouced from Ref. [343] Abstract.

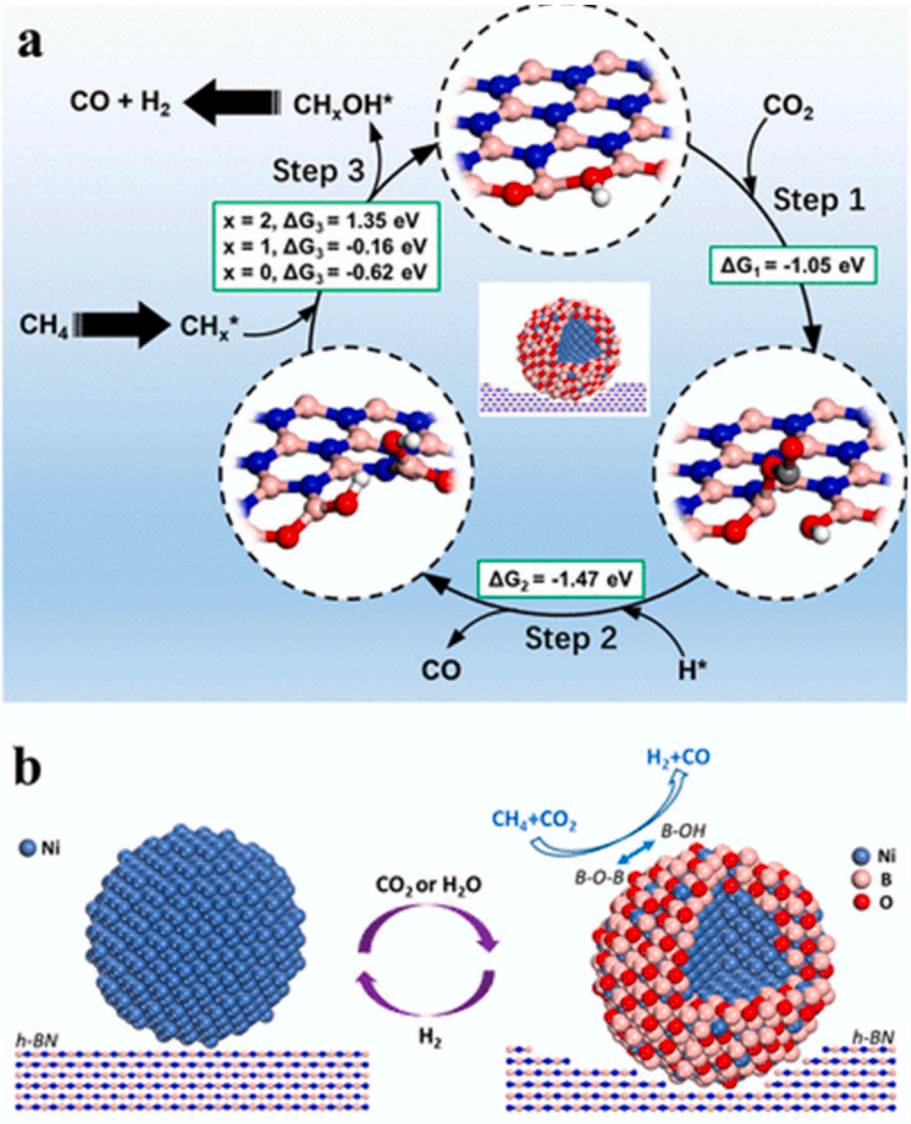

Fig. 67. (a) DRM catalytic cycle on Ni@BO_x based on experimental and DFT calculation results. B, N, O, C, and H atoms are marked by pink, blue, red, gray, and white balls, respectively. (b) Classical SMSI effect in Ni/h-BN catalyst. Reversible structure evolution between bare Ni NPs and Ni@BO_x induced by CO_2 or/and H_2O in the DRM reaction atmosphere is shown. Reproduced from Ref. [343].

starting material for production of more valuable compounds (CO, hydrocarbons). The hydrogenation of CO_2 to CO and hydrocarbons with thermal- and photocatalytic application is very promising [137, 371–373]. In the investigation with Pt@h-BN nanoreactors it turned out that as the number of h-BN coating layers increases, the selectivity of photocatalysis is altered from nearly 100 % CO_2 to CO to nearly 100 % CO_2 to CH_4 [319]. In situ characterization and theoretical calculation showed that the optimal 3-layer h-BN coating creates the best confinement effect with more CO_2^- intermediate complex production and with a higher selectivity. The important step is the C–O bond cleavage in CO molecules and the key intermediate is the negatively charged CO_2 (CO_2^-). This work offers a new direction for the gas–solid phase photocatalysis of CO_2 to hydrocarbon formation using h-BN assisted confinement effect, with Pt nanoparticles.

The use of modified h-BN to tune a semiconductor photocatalyst is one of the viable ways for the evolution of H_2 by water splitting [39,374, 375]. This possibility is due to the unique properties of the h-BN, because it can suppress recombination of the photogenerated charge carriers and hence enhance in the redox processes. Very recently, h-BN nanosheets were modified with Ni_2P and with excess boron. The h-BN (B)–Ni_2P composite coating was investigated in solar water splitting.

Combining the narrow band-gap (E_g~1 eV) semiconductor Ni_2P with the insulator (E_g~6 eV) h-BN sheet, a serious drop in the recombination rate of the photogenerated charge carriers was observed. The transfer of the holes onto the h-BN sheets prevents their recombination with excited electrons. The proposed photocatalytic hydrogen production is schematically shown in Fig. 68. Excess boron enhanced the activity of the composite. This boron increased the concentration of negative charge. The combined effect of the primary photocatalyst and boron enhanced the rate of H_2 evolution. It was pointed out that by fluorine doping the band gap of h-BN nanosheets drastically decreased [184]. Bi-layer structures can be formed with different F doping ratios via van der Waals interaction. Based on first-principles calculations, it was demonstrated that h-BNNS bi-layers can be converted to visible light absorption materials through band-gap tuning. The band edge positions of the F-doped h-BNNS bi-layers with doping ratios of 6.25 at.%, 25 at.%, 37.5 at.%, and 50 at.% are all well aligned to straddle the redox potentials of water at pH = 0, which can be used for water splitting. These nanocomposite structures give a possibility to construct materials for photo-voltaic cells and develop new metal-free photocatalysts applied for example for water splitting.

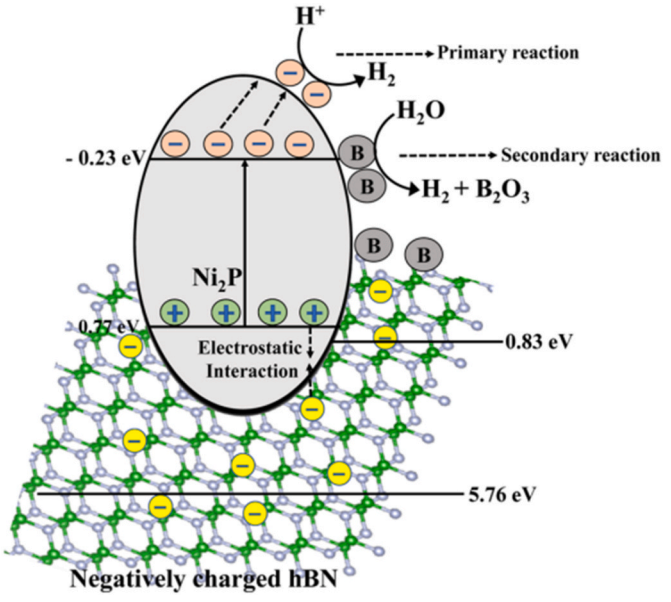

Fig. 68. Schematic illustration of the proposed mechanism for the photocatalytic H_2 production in the h-BN(B)–Ni_2P composite coating. Reproduced from Ref. [39].

7. Summary and outlook

The intensive worldwide research in the last 15 years executed for the fabrication, characterization and application of all possible 2D materials possessing atomic thickness and macroscopic lateral extent resulted in an exceptionally great success. This achievement is partially due to the highly developed arsenal of surface science techniques widened continuously in the last 60 years and ready for atomic scale characterization of solid state material surfaces. The other sources of the success were undoubtedly coming from one side the existence and wide application of fast quantum mechanical calculation, from another side the huge international community of research institutes interested in finding new materials and new perspectives or their application in different hot topics like energy science, nanoelectronics and green chemistry. This latter one connects mainly to classical heterogeneous catalysis and its modern sub-areas like nanocatalysis, single atom catalysis or chemical nanosensorics.

The present work is dedicated mainly to the different aspects of the characterization and application of a single 2D material, namely hexagonal boron nitride (h-BN). Nevertheless, the structure of this review is going toward the gradual increase of the complexity of the related h-BN based materials (starting from its metal supported forms, its decoration by metal atoms or molecules, investigation of the appearing chemical reactions, up to the application fields of the related catalytic processes) can serve as a good example for similar future studies on other 2D materials, as well.

The monolayer h-BN synthesis has been successfully performed more than two decades ago, however experimental efforts are developing nowadays in this field, especially in the atomically-thin h-BN direction. Within the h-BN nanosheets subject, we put in the focus the formation, characterization and application of the “nanomesh” produced on metals. The unique properties of highly regular corrugated h-BN nanomesh structure offer excellent possibility of the adsorbed atoms or molecules for a tailored (template) adsorption configuration. We kindly call for further investigations in this direction. The nanomesh structure may direct and control the adsorption of molecules and metal nanoparticles in appropriate electronic and geometric configuration, which can lead to catalytic reactions with the desirable selectivity and activity. Structure determination of 2D h-BN nanosheets is in the focus of material science, nanoscience and surface science, as well. We emphasize that the h-BN structure will play a significant role in catalysis and chemical nanosensorics not only as a support but as an active component. In many cases the h-BN materials behave as an inactive partner but in certain cases the functionalized and/or vacancy-BN can initiate new thermal-, photo- and electrocatalytic properties. Actually, this research area might demonstrate exciting progress in the coming years.

The controlled modification of h-BN nanosheets with different elements, mainly with metals, and tailored interface engineering at h-BN/metal support offers multifunctional applications. The area of potential technological applications is continuously broadening with the combination of h-BN with different (other 2D) materials to form heterostructures and very intriguing interfaces. 2D h-BN is being extensively investigated in electronics, optoelectronic, spintronic and magnetic devices due to its electronic and photonic properties. To date, a few reports discussed the interface engineering by combining h-BN nanosheets with graphene in energy conversion and electrochemical energy storage devices to further improve their performance. 2D h-BN nanoflakes to passivate the surface states of some semiconductor films in solar cell applications were studied in order to improve the performance by reducing carrier recombination. Over the past few years, considerable efforts have been devoted to the functionalization of 2D materials, including h-BN and graphene to improve their properties of several types of sensing, energy conversion, and storage devices [376]. A few

experimental and theoretical studies demonstrated that chemical functionalization of few-layered h-BN nanosheets is able to decrease and tune the bandgap of h-BN nanosheets, which further expands its application area. In the present review we also highlight some examples where the nanopores containing 2D h-BN offer exciting opportunities for applications in optical modulation, DNA sequencing, and quantum information technologies. The in-situ fabrication of h-BN multilayers in controlled size, thickness and structural quality needs to be further expanded.

As final concluding remarks of the thoughts above, we would like to emphasize that research activity in the field of 2D materials is far from „the end". For example, the recent first steps toward combining 2D materials (their vertical or horizontal nanocomposites) will certainly deliver several unexpected new breakthroughs and perspectives. The research on the formation and characterization of heterobilayers, where h-BN is one of the layers, will definitely lead to new applications in the field of 2D devices, such as p-n junctions, or thermoelectric devices. Furthermore, the modification of BN nanostructures with carbon is introduced into the focus of research trends nowadays. This effort will be further amplified in the near future. Along this concept, atomic 2D materials can be achieved by the formation of uniform hexagons consisting of $(BCN)_2$. This scheme can lead one to a new horizon, namely, the immediate formation of BCN type 2D materials by using special precursor molecules [11,77]. This way can broaden the range of studied materials to the so-called "BCN triangle". Quite importantly, semiconducting materials with tunable band gap can be obtained this way. Among others, the ternary semiconductor boron carbon nitride (B–C–N alloy) can catalyze hydrogen or oxygen evolution from water as well as carbon dioxide reduction under visible light illumination.

CRediT authorship contribution statement

László Óvári: Writing – review & editing, Writing – original draft, Conceptualization. **Arnold Péter Farkas:** Writing – original draft, Visualization, Methodology, Formal analysis. **Krisztián Palotás:** Writing – original draft, Validation, Software, Methodology, Investigation, Formal analysis. **Gábor Vári:** Validation, Investigation, Data curation. **Imre Szenti:** Visualization, Investigation. **András Berkó:** Writing – original draft, Visualization, Formal analysis. **János Kiss:** Writing – review & editing, Writing – original draft, Validation, Supervision, Data curation, Conceptualization. **Zoltán Kónya:** Writing – review & editing, Supervision, Funding acquisition.

Declaration of competing interest

The authors declare that they have no known competing financial interests or personal relationships that could have appeared to influence the work reported in this paper.

Acknowledgement

This project has received funding from the HUN-REN Hungarian Research Network. The authors are grateful for the funds of NKFIH - OTKA - SNN 135918, K_21 138714, and Project no. RRF-2.3.1-21-2022-00009, titled National Laboratory for Renewable Energy has been implemented with the support provided by the Recovery and Resilience Facility of the European Union within the framework of Program Széchenyi Plan Plus. K. Palotás acknowledges the National Research Development and Innovation Office of Hungary (NKFIH, Grant No. FK124100), the János Bolyai Research Grant of the Hungarian Academy of Sciences (Grant No. BO/292/21/11) and the New National Excellence Program of the Ministry for Culture and Innovation from NKFIH Fund (Grant No. ÚNKP-23-5-BME-12). The ELI-ALPS project (GINOP-2.3.6-15-2015-00001) was supported by the European Union and co-financed by the European Regional Development Fund.

References

[1] R. Arenal, A. Lopez-Bezanilla, Boron nitride materials: an overview from 0D to 3D (nano)structures, Wiley Interdiscip. Rev. Comput. Mol. Sci. 5 (2015) 299–309, https://doi.org/10.1002/wcms.1219.
[2] D. Golberg, Y. Bando, Y. Huang, T. Terao, M. Mitome, C. Tang, C. Zhi, Boron nitride nanotubes and nanosheets, ACS Nano 4 (2010) 2979–2993, https://doi.org/10.1021/nn1006495.
[3] T. Hegedűs, D. Takács, L. Vásárhelyi, I. Szilágyi, Z. Kónya, Specific ion effects on aggregation and charging properties of boron nitride nanospheres, Langmuir 37 (2021) 2466–2475, https://doi.org/10.1021/acs.langmuir.0c03533.
[4] L. Vásárhelyi, T. Hegedűs, S. Sáringer, G. Ballai, I. Szilágyi, Z. Kónya, Stability of boron nitride nanosphere dispersions in the presence of polyelectrolytes, Langmuir 37 (2021) 5399–5407, https://doi.org/10.1021/acs.langmuir.1c00656.
[5] A. Pakdel, C. Zhi, Y. Bando, D. Golberg, Low-dimensional boron nitride nanomaterials, Mater. Today 15 (2012) 256–265, https://doi.org/10.1016/S1369-7021(12)70116-5.
[6] X.-F. Jiang, Q. Weng, X.-B. Wang, X. Li, J. Zhang, D. Golberg, Y. Bando, Recent progress on fabrications and applications of boron nitride nanomaterials: a review, J. Mater. Sci. Technol. 31 (2015) 589–598, https://doi.org/10.1016/j.jmst.2014.12.008.
[7] M. Corso, W. Auwärter, M. Muntwiler, A. Tamai, T. Greber, J. Osterwalder, Boron nitride nanomesh, Science 303 (2004) 217–220, https://doi.org/10.1126/science.1091979.
[8] W. Auwärter, M. Muntwiler, J. Osterwalder, T. Greber, Defect lines and two-domain structure of hexagonal boron nitride films on Ni(111), Surf. Sci. 545 (2003) L735–L740, https://doi.org/10.1016/j.susc.2003.08.046.
[9] S. Joshi, D. Ecija, R. Koitz, M. Iannuzzi, A.P. Seitsonen, J. Hutter, H. Sachdev, S. Vijayaraghavan, F. Bischoff, K. Seufert, J.V. Barth, W. Auwärter, Boron nitride on Cu(111): an electronically corrugated monolayer, Nano Lett. 12 (2012) 5821–5828, https://doi.org/10.1021/nl303170m.
[10] A. Nagashima, N. Tejima, Y. Gamou, T. Kawai, C. Oshima, Electronic structure of monolayer hexagonal boron nitride physisorbed on metal surfaces, Phys. Rev. Lett. 75 (1995) 3918–3921, https://doi.org/10.1103/PhysRevLett.75.3918.
[11] S.D. Nehate, A.K. Saikumar, A. Prakash, K.B. Sundaram, A review of boron carbon nitride thin films and progress in nanomaterials, Mater, Today Adv. 8 (2020) 100106, https://doi.org/10.1016/j.mtadv.2020.100106.
[12] M. Jana, R.N. Singh, Progress in CVD synthesis of layered hexagonal boron nitride with tunable properties and their applications, Int. Mater. Rev. 63 (2018) 162–203, https://doi.org/10.1080/09506608.2017.1322833.
[13] M. Garnica, M. Schwarz, J. Ducke, Y. He, F. Bischoff, J.V. Barth, W. Auwärter, D. Stradi, Comparative study of the interfaces of graphene and hexagonal boron nitride with silver, Phys. Rev. B 94 (2016) 155431, https://doi.org/10.1103/PhysRevB.94.155431.
[14] M. Xu, T. Liang, M. Shi, H. Chen, Graphene-like two-dimensional materials, Chem. Rev. 113 (2013) 3766–3798, https://doi.org/10.1021/cr300263a.
[15] W. Auwärter, Hexagonal boron nitride monolayers on metal supports: versatile templates for atoms, molecules and nanostructures, Surf. Sci. Rep. 74 (2019) 1–95, https://doi.org/10.1016/j.surfrep.2018.10.001.
[16] S. Roy, X. Zhang, A.B. Puthirath, A. Meiyazhagan, S. Bhattacharyya, M. M. Rahman, G. Babu, S. Susarla, S.K. Saju, M.K. Tran, L.M. Sassi, M.A.S.R. Saadi, J. Lai, O. Sahin, S.M. Sajadi, B. Dharmarajan, D. Salpekar, N. Chakingal, A. Baburaj, X. Shuai, A. Adumbumkulath, K.A. Miller, J.M. Gayle, A. Ajnsztajn, T. Prasankumar, V.V.J. Harikrishnan, V. Ojha, H. Kannan, A.Z. Khater, Z. Zhu, S. A. Iyengar, P.A. da S. Autreto, E.F. Oliveira, G. Gao, A.G. Birdwell, M.R. Neupane, T.G. Ivanov, J. Taha-Tijerina, R.M. Yadav, S. Arepalli, R. Vajtai, P.M. Ajayan, Structure, properties and applications of two-dimensional hexagonal boron nitride, Adv. Mater. 33 (2021) 2101589, https://doi.org/10.1002/adma.202101589.
[17] A. Hemmi, A.P. Seitsonen, T. Greber, H. Cun, The winner takes it all: carbon supersedes hexagonal boron nitride with graphene on transition metals at high temperatures, Small 18 (2022) 1–9, https://doi.org/10.1002/smll.202205184.
[18] S.M. Sharker, Hexagonal boron nitrides (white graphene): a promising method for cancer drug delivery, Int. J. Nanomed. 14 (2019) 9983–9993, https://doi.org/10.2147/IJN.S205095.
[19] Z. Liu, T.B. Marder, B-N versus C-C: how similar are they? Angew. Chem. Int. Ed. 47 (2008) 242–244, https://doi.org/10.1002/anie.200703535.
[20] K. Küster, Z. Hooshmand, D.P. Rosenblatt, S. Koslowski, D. Le, U. Starke, T. S. Rahman, K. Kern, U. Schlickum, Growth of graphene nanoflakes/h -BN heterostructures, Adv. Mater. Interfac. 8 (2021) 2100766, https://doi.org/10.1002/admi.202100766.
[21] L. Lindsay, D.A. Broido, Enhanced thermal conductivity and isotope effect in single-layer hexagonal boron nitride, Phys. Rev. B 84 (2011) 155421, https://doi.org/10.1103/PhysRevB.84.155421.
[22] L. An, Y. Yu, Q. Cai, S. Mateti, L.H. Li, Y.I. Chen, Hexagonal boron nitride nanosheets: preparation, heat transport property and application as thermally conductive fillers, Prog. Mater. Sci. 138 (2023) 101154, https://doi.org/10.1016/j.pmatsci.2023.101154.
[23] A.P. Farkas, Á. Szitás, D. Jurdi, K. Palotás, J. Kiss, Z. Kónya, Selective transformation of ethanol to acetaldehyde catalyzed by Au/h-BN interface prepared on Rh(111) surface, Appl. Catal. Gen. 592 (2020) 117440, https://doi.org/10.1016/j.apcata.2020.117440.
[24] A. Pakdel, Y. Bando, D. Golberg, Nano boron nitride flatland, Chem. Soc. Rev. 43 (2014) 934–959, https://doi.org/10.1039/C3CS60260E.

[25] M. Yankowitz, J. Xue, B.J. LeRoy, Graphene on hexagonal boron nitride, J. Phys. Condens. Matter 26 (2014) 303201, https://doi.org/10.1088/0953-8984/26/30/303201.

[26] Y. Jiang, J. Mao, J. Duan, X. Lai, K. Watanabe, T. Taniguchi, E.Y. Andrei, Visualizing strain-induced pseudomagnetic fields in graphene through an hBN magnifying glass, Nano Lett. 17 (2017) 2839–2843, https://doi.org/10.1021/acs.nanolett.6b05228.

[27] Á. Szitás, A.P. Farkas, V. Faur, N. Bera, J. Kiss, Z. Kónya, Investigation of the adsorption properties of cyclic C6 molecules on h-BN/Rh(111) surface, efforts to cover the boron nitride nanomesh by graphene, Surface. Interfac. 32 (2022) 102034, https://doi.org/10.1016/j.surfin.2022.102034.

[28] S. Moon, J. Kim, J. Park, S. Im, J. Kim, I. Hwang, J.K. Kim, Hexagonal boron nitride for next-generation photonics and electronics, Adv. Mater. 35 (2023) 2204161, https://doi.org/10.1002/adma.202204161.

[29] C. Su, F. Zhang, S. Kahn, B. Shevitski, J. Jiang, C. Dai, A. Ungar, J.-H. Park, K. Watanabe, T. Taniguchi, J. Kong, Z. Tang, W. Zhang, F. Wang, M. Crommie, S. G. Louie, S. Aloni, A. Zettl, Tuning colour centres at a twisted hexagonal boron nitride interface, Nat. Mater. 21 (2022) 896–902, https://doi.org/10.1038/s41563-022-01303-4.

[30] C. Dai, D. Popple, C. Su, J.-H. Park, K. Watanabe, T. Taniguchi, J. Kong, A. Zettl, Evolution of nanopores in hexagonal boron nitride, Commun. Chem. 6 (2023) 108, https://doi.org/10.1038/s42004-023-00899-1.

[31] J. Dong, L. Gao, Q. Fu, Hexagonal boron nitride meeting metal: a new opportunity and territory in heterogeneous catalysis, J. Phys. Chem. Lett. 12 (2021) 9608–9619, https://doi.org/10.1021/acs.jpclett.1c02626.

[32] H. Chen, D. Jiang, Z. Yang, S. Dai, Engineering nanostructured interfaces of hexagonal boron nitride-based materials for enhanced catalysis, Acc. Chem. Res. 56 (2023) 52–65, https://doi.org/10.1021/acs.accounts.2c00564.

[33] M. Turner, V.B. Golovko, O.P.H. Vaughan, P. Abdulkin, A. Berenguer-Murcia, M. S. Tikhov, B.F.G. Johnson, R.M. Lambert, Selective oxidation with dioxygen by gold nanoparticle catalysts derived from 55-atom clusters, Nature 454 (2008) 981–983, https://doi.org/10.1038/nature07194.

[34] J.T. Grant, C.A. Carrero, F. Goeltl, J. Venegas, P. Mueller, S.P. Burt, S.E. Specht, W.P. McDermott, A. Chieregato, I. Hermans, Selective oxidative dehydrogenation of propane to propene using boron nitride catalysts, Science 354 (2016) 1570–1573, https://doi.org/10.1126/science.aaf7885.

[35] Z. Han, L. Wang, Y. Cao, S. Xu, J. Wu, X. Wang, P. He, H. Liu, H. Li, Highly dispersed Ru nanoclusters anchored on hexagonal boron nitride for efficient and stable hydrogenation of aromatic amines to alicyclic amines, Ind. Eng. Chem. Res. 62 (2023) 11504–11516, https://doi.org/10.1021/acs.iecr.3c00985.

[36] J.C.S. Wu, S.-J. Lin, Novel BN supported bi-metal catalyst for oxydehydrogenation of propane, Chem. Eng. J. 140 (2008) 391–397, https://doi.org/10.1016/j.cej.2007.11.009.

[37] Y. Cao, P. Maitarad, M. Gao, T. Taketsugu, H. Li, T. Yan, L. Shi, D. Zhang, Defect-induced efficient dry reforming of methane over two-dimensional Ni/h-boron nitride nanosheet catalysts, Appl. Catal. B Environ. 238 (2018) 51–60, https://doi.org/10.1016/j.apcatb.2018.07.001.

[38] Z. Zhang, J. Su, A.S. Matias, M. Gordon, Y.-S. Liu, J. Guo, C. Song, C. Dun, D. Prendergast, G.A. Somorjai, J.J. Urban, Enhanced and stabilized hydrogen production from methanol by ultrasmall Ni nanoclusters immobilized on defect-rich h-BN nanosheets, Proc. Natl. Acad. Sci. USA 117 (2020) 29442–29452, https://doi.org/10.1073/pnas.2015897117.

[39] M.S. Meera, S.K. Sasidharan, A. Hossain, J. Kiss, Z. Kónya, L. Elias, S.M.A. Shibli, Effect of excess B in Ni 2 P-coated boron nitride on the photocatalytic hydrogen evolution from water splitting, ACS Appl. Energy Mater. 5 (2022) 3578–3586, https://doi.org/10.1021/acsaem.1c04086.

[40] H. Liu, X. Zhang, Y. Li, X. Li, C. Dong, D. Wu, C. Tang, S. Chou, F. Fang, X. Du, Conductive boron nitride as promising catalyst support for the oxygen evolution reaction, Adv. Energy Mater. 10 (2020) 1902521, https://doi.org/10.1002/aenm.201902521.

[41] Y. Chen, J. Cai, P. Li, G. Zhao, G. Wang, Y. Jiang, J. Chen, S.X. Dou, H. Pan, W. Sun, Hexagonal boron nitride as a multifunctional support for engineering efficient electrocatalysts toward the oxygen reduction reaction, Nano Lett. 20 (2020) 6807–6814, https://doi.org/10.1021/acs.nanolett.0c02782.

[42] J. Pu, K. Zhang, Z. Wang, C. Li, K. Zhu, Y. Yao, G. Hong, Synthesis and modification of boron nitride nanomaterials for electrochemical energy storage: from theory to application, Adv. Funct. Mater. 31 (2021) 2106315, https://doi.org/10.1002/adfm.202106315.

[43] N. Goel, M. Kumar, Recent advances in ultrathin 2D hexagonal boron nitride based gas sensors, J. Mater. Chem. C 9 (2021) 1537–1549, https://doi.org/10.1039/D0TC05855F.

[44] H.P. Koch, R. Laskowski, P. Blaha, K. Schwarz, Adsorption of small gold clusters on the h-BN/Rh(111) nanomesh, Phys. Rev. B 86 (2012) 155404, https://doi.org/10.1103/PhysRevB.86.155404.

[45] Y. Zhang, Y. Zhang, D. Ma, Q. Ji, W. Fang, J. Shi, T. Gao, M. Liu, Y. Gao, Y. Chen, L. Xu, Z. Liu, Mn atomic layers under inert covers of graphene and hexagonal boron nitride prepared on Rh(111), Nano Res. 6 (2013) 887–896, https://doi.org/10.1007/s12274-013-0365-z.

[46] A.B. Preobrajenski, M.A. Nesterov, M.L. Ng, A.S. Vinogradov, N. Mårtensson, Monolayer h-BN on lattice-mismatched metal surfaces: on the formation of the nanomesh, Chem. Phys. Lett. 446 (2007) 119–123, https://doi.org/10.1016/j.cplett.2007.08.028.

[47] M.C. Patterson, B.F. Habenicht, R.L. Kurtz, L. Liu, Y. Xu, P.T. Sprunger, Formation and stability of dense arrays of Au nanoclusters on hexagonal boron nitride/Rh (111), Phys. Rev. B 89 (2014) 205423, https://doi.org/10.1103/PhysRevB.89.205423.

[48] R. Gubó, G. Vári, J. Kiss, A.P. Farkas, K. Palotás, L. Óvári, A. Berkó, Z. Kónya, Tailoring the hexagonal boron nitride nanomesh on Rh(111) with gold, Phys. Chem. Chem. Phys. 20 (2018) 15473–15485, https://doi.org/10.1039/C8CP00790J.

[49] L.H. de Lima, T. Greber, M. Muntwiler, The true corrugation of a h-BN nanomesh layer, 2D Mater. 7 (2020) 035006, https://doi.org/10.1088/2053-1583/ab81ae.

[50] L. Bignardi, P. Lacovig, R. Larciprete, D. Alfè, S. Lizzit, A. Baraldi, Exploring 2D materials at surfaces through synchrotron-based core-level photoelectron spectroscopy, Surf. Sci. Rep. 78 (2023) 100586, https://doi.org/10.1016/j.surfrep.2023.100586.

[51] J.D. Albar, V.V. Korolkov, M. Baldoni, K. Watanabe, T. Taniguchi, E. Besley, P. H. Beton, Adsorption of hexacontane on hexagonal boron nitride, J. Phys. Chem. C 122 (2018) 27575–27581, https://doi.org/10.1021/acs.jpcc.8b10167.

[52] A. Matković, J. Genser, D. Lüftner, M. Kratzer, R. Gajić, P. Puschnig, C. Teichert, Epitaxy of highly ordered organic semiconductor crystallite networks supported by hexagonal boron nitride, Sci. Rep. 6 (2016) 38519, https://doi.org/10.1038/srep38519.

[53] Y. Don Park, J.A. Lim, H.S. Lee, K. Cho, Interface engineering in organic transistors, Mater. Today 10 (2007) 46–54, https://doi.org/10.1016/S1369-7021(07)70019-6.

[54] W. Han, J. Wang, S. Liu, C. Ge, S. Cao, B. Song, J. Wang, X. Zhang, Spectral properties of spherical boron nitride prepared using carbon spheres as template, Ceram. Int. 43 (2017) 3569–3575, https://doi.org/10.1016/j.ceramint.2016.11.192.

[55] C. Tang, Y. Bando, C. Liu, S. Fan, J. Zhang, X. Ding, D. Golberg, Thermal conductivity of nanostructured boron nitride materials, J. Phys. Chem. B 110 (2006) 10354–10357, https://doi.org/10.1021/jp0607014.

[56] H. Strakov, G. Hackl, N. Popovska, H. Gerhard, Kinetics and film properties of boron nitride derived from trimethoxyborane/ammonia by chemical vapor deposition, Chem. Vap. Depos. 10 (2004) 325–330, https://doi.org/10.1002/cvde.200306311.

[57] J. Zhang, B. Tan, X. Zhang, F. Gao, Y. Hu, L. Wang, X. Duan, Z. Yang, P. Hu, Atomically thin hexagonal boron nitride and its heterostructures, Adv. Mater. 33 (2021) 2000769, https://doi.org/10.1002/adma.202000769.

[58] C. Tang, Y. Bando, Y. Huang, C. Zhi, D. Golberg, Synthetic routes and formation mechanisms of spherical boron nitride nanoparticles, Adv. Funct. Mater. 18 (2008) 3653–3661, https://doi.org/10.1002/adfm.200800493.

[59] A. Acharya, S. Sharma, X. Liu, D. Zhang, Y.K. Yap, A Review on van der Waals Boron Nitride Quantum Dots, C 7 (2021) 35, https://doi.org/10.3390/c7020035.

[60] S. Angizi, S.A.A. Alem, M. Hasanzadeh Azar, F. Shayeganfar, M.I. Manning, A. Hatamie, A. Pakdel, A. Simchi, A comprehensive review on planar boron nitride nanomaterials: from 2D nanosheets towards 0D quantum dots, Prog. Mater. Sci. 124 (2022) 100884, https://doi.org/10.1016/j.pmatsci.2021.100884.

[61] K.F. Huo, Z. Hu, F. Chen, J.J. Fu, Y. Chen, B.H. Liu, J. Ding, Z.L. Dong, T. White, Synthesis of boron nitride nanowires, Appl. Phys. Lett. 80 (2002) 3611–3613, https://doi.org/10.1063/1.1479213.

[62] F. Deepak, C. Vinod, K. Mukhopadhyay, A. Govindaraj, C.N. Rao, Boron nitride nanotubes and nanowires, Chem. Phys. Lett. 353 (2002) 345–352, https://doi.org/10.1016/S0009-2614(02)00007-6.

[63] R. Arenal, O. Stephan, J. Lou Cochon, A. Loiseau, Root-growth mechanism for single-walled boron nitride nanotubes in laser vaporization technique, J. Am. Chem. Soc. 129 (2007) 16183–16189, https://doi.org/10.1021/ja076135n.

[64] Y.Y.J. Chen, H.Z. Zhang, Y.Y.J. Chen, Pure boron nitride nanowires produced from boron triiodide, Nanotechnology 17 (2006) 786–789, https://doi.org/10.1088/0957-4484/17/3/028.

[65] B. McLean, G.B. Webber, A.J. Page, Boron nitride nanotube nucleation via network fusion during catalytic chemical vapor deposition, J. Am. Chem. Soc. 141 (2019) 13385–13393, https://doi.org/10.1021/jacs.9b03484.

[66] G. Wang, Y. Yan, X. Zhang, X. Gao, Z. Xie, Three-dimensional porous hexagonal boron nitride fibers as metal-free catalysts with enhanced catalytic activity for oxidative dehydrogenation of propane, Ind. Eng. Chem. Res. 60 (2021) 17949–17958, https://doi.org/10.1021/acs.iecr.1c04011.

[67] I. Szenti, T. Hegedűs, J. Kiss, Z. Kónya, Catalytic behavior of Pt nanoparticles on hexagonal boron-nitride fibers as a truly inert support in CO2 hydrogenation reaction, Eur. Conf. Surf. Sci., Lodz,poland (2023). https://ecoss36.eu/pdf/ECOSS36_ConferenceAbstractBook.pdf.

[68] C. Wu, B. Wang, N. Wu, C. Han, X. Zhang, Y. Wang, In situ molten phase-assisted self-healing for maintaining fiber morphology during conversion from melamine diborate to boron nitride, RSC Adv. 10 (2020) 11105–11110, https://doi.org/10.1039/C9RA10292B.

[69] C.W. Chang, W.-Q. Han, A. Zettl, Thermal conductivity of B-C-N and BN nanotubes, J. Vac. Sci. Technol. B Microelectron. Nanom. Struct. 23 (2005) 1883, https://doi.org/10.1116/1.2008266.

[70] S.Y. Kim, J. Park, H.C. Choi, J.P. Ahn, J.Q. Hou, H.S. Kang, X-Ray photoelectron spectroscopy and first principles calculation of BCN nanotubes, J. Am. Chem. Soc. 129 (2007) 1705–1716, https://doi.org/10.1021/ja067592r.

[71] S.H. Lim, J. Luo, W. Ji, J. Lin, Synthesis of boron nitride nanotubes and its hydrogen uptake, Catal. Today 120 (2007) 346–350, https://doi.org/10.1016/j.cattod.2006.09.016.

[72] J. Yu, Y. Chen, B.M. Cheng, Dispersion of boron nitride nanotubes in aqueous solution with the help of ionic surfactants, Solid State Commun. 149 (2009) 763–766, https://doi.org/10.1016/j.ssc.2009.03.001.

[73] Y. Chen, J. Fitz Gerald, J.S. Williams, S. Bulcock, Synthesis of boron nitride nanotubes at low temperatures using reactive ball milling, Chem. Phys. Lett. 299 (1999) 260–264, https://doi.org/10.1016/S0009-2614(98)01252-4.

[74] R.S. Jones, S. Gonzalez-Munoz, I. Griffiths, P. Holdway, K. Evers, S. Luanwuthi, B. M. Maciejewska, O. Kolosov, N. Grobert, Thermal conductivity of carbon/boron nitride heteronanotube and boron nitride nanotube buckypapers: implications for thermal management composites, ACS Appl. Nano Mater. 6 (2023) 15374–15384, https://doi.org/10.1021/acsanm.3c01147.
[75] H. Sohrabi, O. Arbabzadeh, M. Falaki, V. Vatanpour, M.R. Majidi, N. Kudaibergenov, S.W. Joo, A. Khataee, Advances in fabrication, physio-chemical properties, and sensing applications of non-metal boron nitride and boron carbon nitride-based nanomaterials, Surface. Interfac. 41 (2023) 103152, https://doi.org/10.1016/j.surfin.2023.103152.
[76] R.Y. Tay, H. Li, H. Wang, J. Lin, Z.K. Ng, R. Shivakumar, A. Bolker, M. Shakerzadeh, S.H. Tsang, E.H.T. Teo, Advanced nano boron nitride architectures: synthesis, properties and emerging applications, Nano Today 53 (2023) 102011, https://doi.org/10.1016/j.nantod.2023.102011.
[77] N. Herrera-Reinoza, A.C. dos Santos, L.H. de Lima, R. Landers, A. de Siervo, Atomically precise bottom-up synthesis of h-BNC: graphene doped with h-BN nanoclusters, Chem. Mater. 33 (2021) 2871–2882, https://doi.org/10.1021/acs.chemmater.1c00081.
[78] B. Hwang, J. Kwon, M. Lee, S.J. Lim, S. Jeon, S. Kim, U. Ham, Y.J. Song, Y. Kuk, Electron-beam assisted growth of hexagonal boron-nitride layer, Curr. Appl. Phys. 13 (2013) 1365–1369, https://doi.org/10.1016/j.cap.2013.04.018.
[79] G. Dong, E.B. Fourré, F.C. Tabak, J.W.M. Frenken, How boron nitride forms a regular nanomesh on Rh(111), Phys. Rev. Lett. 104 (2010) 096102, https://doi.org/10.1103/PhysRevLett.104.096102.
[80] E.M. Freiberger, F. Düll, P. Bachmann, J. Steinhauer, F.J. Williams, H.-P. Steinrück, C. Papp, h -BN in the making: the surface chemistry of borazine on Rh(111), J. Chem. Phys. 160 (2024) 154706, https://doi.org/10.1063/5.0202431.
[81] A.P. Farkas, P. Török, F. Solymosi, J. Kiss, Z. Kónya, Investigation of the adsorption properties of borazine and characterisation of boron nitride on Rh(1 1 1) by electron spectroscopic methods, Appl. Surf. Sci. 354 (2015) 367–372, https://doi.org/10.1016/j.apsusc.2015.05.060.
[82] T. Weiss, A. Baklanov, G.S. Michelitsch, K. Reuter, M. Schwarz, M. Garnica, W. Auwärter, Adsorption, single-molecule manipulation, and self-assembly of borazine on Ag(111), Adv. Mater. Interfac. 11 (2024), https://doi.org/10.1002/admi.202300774.
[83] W. Auwärter, H.U. Suter, H. Sachdev, T. Greber, Synthesis of one monolayer of hexagonal boron nitride on Ni(111) from B-trichloroborazine (ClBNH) 3, Chem. Mater. 16 (2004) 343–345, https://doi.org/10.1021/cm034805s.
[84] F. Müller, K. Stöwe, H. Sachdev, Symmetry versus commensurability: epitaxial growth of hexagonal boron nitride on Pt(111) from B-trichloroborazine (ClBNH) 3, Chem. Mater. 17 (2005) 3464–3467, https://doi.org/10.1021/cm048629e.
[85] R.M. Desrosiers, D.W. Greve, A.J. Gellman, Nucleation of boron nitride thin films on Ni(100), Surf. Sci. 382 (1997) 35–48, https://doi.org/10.1016/S0039-6028(97)00092-7.
[86] J. Kiss, K. Révész, G. Klivényi, F. Solymosi, Preparation of a boron nitride single layer on a polycrystalline Rh surface, Appl. Surf. Sci. 264 (2013) 838–844, https://doi.org/10.1016/j.apsusc.2012.10.157.
[87] J.-W. He, D.W. Goodman, Interaction of borazine with a Re(0001) surface, studied by LEED, TDS, AES and ELS, Surf. Sci. 232 (1990) 138–148, https://doi.org/10.1016/0039-6028(90)90594-X.
[88] M.T. Paffett, R.J. Simonson, P. Papin, R.T. Paine, Borazine adsorption and decomposition at Pt(111) and Ru(001) surfaces, Surf. Sci. 232 (1990) 286–296, https://doi.org/10.1016/0039-6028(90)90121-N.
[89] R.J. Simonson, M.T. Paffett, M.E. Jones, B.E. Koel, A vibrational study of borazine adsorbed on Pt(111) and Au(111) surfaces, Surf. Sci. 254 (1991) 29–44, https://doi.org/10.1016/0039-6028(91)90635-6.
[90] A.P. Seitsonen, T. Greber, Growing sp 2 materials on transition metals: calculated atomic adsorption energies of hydrogen, boron, carbon, nitrogen, and oxygen atoms, C 2 and BN dimers, C 6 and (BN) 3 hexamers, graphene and h-BN with and without atomic vacancies, Nanoscale Adv. 6 (2024) 268–275, https://doi.org/10.1039/D3NA00472D.
[91] G.E. Wood, Z.P.L. Laker, A.J. Marsden, G.R. Bell, N.R. Wilson, In situ gas analysis during the growth of hexagonal boron nitride from ammonia borane, Mater. Res. Express 4 (2017) 115905, https://doi.org/10.1088/2053-1591/aa9a7f.
[92] V. Babenko, G. Lane, A.A. Koos, A.T. Murdock, K. So, J. Britton, S.S. Meysami, J. Moffat, N. Grobert, Time dependent decomposition of ammonia borane for the controlled production of 2D hexagonal boron nitride, Sci. Rep. 7 (2017) 14297, https://doi.org/10.1038/s41598-017-14663-8.
[93] F. Müller, S. Hüfner, H. Sachdev, S. Gsell, M. Schreck, Epitaxial growth of hexagonal boron nitride monolayers by a three-step boration-oxidation-nitration process, Phys. Rev. B 82 (2010) 075405, https://doi.org/10.1103/PhysRevB.82.075405.
[94] A. Tillekaratne, M. Trenary, Adsorption and dehydrogenation of decaborane on the Pt(111) surface, J. Phys. Chem. C 113 (2009) 13847–13854, https://doi.org/10.1021/jp903624g.
[95] C.W. Hamilton, R.T. Baker, A. Staubitz, I. Manners, B–N compounds for chemical hydrogenstorage, Chem. Soc. Rev. 38 (2009) 279–293, https://doi.org/10.1039/B800312M.
[96] W. Li, L. Jiang, W. Jiang, Y. Wu, X. Guo, Z. Li, H. Yuan, M. Luo, Recent advances of boron nitride nanosheets in hydrogen storage application, J. Mater. Res. Technol. 26 (2023) 2028–2042, https://doi.org/10.1016/j.jmrt.2023.08.035.
[97] P.M. Revabhai, R.K. Singhal, H. Basu, S.K. Kailasa, Progress on boron nitride nanostructure materials: properties, synthesis and applications in hydrogen storage and analytical chemistry, J. Nanostructure Chem. 13 (2023) 1–41, https://doi.org/10.1007/s40097-022-00490-5.
[98] S. Guan, Y. Liu, H. Zhang, R. Shen, H. Wen, N. Kang, J. Zhou, B. Liu, Y. Fan, J. Jiang, B. Li, Recent advances and perspectives on supported catalysts for heterogeneous hydrogen production from ammonia borane, Adv. Sci. 10 (2023) 1–49, https://doi.org/10.1002/advs.202300726.
[99] A. Ruckhofer, M. Sacchi, A. Payne, A.P. Jardine, W.E. Ernst, N. Avidor, A. Tamtögl, Evolution of ordered nanoporous phases during h-BN growth: controlling the route from gas-phase precursor to 2D material by in situ monitoring, Nanoscale Horizons 7 (2022) 1388–1396, https://doi.org/10.1039/D2NH00353H.
[100] A. Nagashima, N. Tejima, Y. Gamou, T. Kawai, C. Oshima, Electronic states of monolayer hexagonal boron nitride formed on the metal surfaces, Surf. Sci. 357–358 (1996) 307–311, https://doi.org/10.1016/0039-6028(96)00134-3.
[101] L. Haug, J.P. Roth, M. Thaler, D. Steiner, A. Menzel, S. Tosoni, G. Pacchioni, E. Bertel, Precursor chemistry of h-BN: adsorption, desorption, and decomposition of borazine on Pt(110), Phys. Chem. Chem. Phys. 22 (2020) 11704–11712, https://doi.org/10.1039/D0CP00112K.
[102] D. Steiner, F. Mittendorfer, E. Bertel, Quasiliquid layer promotes hexagonal boron nitride (h-BN) single-domain growth: h-BN on Pt(110), ACS Nano 13 (2019) 7083–7090, https://doi.org/10.1021/acsnano.9b02377.
[103] M. Thaler, D. Steiner, A. Menzel, F. Mittendorfer, E. Bertel, Single-domain h-BN on Pt(110): electronic structure, correlation, and bonding, Phys. Rev. Res. 2 (2020) 043156, https://doi.org/10.1103/PhysRevResearch.2.043156.
[104] D. Steiner, M. Thaler, T. Mairegger, F. Mittendorfer, E. Bertel, Nonclassical nucleation of hexagonal boron nitride enables independent control of nucleation and growth rate, J. Phys. Chem. C 127 (2023) 11559–11569, https://doi.org/10.1021/acs.jpcc.3c00206.
[105] Y.-R. Lin, M. Franke, S. Parhizkar, M. Raths, V. Wen-zhe Yu, T.-L. Lee, S. Soubatch, V. Blum, F.S. Tautz, C. Kumpf, F.C. Bocquet, Boron nitride on SiC (0001), Phys. Rev. Mater. 6 (2022) 064002, https://doi.org/10.1103/PhysRevMaterials.6.064002.
[106] A. Staubitz, A.P.M. Robertson, I. Manners, Ammonia-borane and related compounds as dihydrogen sources, Chem. Rev. 110 (2010) 4079–4124, https://doi.org/10.1021/cr100088b.
[107] P. Bachmann, F. Düll, F. Späth, U. Bauer, H.-P. Steinrück, C. Papp, A HR-XPS study of the formation of h-BN on Ni(111) from the two precursors, ammonia borane and borazine, J. Chem. Phys. 149 (2018) 164709, https://doi.org/10.1063/1.5051595.
[108] P. Arias, A. Ebnonnasir, C.V. Ciobanu, S. Kodambaka, Growth kinetics of two-dimensional hexagonal boron nitride layers on Pd(111), Nano Lett. 20 (2020) 2886–2891, https://doi.org/10.1021/acs.nanolett.0c00704.
[109] K. Park, G.H. Kim, S. Jeong, Atomistic processes of boron and nitrogen near the Pt (111) surface, Appl. Surf. Sci. 537 (2021) 147901, https://doi.org/10.1016/j.apsusc.2020.147901.
[110] K. Yeo, S. Jeong, Machine learning insight into h-BN growth on Pt(111) from atomic states, Appl. Surf. Sci. 621 (2023) 156893, https://doi.org/10.1016/j.apsusc.2023.156893.
[111] M.S. Islam, A.A.M. Mazumder, M.U. Sohag, M.M.H. Sarkar, C. Stampfl, J. Park, Growth mechanisms of monolayer hexagonal boron nitride (h-BN) on metal surfaces: theoretical perspectives, Nanoscale Adv. (2023) 1043–1059, https://doi.org/10.1039/D3NA00382E.
[112] K. Yeo, K. Park, S. Jeong, Neural network approach to diffusion of B and N adatoms on the Pt(111) surface, Curr. Appl. Phys. 39 (2022) 62–69, https://doi.org/10.1016/j.cap.2022.03.018.
[113] L.-P. Ding, Y.J. Guo, J.H. Zeng, Z.A. Guo, Y.-R. Zhao, P. Shao, Nucleation mechanism of h-BN on the Au(111) surface, J. Phys. Chem. C 128 (2024) 234–241, https://doi.org/10.1021/acs.jpcc.3c06641.
[114] S. Liu, A.C.T. van Duin, D.M. van Duin, B. Liu, J.H. Edgar, Atomistic insights into nucleation and Formation of hexagonal boron nitride on nickel from first-principles-based reactive molecular dynamics simulations, ACS Nano 11 (2017) 3585–3596, https://doi.org/10.1021/acsnano.6b06736.
[115] S. Liu, J. Comer, A.C.T. van Duin, D.M. van Duin, B. Liu, J.H. Edgar, Predicting the preferred morphology of hexagonal boron nitride domain structure on nickel from ReaxFF-based molecular dynamics simulations, Nanoscale 11 (2019) 5607–5616, https://doi.org/10.1039/C8NR10291K.
[116] K.Y. Ma, L. Zhang, S. Jin, Y. Wang, S.I. Yoon, H. Hwang, J. Oh, D.S. Jeong, M. Wang, S. Chatterjee, G. Kim, A.-R. Jang, J. Yang, S. Ryu, H.Y. Jeong, R. S. Ruoff, M. Chhowalla, F. Ding, H.S. Shin, Epitaxial single-crystal hexagonal boron nitride multilayers on Ni (111), Nature 606 (2022) 88–93, https://doi.org/10.1038/s41586-022-04745-7.
[117] H. Cun, Z. Miao, A. Hemmi, Y. Al-Hamdani, M. Iannuzzi, J. Osterwalder, M. S. Altman, T. Greber, High-quality hexagonal boron nitride from 2D distillation, ACS Nano 15 (2021) 1351–1357, https://doi.org/10.1021/acsnano.0c08616.
[118] Z. Wang, M.J. Meziani, A.K. Patel, P. Priego, K. Wirth, P. Wang, Y.-P. Sun, Boron nitride nanosheets from different preparations and correlations with their material properties, Ind. Eng. Chem. Res. 58 (2019) 18644–18653, https://doi.org/10.1021/acs.iecr.9b03930.
[119] C. Martínez-Jiménez, A. Chow, A.D. Smith McWilliams, A.A. Martí, Hexagonal boron nitride exfoliation and dispersion, Nanoscale 15 (2023) 16836–16873, https://doi.org/10.1039/D3NR03941B.
[120] A.E. Naclerio, P.R. Kidambi, A review of scalable hexagonal boron nitride (h -BN) synthesis for present and future applications, Adv. Mater. 35 (2023) 2207374, https://doi.org/10.1002/adma.202207374.
[121] Y. Hattori, T. Taniguchi, K. Watanabe, M. Kitamura, Antireflection substrates for determining the number of layers of few-layer hexagonal boron nitride films and for visualizing organic monolayers, ACS Appl. Nano Mater. (2023), https://doi.org/10.1021/acsanm.3c04075.

[122] V.L. Solozhenko, A.G. Lazarenko, J.-P. Petitet, A.V. Kanaev, Bandgap energy of graphite-like hexagonal boron nitride, J. Phys. Chem. Solid. 62 (2001) 1331–1334, https://doi.org/10.1016/S0022-3697(01)00030-0.
[123] L. Britnell, R.V. Gorbachev, R. Jalil, B.D. Belle, F. Schedin, A. Mishchenko, T. Georgiou, M.I. Katsnelson, L. Eaves, S.V. Morozov, N.M.R. Peres, J. Leist, A. K. Geim, K.S. Novoselov, L.A. Ponomarenko, Field-effect tunneling transistor based on vertical graphene heterostructures, Science 335 (2012) 947–950, https://doi.org/10.1126/science.1218461.
[124] E.Y. Andrei, D.K. Efetov, P. Jarillo-Herrero, A.H. MacDonald, K.F. Mak, T. Senthil, E. Tutuc, A. Yazdani, A.F. Young, The marvels of moiré materials, Nat. Rev. Mater. 6 (2021) 201–206, https://doi.org/10.1038/s41578-021-00284-1.
[125] Z. Jin, Z. Ji, Y. Zhong, Y. Jin, X. Hu, X. Zhang, L. Zhu, X. Huang, T. Li, X. Cai, L. Zhou, Controlled Synthesis of a Two-Dimensional Non-van der Waals Ferromagnet toward a Magnetic Moirè Superlattice, ACS Nano 16 (2022) 7572–7579, https://doi.org/10.1021/acsnano.1c11018.
[126] W. Auwärter, T.J. Kreutz, T. Greber, J. Osterwalder, XPD and STM investigation of hexagonal boron nitride on Ni(111), Surf. Sci. 429 (1999) 229–236, https://doi.org/10.1016/S0039-6028(99)00381-7.
[127] A.B. Preobrajenski, A.S. Vinogradov, M.L. Ng, E. Ćavar, R. Westerström, A. Mikkelsen, E. Lundgren, N. Mårtensson, Influence of chemical interaction at the lattice-mismatched h−BN/Rh(111) and h-BN/Pt(111) interfaces on the overlayer morphology, Phys. Rev. B 75 (2007) 245412, https://doi.org/10.1103/PhysRevB.75.245412.
[128] A.J. Martínez-Galera, J.M. Gómez-Rodríguez, Influence of metal support in-plane symmetry on the corrugation of hexagonal boron nitride and graphene monolayers, Nano Res. 11 (2018) 4643–4653, https://doi.org/10.1007/s12274-018-2045-5.
[129] M. Corso, T. Greber, J. Osterwalder, h-BN on Pd(110): a tunable system for self-assembled nanostructures? Surf. Sci. 577 (2005) L78–L84, https://doi.org/10.1016/j.susc.2005.01.015.
[130] F. Schulz, R. Drost, S.K. Hämäläinen, T. Demonchaux, A.P. Seitsonen, P. Liljeroth, Epitaxial hexagonal boron nitride on Ir(111): a work function template, Phys. Rev. B 89 (2014) 235429, https://doi.org/10.1103/PhysRevB.89.235429.
[131] M. Will, N. Atodiresei, V. Caciuc, P. Valerius, C. Herbig, T. Michely, A monolayer of hexagonal boron nitride on Ir(111) as a template for cluster superlattices, ACS Nano 12 (2018) 6871–6880, https://doi.org/10.1021/acsnano.8b02127.
[132] Q. Chen, Y. Chen, M. Ju, X. Shi, P. Wang, H. Chen, H. Yuan, Sm cluster on hexagonal boron nitride supported by Ir(111): formation of magnetic cluster superlattice Sm13@h-BN|Ir(111), Appl. Surf. Sci. 604 (2022) 154478, https://doi.org/10.1016/j.apsusc.2022.154478.
[133] M. Liu, Y. Li, P. Chen, J. Sun, D. Ma, Q. Li, T. Gao, Y. Gao, Z. Cheng, X. Qiu, Y. Fang, Y. Zhang, Z. Liu, Quasi-freestanding monolayer heterostructure of graphene and hexagonal boron nitride on Ir(111) with a zigzag boundary, Nano Lett. 14 (2014) 6342–6347, https://doi.org/10.1021/nl502780u.
[134] F.H. Farwick zum Hagen, D.M. Zimmermann, C.C. Silva, C. Schlueter, N. Atodiresei, W. Jolie, A.J. Martínez-Galera, D. Dombrowski, U.A. Schröder, M. Will, P. Lazić, V. Caciuc, S. Blügel, T.-L. Lee, T. Michely, C. Busse, Structure and growth of hexagonal boron nitride on Ir(111), ACS Nano 10 (2016) 11012–11026, https://doi.org/10.1021/acsnano.6b05819.
[135] F. Donati, S. Rusponi, S. Stepanow, C. Wäckerlin, A. Singha, L. Persichetti, R. Baltic, K. Diller, F. Patthey, E. Fernandes, J. Dreiser, Ž. Šljivančanin, K. Kummer, C. Nistor, P. Gambardella, H. Brune, Magnetic remanence in single atoms, Science 352 (2016) 318–321, https://doi.org/10.1126/science.aad9898.
[136] C. Papp, From flat surfaces to nanoparticles: in situ studies of the reactivity of model catalysts, Catal. Lett. 147 (2017) 2–19, https://doi.org/10.1007/s10562-016-1925-0.
[137] J. Kiss, Á. Kukovecz, Z. Kónya, Beyond nanoparticles: the role of sub-nanosized metal species in heterogeneous catalysis, Catal. Lett. 149 (2019) 1441–1454, https://doi.org/10.1007/s10562-019-02734-6.
[138] A.A. Khajetoorians, J. Wiebe, B. Chilian, R. Wiesendanger, Realizing all-spin–based logic operations atom by atom, Science 332 (2011) 1062–1064, https://doi.org/10.1126/science.1201725.
[139] M. Thomas, B. Jason, S. Affan, B. Alexander, H. Tobias, F. Jeison, Growth of aligned and twisted hexagonal boron nitride on Ir(110). https://doi.org/10.48550/arXiv.2308.06074, 2023.
[140] D.S. Kim, R.C. Dominguez, R. Mayorga-Luna, D. Ye, J. Embley, T. Tan, Y. Ni, Z. Liu, M. Ford, F.Y. Gao, S. Arash, K. Watanabe, T. Taniguchi, S. Kim, C.-K. Shih, K. Lai, W. Yao, L. Yang, X. Li, Y. Miyahara, Electrostatic moiré potential from twisted hexagonal boron nitride layers, Nat. Mater. (2023), https://doi.org/10.1038/s41563-023-01637-7.
[141] A. Goriachko, He, M. Knapp, H. Over, M. Corso, T. Brugger, S. Berner, J. Osterwalder, T. Greber, Self-assembly of a hexagonal boron nitride nanomesh on Ru(0001), Langmuir 23 (2007) 2928–2931, https://doi.org/10.1021/la062990t.
[142] J. Lu, P.S.E. Yeo, Y. Zheng, H. Xu, C.K. Gan, M.B. Sullivan, A.H. Castro Neto, K. P. Loh, Step flow versus mosaic film growth in hexagonal boron nitride, J. Am. Chem. Soc. 135 (2013) 2368–2373, https://doi.org/10.1021/ja3117735.
[143] Y. Yang, Q. Fu, M. Wei, H. Bluhm, X. Bao, Stability of BN/metal interfaces in gaseous atmosphere, Nano Res. 8 (2015) 227–237, https://doi.org/10.1007/s12274-014-0639-0.
[144] Y. Qi, Z. Zhang, B. Deng, X. Zhou, Q. Li, M. Hong, Y. Li, Z. Liu, Y. Zhang, Irreparable defects produced by the patching of h -BN frontiers on strongly interacting Re(0001) and their electronic properties, J. Am. Chem. Soc. 139 (2017) 5849–5856, https://doi.org/10.1021/jacs.7b00647.
[145] N.A. Vinogradov, A.A. Zakharov, M.L. Ng, A. Mikkelsen, E. Lundgren, N. Mårtensson, A.B. Preobrajenski, One-dimensional corrugation of the h -BN monolayer on Fe(110), Langmuir 28 (2012) 1775–1781, https://doi.org/10.1021/la2035642.
[146] X. Gao, S. Wang, S. Lin, Defective hexagonal boron nitride nanosheet on Ni(111) and Cu(111): stability, electronic structures, and potential applications, ACS Appl. Mater. Interfaces 8 (2016) 24238–24247, https://doi.org/10.1021/acsami.6b08097.
[147] L. Fernandez, A.A. Makarova, C. Laubschat, D.V. Vyalikh, D.Y. Usachov, J. E. Ortega, F. Schiller, Boron nitride monolayer growth on vicinal Ni(111) surfaces systematically studied with a curved crystal, 2D Mater. 6 (2019) 025013, https://doi.org/10.1088/2053-1583/ab01e7.
[148] A.B. Preobrajenski, A.S. Vinogradov, N. Mårtensson, Ni 3d–BN π hybridization at the h−BN/Ni(111) interface observed with core-level spectroscopies, Phys. Rev. B 70 (2004) 165404, https://doi.org/10.1103/PhysRevB.70.165404.
[149] K. Ali, L. Fernández, M.A. Kherelden, A.A. Makarova, I. Píš, F. Bondino, J. Lawrence, D.G. de Oteyza, D.Y. Usachov, D.V. Vyalikh, F.J. García de Abajo, Z. M.A. El-Fattah, J.E. Ortega, F. Schiller, Atomically-precise texturing of hexagonal boron nitride nanostripes, Adv. Sci. 8 (2021) 2101455, https://doi.org/10.1002/advs.202101455.
[150] H. Chen, H. Liu, Z. Zhang, K. Hu, X. Fang, Nanostructured photodetectors: from ultraviolet to terahertz, Adv. Mater. 28 (2016) 403–433, https://doi.org/10.1002/adma.201503534.
[151] R. Stania, W. Heckel, I. Kalichava, C. Bernard, T.C. Kerscher, H.Y. Cun, P. R. Willmott, B. Schönfeld, J. Osterwalder, S. Müller, T. Greber, Self-assembly of nanoscale lateral segregation profiles, Phys. Rev. B 93 (2016) 161402, https://doi.org/10.1103/PhysRevB.93.161402.
[152] G. Halasi, C. Vass, K.M. Yu, G. Vári, A.P. Farkas, K. Palotás, A. Berkó, J. Kiss, Z. Kónya, M. Aeschlimann, B. Stadtmüller, P. Dombi, L. Óvári, Enhancing the dipole ring of hexagonal boron nitride nanomesh by surface alloying, Npj 2D Mater. Appl. (2024). Completed accept, reference number: [NPJ2DMATERIALS-01764R].
[153] J. Gómez Díaz, Y. Ding, R. Koitz, A.P. Seitsonen, M. Iannuzzi, J. Hutter, Hexagonal boron nitride on transition metal surfaces, Theor. Chem. Acc. 132 (2013) 1350, https://doi.org/10.1007/s00214-013-1350-z.
[154] J. Klimeš, D.R. Bowler, A. Michaelides, Chemical accuracy for the van der Waals density functional, J. Phys. Condens. Matter 22 (2010) 022201, https://doi.org/10.1088/0953-8984/22/2/022201.
[155] J. Klimeš, D.R. Bowler, A. Michaelides, Van der Waals density functionals applied to solids, Phys. Rev. B 83 (2011) 195131, https://doi.org/10.1103/PhysRevB.83.195131.
[156] F. Schulz, P. Liljeroth, A.P. Seitsonen, Benchmarking van der Waals-treated DFT: The case of hexagonal boron nitride and graphene on Ir(111), Phys. Rev. Mater. 3 (2019) 084001, https://doi.org/10.1103/PhysRevMaterials.3.084001.
[157] W.C. McKee, V. Meunier, Y. Xu, Reconciling the electronic and geometric corrugations of the hexagonal boron nitride and graphene nanomeshes, Surf. Sci. 642 (2015) L16–L19, https://doi.org/10.1016/j.susc.2015.06.014.
[158] G. Vári, C. Vass, G. Halasi, L. Szabó, K. Palotás, P. Dombi, A. Berkó, L. Óvári, Z. Kónya, New insights into thermal processes of metal deposits on h-BN/Rh(1 1 1): a comparison of Au and Rh, Appl. Surf. Sci. 623 (2023) 157041, https://doi.org/10.1016/j.apsusc.2023.157041.
[159] Q. Zhang, J. Yu, P. Ebert, C. Zhang, C.-R. Pan, M.-Y. Chou, C.-K. Shih, C. Zeng, S. Yuan, Tuning band gap and work function modulations in monolayer hBN/Cu (111) heterostructures with moirè patterns, ACS Nano 12 (2018) 9355–9362, https://doi.org/10.1021/acsnano.8b04444.
[160] M. Hengsberger, D. Leuenberger, A. Schuler, S. Roth, M. Muntwiler, Dynamics of excited interlayer states in hexagonal boron nitride monolayers, J. Phys. D Appl. Phys. 53 (2020) 203001, https://doi.org/10.1088/1361-6463/ab70c6.
[161] E.S. Penev, N. Marzari, B.I. Yakobson, Theoretical prediction of two-dimensional materials, behavior, and properties, ACS Nano 15 (2021) 5959–5976, https://doi.org/10.1021/acsnano.0c10504.
[162] H.J. Kulik, T. Hammerschmidt, J. Schmidt, S. Botti, M.A.L. Marques, M. Boley, M. Scheffler, M. Todorović, P. Rinke, C. Oses, A. Smolyanyuk, S. Curtarolo, A. Tkatchenko, A.P. Bartók, S. Manzhos, M. Ihara, T. Carrington, J. Behler, O. Isayev, M. Veit, A. Grisafi, J. Nigam, M. Ceriotti, K.T. Schütt, J. Westermayr, M. Gastegger, R.J. Maurer, B. Kalita, K. Burke, R. Nagai, R. Akashi, O. Sugino, J. Hermann, F. Noé, S. Pilati, C. Draxl, M. Kuban, S. Rigamonti, M. Scheidgen, M. Esters, D. Hicks, C. Toher, P.V. Balachandran, I. Tamblyn, S. Whitelam, C. Bellinger, L.M. Ghiringhelli, Roadmap on Machine learning in electronic structure, Electron, Structures 4 (2022) 023004, https://doi.org/10.1088/2516-1075/ac572f.
[163] F.D. Natterer, F. Patthey, H. Brune, Distinction of nuclear spin states with the scanning tunneling microscope, Phys. Rev. Lett. 111 (2013) 175303, https://doi.org/10.1103/PhysRevLett.111.175303.
[164] F.D. Natterer, F. Patthey, H. Brune, Resonant-enhanced spectroscopy of molecular rotations with a scanning tunneling microscope, ACS Nano 8 (2014) 7099–7105, https://doi.org/10.1021/nn501999k.
[165] M. Wei, Q. Fu, H. Wu, A. Dong, X. Bao, Hydrogen intercalation of graphene and boron nitride monolayers grown on Pt(111), Top. Catal. 59 (2016) 543–549, https://doi.org/10.1007/s11244-015-0516-4.
[166] F. Späth, J. Gebhardt, F. Düll, U. Bauer, P. Bachmann, C. Gleichweit, A. Görling, H.-P. Steinrück, C. Papp, Hydrogenation and hydrogen intercalation of hexagonal boron nitride on Ni(111): reactivity and electronic structure, 2D Mater. 4 (2017) 035026, https://doi.org/10.1088/2053-1583/aa7d6b.
[167] E. Marie Freiberger, F. Späth, U. Bauer, F. Düll, P. Bachmann, J. Steinhauer, F. Hemauer, N.J. Waleska, V. Schwaab, H. Steinrück, C. Papp, Selective oxygen and hydrogen functionalization of the h -BN/Rh(111) nanomesh, Chem. Eur J. 27 (2021) 13172–13180, https://doi.org/10.1002/chem.202101946.

[168] F. Späth, H.R. Soni, J. Steinhauer, F. Düll, U. Bauer, P. Bachmann, W. Hieringer, A. Görling, H. Steinrück, C. Papp, Oxygen functionalization of hexagonal boron nitride on Ni(111), Chem. Eur J. 25 (2019), https://doi.org/10.1002/chem.201901504 chem.201901504.
[169] F. Späth, J. Steinhauer, F. Düll, U. Bauer, P. Bachmann, H.-P. Steinrück, C. Papp, Reaction of hydrogen and oxygen on h -BN, J. Phys. Chem. C 124 (2020) 18141–18146, https://doi.org/10.1021/acs.jpcc.0c05299.
[170] H. Ma, T. Brugger, S. Berner, Y. Ding, M. Iannuzzi, J. Hutter, J. Osterwalder, T. Greber, Nano-ice on boron nitride nanomesh: accessing proton disorder, ChemPhysChem 11 (2010) 399–403, https://doi.org/10.1002/cphc.200900857.
[171] Y. Ding, M. Iannuzzi, J. Hutter, Nano-ice models for the water aggregates observed on the h-BN/Rh(111) nanomesh, J. Phys. Condens. Matter 24 (2012) 445002, https://doi.org/10.1088/0953-8984/24/44/445002.
[172] E.M. Freiberger, J. Steffen, N.J. Waleska-Wellnhofer, F. Hemauer, V. Schwaab, A. Görling, H.-P. Steinrück, C. Papp, Bromination of 2D materials, Nanotechnology 35 (2024) 145703, https://doi.org/10.1088/1361-6528/ad1201.
[173] W.C. McKee, M.C. Patterson, D. Huang, J.R. Frick, R.L. Kurtz, P.T. Sprunger, L. Liu, Y. Xu, CO adsorption on Au nanoparticles grown on hexagonal boron nitride/Rh(111), J. Phys. Chem. C 120 (2016) 10909–10918, https://doi.org/10.1021/acs.jpcc.6b01645.
[174] A.P. Farkas, Á. Szitás, G. Vári, R. Gubó, L. Óvári, A. Berkó, J. Kiss, Z. Kónya, Effect of gold on the adsorption properties of acetaldehyde on clean and h-BN covered Rh(111) surface, Top. Catal. 61 (2018) 1247–1256, https://doi.org/10.1007/s11244-018-0979-1.
[175] H. Guo, A.J. Martínez-Galera, J.M. Gómez-Rodríguez, C60 self-orientation on hexagonal boron nitride induced by intermolecular coupling, Nanotechnology 32 (2021) 025711, https://doi.org/10.1088/1361-6528/abbbb2.
[176] Á. Szitás, R. Gubó, T. Pásztor, A.P. Farkas, T. Ajtai, L. Óvári, K. Palotás, A. Berkó, Z. Kónya, Adsorption of azobenzene on hexagonal boron nitride nanomesh supported by Rh(111), J. Phys. Chem. C 124 (2020) 14182–14194, https://doi.org/10.1021/acs.jpcc.0c01725.
[177] M. Iannuzzi, F. Tran, R. Widmer, T. Dienel, K. Radican, Y. Ding, J. Hutter, O. Gröning, Site-selective adsorption of phthalocyanine on h-BN/Rh(111) nanomesh, Phys. Chem. Chem. Phys. 16 (2014) 12374–12384, https://doi.org/10.1039/C4CP01466A.
[178] F. Schulz, R. Drost, S.K. Hämäläinen, P. Liljeroth, Templated self-assembly and local doping of molecules on epitaxial hexagonal boron nitride, ACS Nano 7 (2013) 11121–11128, https://doi.org/10.1021/nn404840h.
[179] H. Cun, A.P. Seitsonen, S. Roth, S. Decurtins, S.-X. Liu, J. Osterwalder, T. Greber, An electron acceptor molecule in a nanomesh: F4TCNQ on h-BN/Rh(111), Surf. Sci. 678 (2018) 183–188, https://doi.org/10.1016/j.susc.2018.04.026.
[180] G. Kim, S.C. Jung, Y.-K. Han, Selectively strong molecular adsorption on boron nitride monolayer induced by transition metal substrate, Curr. Appl. Phys. 13 (2013) 2059–2063, https://doi.org/10.1016/j.cap.2013.09.010.
[181] A. Goriachko, A.A. Zakharov, H. Over, Oxygen-etching of h-BN/Ru(0001) nanomesh on the nano- and mesoscopic scale, J. Phys. Chem. C 112 (2008) 10423–10427, https://doi.org/10.1021/jp802359u.
[182] D.-Q. Hoang, D.-K. Pham, T. Van Vu, T.-D. Hoang, D.M. Hoat, V.-A. Dao, Effects of the gas molecules (H2, CO, NO) and transition metal atoms (Cr, Au) adsorbed on hexagonal boron nitride layers, J. Phys. Soc. Japan 90 (2021) 114601, https://doi.org/10.7566/JPSJ.90.114601.
[183] U. Burghaus, Gas-surface interactions on two-dimensional crystals, Surf. Sci. Rep. 74 (2019) 141–177, https://doi.org/10.1016/j.surfrep.2019.01.001.
[184] J. Zhang, B. Zhang, Y. Yu, C.-M. Wang, First-principles insights of electronic and optical properties of F-doped hexagonal boron nitride nanosheets for photocatalytic water splitting, EPL (Europhysics Lett. 127 (2019) 67003, https://doi.org/10.1209/0295-5075/127/67003.
[185] H. Li, H. Ran, Y. Li, N. Lv, J. Yin, J. Zhang, C. Wang, W. Jiang, W. Zhu, H. Li, H. Ji, Comparative study of halogen-doped (X Cl, Br, I) hexagonal boron nitride: a promising strategy to enhance the capacity of adsorptive desulfurization, J. Environ. Chem. Eng. 9 (2021) 105886, https://doi.org/10.1016/j.jece.2021.105886.
[186] M. Son, H. Lim, M. Hong, H.C. Choi, Direct growth of graphene pad on exfoliated hexagonal boron nitride surface, Nanoscale 3 (2011) 3089, https://doi.org/10.1039/c1nr10504c.
[187] A. Mehler, N. Néel, E. Voloshina, Y. Dedkov, J. Kröger, Second floor of flatland: epitaxial growth of graphene on hexagonal boron nitride, Small 17 (2021) 2102747, https://doi.org/10.1002/smll.202102747.
[188] T. Zhang, R. Li, X. Hao, Q. Zhang, H. Yang, Y. Hou, B. Hou, L. Jia, K. Jiang, Y. Zhang, X. Wu, X. Zhuang, L. Liu, Y. Yao, W. Guo, Y. Wang, Ullmann-like covalent bond coupling without participation of metal atoms, ACS Nano 17 (2023) 4387–4395, https://doi.org/10.1021/acsnano.2c09467.
[189] F. Ullmann, J. Bielecki, Ueber Synthesen in der Biphenylreihe, Berichte Der Dtsch, Chem. Gesellschaft 34 (1901) 2174–2185, https://doi.org/10.1002/cber.190103402141.
[190] Q. Yang, Y. Zhao, D. Ma, Cu-mediated ullmann-type cross-coupling and industrial applications in route design, process development, and scale-up of pharmaceutical and agrochemical processes, Org. Process Res. Dev. 26 (2022) 1690–1750, https://doi.org/10.1021/acs.oprd.2c00050.
[191] Z. Zeng, D. Guo, T. Wang, Q. Chen, A. Matěj, J. Huang, D. Han, Q. Xu, A. Zhao, P. Jelínek, D.G. de Oteyza, J.-S. McEwen, J. Zhu, Chemisorption-induced Formation of biphenylene dimer on Ag(111), J. Am. Chem. Soc. 144 (2022) 723–732, https://doi.org/10.1021/jacs.1c08284.
[192] Q. Fan, L. Yan, M.W. Tripp, O. Krejčí, S. Dimosthenous, S.R. Kachel, M. Chen, A. S. Foster, U. Koert, P. Liljeroth, J.M. Gottfried, Biphenylene network: a nonbenzenoid carbon allotrope, Science 372 (2021) 852–856, https://doi.org/10.1126/science.abg4509.
[193] H. Yang, T. Zhang, M. Liu, L. Liu, X. Wu, Y. Wang, Moirè pattern dislocation in continuous atomic lattice of monolayer h-BN, ACS Appl. Electron. Mater. 4 (2022) 891–896, https://doi.org/10.1021/acsaelm.2c00013.
[194] M. Kratzer, A. Matkovic, C. Teichert, Adsorption and epitaxial growth of small organic semiconductors on hexagonal boron nitride, J. Phys. D Appl. Phys. 52 (2019) 383001, https://doi.org/10.1088/1361-6463/ab29cb.
[195] Y.-C. Hsieh, Z.-Y. Lin, S.-J. Fung, W.-S. Lu, S.-C. Ho, S.-P. Hong, S.-Z. Ho, C.-H. Huang, K. Watanabe, T. Taniguchi, Y.-H. Chan, Y.-C. Chen, C.-L. Wu, T.-M. Chen, Engineering the strain and interlayer excitons of 2D materials via lithographically engraved hexagonal boron nitride, Nano Lett. 23 (2023) 7244–7251, https://doi.org/10.1021/acs.nanolett.3c01208.
[196] G. Melani, J.P. Guerrero-Felipe, A.M. Valencia, J. Krumland, C. Cocchi, M. Iannuzzi, Donors, acceptors, and a bit of aromatics: electronic interactions of molecular adsorbates on hBN and MoS 2 monolayers, Phys. Chem. Chem. Phys. 24 (2022) 16671–16679, https://doi.org/10.1039/D2CP01502A.
[197] A. Mehler, N. Néel, J. Kröger, Dissimilar decoupling behavior of two-dimensional materials on metal surfaces, J. Phys. Chem. Lett. 11 (2020) 5204–5211, https://doi.org/10.1021/acs.jpclett.0c01320.
[198] E. Rheinfrank, M. Pörtner, M. del C. Nuñez Beyerle, F. Haag, P.S. Deimel, F. Allegretti, K. Seufert, J.V. Barth, M.-L. Bocquet, P. Feulner, W. Auwärter, Actinide coordination chemistry on surfaces: synthesis, manipulation, and properties of thorium bis(porphyrinato) complexes, J. Am. Chem. Soc. 143 (2021) 14581–14591, https://doi.org/10.1021/jacs.1c04982.
[199] D.M. Zimmermann, K. Seufert, L. Đorđević, T. Hoh, S. Joshi, T. Marangoni, D. Bonifazi, W. Auwärter, Self-assembly and spectroscopic fingerprints of photoactive pyrenyl tectons on h BN/Cu(111), Beilstein J. Nanotechnol. 11 (2020) 1470–1483, https://doi.org/10.3762/bjnano.11.130.
[200] M. Pörtner, Y. Wei, A. Riss, K. Seufert, M. Garnica, J.V. Barth, A.P. Seitsonen, L. Diekhöner, W. Auwärter, Charge state control of F16CoPc on h -BN/Cu(111), Adv. Mater. Interfac. 7 (2020) 2000080, https://doi.org/10.1002/admi.202000080.
[201] A. Riss, M. Richter, A.P. Paz, X.-Y. Wang, R. Raju, Y. He, J. Ducke, E. Corral, M. Wuttke, K. Seufert, M. Garnica, A. Rubio, J.V. Barth, A. Narita, K. Müllen, R. Berger, X. Feng, C.-A. Palma, W. Auwärter, Polycyclic aromatic chains on metals and insulating layers by repetitive [3+2] cycloadditions, Nat. Commun. 11 (2020) 1490, https://doi.org/10.1038/s41467-020-15210-2.
[202] V.V. Korolkov, S.A. Svatek, A. Summerfield, J. Kerfoot, L. Yang, T. Taniguchi, K. Watanabe, N.R. Champness, N.A. Besley, P.H. Beton, van der Waals-Induced Chromatic Shifts in Hydrogen-Bonded Two-Dimensional Porphyrin Arrays on Boron Nitride, ACS Nano 9 (2015) 10347–10355, https://doi.org/10.1021/acsnano.5b04443.
[203] A. Kumar, K. Banerjee, P. Liljeroth, Molecular assembly on two-dimensional materials, Nanotechnology 28 (2017) 082001, https://doi.org/10.1088/1361-6528/aa564f.
[204] M. Neumann, X. Wei, L. Morales-Inostroza, S. Song, S.-G. Lee, K. Watanabe, T. Taniguchi, S. Götzinger, Y.H. Lee, Organic molecules as origin of visible-range single photon emission from hexagonal boron nitride and mica, ACS Nano 17 (2023) 11679–11691, https://doi.org/10.1021/acsnano.3c02348.
[205] A. Sajid, M.J. Ford, J.R. Reimers, Single-photon emitters in hexagonal boron nitride: a review of progress, Rep. Prog. Phys. 83 (2020) 044501, https://doi.org/10.1088/1361-6633/ab6310.
[206] D. Kozawa, S.X. Li, T. Ichihara, A.G. Rajan, X. Gong, G. He, V.B. Koman, Y. Zeng, M. Kuehne, K.S. Silmore, D. Parviz, P. Liu, A.T. Liu, S. Faucher, Z. Yuan, J. Warner, D. Blankschtein, M.S. Strano, Discretized hexagonal boron nitride quantum emitters and their chemical interconversion, Nanotechnology 34 (2023) 115702, https://doi.org/10.1088/1361-6528/aca984.
[207] F. Hayee, L. Yu, J.L. Zhang, C.J. Ciccarino, M. Nguyen, A.F. Marshall, I. Aharonovich, J. Vučković, P. Narang, T.F. Heinz, J.A. Dionne, Revealing multiple classes of stable quantum emitters in hexagonal boron nitride with correlated optical and electron microscopy, Nat. Mater. 19 (2020) 534–539, https://doi.org/10.1038/s41563-020-0616-9.
[208] C. Toninelli, I. Gerhardt, A.S. Clark, A. Reserbat-Plantey, S. Götzinger, Z. Ristanović, M. Colautti, P. Lombardi, K.D. Major, I. Deperasińska, W. H. Pernice, F.H.L. Koppens, B. Kozankiewicz, A. Gourdon, V. Sandoghdar, M. Orrit, Single organic molecules for photonic quantum technologies, Nat. Mater. 20 (2021) 1615–1628, https://doi.org/10.1038/s41563-021-00987-4.
[209] D.J. Rizzo, Q. Dai, C. Bronner, G. Veber, B.J. Smith, M. Matsumoto, S. Thomas, G. D. Nguyen, P.R. Forrester, W. Zhao, J.H. Jørgensen, W.R. Dichtel, F.R. Fischer, H. Li, J.-L. Bredas, M.F. Crommie, Revealing the local electronic structure of a single-layer covalent organic framework through electronic decoupling, Nano Lett. 20 (2020) 963–970, https://doi.org/10.1021/acs.nanolett.9b03998.
[210] D. Kumar, J. Hellerstedt, B. Lowe, A. Schiffrin, Mesoscopic 2D molecular self-assembly on an insulator, Nanotechnology 34 (2023), https://doi.org/10.1088/1361-6528/acba20.
[211] W.C. McKee, M.C. Patterson, J.R. Frick, P.T. Sprunger, Y. Xu, Adsorption of transition metal adatoms on h-BN/Rh(111): implications for nanocluster self-assembly, Catal. Today 280 (2017) 220–231, https://doi.org/10.1016/j.cattod.2016.09.030.
[212] F. Wu, D. Huang, Y. Yue, L. Liu, Template growth of Au, Ni and Ni–Au nanoclusters on hexagonal boron nitride/Rh(111): a combined STM, TPD and AES study, RSC Adv. 7 (2017) 44169–44177, https://doi.org/10.1039/C7RA08880A.

[213] X. Dong, L. Zhang, M. Yoon, P. Zhang, The role of substrate on stabilizing new phases of two-dimensional tin, 2D Mater. 8 (2021) 045003, https://doi.org/10.1088/2053-1583/ac1255.
[214] L. Óvári, A. Berkó, G. Vári, R. Gubó, A.P. Farkas, Z. Kónya, The growth and thermal properties of Au deposited on Rh(111): formation of an ordered surface alloy, Phys. Chem. Chem. Phys. 18 (2016) 25230–25240, https://doi.org/10.1039/C6CP02128J.
[215] F. Müller, S. Grandthyll, Monolayer formation of hexagonal boron nitride on Ag (001), Surf. Sci. 617 (2013) 207–210, https://doi.org/10.1016/j.susc.2013.07.024.
[216] F. Müller, S. Hüfner, H. Sachdev, R. Laskowski, P. Blaha, K. Schwarz, Epitaxial growth of hexagonal boron nitride on Ag(111), Phys. Rev. B 82 (2010) 113406, https://doi.org/10.1103/PhysRevB.82.113406.
[217] L. Camilli, E. Sutter, P. Sutter, Growth of two-dimensional materials on non-catalytic substrates: h-BN/Au(111), 2D Mater. 1 (2014) 025003, https://doi.org/10.1088/2053-1583/1/2/025003.
[218] A. Fedorov, C.S. Praveen, N.I. Verbitskiy, D. Haberer, D. Usachov, D.V. Vyalikh, A. Nefedov, C. Wöll, L. Petaccia, S. Piccinin, H. Sachdev, M. Knupfer, B. Büchner, S. Fabris, A. Grüneis, Efficient gating of epitaxial boron nitride monolayers by substrate functionalization, Phys. Rev. B 92 (2015) 125440, https://doi.org/10.1103/PhysRevB.92.125440.
[219] H. Hibino, S. Wang, C.M. Orofeo, H. Kageshima, Growth and low-energy electron microscopy characterizations of graphene and hexagonal boron nitride, Prog. Cryst. Growth Char. Mater. 62 (2016) 155–176, https://doi.org/10.1016/j.pcrysgrow.2016.04.008.
[220] C.M. Orofeo, S. Suzuki, H. Kageshima, H. Hibino, Growth and low-energy electron microscopy characterization of monolayer hexagonal boron nitride on epitaxial cobalt, Nano Res. 6 (2013) 335–347, https://doi.org/10.1007/s12274-013-0310-1.
[221] J. Beatty, Y. Cao, I. Tanabe, M. Sky Driver, P.A. Dowben, J.A. Kelber, Atomic layer-by-layer deposition of h-BN(0001) on cobalt: a building block for spintronics and graphene electronics, Mater. Res. Express 1 (2014) 046410, https://doi.org/10.1088/2053-1591/1/4/046410.
[222] M.S. Driver, J.D. Beatty, O. Olanipekun, K. Reid, A. Rath, P.M. Voyles, J. A. Kelber, Atomic layer epitaxy of h-BN(0001) multilayers on Co(0001) and molecular beam epitaxy growth of graphene on h-BN(0001)/Co(0001), Langmuir 32 (2016) 2601–2607, https://doi.org/10.1021/acs.langmuir.5b03653.
[223] D.Y. Usachov, A.V. Tarasov, K.A. Bokai, V.O. Shevelev, O.Y. Vilkov, A. E. Petukhov, A.G. Rybkin, I.I. Ogorodnikov, M.V. Kuznetsov, M. Muntwiler, F. Matsui, L.V. Yashina, C. Laubschat, D.V. Vyalikh, Site- and spin-dependent coupling at the highly ordered h-BN/Co(0001) interface, Phys. Rev. B 98 (2018) 195438, https://doi.org/10.1103/PhysRevB.98.195438.
[224] V.O. Shevelev, K.A. Bokai, O.Y. Vilkov, A.A. Makarova, D.Y. Usachov, Oxidation of h-BN on strongly and weakly interacting metal surfaces, Nanotechnology 30 (2019) 234004, https://doi.org/10.1088/1361-6528/ab0863.
[225] F. Müller, S. Hüfner, H. Sachdev, One-dimensional structure of boron nitride on chromium (110) – a study of the growth of boron nitride by chemical vapour deposition of borazine, Surf. Sci. 602 (2008) 3467–3476, https://doi.org/10.1016/j.susc.2008.06.037.
[226] N. Coudurier, M. Chubarov, R. Boichot, F. Mercier, E. Blanquet, R. Reboud, S. Lay, A. Crisci, S. Coindeau, T. Encinas, M. Pons, Growth of boron nitride films on w-AlN (0001), 4° off-cut 4H-SiC (0001), W (110) and Cr (110) substrates by Chemical Vapor Deposition, Cryst. Res. Technol. 51 (2016) 231–238, https://doi.org/10.1002/crat.201500284.
[227] X. Song, J. Gao, Y. Nie, T. Gao, J. Sun, D. Ma, Q. Li, Y. Chen, C. Jin, A. Bachmatiuk, M.H. Rümmeli, F. Ding, Y. Zhang, Z. Liu, Chemical vapor deposition growth of large-scale hexagonal boron nitride with controllable orientation, Nano Res. 8 (2015) 3164–3176, https://doi.org/10.1007/s12274-015-0816-9.
[228] J. Dong, L. Zhang, X. Dai, F. Ding, The epitaxy of 2D materials growth, Nat. Commun. 11 (2020), https://doi.org/10.1038/s41467-020-19752-3.
[229] C. Herrmann, P. Omelchenko, K.L. Kavanagh, Growth of h-BN on copper (110) in a LEEM, Surf. Sci. 669 (2018) 133–139, https://doi.org/10.1016/j.susc.2017.11.021.
[230] L. Li, Y. Zhang, R. Zhang, Z. Han, H. Dong, G. Yu, D. Geng, H.Y. Yang, A minireview on chemical vapor deposition growth of wafer-scale monolayer h -BN single crystals, Nanoscale 13 (2021) 17310–17317, https://doi.org/10.1039/D1NR04034K.
[231] M. Schwarz, A. Riss, M. Garnica, J. Ducke, P.S. Deimel, D.A. Duncan, P.K. Thakur, T.-L. Lee, A.P. Seitsonen, J.V. Barth, F. Allegretti, W. Auwärter, Corrugation in the weakly interacting hexagonal-BN/Cu(111) system: structure determination by combining noncontact atomic force microscopy and X-ray standing waves, ACS Nano 11 (2017) 9151–9161, https://doi.org/10.1021/acsnano.7b04022.
[232] R. Koitz, A.P. Seitsonen, M. Iannuzzi, J. Hutter, Structural and electronic properties of a large-scale Moirè pattern of hexagonal boron nitride on Cu(111) studied with density functional theory, Nanoscale 5 (2013) 5589, https://doi.org/10.1039/c3nr00709j.
[233] T. Hartl, M. Will, P. Bampoulis, D. Herrmann, P. Valerius, C. Herbig, V. Boix de la Cruz, P. Lacovig, V. Vonk, S. Chung, A. Stierle, S. Lizzit, J. Knudsen, T. Michely, Carbon embedding of Pt cluster superlattices templated by hexagonal boron nitride on Ir(111), J. Phys. Chem. C 125 (2021) 23435–23444, https://doi.org/10.1021/acs.jpcc.1c06829.
[234] I. Gallardo, A. Arnau, F. Delgado, R. Baltic, A. Singha, F. Donati, C. Wäckerlin, J. Dreiser, S. Rusponi, H. Brune, Large effect of metal substrate on magnetic anisotropy of Co on hexagonal boron nitride, New J. Phys. 21 (2019) 073053, https://doi.org/10.1088/1367-2630/ab3077.
[235] M. Petrović, Sequential lithium deposition on hexagonal boron nitride monolayer on Ir(111): identifying intercalation and adsorption, Surf. Sci. 706 (2021) 121786, https://doi.org/10.1016/j.susc.2020.121786.
[236] F. Orlando, P. Lacovig, L. Omiciuolo, N.G. Apostol, R. Larciprete, A. Baraldi, S. Lizzit, Epitaxial growth of a single-domain hexagonal boron nitride monolayer, ACS Nano 8 (2014) 12063–12070, https://doi.org/10.1021/nn5058968.
[237] F. Schulz, J. Ritala, O. Krejčí, A.P. Seitsonen, A.S. Foster, P. Liljeroth, Elemental identification by combining atomic force microscopy and kelvin probe force microscopy, ACS Nano 12 (2018) 5274–5283, https://doi.org/10.1021/acsnano.7b08997.
[238] D. Usachov, A. Fedorov, O. Vilkov, V.K. Adamchuk, L.V. Yashina, L. Bondarenko, A.A. Saranin, A. Grüneis, D.V. Vyalikh, Experimental and computational insight into the properties of the lattice-mismatched structures: monolayers of h-BN and graphene on Ir(111), Phys. Rev. B 86 (2012) 155151, https://doi.org/10.1103/PhysRevB.86.155151.
[239] M. Petrović, U. Hagemann, M. Horn-von Hoegen, F.-J. Meyer zu Heringdorf, Microanalysis of single-layer hexagonal boron nitride islands on Ir(111), Appl. Surf. Sci. 420 (2017) 504–510, https://doi.org/10.1016/j.apsusc.2017.05.155.
[240] F. Orlando, R. Larciprete, P. Lacovig, I. Boscarato, A. Baraldi, S. Lizzit, Epitaxial growth of hexagonal boron nitride on Ir(111), J. Phys. Chem. C 116 (2012) 157–164, https://doi.org/10.1021/jp207571n.
[241] M. Will, T. Hartl, V. Boix de la Cruz, P. Lacovig, S. Lizzit, J. Knudsen, T. Michely, P. Bampoulis, Growth, stability, and electronic decoupling of Pt clusters on h-BN/Ir(111), J. Phys. Chem. C 125 (2021) 3880–3889, https://doi.org/10.1021/acs.jpcc.0c10136.
[242] T. Hartl, D. Herrmann, M. Will, Y. Falke, A. Grüneis, T. Michely, P. Bampoulis, Silicon cluster arrays on the monolayer of hexagonal boron nitride on Ir(111), J. Phys. Chem. C 126 (2022) 6809–6814, https://doi.org/10.1021/acs.jpcc.2c00694.
[243] J. Cai, W. Jolie, C.C. Silva, M. Petrović, C. Schlueter, T. Michely, M. Kralj, T.-L. Lee, C. Busse, Modifying the geometric and electronic structure of hexagonal boron nitride on Ir(111) by Cs adsorption and intercalation, Phys. Rev. B 98 (2018) 195443, https://doi.org/10.1103/PhysRevB.98.195443.
[244] M.P. Allan, S. Berner, M. Corso, T. Greber, J. Osterwalder, Tunable self-assembly of one-dimensional nanostructures with orthogonal directions, Nanoscale Res. Lett. 2 (2007) 94, https://doi.org/10.1007/s11671-006-9036-2.
[245] H. Tian, Y. He, P. Das, Z. Cui, W. Shi, A. Khanaki, R.K. Lake, J. Liu, Growth dynamics of millimeter-sized single-crystal hexagonal boron nitride monolayers on secondary recrystallized Ni (100) substrates, Adv. Mater. Interfac. 6 (2019) 1901198, https://doi.org/10.1002/admi.201901198.
[246] H. Chou, S. Majumder, A. Roy, M. Catalano, P. Zhuang, M. Quevedo-Lopez, L. Colombo, S.K. Banerjee, Dependence of h-BN film thickness as grown on nickel single-crystal substrates of different orientations, ACS Appl. Mater. Interfaces 10 (2018) 44862–44870, https://doi.org/10.1021/acsami.8b16816.
[247] Z. Cui, Y. He, H. Tian, A. Khanaki, L. Xu, W. Shi, J. Liu, Study of direct tunneling and dielectric breakdown in molecular beam epitaxial hexagonal boron nitride monolayers using metal–insulator–metal devices, ACS Appl. Electron. Mater. 2 (2020) 747–755, https://doi.org/10.1021/acsaelm.9b00816.
[248] Y.-H. Lee, K.-K. Liu, A.-Y. Lu, C.-Y. Wu, C.-T. Lin, W. Zhang, C.-Y. Su, C.-L. Hsu, T.-W. Lin, K.-H. Wei, Y. Shi, L.-J. Li, Growth selectivity of hexagonal-boron nitride layers on Ni with various crystal orientations, RSC Adv. 2 (2012) 111–115, https://doi.org/10.1039/C1RA00703C.
[249] T. Greber, L. Brandenberger, M. Corso, A. Tamai, J. Osterwalder, Single layer hexagonal boron nitride films on Ni(110), E-Journal Surf. Sci. Nanotechnol. 4 (2006) 410–413, https://doi.org/10.1380/ejssnt.2006.410.
[250] H. Cho, S. Park, D.-I. Won, S.O. Kang, S.-S. Pyo, D.-I. Kim, S.M. Kim, H.C. Kim, M. J. Kim, Growth kinetics of white graphene (h-BN) on a planarised Ni foil surface, Sci. Rep. 5 (2015) 11985, https://doi.org/10.1038/srep11985.
[251] A. Ismach, H. Chou, D.A. Ferrer, Y. Wu, S. McDonnell, H.C. Floresca, A. Covacevich, C. Pope, R. Piner, M.J. Kim, R.M. Wallace, L. Colombo, R.S. Ruoff, Toward the controlled synthesis of hexagonal boron nitride films, ACS Nano 6 (2012) 6378–6385, https://doi.org/10.1021/nn301940k.
[252] E. Rokuta, Y. Hasegawa, K. Suzuki, Y. Gamou, C. Oshima, A. Nagashima, Phonon dispersion of an epitaxial monolayer film of hexagonal boron nitride on Ni(111), Phys. Rev. Lett. 79 (1997) 4609–4612, https://doi.org/10.1103/PhysRevLett.79.4609.
[253] I. Shimoyama, Y. Baba, T. Sekiguchi, K. Nath, NEXAFS spectra of an epitaxial boron nitride film on Ni, J. Electron. Spectrosc. Relat. Phenom. 137–140 (1 1 1) (2004) 573–578, https://doi.org/10.1016/j.elspec.2004.02.040.
[254] D. Usachov, V.K. Adamchuk, D. Haberer, A. Grüneis, H. Sachdev, A. B. Preobrajenski, C. Laubschat, D.V. Vyalikh, Quasifreestanding single-layer hexagonal boron nitride as a substrate for graphene synthesis, Phys. Rev. B 82 (2010) 075415, https://doi.org/10.1103/PhysRevB.82.075415.
[255] W. Auwärter, M. Muntwiler, T. Greber, J. Osterwalder, Co on h -BN/Ni(111): from island to island-chain formation and Co intercalation, Surf. Sci. 511 (2002) 379–386, https://doi.org/10.1016/S0039-6028(02)01545-5.
[256] M. Cattelan, B. Markman, G. Lucchini, P.K. Das, I. Vobornik, J.A. Robinson, S. Agnoli, G. Granozzi, New strategy for the growth of complex heterostructures based on different 2D materials, Chem. Mater. 27 (2015) 4105–4113, https://doi.org/10.1021/acs.chemmater.5b01170.
[257] S. Banerjee, S. Nigam, C. Majumder, Structure and stability of Au, Au2 and Au8 cluster on Ni(111) supported h-BN sheet: role of size and support towards oxygen bond activation, Phys. E Low-Dimensional Syst. Nanostructures 147 (2023) 115561, https://doi.org/10.1016/j.physe.2022.115561.
[258] S. Banerjee, C. Majumder, Stability and electronic properties of Au atom doped hexagonal boron nitride sheet on Ni(111) support: role of vacancy defects and

supports towards single atom catalysis, Appl. Surf. Sci. 515 (2020) 145978, https://doi.org/10.1016/j.apsusc.2020.145978.
[259] M. Morscher, M. Corso, T. Greber, J. Osterwalder, Formation of single layer h-BN on Pd(111), Surf. Sci. 600 (2006) 3280–3284, https://doi.org/10.1016/j.susc.2006.06.016.
[260] S. Kerschbaumer, N. Memmel, Copper clusters on h-BN-covered Pt(110): nucleation, stability, and local surface potential, J. Phys. Chem. C 126 (2022) 11365–11371, https://doi.org/10.1021/acs.jpcc.2c02266.
[261] M. Kim, S.W. Moon, G. Kim, S.I. Yoon, K. Kim, S.K. Min, H.S. Shin, Effect of Pt crystal surface on hydrogenation of monolayer h-BN and its conversion to graphene, Chem. Mater. 32 (2020) 4584–4590, https://doi.org/10.1021/acs.chemmater.0c00736.
[262] A.C.E. Onslow, R. Bogacz, M.W. Jones, Quantifying phase–amplitude coupling in neuronal network oscillations, Prog. Biophys. Mol. Biol. 105 (2011) 49–57, https://doi.org/10.1016/j.pbiomolbio.2010.09.007.
[263] R.J. Simonson, M. Trenary, An infrared study of the adsorption of borazine, (BHNH)3, on the Pt(111) surface, J. Electron. Spectrosc. Relat. Phenom. 54–55 (1990) 717–728, https://doi.org/10.1016/0368-2048(90)80264-B.
[264] E. Ćavar, R. Westerström, A. Mikkelsen, E. Lundgren, A.S. Vinogradov, M.L. Ng, A.B. Preobrajenski, A.A. Zakharov, N. Mårtensson, A single h-BN layer on Pt(111), Surf. Sci. 602 (2008) 1722–1726, https://doi.org/10.1016/j.susc.2008.03.008.
[265] T. Watanabe, Y. Yamada, A. Koide, S. Entani, S. Li, Z.I. Popov, P.B. Sorokin, H. Naramoto, M. Sasaki, K. Amemiya, S. Sakai, Interface-induced perpendicular magnetic anisotropy of Co nanoparticles on single-layer h-BN/Pt(111), Appl. Phys. Lett. 112 (2018) 022407, https://doi.org/10.1063/1.5010836.
[266] R. Laskowski, P. Blaha, Ab initio study of h − BN nanomeshes on Ru(001), Rh (111), and Pt(111), Phys. Rev. B 81 (2010) 075418, https://doi.org/10.1103/PhysRevB.81.075418.
[267] Y. Qi, N. Han, Y. Li, Z. Zhang, X. Zhou, B. Deng, Q. Li, M. Liu, J. Zhao, Z. Liu, Y. Zhang, Strong adlayer–substrate interactions "break" the patching growth of h -BN onto graphene on Re(0001), ACS Nano 11 (2017) 1807–1815, https://doi.org/10.1021/acsnano.6b07773.
[268] A.J. Martínez-Galera, J.M. Gómez-Rodríguez, Structural and electronic properties of 3,4,9,10-perylene tetracarboxylic dianhydride on h-BN/Rh(110), J. Phys. Chem. C 123 (2019) 1866–1873, https://doi.org/10.1021/acs.jpcc.8b10810.
[269] Y. Sugiyama, C. Bernard, Y. Okuyama, S. Ideta, K. Tanaka, T. Greber, T. Hirahara, Flattening and manipulation of the electronic structure of h-BN/Rh(111) nanomesh upon Sn intercalation, Surf. Sci. 672–673 (2018) 33–38, https://doi.org/10.1016/j.susc.2018.03.007.
[270] F. Düll, J. Steinhauer, F. Späth, U. Bauer, P. Bachmann, H.-P. Steinrück, S. Wickert, R. Denecke, C. Papp, Ethylene: its adsorption, reaction, and coking on Pt/h -BN/Rh(111) nanocluster arrays, J. Chem. Phys. 152 (2020) 224710, https://doi.org/10.1063/5.0011616.
[271] S. Berner, M. Corso, R. Widmer, O. Groening, R. Laskowski, P. Blaha, K. Schwarz, A. Goriachko, H. Over, S. Gsell, M. Schreck, H. Sachdev, T. Greber, J. Osterwalder, Boron nitride nanomesh: functionality from a corrugated monolayer, Angew. Chem. Int. Ed. 46 (2007) 5115–5119, https://doi.org/10.1002/anie.200700234.
[272] A.B. Preobrajenski, M.L. Ng, N.A. Vinogradov, A.S. Vinogradov, E. Lundgren, A. Mikkelsen, N. Mårtensson, Impact of oxygen coadsorption on intercalation of cobalt under the h-BN nanomesh, Nano Lett. 9 (2009) 2780–2787, https://doi.org/10.1021/nl901316p.
[273] F.D. Natterer, F. Patthey, H. Brune, Ring state for single transition metal atoms on boron nitride on Rh(111), Phys. Rev. Lett. 109 (2012) 066101, https://doi.org/10.1103/PhysRevLett.109.066101.
[274] N.J. Waleska, F. Düll, P. Bachmann, F. Hemauer, J. Steinhauer, C. Papp, Reactivity and passivation of Fe nanoclusters on h- BN/Rh(111), Chem. Eur J. 27 (2021) 17087–17093, https://doi.org/10.1002/chem.202102590.
[275] F. Düll, M. Meusel, F. Späth, S. Schötz, U. Bauer, P. Bachmann, J. Steinhauer, H.-P. Steinrück, A. Bayer, C. Papp, Growth and stability of Pt nanoclusters from 1 to 50 atoms on h-BN/Rh(111), Phys. Chem. Chem. Phys. 21 (2019) 21287–21295, https://doi.org/10.1039/C9CP04095A.
[276] R. Laskowski, P. Blaha, Unraveling the structure of the h-BN/Rh(111) nanomesh with ab initio calculations, J. Phys. Condens. Matter 20 (2008) 064207, https://doi.org/10.1088/0953-8984/20/6/064207.
[277] H.P. Koch, R. Laskowski, P. Blaha, K. Schwarz, Adsorption of gold atoms on the h-BN/Rh(111) nanomesh, Phys. Rev. B 84 (2011) 245410, https://doi.org/10.1103/PhysRevB.84.245410.
[278] I. Brihuega, C.H. Michaelis, J. Zhang, S. Bose, V. Sessi, J. Honolka, M. Alexander Schneider, A. Enders, K. Kern, Electronic decoupling and templating of Co nanocluster arrays on the boron nitride nanomesh, Surf. Sci. 602 (2008) L95–L99, https://doi.org/10.1016/j.susc.2008.04.040.
[279] A. Goriachko, Y.B. He, H. Over, Complex growth of NanoAu on BN nanomeshes supported by Ru(0001), J. Phys. Chem. C 112 (2008) 8147–8152, https://doi.org/10.1021/jp7119608.
[280] D. Martoccia, T. Brugger, M. Björck, C.M. Schlepütz, S.A. Pauli, T. Greber, B. D. Patterson, P.R. Willmott, h-BN/Ru(0001) nanomesh: a 14-on-13 superstructure with 3.5nm periodicity, Surf. Sci. 604 (2010) L16–L19, https://doi.org/10.1016/j.susc.2010.01.003.
[281] H. Li, R. Zhao, Dissociation of ammonia borane and its subsequent nucleation on the Ru(0001) surface revealed by density functional theoretical simulations, Phys. Chem. Chem. Phys. 24 (2022) 12226–12235, https://doi.org/10.1039/D1CP05957B.
[282] T. Brugger, S. Günther, B. Wang, J.H. Dil, M.-L. Bocquet, J. Osterwalder, J. Wintterlin, T. Greber, Comparison of electronic structure and template function of single-layer graphene and a hexagonal boron nitride nanomesh on Ru(0001), Phys. Rev. B 79 (2009) 045407, https://doi.org/10.1103/PhysRevB.79.045407.
[283] J. Cai, R. Ohmann, C. Busse, Sub-Poissonian distribution of Cs and K ions in the valleys of hBN/Ru(0001), Phys. Rev. B 104 (2021) 115417, https://doi.org/10.1103/PhysRevB.104.115417.
[284] M. Gao, M. Nakahara, A. Lyalin, T. Taketsugu, Catalytic activity of gold clusters supported on the h-BN/Au(111) surface for the hydrogen evolution reaction, J. Phys. Chem. C 125 (2021) 1334–1344, https://doi.org/10.1021/acs.jpcc.0c08826.
[285] H. Brongersma, M. Draxler, M. Deridder, P. Bauer, Surface composition analysis by low-energy ion scattering, Surf. Sci. Rep. 62 (2007) 63–109, https://doi.org/10.1016/j.surfrep.2006.12.002.
[286] M.L. Ng, A.B. Preobrajenski, A.S. Vinogradov, N. Mårtensson, Formation and temperature evolution of Au nanoparticles supported on the h-BN nanomesh, Surf. Sci. 602 (2008) 1250–1255, https://doi.org/10.1016/j.susc.2008.01.028.
[287] I. Lončarić, Z. Rukelj, V.M. Silkin, V. Despoja, Strong two-dimensional plasmon in Li-intercalated hexagonal boron-nitride film with low damping, Npj 2D Mater. Appl. 2 (2018) 33, https://doi.org/10.1038/s41699-018-0078-y.
[288] F. Zhang, K. Németh, J. Bareño, F. Dogan, I.D. Bloom, L.L. Shaw, Experimental and theoretical investigations of functionalized boron nitride as electrode materials for Li-ion batteries, RSC Adv. 6 (2016) 27901–27914, https://doi.org/10.1039/C6RA03141B.
[289] D. Talukdar, S.S. Bora, G.A. Ahmed, Electronic, optical, and adsorption properties of Li-doped hexagonal boron nitride: a GW approach, Phys. Chem. Chem. Phys. 26 (2024) 4021–4028, https://doi.org/10.1039/D3CP04710E.
[290] J. Zuo, Y. Dang, P. Zhai, B. Li, L. Wang, M. Wang, Z. Yang, Q. Chen, X. Gu, Z. Li, P. Tang, Y. Gong, Fast lithium ion transport pathways constructed by two-dimensional boron nitride nanoflakes in quasi-solid-state polymer electrolyte, Nano Lett. 23 (2023) 8106–8114, https://doi.org/10.1021/acs.nanolett.3c02169.
[291] A. Das, V. Yadav, C.V. Krishnamurthy, M. Jaiswal, Percolative proton transport in hexagonal boron nitride membranes with edge-functionalization, Nanoscale Adv. 5 (2023) 4901–4910, https://doi.org/10.1039/D3NA00524K.
[292] L. Khalil, C. Ernandes, J. Avila, A. Rousseau, P. Dudin, N.D. Zhigadlo, G. Cassabois, B. Gil, F. Oehler, J. Chaste, A. Ouerghi, High p doped and robust band structure in Mg-doped hexagonal boron nitride, Nanoscale Adv. 5 (2023) 3225–3232, https://doi.org/10.1039/D2NA00843B.
[293] J. Guo, H. Liu, D. Li, J. Wang, X. Djitcheu, D. He, Q. Zhang, A minireview on the synthesis of single atom catalysts, RSC Adv. 12 (2022) 9373–9394, https://doi.org/10.1039/D2RA00657J.
[294] E.C. Kohlrausch, H.A. Centurion, R.W. Lodge, X. Luo, T. Slater, M.J.L. Santos, S. Ling, V.R. Mastelaro, M.J. Cliffe, R.V. Goncalves, J. Alves Fernandes, A high-throughput, solvent free method for dispersing metal atoms directly onto supports, J. Mater. Chem. A 9 (2021) 26676–26679, https://doi.org/10.1039/D1TA08372D.
[295] G. Di Liberto, L.A. Cipriano, G. Pacchioni, Universal principles for the rational design of single atom electrocatalysts? Handle with care, ACS Catal. 12 (2022) 5846–5856, https://doi.org/10.1021/acscatal.2c01011.
[296] J. Datta, C. Majumder, Stabilizing Co, Ni and Cu on the h-BN surface: using O-O bond activation to probe their performance as single atom catalyst, Catal. Today 370 (2021) 75–82, https://doi.org/10.1016/j.cattod.2020.10.021.
[297] J. Datta, C. Majumder, Entrapping metal atom on hexagonal boron nitride monolayer for high performance single-atom-catalyst: role of vacancy defects and metal support, Appl. Surf. Sci. 614 (2023) 156061, https://doi.org/10.1016/j.apsusc.2022.156061.
[298] I. Popov, S. Ghaderzadeh, E.C. Kohlrausch, L.T. Norman, T.J.A. Slater, G.N. Aliev, H. Alhabeadi, A. Kaplan, W. Theis, A.N. Khlobystov, J.A. Fernandes, E. Besley, Chemical kinetics of metal single atom and nanocluster formation on surfaces: an example of Pt on hexagonal boron nitride, Nano Lett. 23 (2023) 8006–8012, https://doi.org/10.1021/acs.nanolett.3c01968.
[299] S. Chahal, T.K. Sahu, S. Kar, S.J. Ray, V. Biju, P. Kumar, Transition metal-doped boron nitride atomic sheets with an engineered bandgap and magnetization, J. Phys. Chem. C 126 (2022) 21084–21093, https://doi.org/10.1021/acs.jpcc.2c06693.
[300] T.-A. Chen, C.-P. Chuu, C.-C. Tseng, C.-K. Wen, H.-S.P. Wong, S. Pan, R. Li, T.-A. Chao, W.-C. Chueh, Y. Zhang, Q. Fu, B.I. Yakobson, W.-H. Chang, L.-J. Li, Wafer-scale single-crystal hexagonal boron nitride monolayers on Cu (111), Nature 579 (2020) 219–223, https://doi.org/10.1038/s41586-020-2009-2.
[301] Z. Liu, Y. Gong, W. Zhou, L. Ma, J. Yu, J.C. Idrobo, J. Jung, A.H. MacDonald, R. Vajtai, J. Lou, P.M. Ajayan, Ultrathin high-temperature oxidation-resistant coatings of hexagonal boron nitride, Nat. Commun. 4 (2013) 2541, https://doi.org/10.1038/ncomms3541.
[302] G. Chilkoor, K. Jawaharraj, B. Vemuri, A. Kutana, M. Tripathi, D. Kota, T. Arif, T. Filleter, A.B. Dalton, B.I. Yakobson, M. Meyyappan, M.M. Rahman, P. M. Ajayan, V. Gadhamshetty, Hexagonal boron nitride for sulfur corrosion inhibition, ACS Nano 14 (2020) 14809–14819, https://doi.org/10.1021/acsnano.0c03625.
[303] M. Scardamaglia, V. Boix, G. D'Acunto, C. Struzzi, N. Reckinger, X. Chen, A. Shivayogimath, T. Booth, J. Knudsen, Comparative study of copper oxidation protection with graphene and hexagonal boron nitride, Carbon N. Y. 171 (2021) 610–617, https://doi.org/10.1016/j.carbon.2020.09.021.
[304] J. Deyerling, I. Piquero-Zulaica, M.A. Ashoush, K. Seufert, M.A. Kher-Elden, Z. M. Abd El-Fattah, W. Auwärter, Formation of an extended quantum dot array driven and autoprotected by an atom-thick h-BN layer, ACS Nano (2022), https://doi.org/10.1021/acsnano.2c10366.
[305] S.-Y. Zhong, S.-Y. Wu, X.-Y. Yu, G.-Q. Shen, L. Yan, K.-L. Xu, First-principles studies of the adsorption and catalytic properties for gas molecules on h-BN

monolayer doped with various transition metal atoms, Catal. Surv. Asia 26 (2022) 69–79, https://doi.org/10.1007/s10563-021-09350-8.
[306] Y. Zhang, C. Qin, L. Zhu, Y. Wang, J. Cao, Adsorption of no 2 , no, NH 3 , and CO on noble metal (Rh, Pd, Ag, Ir, Pt, Au)-Modified hexagonal boron nitride monolayers: a first-principles study, Langmuir 40 (2024) 1058–1071, https://doi.org/10.1021/acs.langmuir.3c03282.
[307] S. Kikkawa, K. Teramura, K. Kato, H. Asakura, S. Hosokawa, T. Tanaka, Formation of CH4 at the metal-support interface of Pt/Al2O3 during hydrogenation of CO2 : operando XAS-DRIFTS study, ChemCatChem 14 (2022), https://doi.org/10.1002/cctc.202101723.
[308] F. Solymosi, M. Pasztor, An infrared study of the influence of carbon monoxide chemisorption on the topology of supported rhodium, J. Phys. Chem. 89 (1985) 4789–4793, https://doi.org/10.1021/j100268a026.
[309] Á. Kukovecz, K. Kordás, J. Kiss, Z. Kónya, Atomic scale characterization and surface chemistry of metal modified titanate nanotubes and nanowires, Surf. Sci. Rep. 71 (2016) 473–546, https://doi.org/10.1016/j.surfrep.2016.06.001.
[310] Á. Kukovecz, G. Pótári, A. Oszkó, Z. Kónya, A. Erdőhelyi, J. Kiss, Probing the interaction of Au, Rh and bimetallic Au–Rh clusters with the TiO2 nanowire and nanotube support, Surf. Sci. 605 (2011) 1048–1055, https://doi.org/10.1016/j.susc.2011.03.003.
[311] D.C. Meier, D.W. Goodman, The influence of metal cluster size on adsorption energies: CO adsorbed on Au clusters supported on TiO2, J. Am. Chem. Soc. 126 (2004) 1892–1899, https://doi.org/10.1021/ja030359y.
[312] C. Lemire, R. Meyer, S.K. Shaikhutdinov, H.-J. Freund, CO adsorption on oxide supported gold: from small clusters to monolayer islands and three-dimensional nanoparticles, Surf. Sci. 552 (2004) 27–34, https://doi.org/10.1016/j.susc.2004.01.029.
[313] Y. Cai Chen, Z. Yan, D.W. Goodman, On the origin of the unique properties of supported Au nanoparticles, J. Am. Chem. Soc. 128 (2006) 6341–6346, https://doi.org/10.1021/ja0557536.
[314] M. Sterrer, M. Yulikov, T. Risse, H.-J. Freund, J. Carrasco, F. Illas, C. Di Valentin, L. Giordano, G. Pacchioni, When the reporter induces the effect: unusual IR spectra of CO on Au1/MgO(001)/Mo(001), Angew. Chem. Int. Ed. 45 (2006) 2633–2635, https://doi.org/10.1002/anie.200504473.
[315] P.-F. Sun, W.-L. Wang, X. Zhao, J.-S. Dang, Defective h-BN sheet embedded atomic metals as highly active and selective electrocatalysts for NH3 fabrication via NO reduction, Phys. Chem. Chem. Phys. 22 (2020) 22627–22634, https://doi.org/10.1039/D0CP03559A.
[316] Y. Zhang, X. Weng, H.H. Li, H.H. Li, M. Wei, J. Xiao, Z. Liu, M. Chen, Q. Fu, X. Bao, Hexagonal boron nitride cover on Pt(111): a new route to tune molecule–metal interaction and metal-catalyzed reactions, Nano Lett. 15 (2015) 3616–3623, https://doi.org/10.1021/acs.nanolett.5b01205.
[317] D. Deng, K.S. Novoselov, Q. Fu, N. Zheng, Z. Tian, X. Bao, Catalysis with two-dimensional materials and their heterostructures, Nat. Nanotechnol. 11 (2016) 218–230, https://doi.org/10.1038/nnano.2015.340.
[318] H. Wu, P. Ren, P. Zhao, Z. Gong, X. Wen, Y. Cui, Q. Fu, X. Bao, Dynamic nanoscale imaging of enriched CO adlayer on Pt(111) confined under h-BN monolayer in ambient pressure atmospheres, Nano Res. 12 (2019) 85–90, https://doi.org/10.1007/s12274-018-2184-8.
[319] W. Bi, Y. Hu, H. Jiang, L. Zhang, C. Li, Revealing the sudden alternation in Pt@h-BN nanoreactors for nearly 100% CO2-to-CH4 photoreduction, Adv. Funct. Mater. 31 (2021) 2010780, https://doi.org/10.1002/adfm.202010780.
[320] M. Mavrikakis, M.A. Barteau, Oxygenate reaction pathways on transition metal surfaces, J. Mol. Catal. Chem. 131 (1998) 135–147, https://doi.org/10.1016/S1381-1169(97)00261-6.
[321] L.V. Mattos, G. Jacobs, B.H. Davis, F.B. Noronha, Production of hydrogen from ethanol: review of reaction mechanism and catalyst deactivation, Chem. Rev. 112 (2012) 4094–4123, https://doi.org/10.1021/cr2000114.
[322] Z. Ferencz, A. Erdőhelyi, K. Baán, A. Oszkó, L. Óvári, Z. Kónya, C. Papp, H.-P. P. Steinrück, J. Kiss, A. Erdohelyi, K. Baán, A. Oszkó, L. Óvári, Z. Kónya, C. Papp, H.-P.P. Steinrück, J. Kiss, Effects of support and Rh additive on Co-based catalysts in the ethanol steam reforming reaction, ACS Catal. 4 (2014) 1205–1218, https://doi.org/10.1021/cs500045z.
[323] M.A. Henderson, Y. Zhou, J.M. White, Polymerization and decomposition of acetaldehyde on rutherium(001), J. Am. Chem. Soc. 111 (1989) 1185–1193, https://doi.org/10.1021/ja00186a004.
[324] C. Houtman, Divergent pathways of acetaldehyde and ethanol decarbonylation on the Rh(111) surface, J. Catal. 130 (1991) 528–546, https://doi.org/10.1016/0021-9517(91)90133-O.
[325] I. Kovács, A.P. Farkas, Á. Szitás, Z. Kónya, J. Kiss, Adsorption, polymerization and decomposition of acetaldehyde on clean and carbon-covered Rh(111) surfaces, Surf. Sci. 664 (2017) 129–136, https://doi.org/10.1016/j.susc.2017.05.016.
[326] I. Kovács, F. Ötvös, A.P. Farkas, J. Kiss, Z. Kónya, A round dance of acetaldehyde molecular ensembles on Rh(111) surface; formation and decomposition of various paraldehyde conformers, J. Mol. Struct. 1264 (2022) 133311, https://doi.org/10.1016/j.molstruc.2022.133311.
[327] M. Haruta, M. Daté, Advances in the catalysis of Au nanoparticles, Appl. Catal. Gen. 222 (2001) 427–437, https://doi.org/10.1016/S0926-860X(01)00847-X.
[328] T.E. James, S.L. Hemmingson, C.T. Campbell, Energy of supported metal catalysts: from single atoms to large metal nanoparticles, ACS Catal. 5 (2015) 5673–5678, https://doi.org/10.1021/acscatal.5b01372.
[329] L. Liu, A. Corma, Metal catalysts for heterogeneous catalysis: from single atoms to nanoclusters and nanoparticles, Chem. Rev. 118 (2018) 4981–5079, https://doi.org/10.1021/acs.chemrev.7b00776.
[330] H.-J. Freund, N. Nilius, T. Risse, S. Schauermann, A fresh look at an old nano-technology: catalysis, Phys. Chem. Chem. Phys. 16 (2014) 8148, https://doi.org/10.1039/c3cp55231d.
[331] H.-J. Freund, The surface science of catalysis and more, using ultrathin oxide films as templates: a perspective, J. Am. Chem. Soc. 138 (2016) 8985–8996, https://doi.org/10.1021/jacs.6b05565.
[332] A. Sápi, T. Rajkumar, J. Kiss, Á. Kukovecz, Z. Kónya, G.A. Somorjai, Metallic nanoparticles in heterogeneous catalysis, Catal. Lett. 151 (2021) 2153–2175, https://doi.org/10.1007/s10562-020-03477-5.
[333] A.F. Lee, D.E. Gawthrope, N.J. Hart, K. Wilson, A Fast XPS study of the surface chemistry of ethanol over Pt{111, Surf. Sci. 548 (2004) 200–208, https://doi.org/10.1016/j.susc.2003.11.004.
[334] A. Gazsi, A. Koós, T. Bánsági, F. Solymosi, Adsorption and decomposition of ethanol on supported Au catalysts, Catal. Today 160 (2011) 70–78, https://doi.org/10.1016/j.cattod.2010.05.007.
[335] H. Ran, J. Yin, J. Zhang, Y. Zhang, J. He, N. Lv, H. Li, H. Li, Group IIIA single-metal atoms anchored on hexagonal boron nitride for selective adsorption desulfurization via S–M bonds, Inorg. Chem. 62 (2023) 4883–4893, https://doi.org/10.1021/acs.inorgchem.2c04228.
[336] S. Kattel, P. Liu, J.G. Chen, Tuning selectivity of CO2 hydrogenation reactions at the metal/oxide interface, J. Am. Chem. Soc. 139 (2017) 9739–9754, https://doi.org/10.1021/jacs.7b05362.
[337] C. Lentz, S.P. Jand, J. Melke, C. Roth, P. Kaghazchi, DRIFTS study of CO adsorption on Pt nanoparticles supported by DFT calculations, J. Mol. Catal. Chem. 426 (2017) 1–9, https://doi.org/10.1016/j.molcata.2016.10.002.
[338] M.J.S. Farias, C. Busó-Rogero, A.A. Tanaka, E. Herrero, J.M. Feliu, Monitoring of CO binding sites on stepped Pt single crystal electrodes in alkaline solutions by in situ FTIR spectroscopy, Langmuir 36 (2020) 704–714, https://doi.org/10.1021/acs.langmuir.9b02928.
[339] Z. Xin, K. Duan, Q. Zhuo, Q. He, X. Zhang, C. Zheng, X. Han, T. Han, Z. Fu, X. Xu, X. Zhao, Novel nanozyme Ag/Fe3O4@h-BN with peroxidase-mimicking and oxidase-mimicking activities for dye degradation, As(V) removal and detection, Chem. Eng. J. 461 (2023) 141589, https://doi.org/10.1016/j.cej.2023.141589.
[340] H. Yang, L. Wang, S. Xu, Y. Cao, P. He, J. Chen, Z. Zheng, H. Li, Green and selective hydrogenation of aromatic diamines over the nanosheet Ru/g-C3N4-H2 catalyst prepared by ultrasonic assisted impregnation-deposition method, Green Energy Environ. 7 (2022) 1361–1376, https://doi.org/10.1016/j.gee.2021.01.003.
[341] R. Qin, L. Zhou, P. Liu, Y. Gong, K. Liu, C. Xu, Y. Zhao, L. Gu, G. Fu, N. Zheng, Alkali ions secure hydrides for catalytic hydrogenation, Nat. Catal. 3 (2020) 703–709, https://doi.org/10.1038/s41929-020-0481-6.
[342] S.J. Tauster, S.C. Fung, R.T.K. Baker, J.A. Horsley, Strong interactions in supported-metal catalysts, Science 211 (1981) 1121–1125, https://doi.org/10.1126/science.211.4487.1121.
[343] J. Dong, Q. Fu, H. Li, J. Xiao, B. Yang, B. Zhang, Y. Bai, T. Song, R. Zhang, L. Gao, J. Cai, H. Zhang, Z. Liu, X. Bao, Reaction-induced strong metal–support interactions between metals and inert boron nitride nanosheets, J. Am. Chem. Soc. 142 (2020) 17167–17174, https://doi.org/10.1021/jacs.0c08139.
[344] Z. Liu, B. Yan, S. Meng, R. Liu, W. Lu, J. Sheng, Y. Yi, A. Lu, Plasma tuning local environment of hexagonal boron nitride for oxidative dehydrogenation of propane, Angew. Chem. Int. Ed. 60 (2021) 19691–19695, https://doi.org/10.1002/anie.202106713.
[345] L. Shi, D. Wang, W. Song, D. Shao, W.W.-P. Zhang, A.A.-H. Lu, Edge-hydroxylated boron nitride for oxidative dehydrogenation of propane to propylene, ChemCatChem 9 (2017) 1788–1793, https://doi.org/10.1002/cctc.201700004.
[346] T. Song, J. Dong, R. Li, X. Xu, M. Hiroaki, B. Yang, R. Zhang, Y. Bai, H. Xin, L. Lin, R. Mu, Q. Fu, X. Bao, Oxidative strong metal–support interactions between metals and inert boron nitride, J. Phys. Chem. Lett. 12 (2021) 4187–4194, https://doi.org/10.1021/acs.jpclett.1c00934.
[347] Y. Xu, Z. An, X. Yu, J. Yao, Q. Lv, H. Yang, Z. Lv, H. Guo, Q. Jiang, W. Liu, L. Wu, L. Tan, Y. Dai, Y. Tang, Enhanced catalytic stability and structural evolution of Rh-BN interface in dry reforming of methane under intensified CO2 partial pressure, J. Catal. 427 (2023) 115094, https://doi.org/10.1016/j.jcat.2023.08.010.
[348] Y. Kim, S. Kang, D. Kang, K.R. Lee, C.K. Song, J. Sung, J.S. Kim, H. Lee, J. Park, J. Yi, Single-phase Formation of Rh2O3 nanoparticles on h-BN support for highly controlled methane partial oxidation to syngas, Angew. Chem. Int. Ed. 60 (2021) 25411–25418, https://doi.org/10.1002/anie.202110292.
[349] P. Torniainen, X. Chu, L. Schmidt, Comparison of monolith-supported metals for the direct oxidation of methane to syngas, J. Catal. 146 (1994) 1–10, https://doi.org/10.1016/0021-9517(94)90002-7.
[350] I. Tavazzi, A. Beretta, G. Groppi, P. Forzatti, Development of a molecular kinetic scheme for methane partial oxidation over a Rh/α-Al2O3 catalyst, J. Catal. 241 (2006) 1–13, https://doi.org/10.1016/j.jcat.2006.03.018.
[351] Y. Wang, Z. Song, D. Ma, H. Luo, D. Liang, X. Bao, Characterization of Rh-based catalysts with EPR, TPR, IR and XPS, J. Mol. Catal. Chem. 149 (1999) 51–61, https://doi.org/10.1016/S1381-1169(99)00181-8.
[352] A.A. Tonkikh, E.N. Voloshina, P. Werner, H. Blumtritt, B. Senkovskiy, G. Güntherodt, S.S.P. Parkin, Y.S. Dedkov, Structural and electronic properties of epitaxial multilayer h-BN on Ni(111) for spintronics applications, Sci. Rep. 6 (2016) 23547, https://doi.org/10.1038/srep23547.
[353] Y. Huang, Y. Gu, X. Liu, T. Deng, S. Dai, J. Qu, G. Yang, L. Qu, Reusable ring-like Fe3O4/Au nanozymes with enhanced peroxidase-like activities for colorimetric-SERS dual-mode sensing of biomolecules in human blood, Biosens. Bioelectron. 209 (2022) 114253, https://doi.org/10.1016/j.bios.2022.114253.

[354] W. Duan, Z. Qiu, S. Cao, Q. Guo, J. Huang, J. Xing, X. Lu, J. Zeng, Pd–Fe3O4 Janus nanozyme with rational design for ultrasensitive colorimetric detection of biothiols, Biosens. Bioelectron. 196 (2022) 113724, https://doi.org/10.1016/j.bios.2021.113724.
[355] T.-M. Tran-Thuy, C.-C. Chen, S.D. Lin, Spectroscopic studies of how moisture enhances CO oxidation over Au/BN at ambient temperature, ACS Catal. 7 (2017) 4304–4312, https://doi.org/10.1021/acscatal.7b01374.
[356] J.C.S. Wu, H.-C. Chou, Bimetallic Rh–Ni/BN catalyst for methane reforming with CO2, Chem. Eng. J. 148 (2009) 539–545, https://doi.org/10.1016/j.cej.2009.01.011.
[357] W. Zhu, Z. Wu, G.S. Foo, X. Gao, M. Zhou, B. Liu, G.M. Veith, P. Wu, K. L. Browning, H.N. Lee, H. Li, S. Dai, H. Zhu, Taming interfacial electronic properties of platinum nanoparticles on vacancy-abundant boron nitride nanosheets for enhanced catalysis, Nat. Commun. 8 (2017) 15291, https://doi.org/10.1038/ncomms15291.
[358] K. Zhang, Y. Feng, F. Wang, Z. Yang, J. Wang, Two dimensional hexagonal boron nitride (2D-hBN): synthesis, properties and applications, J. Mater. Chem. C 5 (2017) 11992–12022, https://doi.org/10.1039/C7TC04300G.
[359] Q. Fu, X. Bao, Surface chemistry and catalysis confined under two-dimensional materials, Chem. Soc. Rev. 46 (2017) 1842–1874, https://doi.org/10.1039/C6CS00424E.
[360] X. Han, Q. Gao, Z. Yan, M. Ji, C. Long, H. Zhu, Electrocatalysis in confined spaces: interplay between well-defined materials and the microenvironment, Nanoscale 13 (2021) 1515–1528, https://doi.org/10.1039/D0NR08237F.
[361] S. Chen, C. Zhu, H. Gu, L. Wang, J. Qi, L. Zhong, Z. Zhang, C. Yang, G. Shi, S. Zhao, S. Li, K. Liu, L. Zhang, Enhanced electrochemical methanation of carbon dioxide at the single-layer hexagonal boron nitride/Cu interfacial perimeter, Nano Lett. 21 (2021) 4469–4476, https://doi.org/10.1021/acs.nanolett.1c01258.
[362] A.M. Kovalskii, I.N. Volkov, N.D. Evdokimenko, O.P. Tkachenko, D.V. Leybo, I. V. Chepkasov, Z.I. Popov, A.T. Matveev, A. Manakhov, E.S. Permyakova, A. S. Konopatsky, A.L. Kustov, D.V. Golberg, D.V. Shtansky, Hexagonal BN- and BNO-supported Au and Pt nanocatalysts in carbon monoxide oxidation and carbon dioxide hydrogenation reactions, Appl. Catal. B Environ. 303 (2022) 120891, https://doi.org/10.1016/j.apcatb.2021.120891.
[363] N. Jia, Q. Weng, Y. Shi, X. Shi, X. Chen, P. Chen, Z. An, Y. Chen, N-doped carbon nanocages: bifunctional electrocatalysts for the oxygen reduction and evolution reactions, Nano Res. 11 (2018) 1905–1916, https://doi.org/10.1007/s12274-017-1808-8.
[364] C. Zhang, B. Wang, X. Shen, J. Liu, X. Kong, S.S.C. Chuang, D. Yang, A. Dong, Z. Peng, A nitrogen-doped ordered mesoporous carbon/graphene framework as bifunctional electrocatalyst for oxygen reduction and evolution reactions, Nano Energy 30 (2016) 503–510, https://doi.org/10.1016/j.nanoen.2016.10.051.
[365] T. Ma, H. Li, X. Zheng, S. Wang, X. Wang, H. Zhao, S. Han, J. Liu, R. Zhang, P. Zhu, Y. Long, J. Cheng, Y. Ma, Y. Zhao, C. Jin, X. Yu, Ultrastrong boron frameworks in ZrB12 : a highway for electron conducting, Adv. Mater. 29 (2017) 1604003, https://doi.org/10.1002/adma.201604003.
[366] C.-Y. Hsu, S.K. Saraswat, A.A. Lagum, A.M. Al-Ma'abreh, F. Molani, T.J. Al-Musawi, A.M.A. Mohamed, M.M. Kadhim, Study the single-atom Mn-doped catalysts on boron nitride sheet surface as cathode for oxygen reduction reaction in proton-exchange membrane fuel cells, Sustain. Chem. Pharm. 33 (2023) 101115, https://doi.org/10.1016/j.scp.2023.101115.
[367] W. Zhan, J. Gao, X. Li, H. Wang, W. Gao, H. Yin, High-efficient OER/ORR bifunctional electrocatalysts based on hexagonal boron nitride enabled by co-doping of transition metal and carbon, Appl. Phys. Lett. 123 (2023) 73901, https://doi.org/10.1063/5.0165605.
[368] D. Perilli, C. Di Valentin, F. Studt, Can single metal atoms trapped in defective h-BN/Cu(111) improve electrocatalysis of the H 2 evolution reaction? J. Phys. Chem. C 124 (2020) 23690–23698, https://doi.org/10.1021/acs.jpcc.0c06750.
[369] J. Beckord, J.T. Diulus, Z. Novotny, J. Osterwalder, M. Hengsberger, Protected ultrathin cuprous oxide film for photocatalysis: excitation and relaxation dynamics, Phys. Rev. Mater. 7 (2023) 045801, https://doi.org/10.1103/PhysRevMaterials.7.045801.
[370] G. Venkateswarlu, D. Madhu, J.V. Rani, An effective performance of F-Doped hexagonal boron nitride nanosheets as cathode material in magnesium battery, Mater. Chem. Phys. 226 (2019) 356–361, https://doi.org/10.1016/j.matchemphys.2019.01.051.
[371] A. Efremova, T. Rajkumar, Á. Szamosvölgyi, A. Sápi, K. Baán, I. Szenti, J. Gómez-Pérez, G. Varga, J. Kiss, G. Halasi, Á. Kukovecz, Z. Kónya, Complexity of a Co3O4 system under ambient-pressure CO2 methanation: influence of bulk and surface properties on the catalytic performance, J. Phys. Chem. C 125 (2021) 7130–7141, https://doi.org/10.1021/acs.jpcc.0c09717.
[372] B. László, K. Baán, A. Oszkó, A. Erdőhelyi, J. Kiss, Z. Kónya, Hydrogen evolution in the photocatalytic reaction between methane and water in the presence of CO2 on titanate and titania supported Rh and Au catalysts, Top. Catal. 61 (2018) 875–888, https://doi.org/10.1007/s11244-018-0936-z.
[373] G. Varga, I. Szenti, J. Kiss, K. Baán, G. Halasi, L. Óvári, Á. Szamosvölgyi, R. Mucsi, E. Dodony, Z. Fogarassy, B. Pécz, L. Olivi, A. Sápi, Á. Kukovecz, Z. Kónya, Decisive role of Cu/Co interfaces in copper cobaltite derivatives for high performance CO2 methanation catalyst, J. CO2 Util. 75 (2023) 102582, https://doi.org/10.1016/j.jcou.2023.102582.
[374] X. Fang, J. Wang, Y. Yu, S. Kang, L. Cui, Self-assembled CdS@BN core-shell photocatalysts for efficient visible-light-driven photocatalytic hydrogen evolution, Int. J. Hydrogen Energy 45 (2020) 14841–14848, https://doi.org/10.1016/j.ijhydene.2020.03.199.
[375] L. Song, S. Zhang, S. Sun, J. Wei, E. Liu, Performance and mechanism on hydrogen evolution of two-dimensional boron nitride under mechanical vibration, Fuel 331 (2023) 125765, https://doi.org/10.1016/j.fuel.2022.125765.
[376] G.S. Selopal, O. Abdelkarim, J. Kaur, J. Liu, L. Jin, Z. Chen, F. Navarro-Pardo, S. Manzhos, S. Sun, A. Yurtsever, H. Zarrin, Z.M. Wang, F. Rosei, Surface engineering of two-dimensional hexagonal boron-nitride for optoelectronic devices, Nanoscale 15 (2023) 15810–15830, https://doi.org/10.1039/D3NR03864E.